Bioelectrochemical Systems: Microbiology, Catalysts, Processes and Applications

Heyang Yuan

Dissertation submitted to the faculty of the Virginia Polytechnic Institute and State University in partial fulfillment of the requirements for the degree of

Doctor of Philosophy
In
Civil Engineering

Zhen He
Amanda J. Morris
Amy J. Pruden-Bagchi
Marc A. Edwards

October 4, 2017
Blacksburg, VA

Keywords: environmental engineering, bioelectrochemical systems, wastewater treatment, desalination, microbial community, antibiotic resistance genes, catalytic materials

Bioelectrochemical Systems: Microbiology, Catalysts, Processes and Applications

Heyang Yuan

ABSTRACT (academic)

The treatment of water and wastewater is energy intensive, and there is an urgent need to develop new approaches to address the water-energy challenges. Bioelectrochemical systems (BES) are energy-efficient technologies that can treat wastewater and simultaneously achieve multiple functions such as energy generation, hydrogen production and/or desalination. The objectives of this dissertation are to understand the fundamental microbiology of BES, develop cost-effective cathode catalysts, optimize the process engineering and identify the application niches. It has been shown in Chapter 2 that electrochemically active bacteria can take advantage of shuttle-mediated EET and create optimal anode salinities for their dominance. A novel statistical model has been developed based on the taxonomic data to understand and predict functional dynamics and current production. In Chapter 3, 4 and 5, three cathode catalyst (i.e., N- and S- co-doped porous carbon nanosheets, N-doped bamboo-like CNTs and MoS_2 coated on CNTs) have been synthesized and showed effective catalysis of oxygen reduction reaction or hydrogen evolution reaction in BES. Chapter 6, 7 and 8 have demonstrated how BES can be combined with forward osmosis to enhance desalination or achieve self-powered hydrogen production. Mathematical models have been developed to predict the performance of the integrated systems. In Chapter 9, BES have been used as a research platform to understand the fate and removal of antibiotic resistant genes under anaerobic conditions. The studies in this dissertation have collectively demonstrated that BES may hold great promise for energy-efficient water and wastewater treatment.

Bioelectrochemical Systems: Microbiology, Catalysts, Processes and Applications

Heyang Yuan

General Audience Abstract

Water and energy are prerequisites to life. Every day, a lot of energy and money are spent on treating wastewater and producing fresh water. Bioelectrochemical systems (BES) are new technologies that can treat water and wastewater with low energy consumption. BES typically consist of an anode (where microorganisms break down organic matter) and a cathode, and work like a battery. Currently, BES are only studied in laboratories and not applied in real-world situations, because the performance needs to be improved and fundamentals remain to be better understood. The studies in this dissertation aim to address these problems and make BES toward practice. It has been shown in Chapter 2 that, under high salinity, some bacteria grow faster in the anode and the BES can produce higher electricity. It is difficult to understand the roles of every bacterium with current molecular techniques, and thus statistical methods are applied to estimate their possible functions. In Chapter 3, 4 and 5, three materials have been fabricated and functioned as the catalysts for electricity generation. Chapter 6, 7 and 8 have demonstrated how BES can be combined with forward osmosis, a spontaneous water diffusion process, to enhance desalination or achieve self-powered hydrogen production. Mathematical equations have been combined to simulate the process of biological metabolisms, water diffusion and ion migration. In Chapter 9, BES have been shown to remove antibiotic resistant gene, an emerging contaminant caused by the excessive use of antibiotics. The studies in this dissertation have collectively demonstrated that BES may be the answer to future water and wastewater treatment.

ACKNOWLEDGEMENTS

Back in 2013, I was trying to find a PhD position in Australia, because "it is close to home". With an ugly GPA and zero publication, I barely got any interview. Right before I was about to give up and plan how to make a living in some small town in China, I learnt from my undergraduate mentor that a friend of his, a Tongji alumni, had recently moved to Virginia Tech and was recruiting PhD students. I wrote an email to his friend, Dr. Zhen He, almost immediately. We had a nice skype talk and things went surprisingly well. At that time, all I knew was to take GRE and finish the application process. I did not know that a wonderful journey was about to start.

These four years would not have been so great without the guidance and support of my advisor, Dr. Zhen He, who not only provided me a wide range of research opportunities, but also shared his wisdom in every aspect of life with me. I would also like to give all my acknowledgments to my committee members, Dr. Amanda Morris, Dr. Amy Pruden and Dr. Marc Edwards for their time and valuable advices on my research.

Thank you all EBBL members: Dr. Fei Zhang, Dr. Zheng Ge, Dr. Jian Li, Dr. Qingyun Ping, Mohan Qin, Dr. Yaobin Lu, Xiaojin Li, Shuai Luo, Shiqiang Zou and Syeed Iskander, for the friendship, encouragement and help. Working with you is the luckiest thing I have ever experienced in my life so far.

I sincerely appreciate Dr. Brian Badgley's generosity for letting me conduct research in his lab and I am grateful to Dr. Shan Sun for sharing her knowledge with me. Many thanks to Dr. Junhong Chen, Dr. Yang Hou, Dr. Chris Yuan and Dr. Jianyang Li for collaborating with us.

I would like to thank EWR staffs Julie Petruska, Jody Smiley and Beth Lucas for their generous help. Thanks to Virginia Tech and the Qatar National Research Funds for providing the funding.

I would like to give my special thanks to my family, who always teach me that mental wealth is the key to true happiness. My deepest thanks are given to my wife, best friend and lover, Chang Liu, for her unconditional support.

I am grateful to be a Tongji and Virginia Tech alumni and will always remember the mottos:
同舟共济
Ut Prosim

TABLE OF CONTENTS

ATTRIBUTION

Each coauthor is duly credited for his or her contribution to this work, both in their sharing of ideas and technical expertise. Coauthors are listed in an alphabetical order (first name).

Amy Pruden, Ph.D., Professor
Department of Civil and Environmental Engineering, Virginia Polytechnic Institute and State University, Blacksburg, VA 24061
Coauthor of chapters 9

Brian D. Badgley, Ph.D., Assistant Professor
Department of Crop and Soil Environmental Sciences, Virginia Polytechnic Institute and State University, Blacksburg, VA 24061
Coauthor of chapters 2

Chris Yingchun Yuan, Ph.D., Associate Professor
Department of Mechanical Engineering, University of Wisconsin- Milwaukee, Milwaukee, WI 53211
Coauthor of chapters 3

Ibrahim M. Abu-Reesh, Ph.D., Professor
Department of Chemical Engineering, College of Engineering, Qatar University, Doha, P.O. Box 2713, Qatar
Coauthor of chapters 1, 2, 6, 7, 8, 9

Jennifer H. Miller, Ph.D.
Department of Civil and Environmental Engineering, Virginia Polytechnic Institute and State University, Blacksburg, VA 24061
Coauthor of chapters 9

Jianyang Li, Ph.D.

Department of Mechanical Engineering, University of Wisconsin- Milwaukee, Milwaukee, WI 53211
Coauthor of chapters 3

Junhong Chen, Ph.D., Professor
Department of Mechanical Engineering, University of Wisconsin-Milwaukee, Milwaukee, WI 53211
Coauthor of chapters 1, 4, 5

Mohan Qin, Ph.D. student
Department of Civil and Environmental Engineering, Virginia Polytechnic Institute and State University, Blacksburg, VA 24061
Coauthor of chapters 1

Shan Sun, Ph.D.
Department of Crop and Soil Environmental Sciences, Virginia Polytechnic Institute and State University, Blacksburg, VA 24061
Coauthor of chapters 2

Shumao Cui, Ph.D.
Department of Mechanical Engineering, University of Wisconsin-Milwaukee, Milwaukee, WI 53211
Coauthor of chapters 5

Xiaoru Guo, Ph.D. student
Department of Mechanical Engineering, University of Wisconsin-Milwaukee, Milwaukee, WI 53211
Coauthor of chapters 4, 5

Yang Hou, Ph.D.

Department of Mechanical Engineering, University of Wisconsin-Milwaukee, Milwaukee, WI 53211
Coauthor of chapters 1, 4, 5

Yaobin Lu, Ph.D.
Department of Civil and Environmental Engineering, Virginia Polytechnic Institute and State University, Blacksburg, VA 24061
Coauthor of chapters 1, 8

Zhen He, Ph.D., Professor
Department of Civil and Environmental Engineering, Virginia Polytechnic Institute and State University, Blacksburg, VA 24061
Coauthor of chapters 1, 2, 3, 4, 5, 6, 7, 8, 9

Zhenhai Wen, Ph.D.
Department of Mechanical Engineering, University of Wisconsin-Milwaukee, Milwaukee, WI 53211
Coauthor of chapters 4, 5

CHAPTER 1: Overview

1.1 Water-energy nexus in water and wastewater treatment

The growing demand for water and energy has become a critical issue in the 21st Century. Globally, there are about 2.5 billion people suffering from water sanitation problems. Meanwhile, more than 1.3 billion people lacking access to electricity [1]. Due to the rapid industrialization and urbanization, the world's water and energy consumption are estimated to increase by 55% by 2050 and 48% by 2040, respectively [1, 2].

There exists a strong nexus between water and energy. Take seawater desalination as an example, reverse osmosis, one of the most commonly used desalination technologies, consumes >2 kW to generate 1 m^3 of freshwater [3]. For wastewater treatment, conventional activated sludge process consumes 0.6 kW m^{-3} of energy, more than 50% of which is attributed to aeration [4]. It is estimated that water and wastewater utilities account for ~4% of the total electricity consumption in the USA, namely 35% of the total municipal energy budgets [5]. Given that fossil fuels are the main energy source, the energy-intensive water and wastewater treatment can cause social-economic impacts and be a major contributor to greenhouse effects.

Wastewater is now considered more as a resource than a waste. Domestic wastewater with 500 mg L^{-1} COD (chemical oxygen demand) is estimated to contain a potential energy of 1.93 kWh m^{-3} [4]. This energy may not be effectively recovered by well-developed anaerobic digestion, which is mainly applied to treat high-strength wastes (e.g., waste sludge). In addition, the inefficient collection could result in the release of CH_4 to the environment, whose global warming impact is 25 times higher that CO_2 [6]. Hence, there is an urgent need to develop energy-efficient and environmentally friendly methods for sustainable water and wastewater treatment.

1.2 Bioelectrochemical systems (BES)

Bioelectrochemical systems (BES) are emerging technologies that can treat wastewater at low energy consumption, and simultaneously achieve various functions such as electricity generation (microbial fuel cells (MFCs)), hydrogen production (microbial electrolysis cells (MECs)), and desalination (microbial desalination cells (MDCs)) [7]. In a typical MFC (Figure 1.1A), microorganisms in the anode degrade organic matter (e.g., acetate, Equation 1.1) and release

electrons extracellularly for respiration. These electrons are transferred spontaneously to the cathode to reduce terminal electron acceptors (e.g., oxygen, Equation 1.2). As such, organic matter is removed and energy is produced. In an MEC (Figure 1.1B), the electrons are driven by a small external voltage of >0.2 V and transferred to the cathode to reduce protons to hydrogen gas (Equation 1.3) at an energy input much lower than that of conventional water splitting [8]. An MDC contains an anion exchange membrane (AEM) and a cation exchange membrane (CEM) between an anode and a cathode to form a desalination chamber [9] (Figure 1.1C). Ions in the salt water are driven by the electrostatic force and migrate to the anode and cathode, and the desalination is accomplished.

$$2HCO_3^- + 9H^+ + 8e^- \rightarrow CH_3COO^- + 4H_2O, E_0 = 0.19\,V\ vs.\ SHE \quad (1.1)$$

$$O_2 + 4H^+ + 4e^- \rightarrow 2H_2O, E_0 = 1.23\,V\ vs.\ SHE \quad (1.2)$$

$$2H^+ + 2e^- \rightarrow H_2, E_0 = 0\,V\ vs.\ SHE \quad (1.3)$$

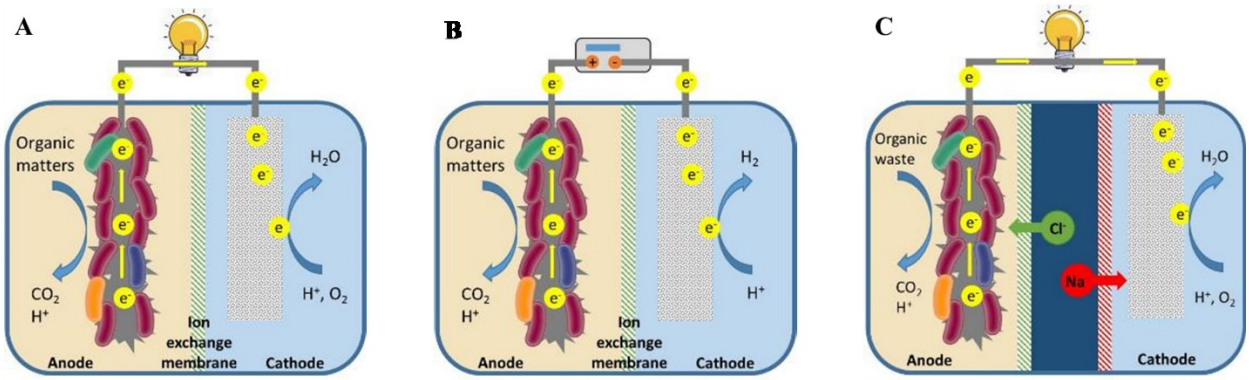

Figure 1.1 Schematic of (A) an MFC, (B) an MEC and (C) an MDC.

BES are advantageous over conventional water and wastewater treatment technologies in many aspects. First, BES are energy efficient. According to the state-of-art technology, an MFC consumes 0.024 kW m^{-3} but produces 0.026 kW m^{-3} [10]. Thus, BES can theoretically achieve a positive energy balance. Second, as an anaerobic biotechnology, BES produce less waste sludge than activated sludge process does. While activated sludge process generates 0.4–0.8 g-volatile suspended solids (VSS) g^{-1}-COD, an MFC produces around 0.1 g-VSS g^{-1}-COD [11]. Because the disposal of the excess sludge consumes additional energy, the low sludge production of BES further highlights their high energy efficiency. Third, BES are resilient to environmental variation

and show strong operation stability [12]. BES do not require exogenous seed and can readily produce electricity by enriching the indigenous microorganisms in the wastewater. Moreover, BES are less sensitive to temperature compared with anaerobic digestion. Last but not least, BES convert organic matter to CO_2 and electricity, which is cleaner and more sustainable compared with anaerobic digestion. Life cycle assessment has suggested that BES may be advantageous over anaerobic digestion regarding the emission of greenhouse gas and hazardous chemicals [13].

Despite the great promise, the practical applications of BES are hindered by the low energy production, inefficient electron transfer and high capital cost [8, 14]. Microorganisms are playing a key role in energy production in BES, but the bioelectrochemical activity and microbial community in the anode are not fully understood. Meanwhile, the electrode materials and the cathode catalysts can account for >50% of capital cost. Platinum is a widely used lab-scale catalyst that can catalyze oxygen reduction reaction (ORR) in MFCs and hydrogen evolution reaction (HER) in MECs, but is not economically viable for large-scale applications. Because of the technological and economical challenges, BES currently do not seem competitive to conventional water and wastewater treatment technologies, and thus the fundamentals of BES warrant deeper understanding, the process needs to be optimized and the application niches should be identified [12].

1.3 Fundamentals of BES: microbiology

Electrochemically active microorganisms (also known as dissimilatory metal-reducing bacteria) can respire the anode electrode via three mechanisms: (1) soluble electron shuttles, (2) redox-active proteins on the cell membrane and/or (3) conductive pili [15]. The detailed extracellular electron transfer (EET) pathways of different organisms can be diverse. For example, *Geobacter*, one of the most widely studied electrochemically active organisms, uses the branched outer-membrane cytochrome system to transfer electrons out of the cell (Figure 1.2A) [16]. Another model organism, *Shewanella oneidensis*, perform EET with the metal-reducing pathway (Figure 1.2B) [17]. Since the first discovery of dissimilatory metal-reducing bacterium in 1999, many bacteria have been found to be capable of EET, including the opportunistic pathogens *Escherichia coli* and *Pseudomonas aeruginosa* [18]. It has been elucidated that *P. aeruginosa* excretes phenazine derivatives (e.g., phenazine-1-carboxylic acid, phenazine-1-carboxamide and

pyocyanin) as electron shuttles for EET [19]. These findings indicate that electrochemically active microorganisms are ubiquitous in the environment.

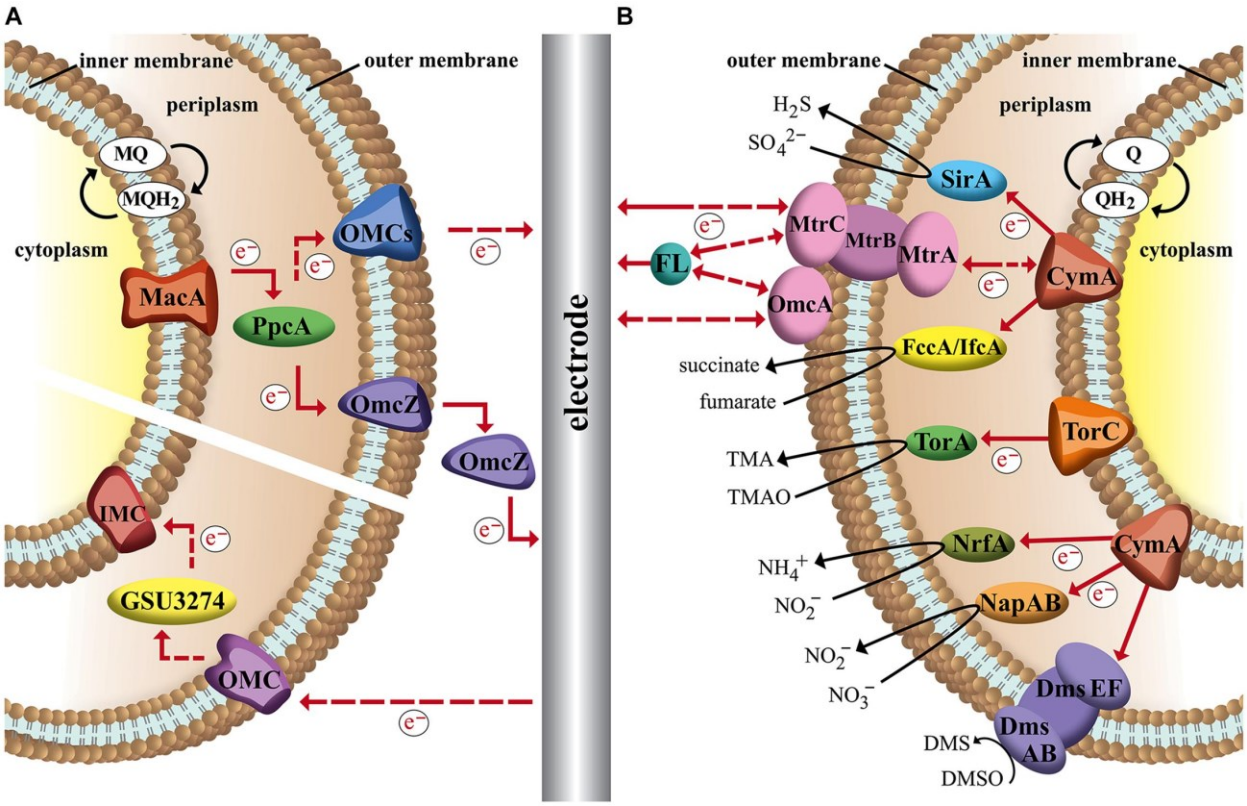

Figure 1.2 Schematic (A) Branched outer membrane cytochromes system of *Geobacter sulfurreducens* and (B) metal-reducing pathway and terminal reductases of *Shewanella oneidensis* [16]. Copyright © 2015 Kracke, Vassilev and Krömer.

Most of the studies on bioelectrochemical activity are conducted with pure cultures or defined co-cultures, and the research of mixed cultures are technically challenging [20]. A novel metatranscriptomic method was developed to study the regulation of global bioelectrochemical activity in the microbial community and demonstrated transcriptional responses of genes related to EET in the presence of electrochemical stimuli [21]. Based on the gene expression of cell activity and metabolism, a metabolic network composed of eleven dominant microbes in the MFC anode was established [22]. Such an "omic" approach presents a powerful tool to understand the functional dynamics of the mixed cultures under environmental changes.

The presence of electrode as an electron acceptor in BES anode favors the growth of electrochemically active microbes, and thus they are constantly found dominant in the anode community [23, 24]. However, the detailed microbial community structure and composition are affected by many factors, such as operational mode, carbon sources and salinity, etc. When an MFC was switched from closed circuit to open circuit, the community structure shifted significantly with denitrifying organisms becoming the dominant species [25], indicating the critical role of the anode electrode in shaping the microbial community. Distinct community structures were also observed when different carbon sources were used [26]. In the MFC fed with leachate, the decreased power density was accompanied by a declined fraction of *Geobacter* [27]. The salinity of the anolyte could be another important factor to the microbial community. It was reported that the Coulombic efficiency of an MFC noticeably dropped when the NaCl concentration in the substrate was higher than 5 g L^{-1}, suggesting an inhibitory effect on the bioelectrochemical activity [28]. A recent study showed that the MFCs under extremely saline conditions (100 – 200 g L^{-1} NaCl) generated low power, and the anode was dominated by *Halanaerobium* (abundance 85.7%), a strictly anaerobic and halophilic chemoorganotroph that had not been reported before [29].

Compared to the abundant studies on MFC, there is limited information regarding the microbial community in MDCs. Similar to the MFC experiments [28], increased NaCl in the middle chamber of a microbial electrodialysis cell led to decreased CE [30]. However, an increased proportion of *Geobacter* and a distinct change of community population were observed at higher NaCl concentration, which did not seem consistent with the declined system performance. The community profile in MDCs was noticeably different from that in MFCs [31], and became less diverse after long-term operation [32]. In another study where four MDCs were hydraulically connected, the first MDC achieved the highest power density, with *Geobacter* not being detected and fermenters being the dominant species [33]. These studies have collectively highlighted the lack of knowledge of microbial ecology in MDCs.

1.4 Fundamentals of BES: electrode

(This section has been published as: Heyang Yuan and Zhen He. "Graphene-modified electrodes for enhancing the performance of microbial fuel cells." Nanoscale (2015): 7, 7022-7029.)

As earlier mentioned, the development of BES has been hindered by the low charge transfer efficiency of electrodes and the high cost of catalysts [14, 34]. To address these issues, a variety of materials and their modifications, including carbon/graphite materials, carbon nanotubes (CNTs), nanostructured materials and non-precious metals, have been studied, as reviewed in detail elsewhere [35, 36]. While these materials have shown certain promise, their applications are still limited by inherent drawbacks such as low specific surface area, low conductivity, poor biocompatibility, and/or complicated synthesis procedures.

Among those newly developed materials, graphene has been of great interest since the first demonstration of its facile isolation in 2004 [37]. This two-dimensional sheet formed of sp^2 hybridized carbon atoms exhibits outstanding physical properties, including high mechanical strength, high thermal conductivity and good elasticity [38-40]. Its maximal specific surface area is estimated to be 2630 $m^2\ g^{-1}$, several times higher than that of other carbon-based nanomaterials [41]. Furthermore, the superior electrical properties make graphene a promising material in applications of electronics. It has been reported that the charge carrier mobility of suspending single layer graphene can be higher than 200000 $cm^2\ V^{-1}\ s^{-1}$ [42]. Consequently, electrons travel in graphene at a Fermi velocity of 10^6 m s^{-1} without scattering, known as ballistic conduction [43]. These unique properties are tunable towards specific applications via different synthetic procedures [44, 45].

Graphene-based materials are a promising candidate for highly efficient BES anode [46, 47]. It has been discussed that graphene-based electrode can enhance EET efficiency, increase specific surface area and improved multi-phase interactions in BES anode [48]. Graphene-based materials have also been studied as the cathode electrode and can carry out ORR via efficient pathway (i.e. four-electron transfer), abundant active sites and high conductivity [49]. Therefore, graphene and its modifications may substantially decrease the loss of electrical potential of both the anode and the cathode electrodes, and are highly attractive for BES application.

In most cases, the enhanced performance of anode electrodes by graphene-based materials is a synergic effect [50-53]. For example, a chitosan/vacuum-stripped graphene scaffold composite with hierarchically porous 3D structure had a specific surface area of 248 m^2 g^{-1} owing to the property of graphene [54]. Meanwhile, its charge transfer resistance was reduced with increased graphene loading, with the lowest value of 150 Ω for 50 wt% among a series of loading rates. Together with the good biofilm adhesion and high production of endogenous mediator stimulated by the biocompatible chitosan, current and power density of the MFC containing this composite as its anode electrode were 16 and 78 times higher than the control with the carbon cloth anode, respectively. The multi-directional improvement was also found in cathode modifications: implantation of mesoporous graphitic C_3N_4 simultaneously facilitated favorable ORR pathway and increased active sites and conductivity [55]. Therefore, synergic effects are desirable as electrode performance benefited from multiplication instead of addition of the enhancement of individual aspects. This may be instructive for the preparation and modification of graphene-based electrode and catalysts in the future.

Despite their great promise in BES, graphene-based materials suffer from relatively complicated synthesis procedures. In general, graphene electrodes are prepared through three steps: graphene oxide (GO) synthesis, GO reduction to graphene, and modification [56]. This approach, and other methods including chemical vapor deposition, unzipping of MWCNTs and detonation, etc., are either burdensome, energy/time-consuming or involved with hazardous chemicals [57-59], thereby not suitable for large-scale applications. In-situ reduction of GO to graphene by bacteria or phytoextracts could be an effective option for anode electrode fabrication, as it meets the requirement of sustainability and green chemistry [60]. For cathode electrode, nitrogen-doped graphene is a competitive material because of its outstanding ORR catalysis, but does not seem to prevail before economic synthesis methods with optimized nitrogen types and contents are developed [61].

By far there was were only a few studies using graphene to enhance performance in BES other than MFCs [62]. In a study of MECs, 3D MoS_2/NG nanosheet aerogels were synthesized through

a facile hydrothermal approach and used to catalyze HER. Although the loading rate of MoS_2/NG aerogels on the cathode electrode was only 25% that of Pt/C, its current density in MFC test was comparable to that of Pt/C. In addition, the MoS_2/NG aerogels outperformed pristine MoS_2 nanosheets and NG aerogels with respect to electrochemistry and catalysis. It can be expected that with the advances in graphene research, there will be more research using graphene materials as electrode and catalyst for improving BES performance in a broad range of applications, and in return that will be beneficial for identifying proper application niches for graphene material and stimulating more graphene research.

1.5 Fundamentals of BES: cathode catalysts

1.5.1 Oxygen reduction reaction catalysts in MFCs

(This section has been published as: Heyang Yuan, Yang Hou, Ibrahim M. Abu-Reesh, Junhong Chen, and Zhen He. "Oxygen reduction reaction catalysts used in microbial fuel cells for energy-efficient wastewater treatment: a review." Materials Horizons (2016): 3, 382-401.)

The ideal ORR catalysts in MFCs are expected to be cost effective and have high catalytic activity, because MFCs are engineered primarily for wastewater treatment, and thus the capital and maintenance costs should be comparable to conventional treatment technologies [12]. At this stage of the development, the energy generated by MFCs is mainly used to balance the energy consumption rather than to generate additional economic benefits [10], further highlighting the importance of economic feasibility of the cathode catalysts. Hence, properties associated with practicality, including simple and large-scale synthesis, low cost, and high durability should be given priority when developing ORR catalysts for MFC applications.

Besides the cost effectiveness, the durability of the ORR catalysts in MFCs is another major challenge, because the cathode is constantly exposed to wastewater containing organic matter, contaminants and microorganisms. In single-chamber MFCs, the catalysts directly contact the wastewater and may be poisoned by the intermediate products such as methanol, chloride, sulfide, etc. [63-65]. Furthermore, organisms can form biofilms on the cathode

surface and degenerate catalytic performance by blocking the O_2 transport [66, 67]. Although in some circumstances the biofilm may serve as a biocatalyst [68], the interaction between the organisms and the catalyst remains unknown and warrants further studies. Similar problems are also found in two-chamber MFCs, where the anode effluent is commonly introduced into the cathode for post-treatment [11]. Poisoning of the catalysts by intermediates leads to high potential loss and reduced power production. Previous studies showed an increased CH_4 production at a lower current, indicating the competition for substrates between exoelectrogens and methanogens [69]. To make MFCs for practical applications, the ORR catalysts must be tolerant to poisoning, resistant to biofouling and able to restore catalytic activity after cleaning.

Whilst ORR catalysts are developed to enhance MFC performance, MFCs also present a powerful tool to study the durability and activity of the catalysts. The assessment using MFCs provides insightful information that cannot be obtained by ex-situ electrochemical characterization methods. For example, multi-cycle cyclic voltammetry (CV) as a method to measure durability is typically accomplished with 6,000-10,000 cycles in ~48 h depending on the scan rate, which is much shorter than the operation period of MFCs (i.e., several weeks to months). Similarly, the chronoamperometric curve for assessing catalytic stability lasts only a few hours, and the typical operation potential (e.g., -0.4 V vs. Ag/AgCl) is much more negative than that in MFCs (i.e., ~0 V vs. Ag/AgCl). Electrochemical impedance spectrometry (EIS) can be used to measure the distribution of internal resistance [70], but the overall internal resistance for calculating the MPD cannot be obtained. In contrast, the measurement of polarization curve and cathode potential in MFCs not only yields the overall internal resistance, but can also be used for comparison of the concentration overpotential at high current output [71]. Moreover, long-term MFC experiments help gain a better understanding of the complicated effects of poisoning and fouling caused by real wastewater [72-74].

It should be noted that the choice of external resistance is critical when performing MFC experiments. The difference in current production between the catalysts of interest and the control Pt/C is artificially diminished by using a large resistance. As aforementioned, the current will

determine the anode potential and will consequently affect the microbial activity, metabolite production and fouling. It is thus recommended that, when evaluating the long-term stability, MFCs should be operated at a high current mode (i.e., low external resistance) and/or a high power mode (i.e., external resistance equals the internal resistance), which are the typical operational conditions in real applications.

MFC cathode catalysts have been comprehensively reviewed and some of the representative catalysts are summarized in Table 1.1. Carbon-based catalysts, particularly N-doped AC, may be the most promising candidate for practical applications. The normalized MPD of 1,210 mW $\$^{-1}$ achieved by the AC mixed with CB is by far the highest reported in the literature. Further studies are needed to understand the roles of AC precursors, elucidate the mechanisms of heteroatom doping and develop a simple treatment for mass production. Metal-based catalysts do not seem competitive compared with carbon materials in terms of durability and cost, but the hybridization of metal and carbon can combine the advantages of the individual components and thus greatly enhance catalytic performance. M-N-C complexes present a new group of catalysts with excellent catalytic activity and high stability, and are particularly attractive with the effective ORR catalysis under alkaline conditions. Finally, biocatalysts are sustainable and free, but the resilience towards fluctuation remains to be improved.

One of the advantages of biocatalysts over abiotic catalysts is the additional treatment of wastewater by microbes. However, recent studies have demonstrated that integrated catalyst-membrane assembly can also produce effluent with high quality [75]. Coating multiwalled CNTs on polyester nonwoven formed an ultrafiltration membrane with a pore size of ~65 nm that could simultaneously produce energy and filtrate wastewater in a single-chamber MFC [76]. The MFC using the membrane modified with a C–Mn–Fe–O catalyst could remove up to 90% COD and 80% NH_4^+-N [77]. In addition to the good performance, the integration of ORR catalysts with membranes can improve system stability. Fouling mitigation was observed when the membrane was coated with different catalysts [78, 79], possibly because the electric field reduced the deposition of sludge on the membrane surface, and the H_2O_2 produced by the cathode removed the foulants [80]. With stable

energy and water production, the catalyst-membrane assembly may be more cost-effective than individual MFCs and membrane bioreactors. It was estimated that the cathode membrane prepared from carbon foam and transition metals cost only 10% of the total price of Pt/C and commercial filtration membranes [81]. Such a combination may provide a new direction in the study of abiotic ORR catalysts for MFC-based wastewater treatment.

Regardless of the catalyst materials, biofouling is almost inevitable when the cathode electrode is exposed to wastewater. The inefficient ORR catalysis, i.e., the 2-e^- pathway with the production of H_2O_2, may provide a solution for the fouling issue. Most of the ORR catalysts discussed in this review produce a considerable amount of H_2O_2 under normal MFC operation. For example, at the MPD, C-CoPc generated a current density of 2.5 A m^{-2} and the corresponding cathode potential of -0.2 V vs. SCE. The electron transfer number at this cathode potential was measured to be 3, with 50% of the ORR product being hydrogen peroxide ions [82]. The high H_2O_2 production, as discussed in the catalyst-membrane assembly, may contribute to fouling mitigation. The study using graphite particles as the cathode electrode could produce 196.5 mg L^{-1} H_2O_2 in 24 h, but did not further investigate the effects on fouling [83]. Therefore, the relation between H_2O_2 production and biofilm formation can be a focus for future research.

The development of ORR catalysts can greatly benefit bioelectrochemical systems (BES) other than MFCs, such as MDCs and MECs. MDCs also use oxygen as the cathode electron acceptor and can achieve simultaneous wastewater treatment and desalination at low energy consumption [84, 85]. While the unit price of the ORR catalysts in MDCs remains the same as in MFCs, the cost effectiveness may be significantly increased when fresh water production and net energy balance are considered. MECs can produce hydrogen gas by using protons as the electron acceptor [86, 87]. Similar to ORR, HER is sluggish and needs the presence of catalysts [62, 88]. Multi-functional catalysts for ORR, OER (oxygen evolution reaction) and HER have recently been reported [89-93], which can make BES a more versatile technology that can be easily switched between MFC and MEC to meet the special requirement of applications. It can be expected that ORR catalysts will play an important role in energy-efficient water and wastewater treatment in the future, and there will be an increasing need for identifying their proper application niches.

Table 1.1 The synthesis/modification, stability and cost-effectiveness of representative ORR catalysts from each category.

	Category	Catalysts/Synthesis	n[a]	MPD[b]	Stability	Cost effectiveness	Ref.
Carbon-based catalysts	Carbon black	Polypyrrole/carbon black composite		401.8 mW m^{-2}	Biofilm formation	15 times that with Pt/C	[94]
	Activated carbon	Activated carbon/carbon black mixture		1210 mW m^{-2}	15% decrease in MPD after 16 months	1,210 mW $-1	[95]
	Carbon nanofibers	Alkaline treatment		61.3 mW m^{-2}		2.6 times that with Pt/C	[96]
	Carbon nanotubes	polyaniline/multi-walled CNTs composite		488 mW m^{-2}		31 mW $$^{-1}$	[97]
	Graphene	N/S co-doped carbon nanosheets	3.5	1.5 W m^{-2}	Stable after 6000 cycles of CV	10 mW $$^{-1}$	[98]
	Other carbon-based catalysts		3.5	2293 mW m^{-2}	Stable in long-term experiments	> 143 mW $-1 (free precursors)	[99]
Metal-based catalysts	Platinum	electron beam evaporation				Reduced Pt loading	[100]
	Silver nanoparticles				Inhibit bacterial growth		[101]
	Perovskite oxides			405 mW m^{-2}	15% decrease in MPD after 15 cycles	116 mW $-1	[102]
Metal-carbon hybrids	Metal-AC	Pyrolysis of Fe-EDTA and AC		1580 mW m^{-2}	No change in MPD after 4.5 months		[103]
	Metal-CNT	NiO/CNT with in-situ reduction and calcination	3.5	670 mW m^{-2}		45 mW $$^{-1}$	[104]
	Metal-graphite	Carbonized AgNPs/Fe3O4/GC	3.98	1712 mW m^{-2}	Inhibit bacterial growth		[105]
	Metal-graphene	N-doped graphene/CoNi alloy encased within bamboo-like CNT	3.63	2.0 mW m^{-2}		150 mW $$^{-1}$	[106]
Metal-nitrogen-carbon complexes	Metalmacrocycles	CoO-FePc mixture		654 mW m^{-2}	85% decrease in MPD after 60 days	11 mW $$^{-1}$	[107]
	N-Fe/Fe3C@C	Pyrolysis of cyanamide and FeCl3	3.98	4.2 W m^{-3}	Stable current output over 6 months	5% of that of Pt	[108]
Biocatalysts	Microorganisms	Mixed culture		554 mW m^{-2}	64% decrease in MPD after 9 cycles	Free	[109]
	Enzymes	Laccase		26 W m^{-3}	4% loss in potential after 5 days		[110]

[a] n, electron transfer number
[b] MPD, the maximum power density

1.5.2 Hydrogen evolution reaction catalysts in MECs

(This section has been published as: Heyang Yuan and Zhen He. "Noble-metal free catalysts for hydrogen evolution reaction in microbial electrolysis cells". The Chemical Record. In press.)

The HER can occur either via the Volmer–Heyrovsky mechanism (Equation 1.4 and Equation 1.5) or the Volmer-Tafel mechanism (Equation 1.4 and Equation 1.6) [111]:

$H_3O^+ + e^- + * \rightarrow H^* + H_2O$ (Volmer reaction in acid solutions, 1.4a)
$H_2O + e^- + * \rightarrow H^* + OH^-$ (Volmer reaction in alkaline solutions, 1.4b)
$H^* + H_3O^+ + e^- \rightarrow H_2 + H_2O$ (Heyrovsky reaction in acid solutions, 1.5a)
$H^* + H_2O + e^- \rightarrow H_2 + OH^-$ (Heyrovsky reaction in acid solutions, 1.5b)
$H^* + H^* \rightarrow H_2 + 2^*$ (Tafel reaction in acid and alkaline solutions, 1.6)

where * is an empty active site on the catalyst and H* indicates a hydrogen atom absorbed on the active site. The mechanisms suggest that the HER catalysis is strongly influenced by the hydrogen binding free energy, ΔG_{H^*}, and predict that an effective HER catalyst should have a $\Delta G_{H^*} \approx 0$. This explains that Pt with a slightly negative ΔG_{H^*} is the most active HER catalyst among a variety of metals [112].

In conventional electrolysis cells, the two half-cell reactions are oxygen evolution reaction in the anode (E^0 = 1.23 V vs. NHE, normal hydrogen electrode) and HER in the cathode (E^0 = 0 V vs. NHE). To overcome the unfavorable thermodynamics, a minimum external voltage of 1.23 V needs to be added. In practice, a higher voltage is applied due to the ohmic, activation and concentration energy losses. On the other hand, in MECs, exoelectrogens catalyze the oxidation of organic matter and produce a negative anode potential (e.g., CH_3COO^-/HCO_3^-, E^0 = -0.19 V vs. NHE). In real situations (e.g., wastewater as the anolyte) where the organic concentration is in millimole range and the pH is around 7, a voltage >0.2 V can lead to significant hydrogen production [86, 113], and thus the energy consumption by MECs is considerably less than that by conventional water splitting systems.

The electrochemical HER catalysis can be evaluated using linear sweep voltammetry (LSV). One parameter of interest from LSV is the onset potential, which is empirically defined as the potential at which the current density reaches 0.05-5 mA cm^{-2} in LSV [114]. Another important information derived from LSV is the Tafel plot, which can be expressed as the reduced Bulter-Volmer equation at large overpotential (e.g., $\eta > 50$ mV), i.e., Tafel equation [115].

$$\eta = b \ln(j_0) - b \ln(j) \quad (1.7)$$

where j_0 is the exchange current density and describes the intrinsic catalytic activity, and b is the Tafel slope that can provide insights into the rate determining step of the catalysis. At small overpotential, the Butler-Volmer equation can be simplified as follow:

$$j = \frac{F}{RT} j_0 \eta \quad (1.8)$$

$$R_{ct} = \frac{\eta}{j} = \frac{RT}{F j_0} \quad (1.9)$$

where F is the Faraday constant, R is the gas constant, T is the temperature, R_{ct} is the charge transfer resistance and related to the activation energy loss. Charge transfer resistance can also be measured using electrochemical impedance spectroscopy (EIS) [70]. Although it is rarely done, the charge transfer resistance obtained from EIS can serve as a supporting data of the R_{ct} calculated from the exchange current in the Tafel plot.

Cyclic voltammetry (CV) can be used to calculate the electrochemical active areas of the catalysts with the Randles-Sevcik equation (Equation 1.10) and a defined redox couple (e.g., ferrocyanide solution) [115]:

$$i_p = (2.69 \times 10^5) n^{3/2} A D^{1/2} C v^{1/2} \quad (1.10)$$

where i_p is the peak current, n is the number of electrons transferred, A is the electrode area, D is the diffusion coefficient of the redox couple, C is the concentration of the redox couple, and v is

the scan rate. In addition, CV over 3000 cycles is commonly used to evaluate the durability of the catalysts.

The ideal HER catalysts in MECs should be catalytically active, cost-effective, easy to synthesis, highly durable, resistant to biofouling and able to restore catalytic activity after proper cleaning. The durability and biofouling of the cathode catalysts in MECs and the consequent low gas purity present the major challenges, because the MEC cathode may be poisoned by organic matter, microorganisms and other chemicals from wastewater. For example, in single-chamber MECs, CO_2 is released via the metabolism of the anode microorganisms, which lowers the fraction of H_2 in the biogas. Moreover, the CO_2 and H_2 are scavenged by hydrogenotrophic methanogens to produce CH_4, further decreasing the H_2 content [116, 117]. In some cases, the microorganisms in the cathode can serve as the HER biocatalysts, but the biofilm may block the proton transport and inactivate the abiotic catalysts. The MECs with degenerated cathode catalysts produce not only less H_2 in the cathode, but also more CH_4 in the anode, as a result of the competition between exoelectrogens and acetoclastic methanogens at high internal resistance [69]. This demonstrates the complicated nature of MECs as a whole and the importance of the cathode catalysts to the overall MEC performance. In this regard, two-chamber MECs seem to be a more practical tool for the studies of cathode catalysts.

HER catalysts are developed to enhance MEC performance, and MECs in turn serve as a research platform to assess the catalyst durability, which is an important parameter not available from the electrochemical techniques. For example, multi-cycle CV is typically measured within 48 h, which is orders of magnitude shorter than the operation time of MECs (i.e., several weeks to months). Similarly, the chronoamperometry for durability analysis lasts for only a few hours, and the typical operation potential (e.g., -0.2 V vs. NHE) is more positive than that of the MEC cathode electrode (i.e., -0.41 V vs. NHE or more negative). Therefore, long-term MEC experiments can help gain a better understanding of the stability of the HER catalysts and should be routinely performed. It should be noted that the choice of external voltage is critical when performing MEC experiments [118]. Whereas the anode potential in electrochemical water splitting is determined by abiotic factors such as ohmic, activation and concentration overpotentials, and responds rapidly when the external voltage is changed, the MEC anode potential is further affected by the biotic factors and

needs up to several days to stabilize. The microbial activity and community in the MEC anode may shift under different external voltage or poised potential [21, 26], and thereby exert effects on the overall internal resistance and the hydrogen production. It is thus recommended that, when evaluating the long-term durability, multiple MECs should be operated at different external voltages and the voltage should be fixed throughout the experiment.

MFC cathode catalysts have been comprehensively reviewed and some of representative HER catalysts from each category are summarized in Table 1.2. Non-precious metals are widely used in bench and large scale experiments, but do not seem economically competitive mainly due to the corrosion behavior. In contrast, carbon-based catalysts, particularly carbon-metal hybrids, may be the most promising candidate for practical applications. The nano-$Mg(OH)_2$/graphene composites not only achieved a hydrogen production rate 1.3 times faster than Pt did, but also remained stable for 2 months with inhibited biofilm growth [119]. Finally, biocathode is sustainable and free, but the catalytic efficiency and the biogas purity need to be improved.

As previously mentioned, one of the MEC functions is to treat organic waste. An integrated catalyst-membrane assembly may be a promising strategy to improve the treatment performance of MECs without compromising the energy production. A nickel-based hollow-fiber membrane with an average pore size of 1 μm was prepared using a combined phase-inversion/sintering method and served the dual function as a HER catalyst and a filtration membrane [120]. The bioreactor with the catalytic membrane yielded a positive net energy and produced an effluent with low organic content. Graphene layer was later directly synthesized on the Ni hollow-fiber membrane to further improve the effluent quality [121]. The catalytic membrane was proven durable with low transmembrane pressure after long-term operation.

Table 1.2 The characteristics of representative HER catalysts from each category. $Rate_{Pt}$ refers to the hydrogen production rate of Pt control in the MEC.

Category	**Catalyst**	**Synthesis/ Community**	**Voltage (V)**	**Rate (m^3 m^{-2} d^{-1})**	**Rate (m^3 m^{-3} d^{-1})**	**$Rate_{Pt}$ (m^3 m^{-3} d^{-1})**	**Cathodic efficiency**	**Stability**	**Cost**	**Ref.**
Ni	Ni 210	Commercial	0.6		1.30	1.6	79%	Corrosion	\$2.82 m^{-2}	[122]
Mo	MoS_2	Commercial	0.7	0.048	1.20	1.8				[123]
Carbon-metal hybrids	NiFe LDH/Ni	Hydrothermal	0.8	0.018	2.11	2.01	97%	Corrosion		[124]
	3D MoS2/N-GAs	Liquid exfoliation/hydrothermal	0.8		0.19	0.31				[62]
	MoS_2@CNT	Hydrothermal	0.8	0.010	0.03	0.03	49%			[88]
	nano-$Mg(OH)_2$/Gr	Hydrothermal	0.7	0.126	0.63	0.49	83%	Stable over two months	1.7% of Pt	[119]
Biocatalysts	Mixed culture	*Desulfovibrio*/*Geobacter*	-0.7 vs. SHE		0.63					[125]
	Mixed culture		0.6	0.047	1.31	1.69	54.3	low CH_4	Free	[126]

Regardless of the catalyst properties, methane production is almost inevitable when organic substrate and microorganisms are present in the cathode. The localized H_2 and high pH may favor the growth of alkaliphilic hydrogenotrophic methanogens on the electrode surface [120]. As a consequence of the favorable micro-environment, CH_4 can account for 86% of the total biogas [117]. Instead of inhibiting methane production, recent studies used MECs to produce biohythane, an emerging fuel composed of biomethane and 5-10% biohydrogen [127]. The MEC produced biohythane 80% faster than an anaerobic digester due to the multiple pathways of biogas production, including fermentative and electrolytic hydrogen production, as well as hydrogenotrophic and electrochemical methanogenesis. The production of biohydrogen and biohythane is a result of the complicated microbial interactions and is thus difficult to be fully explored with experimental methods [128, 129]. We have previously developed models to simulate the system performance of microbial desalination cells [130, 131], and believe that mathematical modeling can provide a better understanding of hydrogen and methane production in MECs [132, 133]. It can be expected that MECs and other BES may be the solution to the problems surrounding water-energy nexus in the future, and the development of HER catalysts will be a key part of their practical applications.

1.6 Process engineering: combining BES with membrane technologies

(This section has been published as: Heyang Yuan and Zhen He. "Integrating Membrane Filtration into Bioelectrochemical Systems as Next Generation Energy-Efficient Wastewater Treatment Technologies for Water Reclamation: A Review." Bioresource Technology (2015): 195, 202-209.)

Although BES can significantly decrease the production of waste sludge [12], the effluent of BES still needs further treatment for direct discharge or reuse. To achieve high-quality effluent for potential reclamation, membrane filtration has been integrated into BES to take advantages of both BES and membrane bioreactors (MBR). Due to the relatively small pore size, the filtration process can effectively remove VSS and pathogens, thereby producing an effluent of high quality [134]. In addition, biomass is retained by the membrane in the reactor to improve treatment efficiency [135]. Based on the pore size, the membranes used in BES can be classified as dynamic membranes (DM, >1 μm) and ultrafiltration (UF, <0.1 μm). Membrane modules can be installed either in an

internal or external configuration. The major studies of integration of membrane filtration in BES are summarized in Table 1.3. These previous studies have collectively demonstrated that the membrane-BES systems possess the benefits of each component, and can address water-energy nexus through energy efficient treatment, energy recovery, and water reclamation. To better understand this integration towards the development of effective treatment technologies, several issues/challenges must be addressed.

First, integrating membrane filtration introduces new factors for energy consumption such as vacuum pressure for extracting final effluent. Although several studies have demonstrated that the membrane-integrated BES could theoretically achieve energy neutral or positive [136-138], energy performance has not been widely presented in the BES studies. A new parameter, normalized energy recovery (NER), has been proposed to present energy consumption and production. NER is expressed in either kWh m^{-3} or kWh kg^{-1}-COD. Future studies should really incorporate NER in data expression, and analyze both energy consumption and recovery to establish an energy balance for the developed system.

Second, like conventional MBRs, membrane fouling will be a significant challenge for the BES integrated with membrane filtration. It is expected that fouling mechanisms will be mostly similar to those in conventional MBRs. However, it will be of interest to investigate the interaction between fouling and electricity generation in the BES integrated with membrane filtration. The interaction could lie in two aspects, electricity generation alleviating membrane fouling and fouling affecting electricity production. Electricity generation could alleviate the fouling condition through stimulating the degradation of organic compounds and creating electrical field force. Moreover, the low pH in the anode due to the microbial respiration may serve as a fouling control when membranes are installed in the anode. ORR in the cathode through the 2-electron process will generate reactive hydroxide radicals, which may inhibit the formation of biofouling on the membrane surface.

Third, mutual benefits between the membrane modules and BES remain further exploration. Whist BES can alleviate membrane fouling, membranes modified with conductivity materials can function as electrode materials, thereby benefiting BES performance. For example, a BES with

conductive nickel-based hollow-fiber membranes as both filtration component and cathode electrode can recover energy in the form of biogas (CH_4 and H_2) [120]. However, energy neutrality could not be achieved in such a system because of the relatively low conversion efficiency of combustion. The membrane's ohmic resistance can be reduced by coating conductive MWCNTs or synthesizing the membrane with nickel [76, 120].

Fourth, the material science of filtration membranes must be advanced to enhance the performance of filtration. For example, fouling can be mitigated by doping polymers such as polydopamine or anthraquinone/polypyrrole in the membrane [139, 140]. In a recent study, the inexpensive carbon powder was used to synthesize filtration membrane-cathode assembly, resulting in a remarkable performance with respect to both wastewater treatment and energy production [141]. These studies are indicative that multi-functional membrane unit may play a critical role in the development of membrane-BES.

Fifth, system scaling-up remains a significant challenge for BES to demonstrate the feasibility of the membrane-BES for practical application. It strongly relates to the configuration, for instance, internal or external integration of membrane modules. Scaling up the membrane-BES should take advantage of the existing efforts of scaling up BES (MFCs, MECs, and MDCs). Moreover, the successful development of MBR and BES models suggests that mathematical modeling can be a powerful tool to help optimize the reactor configuration and predict system performance [131, 142]. As one of the most critical parameters for scaling up, the cost of membrane-BES should be reported in details in future studies to help researchers better understand the limitations of the system. The cost to benefit ratio is another helpful index to compare membrane-BES with existing technologies. While the large-scale membrane-BES system is difficult to be established and no data are currently available for the analysis of economic feasibility and life cycle assessment, the comparison between liter-scale systems and milliliter-scale systems may provide insight into the performance, cost and environmental impact at larger scale.

Table 1.3 Summary of the studies about the membrane-integrated BES.

Membrane	Pore size	Configuration	Carbon source	COD removal (%)	NH_4^+-N removal (%)	Turbidity (NTU)	Maximum power density	Ref.
SS mesh	40 μm	separator/cathode	acetate	86.6-93.9	92.7-99.6	~0.8	4.35 W m^{-3}	[136]
nylon mesh	74 μm	cathode		89.6		~0.8	6.0 W m^{-3}	[143]
pyrrole-modified polyester filter cloth		cathode	glucose	~100			2.6 mW m^{-2}	[144]
non-woven cloth	50 μm	cathode	acetate	87.4-91.2	69.5-97.6	<2	7.6 W m^{-3}	[144]
SS mesh	48 μm	separator/cathode	acetate	81.0-92.8	95.3-98.5	0.80	8.56 W m^{-3}	[145]
SS mesh	15 μm	cathode	sucrose	91.9-95.3			0.15 W m^{-3}	[78]
SS mesh	13 μm	cathode	glucose	96.4		2.82	0.12 W m^{-3}	[146]
carbon felt				95.5		4.98	1.25 W m^{-3}	
microfiltration membrane	0.45 μm	separator	acetate				831 mW m^{-2}	[147]
			farm wastewater	81.6			746 mW m^{-2}	
nickel-based hollow fiber membrane	1 μm	cathode	acetate	>95				[120]
anthraquinone–disulphonate/polypyrrole composite modified polyester flat membrane	9.8 μm	cathode	glucose	92.5	70.6		0.35 W m^{-3}	[140]
carbon filtration membrane	0.553 μm	cathode	acetate	93.7	96.2		581.5 mW m^{-2}	[141]
UF membrane	0.5 kDa	separator	acetate				5 mW m^{-2}	[148]
	1 kDa						36 mW m^{-2}	
	3 kDa						36 mW m^{-2}	
UF membrane	1 kDa	separator	glucose	52.0			324 mW m^{-2}	[149]
	5 kDa			60.0			138 mW m^{-2}	
	10 kDa			57.4			54 mW m^{-2}	
PVDF hollow-fiber UF membrane	0.02 μm	anode	acetate	45.3-57.8		0.41	3 W m^{-3}	[150]
			primary effluent	86.9-90.2	9.1-50.0	0.45-0.75	1.5 W m^{-3}	
UF membrane	1 kDa	separator	acetate	>90			53.5 mW m^{-2}	[151]
PVDF hollow fiber UF membrane	0.02 μm	cathode	acetate	90.4-95.4	83.0	1.0-1.2	27 W m^{-3}	[152]
			cheese plant effluent	84.4-91.9	62.2	1.8-2.4		
polyester nonwoven membrane base coated with MWCNTs	0.065 μm	separator/cathode	domestic wastewater	97.3	97.3	<0.1	6.8 W m^{-3}	[76]

PVDF hollow fiber UF membrane	0.1 μm	external	glucose	86.7	93.0		51 mW m^{-2}	[153]
UF membrane + polyvinglidene fluoride UF membrane	30 kDa + 0.1 μm	separator + external	glucose	94.0	85.0	0.70	40 mW m^{-2}	[154]
UF membrane + polyvinglidene fluoride UF membrane	30 kDa + 0.1 μm	separator + external	glucose				60 mW m^{-2}	[155]
polydopamine modified UF membrane	1 kDa	separator	glucose				159.8 mW m^{-2}	[139]
regenerated cellulose UF membrane	1 kDa	separator	glucose	93.0			129.4 mW m^{-2}	[156]
UF membrane	~0.01 μm	external	domestic wastewater	87.0			25.1 mW m^{-2}	[157]
PVDF hollow fiber UF membrane	0.02 μm	anode	acetate	91.6		1.00	1.8 W m^{-3}	[137]
		anode + external	acetate	95.0		1.60		
PVDF hollow fiber UF membrane	0.1 μm	external	primary effluent	86.2			86.9 mW m^{-2}	[158]
hollow fiber UF membrane	0.4 μm	cathode	acetate	91.6	31.7		1.16 W m^{-3}	[159]
regenerated cellulose UF membrane	1 kDa	separator	acetate				122.2-160.5 mW m^{-2}	[160]
PVDF hollow fiber UF membrane	15 kDa	cathode	acetate	91.3	99.0			[161]
			primary effluent	84.5				
PVDF hollow fiber UF membrane	0.03 μm	cathode	glucose + starch	95.1	95.2		2.18 W m^{-3}	[162]

Last but not least, emerging trace contaminants such as pharmaceuticals, antibiotics and personal care products have raised increasing attention in recent years due to their potential environmental risks and adverse effects to human health [163-165]. MBR, benefiting from the combination of biodegradation and membrane filtration, is believed to remove trace contaminants more effectively than activated sludge process do [166]. A recent study demonstrated that the removal of p-fluoronitrobenzene was significantly enhanced by the cathodic reduction in a BES [167]. It is therefore expected that membrane-BES will combine the advantages of the individual technologies and may hold great promise for the removal of emerging contaminants.

1.7 Process engineering: combining BES with forward osmosis

(This section has been published as: Heyang Yuan and Zhen He. "Integrating Membrane Filtration into Bioelectrochemical Systems as Next Generation Energy-Efficient Wastewater Treatment Technologies for Water Reclamation: A Review." Bioresource Technology (2015): 195, 202-209.)

An forward osmosis (FO) process refers to the movement of water molecules from a low-salinity solution (feed) through a semipermeable membrane to a high-salinity solution (draw) under an osmotic pressure gradient. Because water permeation is a natural process with relatively low flux, FO is advantageous over conventional membrane technologies such as reverse osmosis, nanofiltration and ultrafiltration, in terms of fouling propensity and energy efficiency [168]. Meanwhile, the small pore size (average pore radius 0.25–0.30 nm) of FO membrane can guarantee rejection of a wide range of contaminants [169]. When wastewater is used as a feed solution and saline water (e.g. seawater) serves as a draw, clean water can be extracted by the osmotic pressure and the volume of wastewater can be greatly reduced [170]. The concentrated feed contains organic matters and nutrients that must be treated before discharge, which provides an opportunity for the synergistic linkage between FO and BES [171].

The first successful integration of FO into BES was demonstrated in an MFC, in which an FO membrane was installed between the anode and cathode to replace the ion exchange membrane [172]. This osmotic MFC (OsMFC) using NaCl solution as a catholyte/draw solution generated ~25% higher electric current than a conventional MFC containing CEM, likely because of the

enhanced proton transport with water flux and smaller membrane resistance. The performance of this OsMFC slightly decreased with artificial seawater (equivalent to 35 g L^{-1} NaCl) as a draw, but was still superior to the conventional MFC, especially in water flux. Further study found that the fouling of FO membrane could enhance electricity generation, but was detrimental to water flux [173], indicating that the role of FO membrane in an OsMFC for ion and water transportation is not well understood. When being used to treat domestic wastewater, the OsMFC was able to remove 74.8% of the soluble COD and reduce the wastewater volume by up to 72.2% depending on HRT, and the water flux reached 2.15 LMH by increasing the recirculation rate to alleviate the concentration polarization [138]. It is worth noting that the relatively low COD removal remained to be further examined because control reactor with ion exchange membrane is missing. An energy analysis indicated that the OsMFC could theoretically generate 0.108 kWh m^{-3} of energy, which was sufficient to drive the pumping, thereby establishing a self-sustained treatment system. To eliminate energy consumption by aeration, an air-cathode was used to replace the immersed cathode, and such an OsMFC achieved a power density 7.5% or 87.0% higher than the MFC equipped with AEM or CEM [174]. It was found that a small proportion of acetate in the anolyte migrated into the catholyte, indicating the potential limitation of current FO membrane fabrication. Recently, a novel layer-by-layer polyelectrolyte FO membrane was fabricated and resulted in a high initial water flux of 18.43 LMH in an OsMFC using 2 M NaCl as a catholyte/draw, suggesting that improving FO membrane will have significant impact on the performance of OsMFC [175]. Further studies are warranted to compare the novel FO membrane with conventional FO membranes based on cellulose triacetate or thin film composite.

FO has also been integrated into microbial electrolysis cells (MECs) for enhancing hydrogen production. It was reported that an osmotic MEC achieved 3 times higher hydrogen production compared to a conventional MEC equipped with CEM [176]. The increased hydrogen production was consistent with the enhanced cathodic efficiency, suggesting a facilitated proton transport with water flux. The researchers also hypothesized that the movement of a small amount of cations and anions across the FO membrane under a concentration gradient, known as reverse salt flux, could lower the ohmic resistance of the electrolyte and consequently facilitate electron transfer. The osmotic MECs represent a new application for the FO-BES integration to produce high-value

products, and may be expanded to microbial electrosynthesis that produce organic compounds from carbon dioxide [177].

Although FO can extract high quality water from wastewater, its diluted draw solution needs further treatment (reconcentration or removal of salts) before reclamation. Salt removal can be accomplished through integrating FO into microbial desalination cells (MDCs), which has higher energy efficiency than conventional desalination technologies such as reverse osmosis, multi-stage flash and electrodialysis [85]. This osmotic MDC (OsMDC) simultaneously realizes wastewater treatment, water extraction and desalination [178]. Although the OsMDC was advantageous in water extraction, its salt removal was outperformed by a convention MDC, likely because that Cl^- was retained in the salt chamber by the FO membrane. To overcome this limitation in salt removal, a conventional MDC was hydraulically linked to an OsMFC to enhance desalination without compromising water extraction [179]. The coupled OsMFC-MDC could remove approximately 10% more COD and 3 times more salts than a conventional MDC. It was concluded that the high-power mode (with an external resistance of 31 Ω, which was equivalent to the internal resistance of the MDC) was more favorable because of the higher energy production (0.16 kWh m^{-3}).

Similar to the UF, external linkage between FO and BES has also been investigated. For example, the previously described OsMFC-MDC system exhibited the enhanced desalination and COD removal compared to conventional MDCs. A further study hydraulically coupled a tubular MDC to an external FO module by introducing the MDC anode effluent into the FO feed chamber and then the FO feed effluent returning back to the cathode of the MDC [180]. Such a flow pattern achieved 75% COD removal, 64% volume reduction of the wastewater, and 80% conductivity reduction of the salt solution with a salt solution HRT of 24 h, all of which were superior to a standalone MDC or FO module. The TDS (total dissolved solid) decrease rate of this coupled system was 22.7 g L^{-1} d^{-1}, which is among the highest reported in the literatures. The FO process contains a large amount of osmotic energy between the feed and draw [181], and this energy can be harvested by pressure retarded osmosis (PRO), in which electrical energy is generated by pressurizing the diluted draw through a hydroturbine. An external PRO module was applied to as pretreatment of an MEC and provide electrical energy to the MEC for hydrogen production [182].

Both experimental results and mathematical modeling of this PRO-MEC system demonstrate its feasibility and identify several major limitations for further development.

Ammonium-based draw solution is attractive to FO application, because of relatively easier recovery of draw solute [183]. An innovative MEC-FO system was developed to recover ammonium from wastewater in the MEC and use the recovered ammonium as a draw solute in the FO to treat the MEC effluent [184]. This system generated an ammonium solution at 0.8 M and successfully reduced the wastewater volume by 50.1% at a maximal water flux of 2.9 LMH; the final effluent after ammonia recovery contained <1 mg L^{-1} NH_3 and no COD. Including nitrogen recovery into the FO-BES integration will make the system more economical and environmental advantageous. However, at the current stage of the development, the MEC-FO system consumed 3.9 kWh m^{-3} energy, more than half of which came from the power supply, implying the necessity of using renewable energy to drive the system and decreasing energy consumption through optimizing the operation.

Table 1.4 Summary of the studies about FO-BES.

Membrane	Configuration	Carbon source	COD removal (%)	Maximum power density	Ref.
FO membrane	separator	acetate		4.74 W m^{-3}	[172]
FO membrane	separator	acetate			[173]
FO membrane	separator	acetate			[178]
FO membrane	separator	acetate	82.5	28.2 W m^{-3}	[138]
		primary effluent	74.8	4.5 W m^{-3}	
cellulose triacetate FO membrane	separator	acetate	90.0	43 W m^{-3}	[174]
FO membrane	separator + external	acetate	>85%	12.45 W m^{-3}	[179]
chitosan [CH; polycation] + PAAc; polyanion	separator	glucose	89.8	27.38 W m^{-3}	[175]
cellulose triacetate FO membrane	external	glucose	60.6		[184]
cellulose triacetate FO membrane	separator	acetate			[176]
cellulose triacetate FO membrane	external	acetate	~80		[180]

1.8 Research objectives

The overall objective of this research is to understand the fundamentals and the applications of BES in water and wastewater treatment. This will be achieved by pursuing the following specific objective:

1) Unravel the microbial population and functional dynamics in BES. As earlier discussed, the electrochemically active microorganisms are the key players of wastewater treatment and energy production, and their roles in the anode community need to be fully understood. Salinity is one of the critical factors of microbial community and functions, and the anodes of MDCs are constantly exposed to high salinity. The salt concentration in the middle chamber of an MDC can determine the ohmic resistance, and consequently affect the current generation and ion migration, both of which are hypothesized to regulate the bioelectrochemical activity and shape the microbial community. Based on the hypothesis, a tubular MDC was constructed and operated at different NaCl concentrations. The microbial community was characterized using 16S rRNA amplicon sequencing, and the functional dynamics and interspecies interactions were further studied with bioinformatics and biostatistics.

2) Develop cathode catalysts for BES applications. The cathode catalyst is one of the limiting factors of BES performance. As previously reviewed, an effective cathode catalyst should be catalytically active, cost-effective and durable. Based on these criteria, nitrogen- and sulfur-co-doped porous carbon nanosheets and nitrogen-doped bamboo-like carbon nanotubes were synthesized as the ORR catalysts, and molybdenum disulfide was coated on highly conductive carbon nanotubes as the HER catalysts. The catalytic mechanisms of these materials were elucidated with electrochemical measurements and their catalytic activities were evaluated in BES.

3) Optimize the process of BES and enhance the performance. Stand-alone BES have some inherent limitations. The combination of BES with other technologies (e.g., membrane filtration and FO) can tackle these challenges and achieve synergetic benefits. In this study, MDCs were first hydraulically coupled with FO and operated at a batch mode. The treatment capacity between the individual components was not balanced because of the faster treatment in the FO than that in the MDC. To address this problem, a continuously operated FO-MDC system was built. A mathematical model was also developed based on the previous FO model, MDC model and PRO-MEC model [131, 182, 185] to understand the effects of flow rate on the FO-MDC system and predict system performance. In addition, FO was operated under

PRO mode to extract osmotic energy, which was then applied to an MEC to achieve self-powered H_2 production.

4) Identify the application niches of BES. BES can be modified to achieve various functions and can be used to remove various contaminants such as heavy metals and xenobiotic. However, the removal of antibiotic resistant genes (ARGs) by BES have not been reported. ARGs are emerging contaminants posing a serious concern to public health [186]. It has been demonstrated that a two-stage thermophilic/mesophilic anaerobic digestion system can efficiently remove ARGs associated with tetracycline resistance [187]. Anaerobic digestion was also used as pre-treatment for aerobic stirred tank reactors and noticeably enhanced the removal of a variety of ARGs [188]. The removal of ARGs under anaerobic conditions is likely associated with the fitness and survival of their host organisms [189]. Based on the previous studies on anaerobic digesters and the fact that the respiratory environment in BES is highly specific, it is hypothesized that ARGs may be removed by the anode/cathode treatment of BES. To examine this hypothesis, an antibiotic resistant *E. coli* strain carrying *intI1*, *sulI* and *tet*(E) was isolated from domestic wastewater and dosed into a tubular BES. The BES was operated under different modes to understand the fate and removal of the ARGs in the reactor.

CHAPTER 2: Unravelling and Reconstructing the Nexus of Salinity, Electricity and Microbial Ecology for Bioelectrochemical Desalination

(This section has been published as: Heyang Yuan, Shan Sun, Ibrahim M. Abu-Reesh, Brian D. Badgley and Zhen He. " Unravelling and reconstructing the nexus of salinity, electricity and microbial ecology for bioelectrochemical desalination." Environmental Science & Technology. In press.)

2.1 Introduction

The growing demand for water and energy has become one of the most critical challenges in the 21st Century. Globally, there are 2.5 billion people suffering from water sanitation problems and 1.3 billion people lacking access tof electricity [190]. Conventional desalination and wastewater treatment methods, such as reverse osmosis and activated sludge processes, are energy-intensive and further exacerbate the stress in water-energy nexus [5, 191]. On the other hand, wastewater, which contains chemical energy and nutrients, are increasingly considered as a usable resource [4]. There is an urgent need to develop new technologies to harvest this energy and achieve sustainable water and wastewater treatment.

bioelectrochemical systems (BES) are an emerging concept that can treat wastewater, convert organic wastes into electricity and simultaneously achieve a variety of functions, such as bioremediation, chemical production and nutrient recovery, etc. [7]. One of the promising configurations of BES is microbial desalination cell (MDC). A typical MDC contains an anion exchange membrane and a cation exchange membrane between an anode and a cathode to form a desalination chamber [9]. The electrochemically active microorganisms in the anode oxidize organic matter in wastewater and release electrons extracellularly for respiration [15]. The electrons are transferred to the cathode when proper electron acceptors (e.g., oxygen) are present. This creates an electrostatic force that drives the ions in the saline water to migrate to the anode and cathode. As such, both saline water and wastewater are treated and electrical current is generated. A recent large-scale MDC system with a total liquid volume of 105 L has demonstrated the potential of this technology in practical applications [192].

As the catalyst for oxidation reaction and electron transfer, the microorganisms in a BES anode play a pivotal role in organic removal and energy production [193]. Anolyte salinity is one of the important factors that can affect the bioelectrochemical activity and microbial community, but its detailed effects remain unclear. For example, in a 650-mM NaCl solution, model organisms *Geobacter sulfurreducens* PCA and *Geobacter metallireducens* GS-15 could not generate current, whereas a novel *Geobacter* species showed high bioelectrochemical activity [194]. Meanwhile, mixed-culture BES could still produce electricity under extremely saline conditions (100 – 250 g L^{-1} NaCl), but the anode was dominated by *Halanaerobium*, a group of halophilic chemoorganotrophs that had not been reported in previous BES studies [29].

Unlike other types of BES, an MDC anode is constantly exposed to high salinity as a consequence of ion migration. The microbial communities in MDC anodes have been found to be distinct from those in other BES [31], and to become less diverse after long-term operation [32]. In contrast to the inhibitory effects high salinity on the performance of other types of BES [28], the current and Coulombic efficiency of MDCs increased with a higher salt concentration in the desalination chamber [130, 180]. Based on these previous studies, it is possible that the microbial community may be self-regulating by interacting with the salt solution in the desalination chamber (Figure A1): as the ions start to migrate, the ohmic resistance of the MDC is reduced and the growth of electrochemically active bacteria is encouraged [69]. Meanwhile, the salinity in the anode increases and the metabolism becomes energetically expensive [195]. The positive effects of conductivity and adverse impacts of salinity on microbial activity eventually reach equilibrium with the development of a stable microbial community. Thus, different microbial community structures may form under varied salt concentrations, and a comprehensive understanding of the salt effects on MDC community structure and function is required for improving energy production and desalination efficiency.

A better understanding of the microbial ecology in MDC anode could also improve modeling of the microbial community, and thereby guide the system design and optimization. With the recent advancements in high-throughput sequencing technologies and bioinformatics tools, the microbial community can be predicted using statistical modeling based on phylogenetic and taxonomic profiles [196]. There have been pioneering studies integrating sequencing data with novel

statistical approaches, such as artificial neural networks, to reconstruct the microbial communities in environmental ecosystems [197]. In addition, genetic and metabolic traits may also be incorporated into artificial neural networks to further elucidate the relationships between functional variation and environmental change and improve model performance [198]. These novel approaches can provide powerful tools to model the microbial community and functional dynamics in MDC anode, leading to the potential prediction of MDC performance.

In this study, a bench-scale tubular MDC was built (Figure A2) and operated at six different salt concentrations to: 1) examine the effects of salinity on system performance, 2) understand the dynamics of anode microbial communities and functions associated with the salt concentrations and 3) develop a statistical model to reconstruct anode microbial community structure and predict the system performance. To achieve these objectives, current generation, COD (chemical oxygen demand) removal and ion concentrations were monitored as the major indicators of MDC performance. The microbial community was characterized using 16S rRNA amplicon sequencing. The extracellular electron transfer (EET) mechanism was identified with cyclic voltammetry (CV). Phylogenetic Investigation of Communities by Reconstruction of Unobserved States (PICRUSt) was applied to further understand the effects of salinity on overall metabolic functions. The data quantifying environmental parameters and dominant taxa were trained to construct Bayesian networks and then combined with logistic regressions to predict current output over a continuous range of NaCl concentration.

2.2 Materials and methods

2.2.1 Reactor setup and operation

A tubular microbial desalination cell (MDC) was constructed as previously described (Figure A2).[199] The MDC had an anode volume of 350 mL and a desalination chamber of 150 mL. A carbon brush (Gordon Brush Mfg. Co., Inc., CA) was used as the anode electrode. A piece of 150-cm^2 carbon cloth (Zoltek Companies, Inc., MO) was coated with 0.5 mg cm^{-2} activated carbon and used as the cathode electrode. The cathode electrode was covered with stainless steel mesh as current collector. The anode and cathode electrode were connected with titanium wire across a 1-Ω resistor. Synthetic wastewater was used as the anolyte (per liter of deionized water): sodium acetate 8 g; NaCl, 0.5 g; $MgSO_4$, 0.015 g; $CaCl_2$, 0.02 g; KH_2PO_4, 0.265 g; K_2HPO_4, 0.535 g;

$NaHCO_3$, 4.2 g; and trace element, 1 mL.[200] The catholyte was 25 mM phosphate buffer saline (PBS).

The MDC was inoculated with anaerobic sludge from a local wastewater treatment plant. Anaerobic sludge is commonly used as an inoculum in various BES reactors. The microbial community in anaerobic sludge in theory bears high diversity and the community can evolve under specific operating conditions. In the previous MDC community studies, the anodes were inoculated with the wastewater of an aeration basin or the effluent of an existing MFC,[31-33] which might not be suitable as MDC inocula considering the low abundance of anaerobes and the low diversity after acclimation. A recent study suggested that mangrove-grown brackish sediment could be a potential inoculum source for BES that were operated at high salinity.[201] However, It has been reported that the predominance of *Geobacter* is consistent with good MFC performance and not related to inoculum sources.[23] Core community has also been identified in 6 different BES from different labs (i.e., different inoculum sources).[202] These findings suggest that inoculum source might not play a major role in shaping the microbial community in BES.

For star-up phase, the MDC was fed with synthetic wastewater and 1 M NaCl solution and operated in a continuous mode with an anode hydraulic retention time (HRT) of 48 h and a desalination chamber HRT of 21 h. The anolyte, catholyte and salt solution were recirculated using a peristaltic pump (BT600-2J, Langer Instruments Corp., NJ) to ensure effective mixing. The pH of the anolyte and catholyte was maintained at 7 using 4 M NaOH and 4 M HCl, respectively, by pH controllers (MC122, Milwaukee Instruments, Inc., NC).

2.2.2 Reactor performance evaluation

Electrical current was monitored throughout the experiments by measuring the voltage on the 1-Ω resistor with a digital multimeter (2700, Keithley Instruments, Inc., OH). Reactor performance was evaluated after the MDC was operated at each NaCl concentration for 21 d. Soluble chemical oxygen demand (COD) was measured using a colorimeter according to the manufacturer's instruction (DR/890, Hach, CO). Coulombic efficiency and current efficiency were calculated as previously described.[85] Conductivity was measured using a bench-top conductivity meter (FiveEasy™ conductivity, Mettler-Toledo, OH). The concentrations of Na^+, Cl^-, K^+ and PO_4^{3-} in

the anode were measured using ion chromatography. The acetate in the effluent was measured by high-performance liquid chromatography (Shimadzu, MD) equipped with an Aminex HPX-87H column (Bio-Rad, CA). Data were collected at room temperature in triplicate.

2.2.3 Electrochemical measurement

Electrochemical measurement was performed after the reactor was operated at each NaCl concentration for 24 d. The MDC was drained and the refilled with fresh anolyte (8 g L^{-1} acetate), catholyte (25 mM PBS) and salt solution (1 M NaCl) to ensure that the difference in electrochemical performance was caused by the anode microorganisms. The drained solutions were stored at 4 °C. After changing the electrolyte, the MDC was switched to open circuit for 3600 s to obtain stable cell voltage. Polarization curve was then measured using a potentiostat (Reference600, Gamry Instruments, PA) at a scan rate of 0.2 mV s^{-1}. The current and power densities were normalized to the anode volume (350 mL). After measuring polarization curve, turnover cyclic voltammetry (CV) was measured with the scan rate ranging from 0.5 to 50 mV s^{-1}. A platinum wire (CH Instruments, Inc., TX) and an Ag/AgCl electrode (3 M KCl, 0.210 V vs. SHE (standard hydrogen electrode), CH Instruments, Inc., TX) were used as the counter electrode and reference, respectively. The formal potential of the redox reaction was extracted from the first derivative of the CV at the scan rate of 1 mV s^{-1}. Electrochemical measurements were completed within 6 h and the drained solutions were pumped back into the MDC to minimize the adverse effects on the microbial community

2.2.4 DNA extraction, sequencing and analysis

Inoculum samples were collected within 24 h from the anode electrode and liquid phase after the MDC was inoculated with the anaerobic sludge. Biomass was harvested after the reactor was operated at each NaCl concentration for 28 d. A piece of anode carbon brush and 1 mL of anolyte were collected and stored immediately at -80 °C. DNA was extracted with the PowerSoil DNA extraction kit (MoBio Laboratories, CA) following the manufacturer's instructions. The V4 region of bacterial 16S rRNA gene was amplified using primer pair 515F and 806R.[203] The 25-µL PCR reaction mixture contained 10 µL 2.5×5 Prime HotMaster mix (5 Prime, MD), 13 µL PCR water (MoBio Laboratories, CA), 0.5 µL of each of the primers (10 µM), and 1 µL of isolated DNA. The thermal cycler protocol was 94 °C for 5 min; 35 cycles of 94 °C for 45 s, 50 °C for 45 s, and 72

°C for 90 s; and a final extension at 72 °C for 10 min. DNA of all samples were amplified in triplicate on a thermal cycler (C1000 Touch™, Bio-Rad, CA) and visualized on 2% agarose gels. The triplicate PCR products were then combined and purified using the UltraClean PCR cleanup kit (MoBio Laboratories, CA). Amplicon concentrations were quantified using a fluorometer (Qubit 2.0, Invitrogen, CA). The purified amplicons were combined in equimolar ratios and sequenced on an Illumina Miseq platform (250PE). The raw reads were deposited in the NCBI BioProject database with the accession number (upload later). The forward and reverse sequencing reads were merged and filtered with USEARCH,[204] with minimum forward-reverse overlap of 150 bp, minimum merged length of 20 bp, expected error <0.5 per read and chimeric sequences removed with UCHIME. Taxonomy was assigned using RDP classifier,[205] with SILVA database as reference.[206] Sequencing data are available in GenBank under BioProject accession number PRJNA384805.

For each NaCl concentration, triplicate samples were collected from the anode electrode and liquid phase, and the total 42 samples resulted in 8,046,011 high quality sequences (on average, 1,059,229 for 6 inoculum samples and 46,747 for 36 MDC samples). One of the 0.2-M biofilm samples was excluded from downstream analysis due to the low sequence reads (< 3,000). The library for each sample was rarefied to an even depth of 10,000 sequences and clustered to 1,627 bacterial operational taxonomic units (OTUs) with a 97% similarity threshold. The plateaus of the rarefaction curves indicated capture of most of the dominant species in the communities (Figure A5). The biofilm samples exhibited significantly higher Shannon and Simpson indices of diversity compared with the liquid samples (Figure A6C and A6E), meaning higher evenness and richness in the biofilm communities. The individual α-diversity indices for biofilm and liquid samples decreased readily as the NaCl concentration was reduced from 2 M to 0.05 M, and were not restored at the end at 4 M (Figure A6B, A6D and A6F). This suggested a potential historical effect of manipulating the salinity on the community diversity, in agreement with the results in a previous long-term MDC study.[32] Such a decrease in diversity may not affect overall bioelectrochemical activity as evidenced by the similar MDC performance at 2 and 4 M (Figure 2.1).

2.2.5 Functional prediction

Phylogenetic Investigation of Communities by Reconstruction of Unobserved States (PICRUSt) was used to predict the metabolic dynamics of the observed microbial communities.[207] OTU table was constructed with a closed-reference OTU picking process against the May 2013 Greengenes database using QIIME with 0.97 similarity,[208] and 90.2% of the reads were mapped to reference. The results were used in PICRUSt pipeline according to the online protocol (http://huttenhower.sph.harvard.edu/galaxy/). The Nearest Sequenced Taxon Index range from 0.12 to 0.39. Functional predictions were assigned to KEGG Ortholog level 3. Twenty-seven environmental functions from 6 level-2 categories (Cell Motility, Carbohydrate Metabolism, Energy Metabolism, Lipid Metabolism, Membrane Transport and Cellular Processes and Signaling, Table A1 and A2) were visualized using Circos,[209]

2.2.6 Statistical analysis

One-way Analysis of Variance (ANOVA) was used to test for significant difference of the MDC performance and PICRUSt results. Two-sample t-test was performed to to test for significant difference of the Bray-Curtis similarities. Linear regression was fitted for current vs. log (NaCl concentration), anodic peak current vs. square root of scan rate and actual vs. predicted values by the Bayesian network. PCoA (based on Bray-Curtis distance) and CCA were conducted using R package "vegan". PERMANOVA was performed to test for the significant difference of PCoA results (N = 999). The relationships between environmental parameters and taxonomic data in CCA were tested for significance with an ANOVA like permutation test (N = 999). A p value of <0.05 was used to identify significant difference.

2.2.7 Bayesian network analysis and prediction

Bayesian networks were constructed from major taxa at different taxonomic levels and 6 environmental parameters to understand the interspecies interactions and the relationships between biotic and abiotic parameters. The taxa were selected with the relative abundance > 1%, and thus 7 phyla, 8 orders and 29 OTUs were used to train the respective networks. First, the abundance of the taxa and the values of the environmental parameters were combined as a single matrix and normalized to between 0 and 1 with equation (1):

$$v\_norm_{ij} = \frac{v_{ij} - min(v_j)}{max(v_j) - min(v_j)} \quad (1)$$

where v_norm_{ij} is the normalized variable j of sample i, v_{ij} is the observed variable j of sample i, $min(v_j)$ and $max(v_j)$ are the minimum and maximum values of variable j. Among the total 18 datasets (triplicate for 6 NaCl concentrations), one of the 1-M biofilm samples and one of the 2-M liquid samples were omitted due to the poor repeatability of the taxonomic data (Figure A8), leaving 16 datasets for network training and validation. Bayesian networks were built with R package "bnlearn" using hill-climbing algorithm, and the parameters of the networks were calculated with Maximum Likelihood parameter estimation method. The networks were tested with leave-one-out cross-validation,[210] i.e., 15 datasets were used to construct a Bayesian network and the remaining one was used to validate the network. The cross-validation was thus performed for 16 times. For each cross-validation, Bray-Curtis similarity between the predicted and actual community was calculated. Meanwhile, Bayesian networks were also validated using relative root-mean square error (RMSE, equation (2)), with y = experimental values, y_{max} = the maximum experimental values and t = the predicted values (i.e., the abundance of the 8 taxa and the values of the 6 environmental parameters):

$$RMSE = \frac{\sqrt{\frac{\sum_{i=1}^{n}(y_i - t_i)^2}{n}}}{y_{max}} \quad (2)$$

A null model based on average taxa abundance was performed to further validate the network modeling approach.[198] After validation, three final Bayesian networks at the phylum, order and OUT level were constructed from the total 16 datasets. The abundance of the major taxa associated with NaCl concentration were fitted with logistic regressions (Figure A18, A19 and A20) as a simplification of pure-culture growth under the influence of NaCl,[211] and subsequently input into the Bayesian networks for current simulation.

2.3 Results and discussion

2.3.1 MDC performance

After start-up, the MDC was operated with varied NaCl concentrations in the desalination chamber to mimic the treatment of industrial saline wastewater, seawater, brackish water and domestic wastewater. The current decreased significantly from 100 mA with 2 M NaCl to 10 mA with 0.05 M NaCl, and rose back to 105 mA with 4 M NaCl (Figure 2.1A). The slight current fluctuation under each concentration was mainly due to the dose of NaOH for pH control. The current changed less noticeably at higher NaCl concentrations (1 - 4 M, 15-mA difference) than at lower values

(0.05 - 0.6 M, 65-mA difference). This implies that further enhancement of the bioelectrochemical activity may be inhibited by the high salinity.

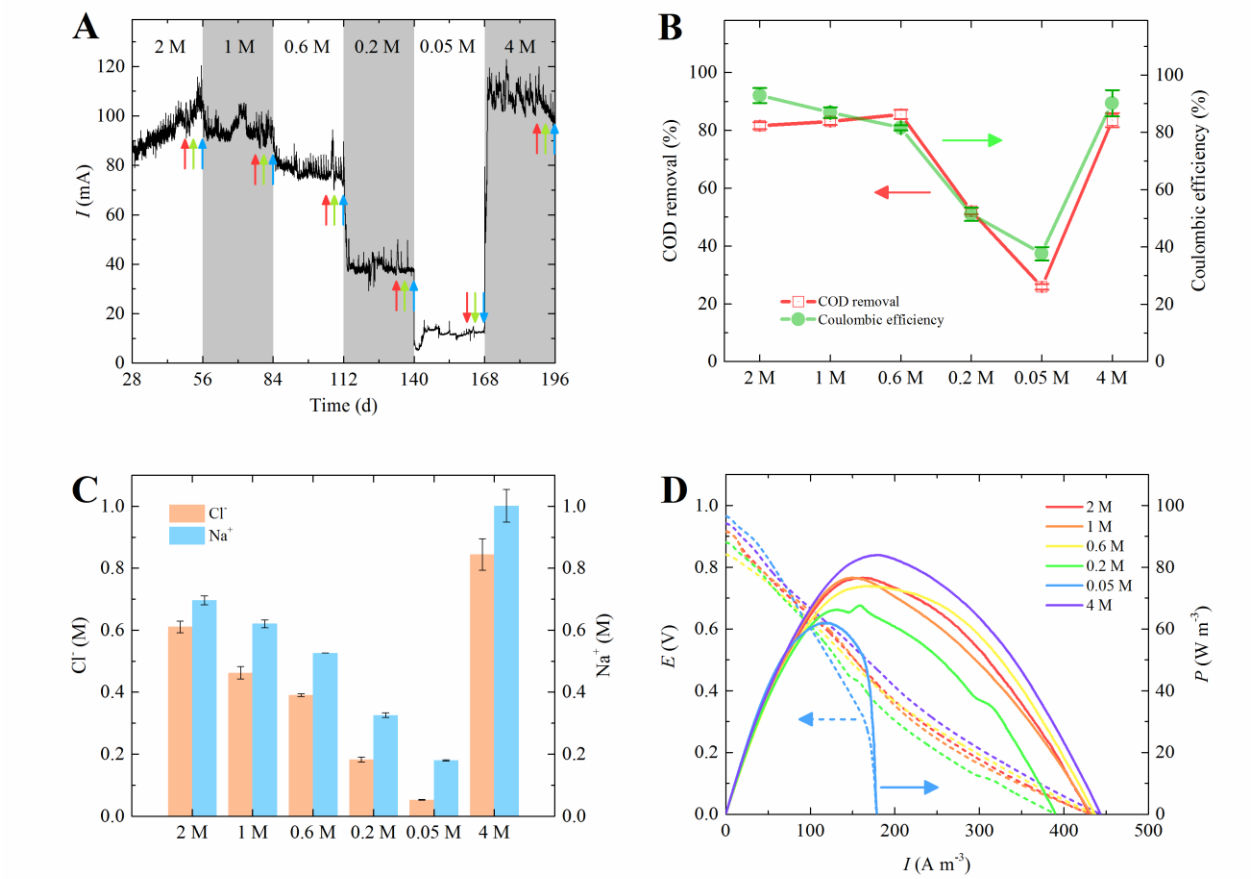

Figure 2.1 (A) Current production; experiment started on day 28 after start-up; red arrows indicate performance measurements, green arrows indicate electrochemical measurements and blue arrows indicate sample collection for DNA extraction. (B) COD removal and Coulombic efficiency. (C) The concentrations of Cl^- and Na^+ in the anode. (D) Polarization curve. Error bars were calculated from triplicate data.

COD removal and Coulombic efficiency were analyzed to examine the effects of organic matter on bioelectrochemical activity (Figure 2.1B). Similar to the trend of current production, COD removal remained unchanged at ~80% at high salt concentrations (Analysis of Variance (ANOVA), $p = 0.53$), with the effluent containing up to 1200 mg L^{-1} COD. The presence of high

acetate content in the effluent was further confirmed using high-performance liquid chromatography (Figure A3). Such a COD concentration was in theory equivalent to ~25 mA of current according to the equation of Coulombic efficiency, and suggested that the sufficient organic matter was not the limiting factor of the relatively unchanged current at high salt concentrations (Figure 2.1A). On the other hand, the lower Coulombic efficiency with 0.2 M and 0.05 NaCl indicated that a considerable proportion of the organic matter was consumed by non-electricity generating microorganisms (Figure 2.1B), implying a shift in the anode community [212].

Chloride ions migrated into the anode as a result of current production. The Cl^- concentration in the anode was positively related to the salt concentration in the desalination chamber and reached the highest of 0.84 M at 4 M (Figure 2.1C). In addition to migration, diffusion also contributed to ion movement [213], which explained the >100% current efficiency (i.e., the ratio between the transported Cl^- ions and the transferred electrons) at 2 and 4 M (Figure A4). The sodium ions, which were mainly from NaOH dosing for pH control, had a higher concentration than Cl^- due to the presence of negatively charged acetate and the resulting bicarbonate. The highly saline anode environment at high NaCl concentration was beneficial for charge transfer, but might also suppress microbial metabolism [214].

The bioelectrochemical activity was directly evaluated using polarization curves (Figure 2.1D). The experiments were conducted with fresh electrolyte and 1 M NaCl solution to ensure that the difference in electrochemical performance was caused solely by the anode microorganisms. The maximum power and current densities followed the order: 4 M > 2 M ≈ 1 M > 0.6 M > 0.2 M > 0.05 M, which was consistent with the current production and COD removal (Figure 2.1A and 2.1B) and reflected a lower bioelectrochemical activity with decreased NaCl concentration. The maximum current of ~150 mA (430 A m^{-3}-anode volume) at high salt range was higher than the 90 – 105 mA obtained under continuous operation (Figure 2.1A), likely because of the high substrate content (8 L^{-1} acetate) and the low osmotic pressure (0.009 M NaCl) of the fresh anolyte. While the polarization curves of 0.2 – 4 M were similar in shape, a sharp decrease at high current density was observed for 0.05 M, meaning that current production was limited by mass transport [71]. Given the high substrate content of fresh anolyte, the mass transport overpotential was

possibly caused by electron mediators. These results collectively suggest that a high salt concentration in the desalination chamber is beneficial for energy production and desalination, but may exert complicated effects on bioelectrochemical activity and possibly on the anode microbial community.

2.3.2 Microbial community dynamics

Principal coordinate analysis (PCoA) based on Bray-Curtis distances among microbial communities revealed significant differences among the microbial communities of the inoculum, the anode electrode and the liquid phase (Figure 2.2A, Permutational Multivariate Analysis of Variance (PERMANOVA), $p < 0.001$). After cultivation at 2 M NaCl, the biofilm and suspended communities were separate from the inoculum. The two communities further shifted away from the inoculum community as the salt concentration decreased, but showed different patterns. At low NaCl concentrations (0.05 – 0.6 M), the biofilm communities diverged from each other (Figure 2.2B), whereas the suspended communities remained clustered together (Figure 2.2C). When the NaCl concentration was returned to 4 M at the end of the experiments, the two communities re-converged and shifted close to the 2 M samples.

Canonical correspondence analysis (CCA) was performed to understand the relationships between the environmental parameters and microbial communities. The biofilm communities cultivated at 2 M and 4 M NaCl showed similar projection onto Cl^-, indicating their adaption to high salinity (Figure A7A). However, the 2-M biofilm communities had much more positive projections on current production, COD removal and maximum power density than the 4-M biofilm communities did ($p < 0.001$). In contrast, the projections of the suspended communities on performance-related environmental parameters roughly followed the order: 4 M ≈ 2 M > 1 M > 0.6 M > 0.2 M ≈ 0.05 M (Figure A7B), consistent with the trend of the actual MDC performance (Figure 2.1). The results thus implied a more critical role of the suspended communities in MDC performance at varied salt concentrations.

At the phylum level, Bacteroidetes (9 – 29%), Firmicutes (12 – 42%), Proteobacteria (15 – 58%), Synergistetes (1 – 14%) and Tenericutes (1 – 14%) were dominant in both biofilm and suspended communities (Figure A8), which agreed with previous studies on BES communities [202]. At the

order level, similar community structure was observed, with Bacteroidales, Clostridiales, Pseudomonadales, Synergistales and Acholeplasmatales being abundant (Figure 2.2D and 2.2E). The composition of the biofilm communities changed slightly under different salinities, but no significant trend was observed. For the liquid samples, the abundance of Pseudomonadales decreased from 20% with 2 M to 5% with 0.05 M, and then increased back to 30% with 4 M (Figure 2.2E). Meanwhile, the abundance of Erysipelotrichales and Synergistales in suspended communities seemed to be negatively correlated with NaCl concentration. The consistent changes may reflect the contribution of the suspended communities to the MDC performance (Figure 2.1). It can be concluded from these results that salinity, a major determinant of microbial community structure in environmental ecosystems [215], strongly affected the suspended communities in the MDC anode.

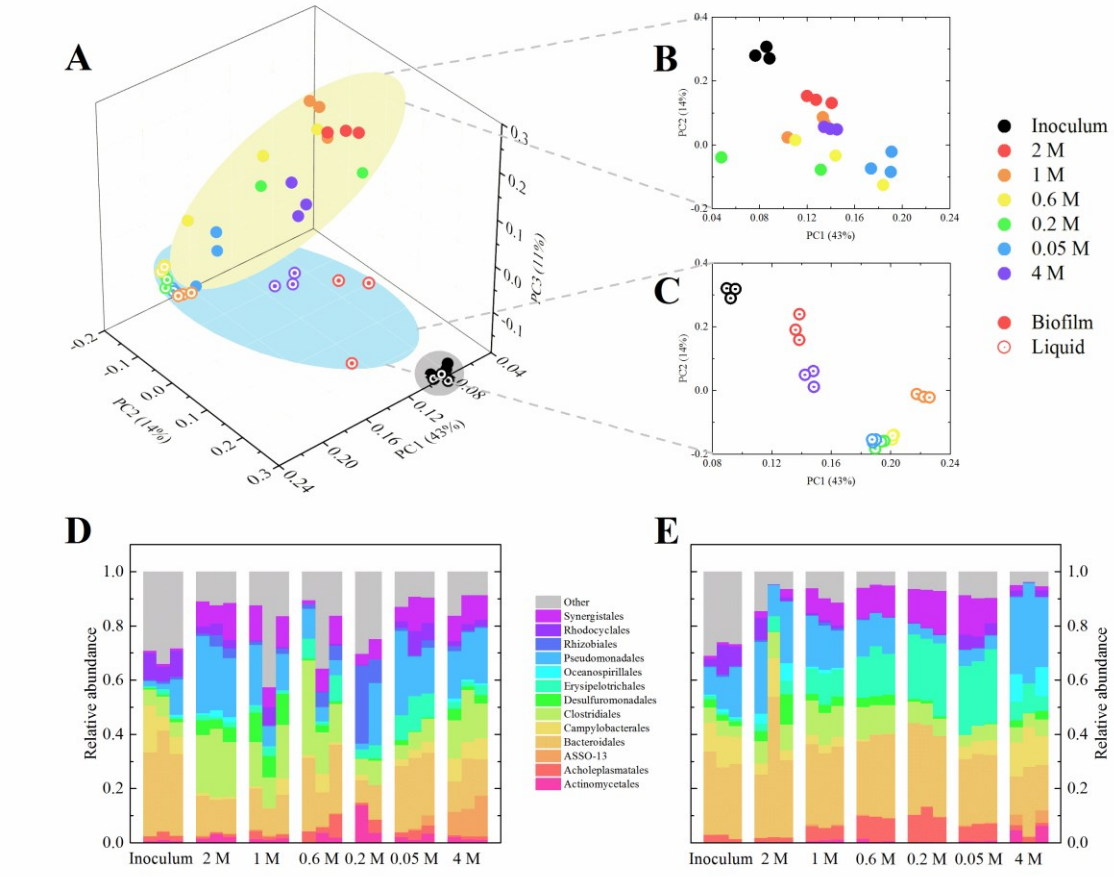

Figure 2.2 (A) Principal coordinate analysis of the biofilm and liquid samples based on the relative abundances of OTUs. (B) Detailed PCoA of the biofilm samples. (C) Detailed PCoA of the liquid samples. (D) Relative abundance of the biofilm samples at the order level. (E) Relative abundance of the liquid samples at the order level.

2.3.3 Microbial community composition

Of the 8 major orders, 36 OTUs had a relative abundance >0.5% and accounted for 53-69% and 71-83% of the total relative abundance in the biofilm and suspended communities, respectively. The affiliated OTUs are summarized in Figure 2.3, and their potential roles in the MDC anode are discussed individually below.

(i) Pseudomonadales. This order was dominated by 4 and 5 OTUs from the genus *Pseudomonas* and *Acinetobacter*, respectively. The 4 *Pseudomonas*-related taxa showed distinct preference regarding site and salinity. OTU 25 (*Pseudomonas brenneri*) and OTU 1781 (*Pseudomonas endophytica*) were found more abundant at low NaCl concentrations in both biofilm and liquid samples. On the other hand, *Pseudomonas xanthomarina*-related OTU 57 was initially the major *Pseudomonas* in the suspended communities (6.7% with 2 M), and was later replaced by the more omnipresent *Pseudomonas caeni*-related OTU 38 (20.5% with 4 M). *Pseudomonas* is among the earliest genera isolated from BES, and is well known for the mediator-based EET using phenazine derivatives, such as pyocyanin, phenazine-1-carboxylic acid and phenazine-1-carboxamide [216]. These electron shuttles, which are regulated by environment-induced quorum sensing (e.g., NaCl concentration) [217], can also be used by other bacteria in mixed cultures as electron acceptors [218]. In addition, phenazine derivatives can function as antibiotics to inhibit competitors, affect transcriptional regulation and modulate the physical characteristics of *Pseudomonas* communities [219]. Based on their "social" behavior and ubiquitous high abundance in anodes, it is speculated that *Pseudomonas spp.* play a key role in shaping the anode community and determining the bioelectrochemical function.

Similar to *Pseudomonas*, the 5 *Acinetobacter*-related OTUs were classified with high confidence (>98% identity) and showed succession with varied NaCl concentration. The dominance shifted from OTU 12 (*Acinetobacter venetianus*) and 514 (*Acinetobacter rudis*) at 2 M to OTU 1362

(*Acinetobacter brisouii*) and 30 (*Acinetobacter gandensis*) at 4 M. Overall, the *Acinetobacter spp.* seem to prefer biofilm environment and high salinity. The high phylogenetic similarity to *Pseudomonas* and the fact that some *Acinetobacter spp.* could reduce chromium implies that the members of this genus may be capable of EET [220]. In fact, *Acinetobacter calcoaceticus* dominated an ethanol-oxidizing BES [221]. An *Acinetobacter sp.* strain Tol 5 was highly adhesive to the anode electrode and performed EET solely via electron shuttles, e.g., phenazine derivatives from *Pseudomonas* [222]. It has been reported that *Pseudomonas* can provide *Brevibacillus sp.* PTH1 and *Enterobacter aerogenes* with phenazine for respiration, leading to their dominance in the respective communities [223, 224]. The high total abundance of *Pseudomonas* and *Acinetobacter* in the MDC under high current conditions (4 M NaCl, 17.9% in biofilm and 28.3% in liquid) suggests that *Acinetobacter spp.* may form symbiotic associations with *Pseudomonas spp.* and actively participate in current production.

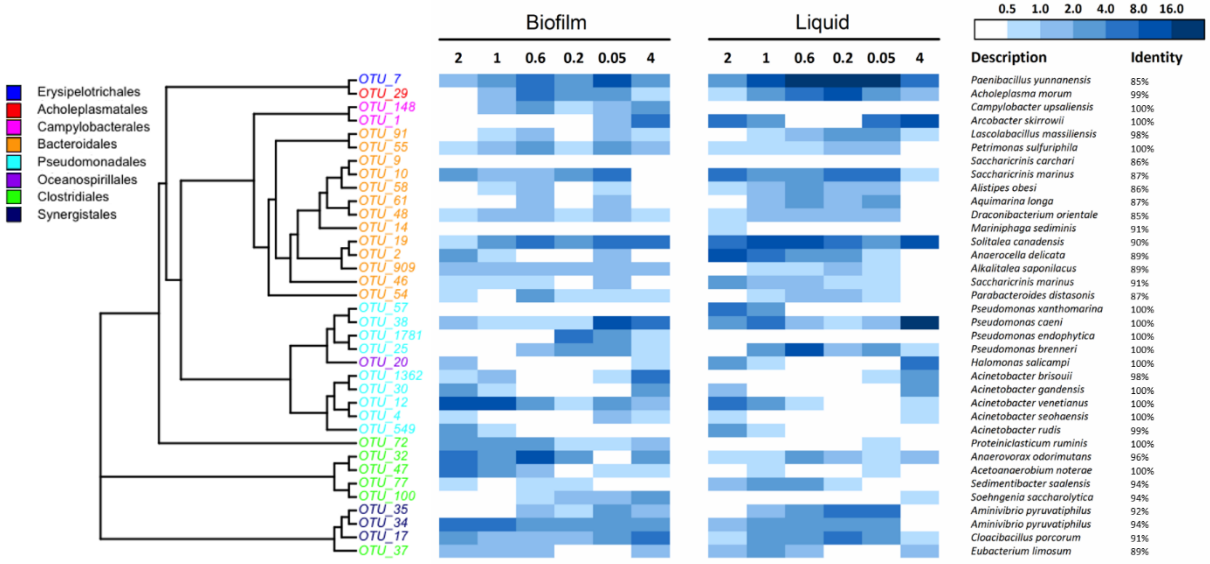

Figure 2.3 Phylogeny and abundance of the 36 major OTUs in biofilm and liquid samples. The relative abundance at each NaCl concentration was the mean of triplicate results, and the OTUs were selected with a relative abundance >0.5%.

(ii) Bacteroidales. The members of this order were highly diverse but poorly identified. OTU 91 and 55 were phylogenetically related and were the only two OTUs that share high identity with known species, *Lascolabacillus massiliensis* and *Petrimonas sulfuriphila*, respectively. *P.*

sulfuriphila was reported to grow optimally in the absence of NaCl [225], which could explain their preference for low salinity in the MDC anode. Bacteroidales are consistently found dominant in anaerobic bioreactors and can contribute to degrading soluble microbial products [226]. Although most of the Bacteroidales-related OTUs in this study are unidentified and their functions remain unclear, the relatively unchanged abundance at different current conditions (Figure 2.2D and 2.2E) suggests that they may not be important drivers of EET.

(iii) Clostridiales. Four of the 6 major Clostridiales-related OTUs (OTU 72, 32, 47 and 37) were frequently observed under medium to high salinities (0.6 – 4 M) and might be associated with current production. However, the EET ability of these taxa has not been previously reported in the literature. It was speculated that their function in the MDC anode could be related to scavenging byproducts of current production, such as inhibitory metabolites, biomass and HCO_3^-. For example, *Proteiniclasticum ruminis* (OTU 72) does not utilize carbohydrates but can digest proteins [227], and thus may feed on dead cells. On the other hand, *Acetoanaerobium noterae* (OTU 47) is known to utilize CO_2 and H_2 to produce acetate [228]. Given the close phylogenetic relationship of this OTU with OTUs 32, 77 and 100, most of the Clostridiales in the MDC anode seem to perform CO_2 fixation and do not directly participate in current production.

(iv) Others. In addition to Pseudomonadales, three dominant OTUs in Campylobacterales and Oceanospirillales might also contribute to electricity generation. *Campylobacter upsaliensis*-related OTU 148 was ubiquitous in the biofilm, while *Arcobacter skirrowii*-related OTU 1 and *Halomonas salicampi*-related OTU 20 were abundant under high current conditions (i.e., high NaCl concentrations). *Arcobacter* and Oceanospirillaceae (the family that *Halomonas* belongs to) from marine sediments have been reported to utilize acetate to reduce manganese oxide [229]. Moreover, a *Halomonas sp.* isolated from Soap Lake could reduce Fe and Cr, implying their potential ability for EET [230]. Based on the high phylogenetic similarity between *A. skirrowii* and *Arcobacter butzleri* ED-1 (an electrochemical active strain isolated from BES) [231], and that between *H. salicampi* and the *Pseudomonas*-related OTUs (Figure 2.3), it is reasonable to speculate that the members from Campylobacterales and Oceanospirillales perform EET and contribute to current production in the MDC anode.

In the remaining taxa, OTU 7 in the family Erysipelotrichales was poorly related to known species and the functions of *Acholeplasma morum*-related OTU-29 was unclear. On the other hand, three OTUs belonged to Synergistales, which were known to ferment amino acids [232]. These taxa exhibited a clear preference for low salinity and the liquid environment. The total relative abundance of these OTUs in the suspended community grew with decreased NaCl concentration, and reached the peak of 45.9% at 0.05 M. Their dominance at low current conditions may be an implication that they are not involved in electricity generation.

2.3.4 Extracellular electron transfer mechanisms

Electrochemically active microorganisms can transfer electrons extracellularly via membrane-bound cytochromes, shuttle molecules or conductive pili [233]. To understand the major EET mechanisms in the MDC anode, CV was measured with fresh electrolyte and 1 M NaCl solution, and the scan rate ranged from 0.05 to 50 mV s^{-1}. The voltammograms showed the typical characteristics of a Nernstian response, including anodic peak current/cathodic peak current = 1 and peak potential being independent of scan rate (Figure A9). Furthermore, the peak current correlated linearly with the square root of the scan rate (Figure 2.4A), indicating that the redox reactions in the anode were reversible and diffusion controlled [115]. This is a clear evidence that the EET in the MDC anode proceeded mainly via shuttle molecules [234].

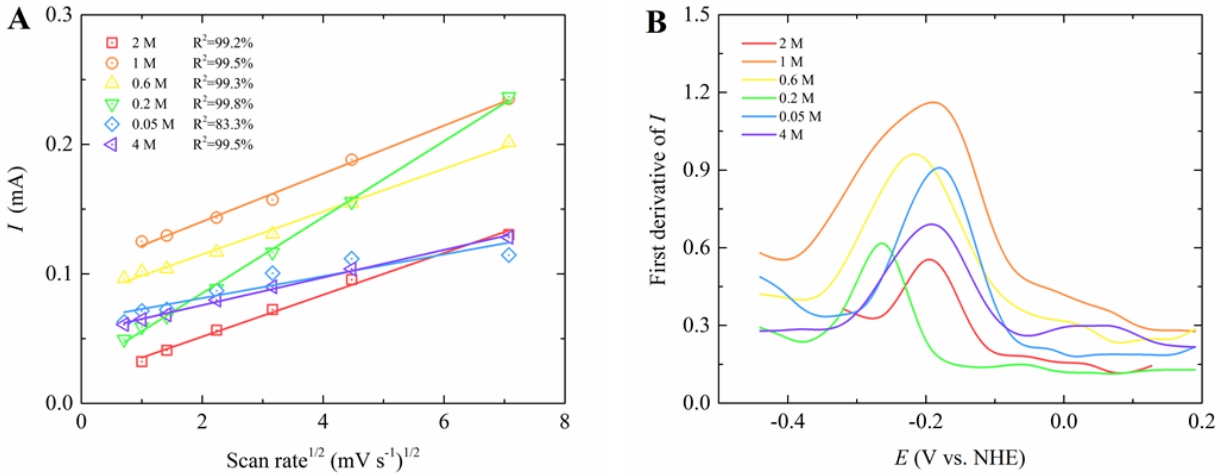

Figure 2.4 (A) Linear correlation between the anodic peak current and the square root of the scan rate (0.5 – 50 mV s^{-1}). (B) First derivative of the CV at the scan rate of 1mV s^{-1} under turn-over condition.

The formal potentials of the shuttle molecules were obtained from the first derivative of the CV at 1 mV s^{-1} under turn-over condition (Figure 2.4B). Two peaks were identified at approximately -180 and -260 mV vs. SHE (standard hydrogen electrode), which could be assigned to the phenazine derivatives, phenazine-1-carboxylic acid and phenazine-1-carboxamide [16, 235]. Initially, the EET was dominated by the more positive redox reaction (2 M, -180 mV vs. SHE). As the NaCl concentration decreased, the EET showed a composite characteristic of both peaks (0.6 M), and then shifted to the more negative redox reaction (0.2 M, -260 mV vs. SHE). Interestingly, the major EET pathway changed back to the more positive redox reaction when the NaCl concentration further dropped to 0.05 M, and remained stable with 4 M. Although the variation of the dominant electron-transfer sites under osmotic pressure remain unclear and warrant further studies, the electrochemical results agree well with the community composition containing a high abundance of *Pseudomonas* (Figure 2.3), and suggest that phenazine-mediated species are the key players of current production in the highly saline anode environment.

2.3.5 Functional prediction

PICRUSt was applied to understand the possible impacts of salinity on the overall microbial activity in the MDC anode [207]. Of the 329 predicted results, 27 environmental functions from 6 categories (Cell Motility, Carbohydrate Metabolism, Energy Metabolism, Lipid Metabolism, Membrane Transport and Cellular Processes and Signaling) were significantly affected (ANOVA, $p < 0.05$, Table A1 and A2).

Figure 2.5 highlights the dynamics of the major functions of the suspended communities, and reveals clear patterns under high salinity. For instance, the significantly high cell mobility (i.e., chemotaxis, motility and flagella assembly) suggests that bacteria may be actively seeking shuttle molecules for respiration [236]. In terms of energy metabolism, carbon fixation becomes more active, which is in good agreement with the high Clostridiales abundance (Figure 2.2 and Figure 2.3) and possibly related with the high HCO_3^- content resulted from the rapid acetate oxidation (Figure 2.1B) [237]. Meanwhile, the high level of oxidative phosphorylation, secretion and electron transfer carriers may be associated with the phenazine-dependent EET. To maintain proper metabolism and survive under high osmotic pressure, microorganisms can either increase

intracellular ion concentration ("salt-in" strategy, K^+ and Cl^- as the main ions), or accumulate organic compatible solutes (e.g., N-acetylglutaminylglutamine amide in *Pseudomonas aeruginosa*) [238]. The K^+ concentration in the liquid phase was higher at higher salinity, possibly implying lower K^+ concentration in the cell (Figure A10). Therefore, the microorganisms in the anode likely produce organic compatible solutes to cope with the highly saline environment, which might explain the upregulated secretion function (Figure 2.5).

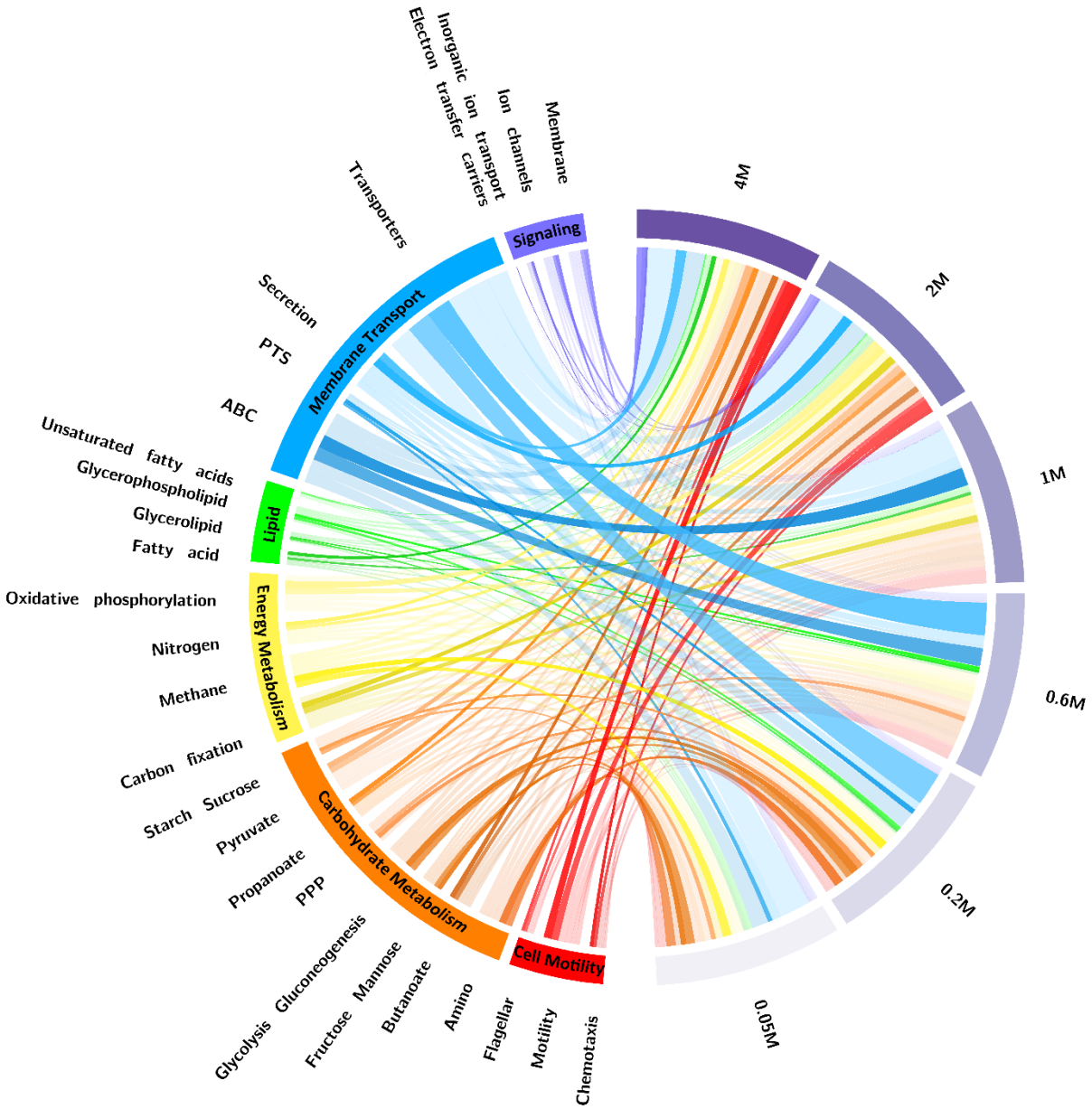

Figure 2.5 The 27 major functions of the suspended communities predicted using PICRUSt and visualized using Circos [207, 209]. The thickness of the band represents the permillage of the function in the predicted data. For each function, there are six bands associated with the six NaCl concentrations, and the two highest permillages were highlighted. Amino, Amino sugar and nucleotide sugar metabolism; PPP, pentose phosphate pathway; ABC, ATP-binding cassette transporters; PTS, phosphotransferase system.

Under low NaCl concentrations, important carbohydrate metabolisms such as glycolysis/gluconeogenesis, pentose phosphate pathway (PPP) and the metabolism of Amino sugar/nucleotide sugar, fructose/mannose and starch/sucrose are predicted to be enhanced (Figure 2.5), possibly because EET-related acetate oxidation is suppressed and more substrates are available to non-EET heterotrophs, syntrophs and methanogens. In agreement, methane metabolism and phosphotransferase system for sugar uptake are upregulated. Overall, PICRUSt provided reasonable predictions of most microbial functions of the suspended communities, but the roles of butanoate and proponate metabolism and membrane transporters in EET under salt stress remain unclear. Similar to the biofilm community dynamics, the predicted biofilm functions do not exhibit significant patterns (Figure A11) and the detailed functions need further elucidation using other functional analyses.

2.3.6 Network analysis

A Bayesian network modeling approach was applied to simulate the dynamics of the microbial community and achieved significantly more accurate prediction than the null model (Figure A12, t-test, $p<0.05$). The community structure was predicted with high accuracy at the phylum level as indicated by the high Bray-Curtis similarity of 90±3% between the actual and the predicted community (Figure A12). The prediction power significantly decreased to 83±5% at the order level and 69±6% at the OTU level (t-test, $p<0.05$). These similarities were noticeably higher than those at the respective levels in a previous study using ANN to predict acid mine drainage communities,[198] highlighting the robustness of Bayesian networks. The declining trend of the accuracy at lower taxonomic levels, which was also observed in the ANN study, was not related to the number of taxa selected for network training,[198] but was likely a result of community redundancy. In a highly defined environment like MDC anode, the community can have a high

level of functional redundancy with serval taxa sharing similar biochemical/bioelectrochemical functions.[239] For example, as discussed earlier, OTUs 57 and 38 were the major *Pseudomonas* in the suspended community and might perform EET, but their dominance shifted as the salt concentration changed (Figure 2.3). The dynamics of those functionally redundant taxa might not be precisely reconstructed by statistical modeling such as Bayesian networks or ANN.

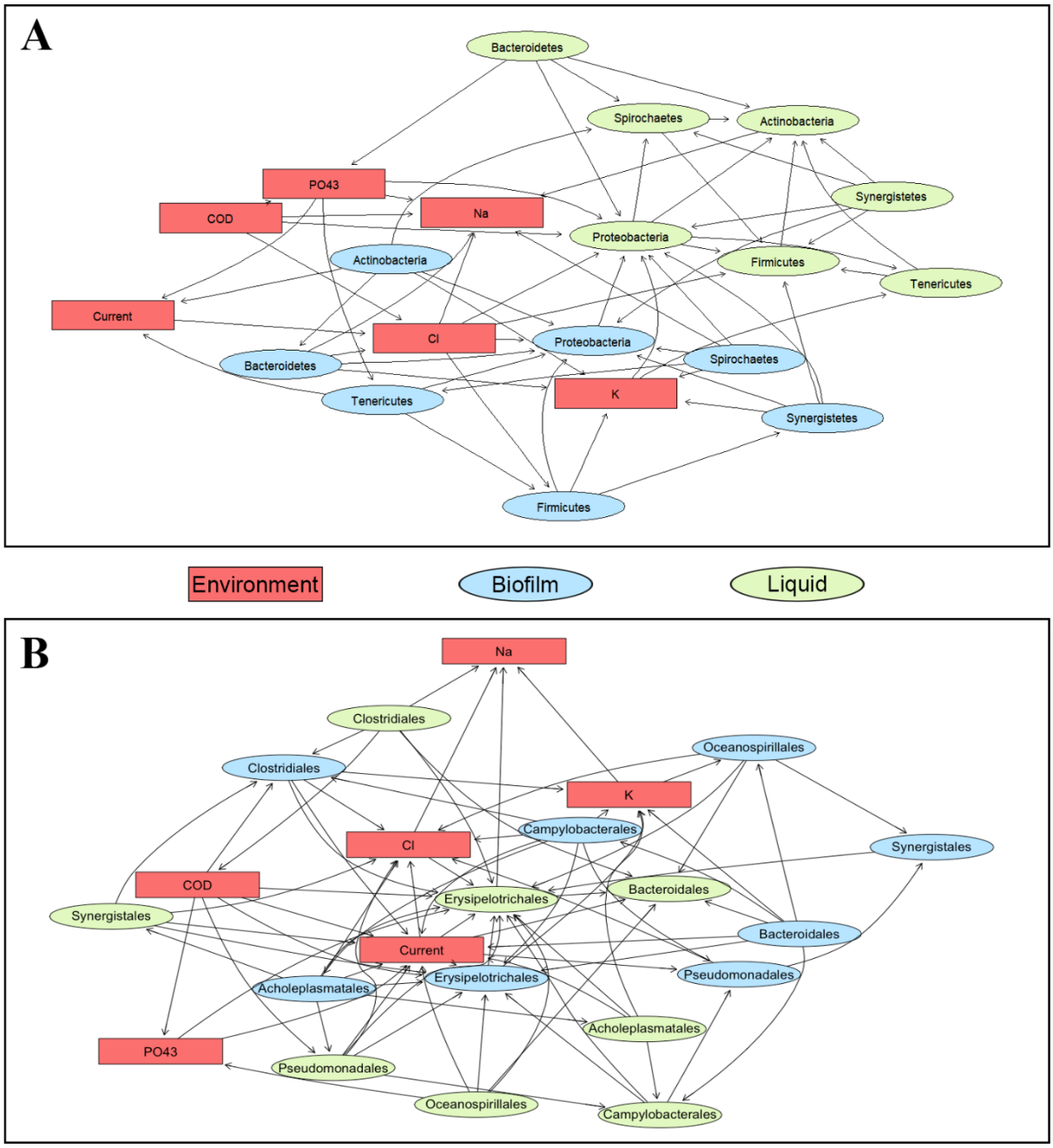

Figure 2.6 (A) The Bayesian network at the phylum level with 7 dominant phyla in the biofilm and suspended communities and 6 environmental parameters. (B) The Bayesian network at the order level with 8 dominant orders in the biofilm and suspended communities and 6 environmental parameters.

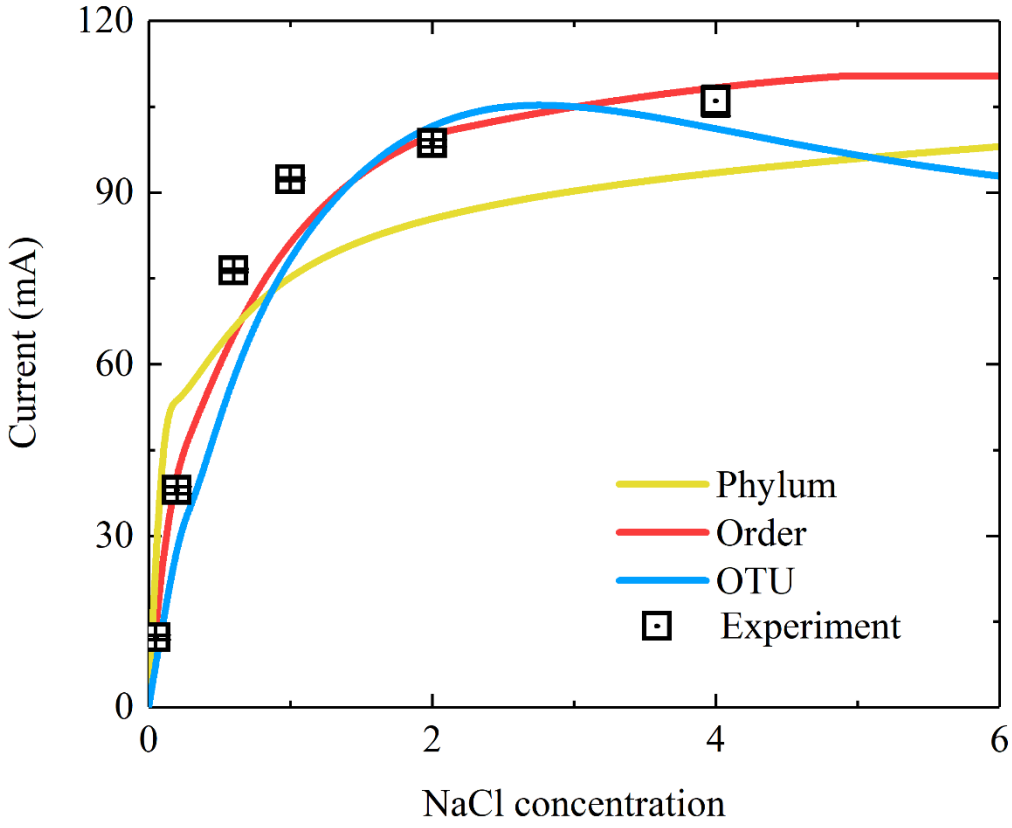

Figure 2.7 The actual and simulated current at different levels. Error bars were calculated from triplicate data.

Bayesian network modeling was further validated by calculating the RMSE. The RMSE at the phylum level ranged from 6% to 21% for the biofilm taxa and from 4% to 26% for the suspended taxa (Figure A13A). Proteobacteria, which was composed of several major EET species, was the best predicted phylum in both communities under all six NaCl concentrations, regardless of the large variations in some of the experimental data (Figure A14). The RMSE was not improved at

the order level (Figure A13B), and the values for Campylobacterales and Synergistales in the biofilm and Oceanospirillales in the liquid reached >30%, mainly due to the over-estimation at low NaCl concentrations (Figure A15). The prediction power further decreased at the OTU level as indicated by the large standard deviations (Figure A13C). Over- and under-prediction of the taxa were frequently observed in both biofilm and suspended communities under all six conditions (Figure A16). Overall, the RMSE results were in accordance with the Bray-Curtis similarities that the anode community could be more accurately predicted at higher taxonomic level.

After the modeling approach was demonstrated as valid according to Bray-Curtis similarities and RMSE, final Bayesian networks were constructed from the whole dataset to further understand the microbial interactions and the potential functions of the major taxa in the MDC anode. Consistent with the low RMSE, the abundance of Proteobacteria was inferred well by the the phylum-level Bayesian network (Figure 2.6A) with low standard deviation. The Proteobacteria were negatively related to other phyla at the same location (i.e., biofilm or liquid), implying competition. In addtion, the occurrence of Proteobacteria was positively dependent on Cl^-, which agreed with experimental data that EET taxa became dominant at high salinities (Figure 2.3). At the order level (Figure 2.6B), the major EET taxa Pseudomonadales was better simulated in the liquid than in the biofilm (standard deviation 0.06 vs. 0.24). Putatively non-EET Erysipelotrichales showed a strong negative correlation with the current (correlation coefficients of -4.08 in the biofilm and -1.61 in the suspended community), while Synergistales and Acholeplasmatales in the suspended community were negatively associated with EET taxa, suggesting that they might not play a role in current production.

The Bayesian networks indicate that environmental parameters can be predicted from taxonomic data (Figure 2.6). For example, current, Cl^- and PO_4^{3-} were simulated with RMSE lower than 7% (Figure A13). The prediction of the current was slightly better with the taxonomic data at the order level as the slope of prediction vs. experiment was closer to 1 (Figure A17A) and standard deviation of the equation was the lowest. The relationships between order abundance, current production, COD removal and PO_4^{3-} concentration indicated that current was not only associated with the three EET orders, but also correlated with the putative non-EET taxa. Current production was continuously simulated and the taxonomic data at the order level yielded the most accurate

prediction (Figure 2.7), with low RMSE ranging from 1.8 to 14.1% (Table A3). It should be noted that the prediction power of the continuous simulation was partly affected by the accuracy of the logistic regressions (Figure A18, A19 and A20) and thus only provided qualitative insights of the system performance. Nevertheless, the simulation at all three taxonomic levels proposed that current production would not be noticeably enhanced with a NaCl concentration higher than ~2 M (Figure 6), possibly because microbial activity would be suppressed by the high salinity.

2.4 Discussion

Adding salt in the electrolyte can reduce ohmic resistance and may be a simple solution to enhance BES performance, but the detailed effects of salinity remain controversial in the literature. It was previously suggested that a NaCl concertation higher than 0.3 M in the desalination chamber might adversely affect electricity generation [30]. However, the present study showed high current production above 0.6 M NaCl (Figure 2.1), and the current (300 A m^{-3}-anode volume or 7 A m^{-2}-cathode electrode area) at 4 M NaCl was one of the highest among MDC studies. As ions accumulated in the MDC anode over a period of time, microorganisms could adapt to the saline environment. In addition, electrochemically active bacteria took advantage of high NaCl concentrations in the desalination chamber and created optimal anode salinities for continued dominance by regulating the bioelectrochemical activity (Figure A1, Figure 2.2 and Figure 2.3). When the NaCl concentration was higher than 1 M, the anode effluent still contained a considerable amount of organic substrate (Figure 2.1B and Figure A3), but it was not converted to electricity, indicating that further enhancement of bioelectrochemical activity may be suppressed by high salinity.

Based on patterns of microbial community structure and phylogeny, *Pseudomonas*, *Acinetobacter*, *Arcobacter* and *Halomonas* are proposed to be the major electrochemically active microorganisms in the MDC anode, utilizing phenazine derivatives as electron shuttles (Figure 2.4). Members of Bacteroidales and Clostridiales might not be involved in EET directly but could play critical roles in sustaining other important functions in the anode community, allowing mixed-culture BES to consistently generate higher current and power than pure-culture BES [18]. For example, members of Bacteroidales may be scavenging dead cells on the electrode [240], thereby creating space for electrochemically active bacteria and facilitating EET kinetics. Hydrogen gas may be produced

from biomass fermentation, and subsequently used together with HCO_3^- by Clostridiales (e.g., *A. noterae*, Figure 2.5) to form acetate. Some Clostridiales, such as *Clostridium ljungdahlii* and *Clostridium aceticum*, have been reported to reduce CO_2 to acetate using an electrode poised at -400 mV vs. SHE as electron donor [241]. A similar process may occur in the MDC anode, but with phenazine derivatives donating electrons. At pH 7, the redox potentials of phenazine-1-carboxylic acid and phenazine-1-carboxamide are calculated to be -360 and -400 mV vs. SHE (onset oxidative potential in CV, Figure A9), which are thermodynamically favorable when coupled with CO_2 reduction to acetate (-296 mV vs. SHE). The hypothesis implies the importance of Clostridiales in carbon cycling and electron flow in the MDC anode, which is consistent with the prediction by PICRUSt and Bayesian network (Figure 2.5 and Figure 2.6), but needs further studies that directly measure functions.

Bayesian networks can help identify interactions between environmental factors and dominant taxa (Figure 2.6) [242], and have been used here for the first time to predict functional output from an engineered system (Figure 2.7). This approach is based on taxonomic data, and avoids the assumption of a simplified microbial community and the estimation of empirical coefficients [243]. For instance, a previous MDC engineering model developed based on a configuration similar to the present study (a tubular reactor with a 300-mL anode and 150 mL-desalination chamber) could not yield satisfactory simulation at high NaCl concentrations without optimizing some key coefficients [131]. In contrast, the taxa-based statistical model in this study can well predict reactor performance over a wide range of salt concentrations with low RMSE. With the advancement in sequencing technologies and biostatistics, such an approach can potentially be expanded to predict the effects of other engineering factors – including COD loading, hydraulic retention time, external resistance and electrode size, etc. – and produce a statistical model that is universally applicable to various types of bioreactors.

In summary, this study has highlighted the potential of MDC as a next-generation energy-efficient water and wastewater treatment technology. High NaCl concentrations in the desalination chamber of an MDC is beneficial for current production and leads to the dominance of shuttle-mediated electrochemically active microorganisms such as *Pseudomonas* and *Acinetobacter*. Members in Bacteroidales and Clostridiales are putatively not capable of EET but may play a role in

maintaining bioelectrochemical functions. By combining engineering methods, molecular techniques, electrochemical measurements and statistical analyses, this study has developed a novel statistical method to understand and predict the performance of engineered biological systems.

CHAPTER 3: Facile Synthesis of MoS2@CNT as an Effective Catalyst for Hydrogen Production in a Microbial Electrolysis Cell

(This section has been published as: Heyang Yuan, Jianyang Li, Chris Yuan, and Zhen He. "Facile synthesis of MoS2@ CNT as an effective catalyst for hydrogen production in microbial electrolysis cells." ChemElectroChem (2014): 1, 1828-1833.)

3.1 Introduction

Hydrogen is considered to be a promising next-generation fuel because of its high heat value and generation from renewable sources [244]. The methods for hydrogen production including stream reforming and water splitting consume a large amount of energy, which can be substantially reduced by using renewable resources such as organic compounds in wastewater [245]. As a new approach for producing hydrogen from renewable sources especially organic wastes, microbial electrolysis cell (MEC) can generate hydrogen gas by taking advantage of microbial respiration with an electrode [86]. In an MEC, exoelectrogens oxidize organic compounds and release electrons to an anode electrode, resulting in a potential of -0.30 V vs. SHE at the anode when acetate acts as an organic source [113]. To drive hydrogen evolution reaction (HER) on a cathode electrode (-0.41 V vs. SHE), an external voltage > 0.11 V will be theoretically required, and in practice a voltage >0.2 V is usually applied to overcome overpotentials [246]. Even with an additional voltage input, the energy consumption in an MEC is still less than the conventional water electrolysis. Moreover, because electrons are generated from wastes, hydrogen production in an MEC will benefit sustainable societal development. MECs have been intensively studied in the past few years [247-249], and a pilot-scale MEC exhibited the feasibility of using winery wastewater as a substrate to produce hydrogen gas [117]. However, further development of MECs is seriously hindered by high capital cost, especially that of cathodic catalysts.

Catalysts are commonly applied to facilitate HER, which is thermodynamically favorable but kinetically slow. Platinum is widely used in bench-scale experiments and shows outstanding productivity [250], but it is not economically viable. Rozendal, Jeremiasse [251] demonstrated the possibility of utilizing biocathode to catalyze hydrogen evolution; however, hydrogenotrophic methanogens could thrive and consume hydrogen gas [128]. From the perspective of stability and performance, metallic and synthetic catalysts may be a better choice. Nickel has a relatively high

catalytic activity and thus has been modified into various forms for MEC applications including powder [122], foam [252], alloy [253] and nano-assembly [254]. Huang, Liu [255] coated carbon paper with palladium via electrochemical deposition and obtained a catalytic efficiency 50 times higher than platinum. In a study using iron-based composite nanorods as catalysts, hydrogen yield was found to be comparable to platinum [256]. Nevertheless, operational complexity and energy consumption during material synthesis accounts for the major issue of the above-mentioned materials.

Molybdenum sulfide (MoS_2) is an exciting catalyst inspired by the research of nitrogenase enzyme [257]. Density functional theory (DFT) calculation suggested that the Mo-edge favored hydrogen binding [257]. In the volcano plot of the exchange current density as a function of Gibbs free energy of adsorbed atomic hydrogen, MoS_2 was found close to platinum, indicating a high potential of HER catalysis [258]. The inherent defect of this material lies in its low conductivity and insufficient active sites [111]. To tackle these problems, MoS_2 has been modified by means of Li+ intercalation, [259] chemical exfoliation [260] and hybridization with graphene oxide [261]. Laursen, Kegnaes [111] coated MoS_2 on multi-wall carbon nanotubes (CNTs) to increase conductivity. Their results revealed that coating could achieve good performance, but excessive treatment, i.e. annealing at high temperature would lead to loss of active edges.

By far there has been only one MEC study using MoS_2 as a HER catalyst [262], in which MoS_2 was not modified but simply mixed with carbon black. Linear sweep voltammograms showed an earlier onset potential for MoS_2 than for Pt. High current density and hydrogen production rate were also obtained in the batch MEC test. However, the amount of MoS_2 loaded on the electrode was 5 times more than that of Pt, making the comparison arguable. Herein, we report a simple facile approach to the fabrication of 1D tabular architecture composed of edge-terminated ultrathin MoS_2 nanosheets and high conductive CNTs (MoS_2/CNT). This unique structural design utilizes combinative merits of edge-terminated MoS_2 and the high conductive CNTs, leading to both enhanced electronic conductivity and increased amount of actives sites. The MoS_2/CNT composites were examined by using electrochemical techniques and in an MEC for hydrogen production.

3.2 Materials and methods

3.2.1 Synthesis of MoS_2/CNT

CNTs (Flo Tube 6000, CNano Technology, Ltd., CA) with an average outer/inner diameter of 7 nm / 3 nm and length of 10 μm was purified by sonicating in concentrated HNO_3 (70% W/W) for 30 min followed by washing with deionized (DI) water and drying at 60 ºC in a vacuum oven. In typical synthesis of the MoS_2/CNT nanocomposite, CNTs was dispersed in 80 mL sodium dodecylbenzene sulfonate (SDBS) solution (2 % w/w) with sonication for 1 h. Then, 15 mg sodium molybdate and 20 mg thiourea were added into the solution subsequently and sonicated for 15 min. The homogenous solution was transferred to a Teflon-lined autoclave and heated at 220 °C for 24 h. Afterward, the dark suspension was collected and rinsed with DI water for several times before drying. MoS_2, MoS_2/CNT-30, and MoS_2/CNT-60 were synthesized by the similar hydrothermal method.

3.2.2 Characterization

Hitachi S-4800 field emission scanning electron microscope (FESEM) and Hitachi H9000 NAR transmission electron microscope (TEM) operating at an acceleration voltage of 300 KV were employed to study the morphology and structure properties. X-ray diffraction (XRD, Bruker D8 Discover A25) was used to identify the crystal structure and phase information with copper K_α radiation. Thermal gravity analysis (TGA, TA SDT 2960) was used to determine the CNT concentration in the nanocomposite. Raman spectra were taken on a Renishaw 1000B Raman spectrometer with a 632.8 nm HeNe laser source. Surface area and pore volume were measured by a multipoint BET nitrogen adsorption/desorption method using Micrometrics ASAP200. Further investigation on the compositions and atomic valence states was collected by HP 5950A X-ray photoelectron spectroscopy (XPS) with Mg Kα as the source and corrected by the C 1s peak at 284.6 eV.

3.2.3 Preparation of the cathode

The synthesized catalysts were coated on a piece of rectangular carbon cloth (PANEX®30PW03, Zoltek Corporation, St.Louis, MO, USA) with an area of 4 cm^2 that was used as a cathode electrode. In more details, 20 mg of the materials (MoS_2 coated on 0%, 30%, 60% and 90% CNT) were mixed with 133 μL Nafion (Sigma-Aldrich, St. Louis, MO, USA) and 17 μL DI water and

applied to the carbon cloth, making a loading rate of 5 mg cm^{-2}. After coating, the carbon cloth was dried in a fume hood for 24 h and then ready for use. A cathode coated with 20 mg of Pt/C (10% wt. Platinum on Carbon Vulcan, Fuel Cell Earth LLC, Wakefield, Ma, USA) was prepared with the same method and served as control.

3.2.4 MEC construction and operation

A two-chamber MEC was built by connecting two glass bottles with a cation exchange membrane (CEM) as a separator (UltexCMI7000, Membranes International, Inc., GlenRock, NJ, USA). The liquid volume of the anodic chamber and the cathodic chamber was 130 and 140 mL, respectively. The anode electrode was a carbon brush (Gordon Brush Mfg.Co., Inc., Commerce, CA, USA) that had been cultivated under a microbial fuel cell mode for three months. The anolyte contained (per liter of DI water): sodium acetate, 1 g; NaCl, 0.5 g; $MgSO_4$, 0.015 g; $CaCl_2$, 0.02 g; KH_2PO_4, 0.53 g; K_2HPO_4, 1.07 g; $NaHCO_3$, 1 g; and trace element, 1 mL [200]. One M PBS (KH2PO4, 53 g; K2HPO4, 107 g) solution was used as a catholyte. An external voltage of 0.8 V was applied to the MEC by connecting the cathode electrode to the negative pole of a power supply (3644A, Circuit Specialists, Inc., Mesa, AZ, USA), the anode electrode to a 0.1-Ω resistor then to the positive pole. The MEC was operated under a batch mode at room temperature. Every 48 h as one cycle, 60 mL of anolyte and 140 mL of catholyte were replaced. Each material was tested in triplicate.

3.2.5 Measurement and analysis

The voltage (U) on the 0.1-Ω resistor was recorded by a digital multimeter (2700, Keithley Instruments, Inc., Cleveland, OH, USA) with a time interval of 5 min. Current (i) was calculated with Ohm's law $i = U/R$. Hydrogen production in the MEC was collected with water displacement and measured with a syringe. Chemical oxygen demand (COD) was measured using a DR/890 colorimeter (HACH Co., Ltd., USA) according to manufacturer's handbook. Linear sweep voltammogram (LSV, scan rate 10 mV s^{-1}) and Tafel plot (scan rate 1 mV s^{-1}) were measured with a potentiostat (Reference600, Gamry Instruments, Warminster, PA, USA). Electrochemical experiments were conducted in a sealed glass bottle containing 120 mL of 1 M PBS solution, where the modified cathode electrodes served as a working electrode, a platinum wire served as a counter electrode, and an Ag/AgCl electrode (CH Instruments, Inc., Austin, TX, USA) acted as a reference electrode. The glass bottle was sparged with nitrogen gas for 15 min prior to each test.

Important parameters including Coulombic efficiency (Equation 3.1), cathodic H_2 recovery (Equation 3.2), overall H_2 recovery (Equation 3.3) and H_2 production rate (Equation 3.4) were calculated as previously described [246, 256]:

$$r_{CE} = \frac{8 \int idt}{FV_{An}\Delta COD} \quad (3.1)$$

$$r_{cat} = \frac{2n_{H_2}F}{\int idt} \quad (3.2)$$

$$r_{H_2} = r_{CE}\, r_{cat} \quad (3.3)$$

$$Q_{H_2} = \frac{V_{H_2}}{A_{cat}t} \quad (3.4)$$

Where F is the Faradaic constant, V_{An} is the anolyte volume, ΔCOD is the removed COD, n_{H2} is the mole of hydrogen production, V_{H2} is the hydrogen volume and t is the time period of one cycle (48 h).

3.3 Results and discussion

3.3.1 Characterization of the catalysts

The synthetic procedure is primarily based on the a simple one-pot hydrothermal reaction in the presence of CNTs. The CNTs was fist purified by sonication in concentrated nitric acid and then dissolved in dilute sodium dodecylbenzene sulfonate (SDBS) solution. Sodium molybdate and thiourea were added in the homogenous solution of the highly-dispersed CNTs. The field emission scanning electron microscopy (FESEM) and transmission electron microscopy (TEM) studies of CNTs show an average diameter of 7 nm and length of 10 µm. The FESEM image of the MoS_2/CNT-90 composite reveals slightly increased diameter (Figure 3.1c and 3.1d) compared to original CNTs (Figure 3.1a and 3.1b). A thin layer of MoS_2 nanosheet on the surface of CNTs is clearly observed by TEM (Figure 3.1d). The lattice spacing is measured to be 0.65 nm corresponding to the interlayer spacing along the z-axis perpendicular to (002) plane of 2H-MoS_2. However, MoS_2/CNT-60 and MoS_2/CNT-30 demonstrate the morphology of MoS_2 flowers embedded in the CNTs networks (Figure B1c and B1d). The increased amount of MoS_2 flowers might block the fast electron transport, which limits the overall electrocatalytic performance. Pristine MoS_2 shows similar flower-like morphology composed of a thick layer of MoS_2

nanosheets (Figure 3.1e), which was measured to approximately 15 layers with a lattice spacing of 0.65 nm (Figure 3.1f).

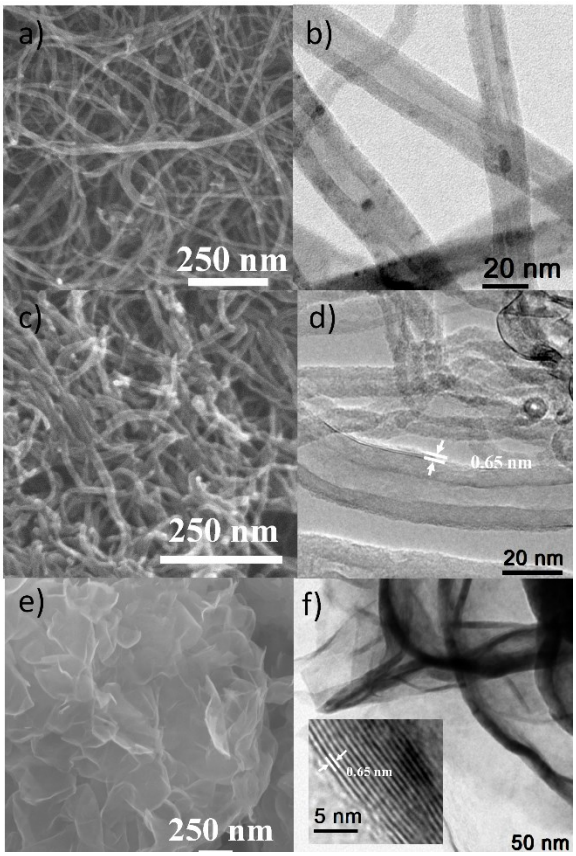

Figure 3.1 FESEM and HRTEM images of (a) and (b) CNT, (c) and (d) MoS_2/CNT-90, (e) and (f) MoS_2. Arrows in (d) indicate a thin layer of MoS2 nanosheet on the surface of CNTs. Inset in (f) is corresponding lattice fringes.

X-ray diffraction (XRD) was employed to investigate the crystal structure and phase information of CNTs, MoS_2 and MoS_2/CNT composites (Figure 3.2a). The spectra of MoS_2, MoS_2/CNT-60, and MoS_2/CNT-30 show typical diffraction peaks of a hexagonal crystal structure, which can be indexed as 2H-MoS_2 with a space group of $P6_3/mmc$ (JCPDS 37-1492). Compared with pristine MoS_2, the (002) peak of MoS_2/CNT-60 and MoS_2/CNT-30 depict a reduced intensity and broadened width, suggesting a smaller mean crystallite size than that of pristine MoS_2. Moreover, there are no observable MoS_2 peaks on the spectrum of MoS_2/CNT-90 probably due to the low concentration of MoS_2 in the nanocomposite. By assuming the remaining product is MoO_3 and no

Mo atom loss during the thermogravimetric analysis (TGA), the amount of MoS_2 in the original nanohybrid is calculated to be 91% (Figure B2), which is close to the material input. Similarly, the Raman spectrum of MoS_2/CNT-90 reveals characteristic peaks of CNT at 1330 cm^{-1} (D band) and 1590 cm^{-1} (G band) with barely observable MoS_2 peaks. However, MoS_2, MoS_2/CNT-30, and MoS_2/CNT-60 exhibits clearly typical peaks of the in-plane E^1_{2g} phonon mode (374 cm^{-1}) and out-of-plane A_{1g} vibration phonon mode (402 cm^{-1}) of MoS_2 (Figure 3.2b), confirming the presence of MoS_2 in the nanocomposite. A close view of all three spectra demonstrates higher intensity of A_{1g} mode than that of E^1_{2g} mode, indicating the formation of edge-terminated MoS_2 film [263]. According to the previous report that edges of an S–Mo–S sheet are the active sites, in particular the $[\bar{1}010]$ Mo-edges have the most advantageous hydrogen binding energy of the edges considered [111]. X-ray photoelectron spectroscopy (XPS) was conducted to study the compositions and atomic valence states of the MoS_2/CNT-90 nanocomposite (Figure 3.2c). The full survey of MoS_2/CNT-90 exhibits signals of sulfur, molybdenum, carbon, and oxygen, confirming the presence of MoS_2 in the nanohybrid. Oxygen was introduced during CNTs purification process. High resolution XPS spectra of Mo 3d and S 2p reveal peaks at 229.1, 232.3, 162.9, and 161.9 eV (Inset of Figure 3.2c), corresponding to Mo $3d_{3/2}$, Mo $3d_{5/2}$, S $2p_{1/2}$, and S $2p_{3/2}$ components of MoS_2, respectively. Moreover, the nitrogen adsorption-desorption isotherms of all five samples show a type IV with H3-type hysteresis loop, indicating the presence of mesoporous structure (Figure 3.2d). The specific surface area and pore volume of MoS_2/CNT-90 using Brunauer–Emmett–Teller (BET) method are measured to be 205 $m^2\ g^{-1}$ and 0.856 $m^3\ g^{-1}$, respectively (Table B1). In comparison, MoS_2/CNT-60 and MoS_2/CNT-30 exhibit much lower surface area and pore volume. Notice that the larger surface area provides more exposed active edge sites, which is anticipated to have an excellent activity for electrocatalytic hydrogen evolution [264].

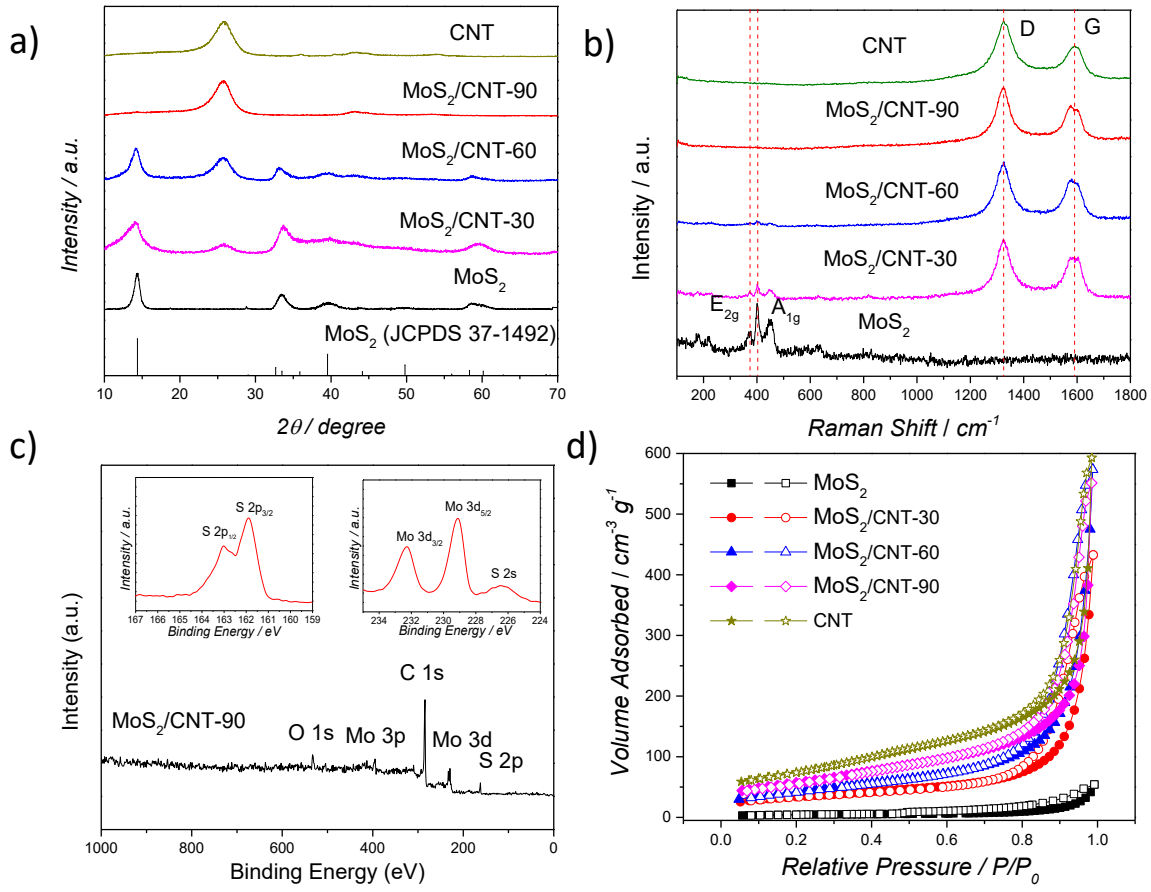

Figure 3.2 (a) XRD patterns, (b) Raman spectra, (c) XPS full survey and the corresponding high resolution Mo 3d and S 2p XPS spectra of MoS_2/CNT-90 nanohybrid (insets), (d) Nitrogen adsorption-desorption isotherms.

3.3.2 Electrochemical performance

The HER activity of MoS_2 composites was first evaluated using LSV. Because the measurement was conducted in 1 M phosphate buffer saline (PBS) with a pH of 7.01±0.01, the potential was normalized according to: $E_{RHE} = E_{measure} + 0.41 + 0.20$ V vs. RHE (reversible hydrogen electrode), where 0.41 V is the shift caused by pH and 0.20 V is due to the use of Ag/AgCl reference electrode. The MoS_2/CNT-90 exhibited early cathodic current at a small overpotential of approximately 70 mV, indicating a high HER activity (Figure 3.3a). On the other hand, late onset potentials were observed with the materials containing 30% and 0% of CNTs, which is in agreement with that in previous research [111, 260, 264]. In contrast, pure CNTs did not show drop until -0.5 V vs. RHE

(data not shown). Tafel plot was conducted for further investigation of the electrochemical property. The Tafel slopes fitted from the plots were ~30 mV dec^{-1} for Pt, and ranged from 59 (CNT-90) to 73 (MoS_2) mV dec^{-1} for the composites (Figure 3.3b).

In theory, three steps may participate in HER in acid media [111, 261, 265, 266], while similar Tafel behavior was also observed previously in PBS solution [267]:

Volmer reaction: $H^+ + e^- \rightarrow H_{ads}, b = 2.3RT/\alpha F \approx 120\ mV\ dec^{-1}$

Heyrovsky reaction: $H_{ads} + H^+ + e^- \rightarrow H_2, b = 2.3RT/(1+\alpha)F \approx 40\ mV\ dec^{-1}$

Tafel reaction: $H_{ads} + H_{ads} \rightarrow H_2, b = 2.3RT/2F \approx 30\ mV\ dec^{-1}$

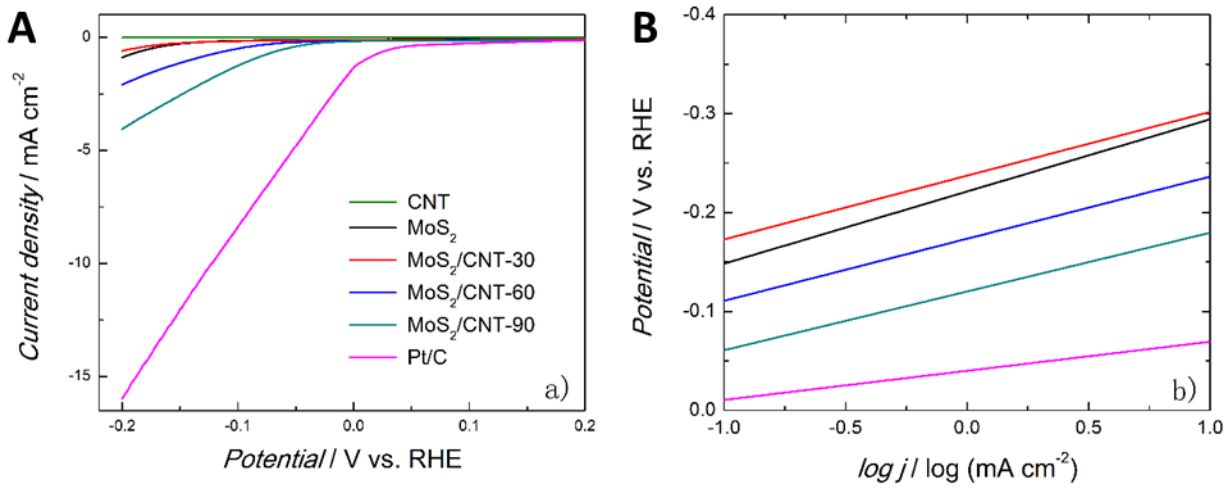

Figure 3.3 (a) linear sweep voltammogram (scan rate 10 mV s^{-1}) and (b) Tafel slope (scan rate 1 mV s^{-1}) measured under 1 M PBS buffer (pH = 7.01±0.01).

Hydrogen is produced through the combination of either Volmer-Heyrovsky mechanism or Volmer-Tafel mechanism. The significance of Tafel slope is that the rate determining step of HER can be identified by comparing calculated and experimental slopes. The measured Tafel plot yielded slopes close to 40 mV dec^{-1}, suggesting that Heyrovsky reaction, i.e. desorption step is limiting the HER kinetics. It should be noted that Tafel slopes of MoS_2 modified with different methods varies in a wide range [263], and thus make the HER mechanism inconclusive. Thus, we tend not to interpret HER mechanism solely based on Tafel slope. However, the plot also provided other valuable information. Figure 3.3b depicts highly similar electrochemical behavior for all

MoS_2 composites despite different CNT contents, indicating similarity of catalytic chemistry on the material surface [268]. On the other hand, the disparity of HER activity shown in Figure 3.3a implies crucial factors other than HER mechanism effecting the catalytic performance.

One inherent problem of MoS_2 as a catalyst is the low conductivity between S-Mo-S sheets bonded by van der Waals force [111], which could be the reason for late onset potential of pure MoS_2. As shown in SEM (Figure 3.1), coating CNTs with MoS_2 did not noticeably change the morphology. In addition, a higher CNT ratio means a lower amount of MoS_2, leading to the reduced active sites, as no other modification was made on MoS_2 [269]. Therefore, the enhanced HER activity with increased CNT content may not correlate with active sites, but is very likely due to increased conductivity [269, 270]. Those results suggest that conductivity could be the main limiting factor when using MoS_2 to catalyze HER.

3.3.3 MEC experiments

Actual hydrogen production catalyzed by MoS_2/CNT was investigated in an MEC operated under a batch mode. The electrical current generation is shown in Figure 3.4. In general, currents decreased over the course of operation due to the consumption of substrates. The Pt catalyst led to relatively stable current generation between 10 and 35 h. A higher content of CNTs in MoS_2/CNTs resulted in a higher current generation. A more detailed comparison can be found in Table 3.1, in which one can see that total coulomb (C_{total}) production roughly follows this order: Pt > CNT-90 > CNT-60 > CNT-30 > MoS_2. This trend is further confirmed by other parameters enumerated in Table 3.1. The calculation shows similar cathodic hydrogen recovery (R_{cat}), indicating a high HER activity of the catalysts. On the other hand, Coulombic efficiency (C_R) of the composites was slightly enhanced by coating, but still inferior to that of Pt. Although different C_R led to a minor difference in overall hydrogen recovery (R_{H2}), it exerted a distinct effect on actual hydrogen production rate (Q_{H2}). While the Q_{H2} of materials containing less CNT was less than 80% of that of Pt, MoS_2/CNT-90 achieved comparable hydrogen production.

The results of the MEC test, including current density, C_{total}, C_R and Q_{H2}, are in agreement with the aforementioned material characterization and electrochemical analysis, justifying the assumption that increasing CNT content could improve the HER activity. Based on the similar

Tafel behavior (Figure 3.3b) we assume that this is principally attributed to the increased conductivity via coating. This hypothesis is supported by the findings in a recent study, in which a catalyst was synthesized by binding amorphous MoS_x on vertical nitrogen-doped CNTs via precursor deposition. [271] The authors of that study demonstrated an optimized structure with the maximum catalytic surface area and sufficient contact between MoS_x and CNTs, and reported small overpotential (~75 mV) and Tafel slope (40 mV dec^{-1}), which is close to our results. Furthermore, their electrochemical impedance spectroscopy (EIS) showed reduced charge transfer resistance for hybrid catalyst compared to pure MoS_x, indicating that the good performance of the MoS_x/CNTs composite is due to electronic coupling between MoS_x and nitrogen-doped CNTs.

In summary, the MoS_2/CNT composites synthesized in this study are promising for future MEC application because of the comparable performance to Pt, simple synthetic procedure and low price. [262] The relevance of active sites and conductivity and the durability of the catalysts will be further investigated in the future. In addition, the material could be further modified to reach an optimal MoS_2:CNT ratio. Tackling these problems will not only improve the hydrogen production catalyzed by MoS_2 composites, but also provide insight into hydrogen evolution catalysis for other materials.

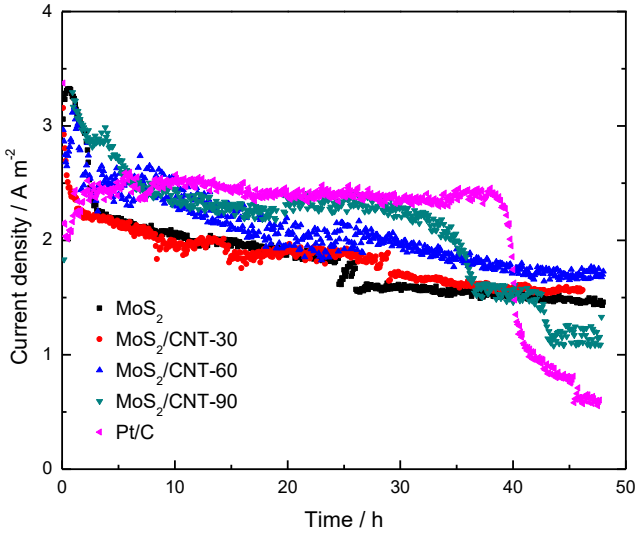

Figure 3.4 Current density of the MEC with MoS_2 composites or Pt serving as a catalyst at an applied voltage of 0.8 V.

Table 3.1 Hydrogen production and efficiencies of the MEC using MoS_2 composites or Pt as a cathode catalyst. Standard deviation is calculated with triplicate experiments.

	C_{total}[a] (C)	C_R[b] (%)	R_{cat}[c] (%)	R_{H2}[d] (%)	Q_{H2}[e] (m^3 H_2 m^{-2} d^{-1})
MoS_2	115.8±12.3	21.6±2.3	46.2±4.3	10.0±1.5	0.0078±0.0014
MoS_2/CNT-30	119.8±3.2	25.3±3.5	43.2±0.6	10.9±1.5	0.0077±0.0002
MoS_2/CNT-60	121.6±19.7	23.3±7.8	46.0±4.0	10.9±4.5	0.0081±0.0008
MoS_2/CNT-90	144.4±3.8	25.7±5.0	49.0±5.5	12.7±3.9	0.0101±0.0007
Pt	146.9±5.9	30.6±3.8	48.0±6.1	14.6±1.6	0.0103±0.0013

[a] C_{total}: Total coulomb.
[b] C_R: Coulombic recovery.
[c] R_{cat}: Cathodic hydrogen recovery.
[d] R_{H2}: Overall hydrogen recovery.
[e] Q_{H2}: Hydrogen production rate.

3.4 Conclusions

In this study, molybdenum disulfide (MoS_2) was coated on nitrogen-doped carbon nanotubes (CNTs) to increase its conductivity, and the synthesized material was examined in an MEC for HER. Linear sweep voltammogram demonstrated the enhanced HER activity with increasing the content of CNTs. Tafel plot yielded slopes ranging from 59 to 73 mV dec^{-1} for the MoS_2 composites, indicating similar chemistry on the surface of the composites compared with the unmodified MoS_2. These data suggest that conductivity may be the main limiting factor for overall HER activity by MoS_2. The MEC test showed that the MoS_2/CNT-90 achieved comparable hydrogen production to the Pt catalyst. The low price of the MoS_2 composites will make it competitive as an effective HER catalyst for MEC application.

CHAPTER 4: Porous Carbon nanosheets co-doped with Nitrogen and Sulfur for Oxygen Reduction Reaction in Microbial Fuel Cells

(This section has been published as: Heyang Yuan, Yang Hou, Zhenhai Wen, Xiaoru Guo, Junhong Chen and Zhen He. Porous carbon nanosheets codoped with nitrogen and sulfur for oxygen reduction reaction in microbial fuel cells. ACS Applied Materials & Interfaces (2015): 7, 18672-18678.)

4.1 Introduction

The oxygen reduction reaction (ORR) is one of the most critical reactions for electrochemical systems. Because ORR is sluggish, platinum is widely used as a catalyst in lab experiments, but is economically not feasible for large-scale applications, which poses a major challenge for fuel cell applications [272]. Non-precious metals such as manganese, iron and cobalt have also been modified and efficient catalysis has been obtained [273, 274]. However, the long-term stability of these metal catalysts remains to be examined.

Carbon materials are of great interest for fuel cells because of their low cost and high stability [44, 275]. Nitrogen-doped carbon catalysts (e.g., carbon nanotubes, nanosheets, graphene etc.) exhibit abundant defect sites, high specific surface area and high conductivity, and thus have drawn great attention in recent years [61, 276, 277]. Enhanced ORR catalysis using nitrogen-doped carbon materials have therefore been extensively reported in previous studies [278, 279]. In addition to nitrogen, heteroatoms such as boron, sulfur and phosphorus have also been doped in carbon-based materials and noticeably enhanced ORR catalysis [280, 281]. The catalytic activity was reported to be further improved by dual doping of N and S [282, 283], and the specific surface area of a sulfur–nitrogen co-doped three-dimensional carbon foam reached up to 850 m^2 g^{-1} [284]. While the synergetic effects of the dopants and the ORR mechanism remained to be explored, dual-doped N/S carbon materials with outstanding ORR catalytic activity may hold great promise for the development of fuel cells.

Another perspective of fuel cells is to generate energy from renewable resources such as wastewater. Wastewater is increasingly recognized as a green resource because of the potential energy and nutrient that it contains [4]. The chemical energy stored in organic matters in wastewater can be directly converted into electricity by microbial fuel cells (MFCs) [285]. In the anode of an MFC, exoelectrogens degrade organics and respire by releasing electrons extracellularly to the anode electrode [18]. When proper electron acceptors (e.g. oxygen) are used in the cathode and the overall reaction of the cell is thermodynamically favorable, the electrons will flow spontaneously through an external circuit to the cathode [113]. As such, wastewater treatment and electricity generation are achieved simultaneously. Similar to chemical fuel cells, oxygen is a common electron acceptor because of its availability and high reduction potential. Therefore, advances in carbon-based materials for ORR catalysis may play an important role in sustainable water and wastewater treatment in future. A variety of carbon-based materials, including activated carbon [286-288] and grapheme [48], have been used as cathode catalyst of MFCs and show great promise in terms of performance and stability.

In this work, we have demonstrated the simple synthesis of N/S co-doped porous carbon nanosheets (N/S-CNS) with abundant active sites and high surface area. The ORR catalysis of the as-prepared catalysts was studied by linear sweep voltammetry, electrochemical impedance spectroscopy and rotating disk electrode measurement. To better understand the catalysis performance, the catalysts were further examined in an MFC. The present work is expected to provide insights into the dual-doping of N and S in carbon materials and the application of such catalysts in MFCs for energy-efficient wastewater and/or water treatment.

4.2 Materials and methods

4.2.1 Synthesis of N/S-CNS

To synthesize the catalysts, 1 g of potassium citrate was annealed in Ar atmosphere at 850 ºC for 2 h at a heating rate of 2 ºC min^{-1} [289]. The porous carbon nanosheets were generated by further treatment of the products as-obtained above with 0.5 M H_2SO_4 solution for overnight followed by washing with deionized water and vacuum drying with a yield of about 41%. Next, the obtained porous carbon nanosheets were dissolved in 10 mL ethanol, followed by addition of 0.5 g diphenyl

disulfide under stirring. Then, the solvent was slowly evaporated at 50 ºC. The remaining powder was further heated at 750 ºC with a rate of 2 ºC min^{-1} and held at that temperature for 2 h under NH_3 atmosphere, resulting in the formation of N/S co-doped porous carbon nanosheets. For comparison, CNS were also doped with solely nitrogen or sulfur.

4.2.2 Characterization

Microstructures of the samples were examined using transmission electron microscopy (TEM, Hitachi H 9000 NAR) and field-emission scanning electron microscopy (FESEM, Hitachi S-4800). X-ray diffraction (XRD) data were obtained with a Scintag XDS 2000 X-ray powder diffractometer (Cu Kα radiation source, λ = 1.5418 Å). Raman spectroscopy was recorded on a (Renishaw 1000B spectrometer with laser excitation (wavelength 633 nm). X-Ray photoelectron spectroscopy (XPS) analysis was performed on HP 5950A equipped with the Mg Kα as the source. Brunauer−Emmet−Teller (BET) surface area was determined by using a Micromeritics ASAP 2010 instrument with N_2 adsorption.

4.2.3 Electrochemical analysis

Five milligram of the synthesized catalysts were mixed with 40 μL of Nafion® perfluorinated ion-exchange resin (Sigma-Aldrich, MO, USA) and 60 μL of deionized water, and applied to a carbon cloth (PANEX®30PW03, Zoltek Corporation, MO, USA) with an area of 1 cm^2 to obtain a loading rate of 5 mg cm^{-2}. After coating, the carbon cloth was dried in a fume hood for 24 h and ready for use [88]. A 1-cm^2 carbon cloth coated with 5 mg cm^{-2} of Pt/C (10% wt. Platinum on Carbon Vulcan, Fuel Cell Earth LLC, Ma, USA) was prepared with the same method and served as control. These electrodes were examined as the working electrode in a three-electrode cell containing 120 mL of 0.1 M PBS (phosphate buffer saline, 5.3 g L^{-1} KH_2PO_4 and 10.7 g L^{-1} K_2HPO_4) with a platinum wire (CH Instruments, Inc., TX, USA) as the counter electrode and an Ag/AgCl electrode (CH Instruments, Inc., TX, USA) as the reference. Linear sweep voltammetry (LSV) was measured with a potentiostat (Reference600, Gamry Instruments, PA, USA) at a scan rate of 10 mV s^{-1}. Electrochemical impedance spectroscopy (EIS) was conducted at the open circuit voltage with a sinusoidal perturbation of 10 mV and the frequency ranging from 10^{-3} to 10^5 Hz. The data were fitted with Gamry Echem Analyst™ software. The electrodes were rinsed with deionized

water and air dried before each test. The electrolyte was aerated for 15 min prior to each experiment, and kept aerating in the headspace during the course of experiments.

Rotating disk electrode (RDE) measurements were conducted in the same three-electrode cell to study the ORR mechanism. A glass carbon tip (diameter 3 mm, BASI, IN, USA) was polished with alumina slurry (PK-4 Polishing kit, BASI, IN, USA) to obtain a mirror-like surface and then washed with deionized water and ethanol. Ink solutions with a concentration of 100 mg mL^{-1} were prepared by mixing 10 mg of the catalyst powder with 40 µL of Nafion® and 60 µL of deionized water. After 10-min ultrasonication, 3.6 µL of the ink solution was pipetted on the glassy carbon RDE tip, making a loading rate of ~5 mg cm^{-2}. The current density was recorded at the scan rate of 10 mV s^{-1} and the rotation rate was varied from 100 to 1,600 rpm (RDE-2, BASI, IN, USA). To maintain a constant O_2 level, the electrolyte was aerated using an air pump (AQUA SUPREME AIR PUMP 2 WATT, DANNER MANUFACTURING, NY, USA) for 15 min and was constantly aerated during the measurement. The electrolyte was then purged with N_2 for 15 min and LSV was conducted to obtain the baseline for each catalyst. The baseline was subtracted and the electron transfer number (n) was calculated from the slope of the Koutecký-Levich plot [115]:

$$\frac{1}{i} = \frac{1}{i_K} + \frac{1}{0.62nFAD_{o2}^{2/3}v^{-1/6}C}\frac{1}{\omega^{1/2}} \quad (1)$$

where i_K is the kinetic current (A), F is the Faradaic constant (96,485 C mol^{-1}), A is the electrode area (0.071 cm^2), D_{O2} is the diffusion coefficient of O_2 in the 0.1 M PBS (2.15 cm^2 s^{-1}) [290], v is the kinematic viscosity of the electrolyte (0.01 cm^2 s^{-1}), C is the O_2 centration in the electrolyte (2.6×10^{-7} mol cm^{-3}) measured using a DO meter (Orion™ Star A213, Thermo Fisher Scientific Inc., MA, USA) and ω is the angular rotation velocity (rad s^{-1}). The durability of the catalysts was investigated by performing RDE at 1,600 RPM after 3,000 and 6,000 cycles of cyclic voltammetry (scan rate 100 mV s^{-1}). All electrochemical experiments were conducted at room temperature for three times.

4.2.4 MFC construction and operation

A two-chamber MFC was constructed by connecting two glass bottles with a cation exchange membrane as the separator (CMI-7000S, Membranes International, Inc., NJ, USA). The liquid volume of the anodic chamber and the cathodic chamber was 130 and 140 mL, respectively. The

anode electrode was a carbon brush (Gordon Brush Mfg. Co., Inc., CA, USA) that had been cultivated in the MFC for over one month. The anolyte contained (per liter of deionized water): sodium acetate, 1.0 g; NaCl, 0.5 g; $MgSO_4$, 0.015 g; $CaCl_2$, 0.02 g; KH_2PO_4, 2.65 g; K_2HPO_4, 5.35 g; $NaHCO_3$, 1.0 g; and trace element, 1.0 mL [200]. The carbon cloth coated with the catalysts was examined as a cathode electrode. The catholyte was 0.1 M PBS solution. The anode and cathode electrodes were connected through a 1-Ω resistor (HARS-X-3-0.001, IET Labs, Inc., NY, USA). The voltage on the resistor was recorded by a digital multimeter (2700, Keithley Instruments, Inc., OH, USA) at a time interval of 5 min. The current of the MFC was calculated according to the Ohm's law. Duplicate polarization curve and power density were measured using the potentiostat at a scan rate of 0.2 mV s^{-1}. The MFC was operated under batch mode at room temperature. The anolyte and catholyte were changed every 24 h. Both the anode and cathode were stirred and the cathode chamber was aerated.

4.3 Results and discussion

4.3.1 Characterization of the catalysts

The morphology and microstructure of as-prepared N/S-CNS were examined by FESEM and TEM. The product is of 2D nanosheet morphology with lateral width ranging from hundreds of nanometers to several micrometers (Figure 4.1a), and the thickness is approximately 23 nm (Figure 4.1b and 4.1c). The N/S-CNS exhibited a highly interconnected 3D framework of randomly stacked nanosheets with porous architecture, similar to the previously reported crumpled graphene particle [279], which may be favorable for the access of electrolyte and shortens transport distance between electrode and electrolyte [62]. TEM analyses further confirmed the layered morphology of the as-synthesized N/S-CNS (Figure 4.1d), which agrees well with the FESEM observation. The partially crinkled nature may be originated from the defective structures formed by nitrogen and sulfur doping (Figure 4.1e) [291]. Many alternative dark and light areas from high-resolution TEM image in Figure 4.1f clearly reveals the presence of numerous pores on the surface of the N/S-CNS.

The crystal structure of N/S-CNS was studied by X-ray diffraction (XRD) measurements. Two broad diffraction peaks centered at around 24.6° and 44.7° can be well assigned to the diffraction from the (002) and (101) planes of graphite carbon, respectively [292],

indicating partial graphitization structure (Figure 4.2a). The Raman spectrum of N/S-CNS shows two main peaks centered at 1,331 and 1,584 cm^{-1}, corresponding to the D and G band, respectively (Figure 4.2b). The D band results from the structurally disordered carbon atoms, whereas the G band corresponds to vibration mode (E2g) for sp2-hybridized graphitic carbon [293]. The intensity ratio of D band to G band (I_D/I_G) is about 1.17, indicating a high degree of disorder [294], owing to the incorporation of defects by N- and S- doping. The smaller peak at 2,660 and 2,909 cm^{-1} can be assigned to a combination of 2D and D + G bands [295, 296].

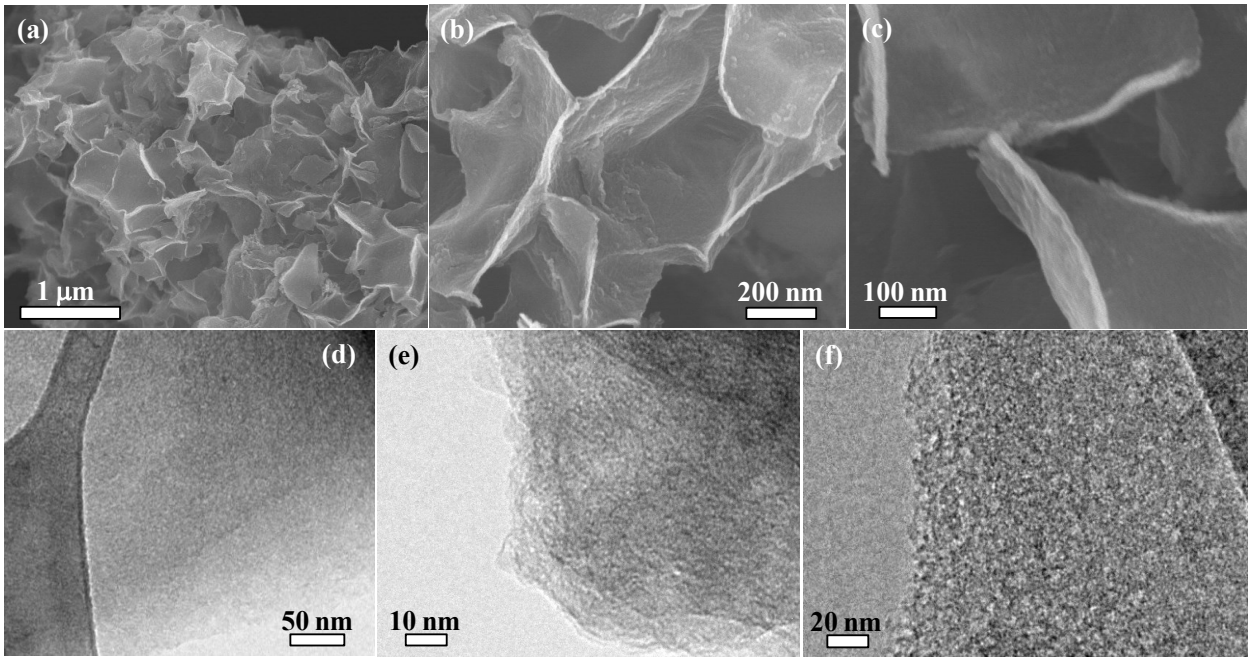

Figure 4.1 FESEM (a-c) and TEM (d-f) images of the N/S-CNS.

The chemical composition of N/S-CNS was characterized by X-ray photoelectron spectroscopy (XPS). Figure 4.2c presents the survey scan spectrum of the nanosheets with characteristic spectra of C 1s, N 1s, S 2p, S 2s, and O 1s, confirming that N and S have been successfully co-doped into the CNS. The contents of N and S elements in the sample are calculated to be 4.6 at.% and 2.4 at.%, respectively. The complex N 1s spectrum could be further deconvoluted into four peaks at 398.5, 399.8, 401.5, and 403.4 eV, corresponding to pyridinic-N, pyrrolic-N, graphitic-N, and oxidized-N, respectively (Figure 4.2d) [91, 297], The high-resolution S 2p peak of the N/S-CNS can be resolved into three different

peaks. The former two peaks at 163.2 and 164.3 eV are in agreement with the reported S $2p_{3/2}$ and S $2p_{1/2}$ (Figure 4.2e) [298], which are attributed to the sulfur binding in –C–S– bonds and conjugated –C=S– bonds, respectively [299]. The third peak at 168.7 eV results from oxidized S [300]. The typical nitrogen adsorption/desorption curve of the resulting N/S-CNS exhibits a type-IV adsorption isotherm, indicating that the nanosheets possess porous structures. The Brunauer–Emmett–Teller (BET) surface area of the N/S-CNS is estimated to be about 1,004 m^2 g^{-1} with a pore volume of 0.8 cm^3 g^{-1} (Figure 4.2f), which is much higher than those reported for N- and S- doped graphene materials (typically in the range of 220 to 820 m^2 g^{-1}) [291, 301-304]. It is believed that the porous materials with a high BET surface area would provide more active sites and thus improve the ORR activity [305, 306].

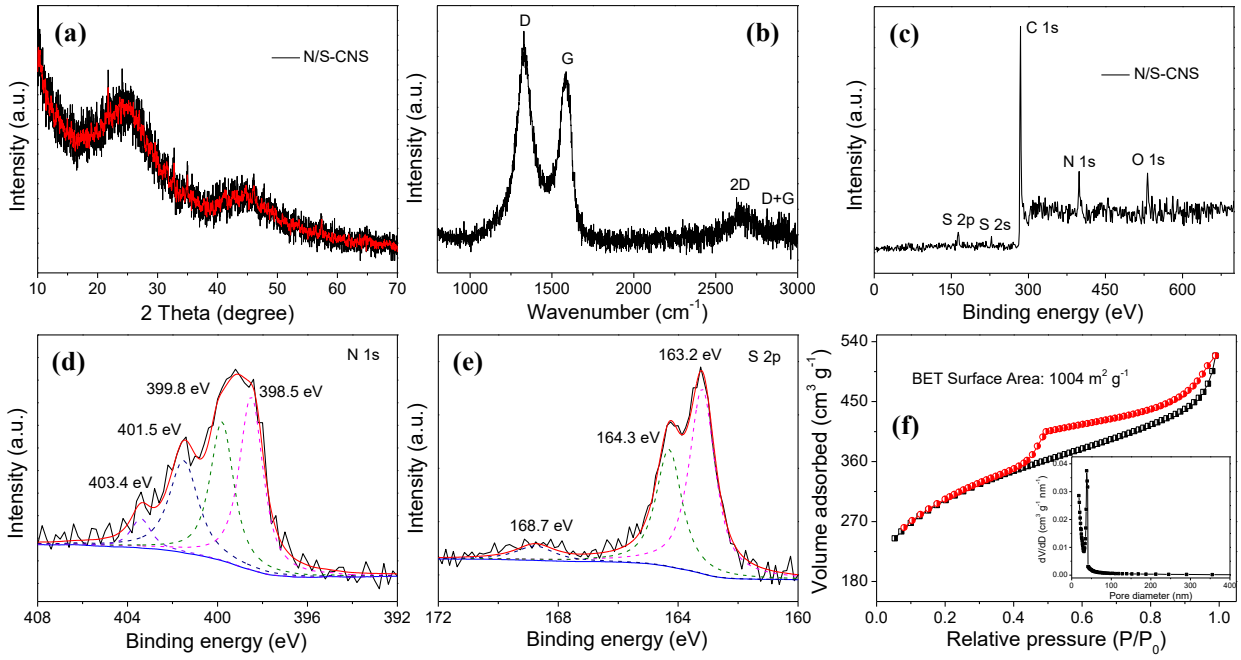

Figure 4.2 XRD pattern (a), Raman spectrum (b), XPS sweep scan (c), high-resolution N 1s XPS spectrum (d), high-resolution S 2p XPS spectrum (e), N_2 adsorption/desorption isotherm (f) for the N/S-CNS. Inset to panel (f) is the corresponding pore size distribution.

4.3.2 Electrochemical performance

It can be seen in Figure 4.3a that the onset potential (i.e. the potential at which the onset of electrochemical current occurs [115]) of N/S-CNS for ORR occurs at -0.05 V vs. Ag/AgCl,

which is approximately 0.15 V later than Pt/C, but distinctly earlier than that of CNS solely doped with nitrogen or sulfur, indicating that dual-doping of the heteroatoms successfully enhanced ORR catalysis. These results are consistent with the RDE measurement, in which the onset potential of N/S-CS occurs at 0.2 V vs. Ag/AgCl (Figure 4.4d), whereas Pt/C shows catalysis at ~0.3 V vs. Ag/AgCl (Figure 4.4a). EIS results suggest that CNS is slightly more conductive than Pt/C (Figure 4.3b). Moreover, the charge transfer resistance of N/S-CNS (14.8 Ω) is also lower than that of Pt/C (22.3 Ω). The reason that N/S-CNS shows lower resistance than Pt/C does but exhibit less catalytic activity (i.e. more negative onset potential), probably because Pt and CNS catalyze ORR through different pathways. Previous studies proposed that ORR could proceed through the one-step four-electron pathway or the less efficient two-electron pathway [272].

To gain insights into the ORR mechanisms of N/S-CNS, RDE was carried out in the same electrolyte (Figure 4.4). The electron transfer number of N/C-CNS calculated from RDE results ranged from 3.41 to 3.68 depending on the potential applied (Figure 4.3c), meaning that ORR on N/S-CNS predominantly followed the 4-e route, but the 2-e pathway is also involved. In contrast, the 2-e transfer is likely to be the major mechanism of ORR on N-CNS and S-CNS (Figure 4.3c). These results are in agreement with the previous findings, in which the electron transfer number of co-doped carbon foam or graphene is close to that of Pt/C [304, 307, 308].

It has been previously discussed that nitrogen-doping may lead to a relatively high positive charge density of the carbon atoms, thereby enhancing ORR activity [309]. The three nitrogen species also contribute differently to ORR catalysis: pyridinic and pyrrolic N favors 4-e pathway, whereas graphitic N adsorbs OOH and reduces O_2 to H_2O_2 via 2-e pathway [48, 287]. For sulfur-doping, since carbon and sulfur atoms have the similar electronegativity, the spin density may play a more important role and thus sulfur atoms are believed to be the active center [281]. Increased activity of carbon atoms was observed by simultaneous incorporation of N and S, and was attributed to the induced asymmetrical spin and charge density [283]. However, the structures and the consequent synergetic effects of N/S co-doped carbon catalysts may differ due to the different synthesis

procedures. Moreover, the specific surface area and the defect sites of the carbon materials may also contribute to the overall catalytic behavior. Therefore, the detailed mechanisms of the N/S-doped porous CNS prepared in the present study warrant further studies. In addition to the remarkable ORR catalysis, the N/S-CNS showed excellent durability as negligible change could be observed after 3,000 and 6,000 cycles of scan (Figure 4.3d). These results collectively demonstrate that the N/S-CNS may be a promising ORR catalyst for fuel cell applications.

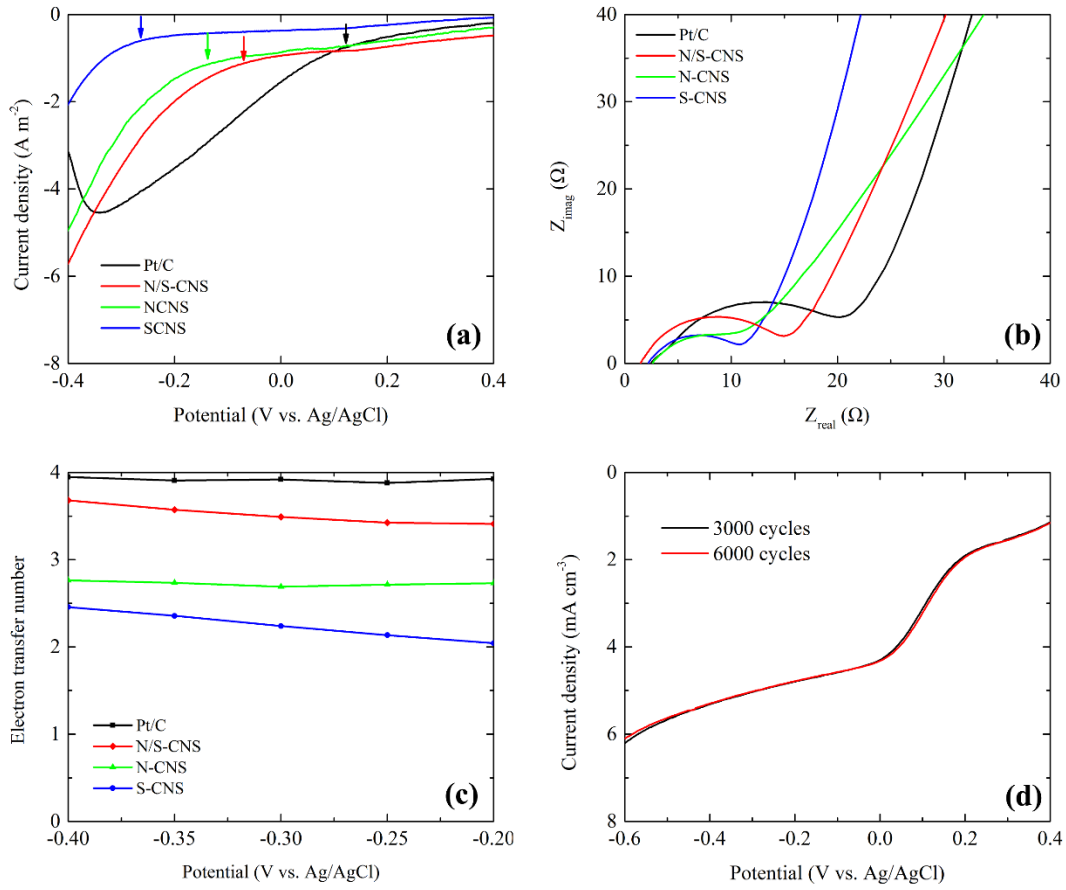

Figure 4.3. (a) LSV (scan rate of 10 mV s^{-1}) in 0.1 PBS, arrows indicate the onset potential, (b) EIS in 0.1 PBS, (c) electron transfer number calculated from the RDE measurement and (d) LSV of N/S-CNS at 1,600 RPM after 3,000 and 6,000 cycles

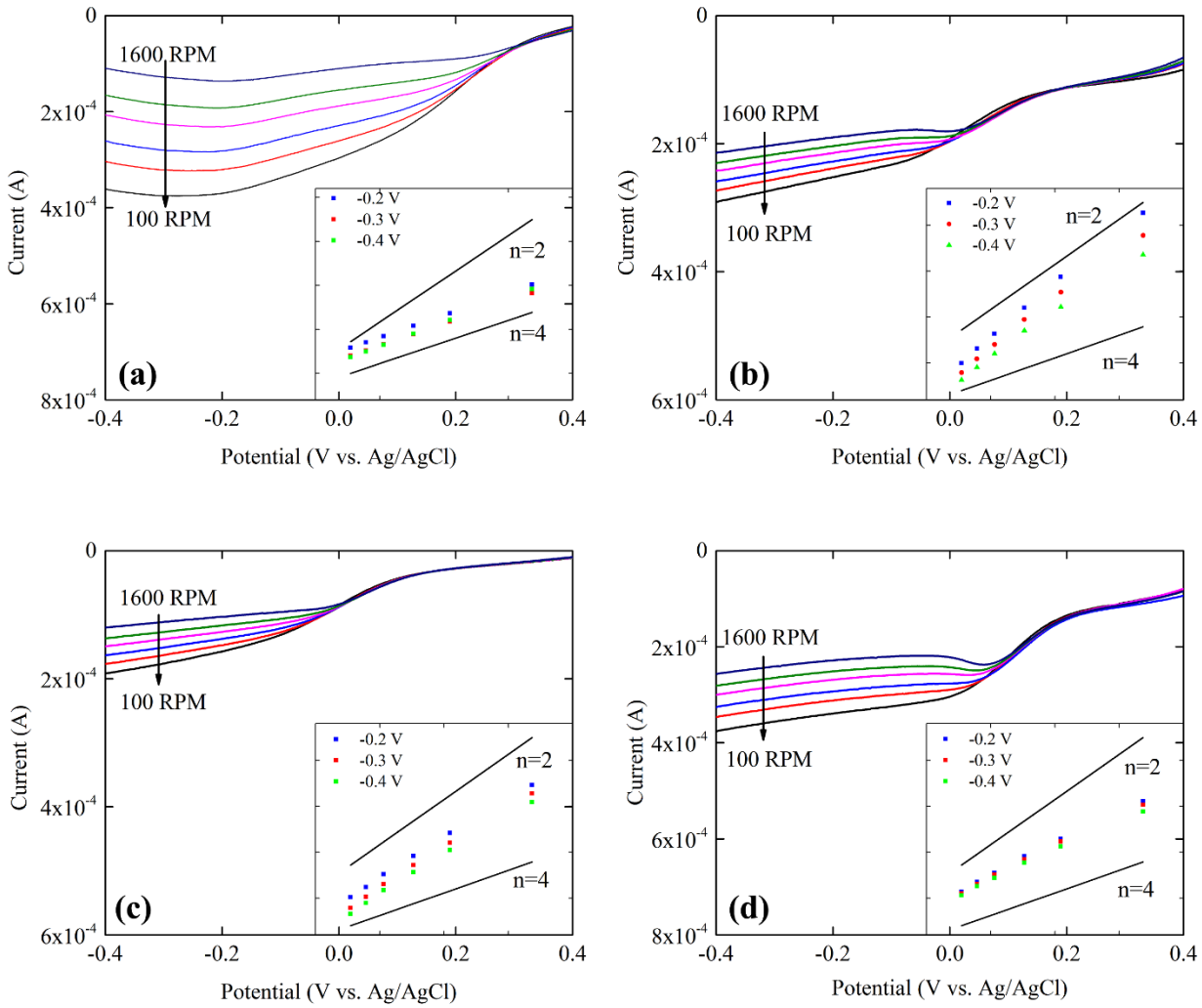

Figure 4.4 RDE results of (a) Pt/C, (b) S-CNS, (c) N-CNS and (d) N/S-CNS. Insets are the K-L plot at -0.2, -0.3 and -0.4 V vs. Ag/AgCl derived from the RDE results. The y-axis of the inset indicates i^{-1} and the x-axis indicates $\omega^{-1/2}$.

4.3.3 MFC performance

It is worth noting that the catalytic performance in a defined three-electrode system may be different from that in an aerated MFC cathode, where factors such as proton transfer and oxygen diffusion may exert effects on the catalysis. Thus, the catalysts were examined in an MFC with 0.1 M PBS as the catholyte to mimic real situations. The current density of the MFC for all catalysts decreased steadily over time due to the consumption of substrates, dropped drastically at 24 h due to the renewal of electrolyte, and rapidly recovered to the previous level (Figure 4.5a). This typical current profile implies that the MFC anode has

been well cultivated and had little effects on the investigation of cathode electrode [88]. Similar to the LSV results, the current density followed this order: Pt/C > N/S-CNS > N-CNS > S-CNS. The MFC with Pt/C generated the highest average current density of 7.3 A m^{-2}, followed by the 6.6 A m^{-2} of N/S-CNS. The N/S-CNS performed slightly better in the second cycle than did in the first one, and yielded comparable current density to that of Pt/C, possibly because of some activation processes of the catalyst.

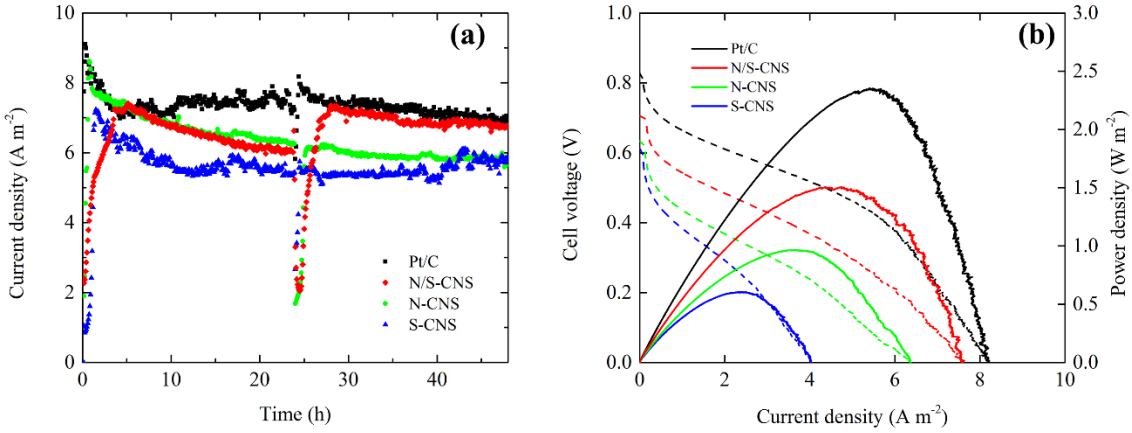

Figure 4.5 (a) Current density and (b) polarization curves of the MFC with different catalysts.

The open circuit voltage and short circuit current density of N/S-CNS were measured to be 0.70 V and 7.6 A m^{-2} (Figure 4.5b), respectively, both of which were slightly lower than those of Pt/C. As a consequence, the maximum power density calculated from the polarization curve was 1.5 W m^{-2} for N/S-CNS and 2.3 W m^{-2} for Pt/C. Interestingly, it can be seen from Figure 4.5b that at a current density higher than 5.5 A m^{-2}, the potential drop of N/S-CNS is less steep than that of Pt/C, indicating a lower potential loss on mass transfer [71]. This result, which implies a more efficient interaction between O_2 and N/S-CNS, together with the high specific surface area (1,004 m^2 g^{-1}) and the comparable current generation in the MFC, suggests that mass transfer is playing a critical role in the overall cell performance in real applications.

While the power density of N/S-CNS is 34.8% lower than that of Pt/C, the comparable current density of N/S-CNS produced by the MFC (9.6% lower than that of Pt/C) indicates the catalyst may be more suitable for current generation than for power production and thus the application niches need to be identified. For example, a previous study suggested that a high current density was favorable for desalination in a microbial desalination cell (MDC) [310], which implies that N/S-CNS could be used as the cathode catalyst of MDCs for sustainable wastewater treatment and seawater desalination. Another advantage of N/S-CNS is the low cost. Given the yield of 41%, the cost of the catalyst for a 1-m^2 cathode is estimated to be $168, which is remarkably lower than that of Pt/C ($2,750). It is therefore expected that the capital cost of MFCs can be significantly reduced by the use of N/S-CNS.

4.4 Conclusions

In summary, we have demonstrated a simple synthesis procedure of co-doped CNS with nitrogen and sulfur and investigated its performance for ORR in an MFC. The modified nanosheets catalyst shows pronounced electrocatalytic activity with enhanced ORR catalysis compared to sole doping of nitrogen or sulfur. The excellent catalytic activities can be ascribed to the synergistic effect of the large surface area with abundant pores and N/S dual-doping, the low ohmic and charge transfer resistance, and the favorable 4-e pathway. The MFC equipped with N/S-CNS achieved comparable current generation to the one with Pt/C, while the cost for N/S-CNS was more than 16 times lower than that of Pt/C. The results collectively represent a significant step towards the development of metal-free catalysts for MFCs.

CHAPTER 5: Nitrogen-doped Graphene/CoNi Alloy Encased within Bamboo-like Carbon Nanotube Hybrids as Cathode Catalysts in Microbial Fuel Cells

(This section has been published as: Yang Hou, Heyang Yuan, Zhenhai Wen, Shumao Cui, Xiaoru Guo, Zhen He, and Junhong Chen. Nitrogen-doped graphene/CoNi alloy encased within bamboo-like carbon nanotube hybrids as cathode catalysts in microbial fuel cells. Journal of Power Sources (2016): 306, 561-568.)

5.1 Introduction

Microbial fuel cells (MFCs) as an evolving wastewater treatment technology has attracted much attention in the past decade [7, 285, 311, 312]. In a typical MFC, organic energy (e.g., organic compounds in wastewater) is directly converted to electricity by taking advantage of microbial extracellular respiration with an electrode [4, 113]. As such, organic removal and electricity generation can be accomplished simultaneously at low energy consumption. Oxygen is widely used as an electron acceptor in MFCs because of its availability and high reduction potential. However, oxygen reduction reaction (ORR) is sluggish and thus often requires the presence of catalysts. Platinum is a common ORR catalyst in bench-scale experiments due to its superior ORR catalytic activity, but is not economically viable in practice, which accounts for the major hindrance for the large-scale application of MFCs [34, 313]. It is estimated that current MFC technology costs 8 € to remove 1 kg of COD, 47% of which comes from the cathode [14]. Therefore, it is of practical significance to develop inexpensive and robust cathode catalysts.

To make MFCs more practical, a variety of catalyst materials have been studied, including carbon/graphite materials, nanostructured materials, and non-precious metals [35, 36, 314]. Among those novel materials, graphene-based catalysts are of great interest due to their excellent electrical conductivity, large specific surface area, and high stability [37, 62, 256, 276, 292]. Moreover, graphene doped with nitrogen exhibits abundant defects sites, which can significantly facilitate ORR catalysis [61]. These unique properties, tunable towards specific applications via different synthesis procedures [44, 275], are highly attractive to MFC applications. Electrodes decorated with modified graphene-based materials have been reported to substantially decrease the loss of electrical potential and enhance the MFC performance

(Table C1) [315]. In a previous study, graphitic carbon nitride was implanted in N-doped graphene and a complete 4-eletron ORR pathway was detected [55]. The MFC equipped with this catalyst achieved higher power density and durability than with platinum. Metals such as manganese, iron, or cobalt have also been decorated in N-doped graphene and noticeably enhanced the power density of MFCs [316-318]. While the synergetic effects of metals and N-doped graphene remain to be understood, these studies collectively suggest that metal/N-doped graphene can be a promising cathode catalyst for MFCs.

In this work, we demonstrate the use of a one-step strategy to prepare a novel N-doped graphene/CoNi-alloy encased within bamboo-like carbon nanotube hybrid (N-G@CoNi/BCNT) in which CoNi alloy particles are encapsulated at the end and/or the middle section of tubes, with many graphene layers inside inner cavities of the BCNT for the first time. The synthesized hybrid was applied on carbon cloth serving as an electrode for the investigation of ORR catalysis by linear sweep voltammetry (LSV) and electrochemical impedance spectroscopy (EIS). The durability of the prepared electrode was examined by cyclic voltammetry (CV) for continuous 3,000 and 6,000 cycles. To better understand the catalysis performance, the electrode was further examined in an MFC. The present work is expected to provide insights into the simplification of the N-G@CoNi/BCNT synthesis and the application of this material in MFCs and/or other biological systems for energy-efficient water and wastewater treatment.

5.2 Materials and methods

5.2.1 Synthesis of Ni-NBCNT

In a typical procedure, 5 g of urea was mixed with 10 mL ethanol dissolved with 0.10 g of $NiCl_2 \bullet 6H_2O$ under stirring with heating at 80 ºC until completely dry. The mixture powder was then transferred to the furnace and heated at 900 ºC at a rate of 2 ºC min^{-1} and maintained at 900 ºC for 1 h under Ar atmosphere. The resulting product was further dispersed in 0.5 M H_2SO_4 solution and stirred overnight to remove any accessible nickel species present on it, resulting in the Ni-NBCNT.

5.2.2 Synthesis of Co-NBCNT

In a typical procedure, 5 g of urea was mixed with 10 mL ethanol dissolved with 0.12 g of $Co(NO_3)_2 \bullet 6H_2O$ under stirring with heating at 80 ºC until completely dry. The mixture powder was then transferred to the furnace and heated at 900 ºC at a rate of 2 ºC min^{-1} and maintained at 900 ºC for 1 h under Ar atmosphere. The resulting product was further dispersed in 0.5 M H_2SO_4 solution and stirred overnight to remove any excessive cobalt species present on it, resulting in the Co-NBCNT.

5.2.3 Synthesis of CoNi-NBCNT (high molar ratio of urea to Co^{2+}/Ni^{2+} ions)

In a typical procedure, 10 g of urea was mixed with 10 mL ethanol dissolved with 0.12 g of $Co(NO_3)_2 \bullet 6H_2O$ and 0.10 g of $NiCl_2 \bullet 6H_2O$ under stirring with heating at 80 ºC until completely dry. The mixture powder was then transferred to the furnace and heated at 900 ºC at a rate of 2 ºC min^{-1} and maintained at 900 ºC for 1 h under Ar atmosphere. The resulting product was further dispersed in 0.5 M H_2SO_4 solution and stirred overnight to remove any excessive cobalt and nickel species present on it, resulting in the CoNi-NBCNT.

5.2.4 Synthesis of N-G@CoNi/BCNT

In a typical procedure, 5 g of urea was mixed with 10 mL ethanol dissolved with 0.12 g of $Co(NO_3)_2 \bullet 6H_2O$ and 0.10 g of $NiCl_2 \bullet 6H_2O$ under stirring and heating at 80 ºC until completely dry. The mixture powder was then transferred to a furnace and heated at 900 ºC at a rate of 2 ºC min^{-1} and maintained at 900 ºC for 1 h under Ar atmosphere. The resulting product was further dispersed in 0.5 M H_2SO_4 solution and stirred overnight to remove any accessible cobalt and nickel species present on it. About 1.0 g black products (N-G@CoNi/BCNT) were obtained for further experiments.

5.2.5 Characterization

The N-G@CoNi/BCNT morphology was examined using a Hitachi H-9000 NAR transmission electron microscope (TEM) and a field emission scanning electron microscope (FESEM, Hitachi S-4800) equipped with an energy-dispersive X-ray (EDX) analytical system. Powder analysis was performed using an X-ray powder diffractometer operating at 40 kV, 40 mA for Cu Kα radiation (λ = 1.5418 Å, Scintag XDS 2000). Raman characterization was carried out using a Renishaw 1000B with a 633 nm laser excitation. Fourier transform infrared (FTIR) spectra were recorded on

a Bruker Vector Fourier transform spectrophotometer. X-ray photoelectron spectroscopy (XPS) was obtained using an HP 5950A equipped with Mg Kα source and the C 1s peak at 284.6 eV as an internal standard. Thermogravimetric analysis (TGA) was carried out on a thermoanalyzer (TA SDT 2960) with a heating rate of 5 °C min^{-1} in an air atmosphere. BET surface area was measured with a Micromeritics ASAP 2020. The inductively coupled plasma–optic emission spectrometry (ICP-OES) tests were performed using a Perkin Elmer Optima 7000DV.

5.2.6 Electrode preparation

The synthesized catalysts were mixed with 40 μL Nafion® perfluorinated ion-exchange resin (Sigma-Aldrich, MO, USA) and 60 μL deionized (DI) water and applied to a carbon cloth (PANEX®30PW03, Zoltek Corporation, MO, USA), yielding a loading rate of 5 mg cm^{-2}. After coating, the carbon cloth was dried in a fume hood for 24 h, cut to 1 cm^2 and ready for use [88]. A carbon cloth coated with 5 mg cm^{-2} of Pt/C (10% wt. Platinum on Carbon Vulcan, Fuel Cell Earth LLC, Ma, USA) was prepared with the same method and served as control.

5.2.7 Electrochemical analysis

Electrochemical experiments were conducted in a three-electrode cell containing 120 mL of 1.0 M PBS (phosphate buffer saline, 53 g L^{-1} KH_2PO_4 and 107 g L^{-1} K_2HPO_4), where the modified electrodes served as the working electrode, platinum wire (CH Instruments, Inc., TX, USA) as the counter electrode, and Ag/AgCl electrode (CH Instruments, Inc., TX, USA) as the reference. LSV was measured with a potentiostat (Reference 600, Gamry Instruments, Warminster, PA, USA) at a scan rate of 5 mV s^{-1} (-0.6 to 0.4 V vs. Ag/AgCl). Tafel slope was derived from the LSV curve. Rotation ring disk electrode (RRDE) was conducted to study the mechanism of ORR. The electron transfer number (n) and H_2O_2 yield ($H_2O_2\%$) were calculated as follows [319]:

$$\mathrm{n} = 4 \times \frac{I_d}{I_d + I_r / N} \quad (5.1)$$

$$H_2O_2(\%) = 200 \times \frac{I_r / N}{I_d + I_r / N} \quad (5.2)$$

where I_d is the disk current, I_r is the ring current, and N = 0.424 is the collection efficiency determined with $Fe(CN)_6^{3-}/Fe(CN)_6^{4-}$. CV was conducted at 100 mV s^{-1} to examine the durability of the prepared electrode (-0.6 to 0.4 V vs. Ag/AgCl). The EIS was carried out at the open circuit

voltage with a frequency ranging from 10^{-2} to 10^{5} Hz and a sinusoidal perturbation of 10 mV and the equivalent circuit is shown in Scheme C1. The PBS solution was aerated for 15 min prior to each experiment, and kept aerating in the headspace in the course of experiments. Electrodes were air dried before each test. All electrochemical experiments were conducted at room temperature for three times.

5.2.8 MFC construction and operation

A two-chamber MFC was built by connecting two glass bottles with a cation exchange membrane (CEM) as the separator (UltexCMI7000, Membranes International, Inc., NJ, USA) (Scheme C2). The liquid volume of the anodic chamber and the cathodic chamber was 130 and 140 mL, respectively. The anode electrode was a carbon brush (length 5 cm, diameter 5.1 cm, Gordon Brush Mfg.Co., Inc., CA, USA) that had been cultivated in the MFC for one month. The anolyte contained (per liter of DI water): sodium acetate, 1.0 g; NaCl, 0.5 g; $MgSO_4$, 0.015 g; $CaCl_2$, 0.02 g; KH_2PO_4, 0.53 g; K_2HPO_4, 1.07 g; $NaHCO_3$, 1.0 g; and trace element, 1.0 mL [200]. The carbon cloth coated with catalysts was examined as the cathode electrode. PBS solution (50 mM) was used as the catholyte. The anode and cathode electrode were connected through a 1-Ω resistor. The voltage on the 1-Ω resistor was recorded by a digital multimeter (2700, Keithley Instruments, Inc., OH, USA) at a time interval of 5 min. The current of the MFC was calculated according to Ohm's law. Polarization curve and power density were measured using the potentiostat. To study the performance of the catalysts under different conductivity and pH, NaCl solution (35 g L^{-1}), tap water, and buffer solutions were prepared and used catholyte. The initial pH of NaCl solution and tap water was controlled at 7.0 using HCl and NaOH. Acid buffer (pH = 4.0) was prepared by mixing 0.2 M sodium acetate and 0.2 M acetic acid at a volume ratio of 9: 41. Neutral buffer (pH = 7.0) was PBS solution and alkaline buffer (pH = 10.0) was purchased from Fisher Scientific (PA, USA). The conductivity of the buffer solutions was controlled at 10.0 mS cm^{-1} using DI water and NaCl solution. The MFC was operated under batch mode with at room temperature. The electrolyte was changed every 24 h. The cathode chamber was stirred and aerated in the course of experiments. All cathode electrodes were examined at room temperature for two cycles.

5.3 Results and discussion

5.3.1 Characterization of the catalysts

The synthesis of N-G@CoNi/BCNT is accomplished by pyrolysis of urea, $Co(NO_3)_2$, and $NiCl_2$, followed by acid treatment of the resulting material. During the process, the Co^{2+}/Ni^{2+} ions were reduced to CoNi alloy nano-catalysts to assist the evolution of gases released from the decomposition of urea into the hybrid (Figure 5.1a). Figure 5.1b shows typical field-emission scanning electron microscopy (FESEM) image of the N-G@CoNi/BCNT, indicating that the sample is dominated by 1D tubular nanostructures. The diameter of the nanotube was estimated to be in the range of 100-200 nm with several μm in length (Figure 5.1b and 5.1c). From an open end of the nanotube shown in Figure 5.1d, an interesting tube-in-tube structure can be clearly observed. Solid dots observed at the tip of the nanotube in Figure 5.1e are determined to be CoNi nanoparticles based on transmission electron microscopy (TEM) images (Figure C1). TEM images and energy dispersive X-ray (EDX) analysis reveal a bamboo-like structure of the individual nanotube in which CoNi nanoparticles are sparsely encapsulated at the end and/or the middle section of the tube (Figure 5.2a, 5.2b and Figure C1), as well as many crumpled stripes composed of random graphene layers formed inside inner cavities of the BCNT (Figure 5.2c and 5.2e). The graphene layers are easily identified with an interlayer spacing of around 0.34 nm (Figure 5.2f). Notably, the named herein bamboo-like structure did not form closed "knots", which is totally different with those of traditional well-defined bamboo-like CNT structure with a diameter ranging from 20 to 60 nm [320, 321]. The main reason is that the diameter of N-G@CoNi/BCNT is so large (over 100 nm) that the graphene nanosheets can only grow into small nanosheets rather than form "knots". Focusing on the inner part of these nanotubes, one can also distinguish some tube-in-tube structures besides crumpled graphene layers, which is consistent with FESEM observations (Figure 5.2d and 5.2e). The diameter of inner tubes is about 50 nm. In this hybrid structure, an effective conducting network can be formed among inner tubes, graphene layers, and outer tubes. In this case, both inner BCNT and crumpled graphene layers may serve not only as conduction paths for shuttling electrons but also as additional active sites for the electrocatalytic process [322].

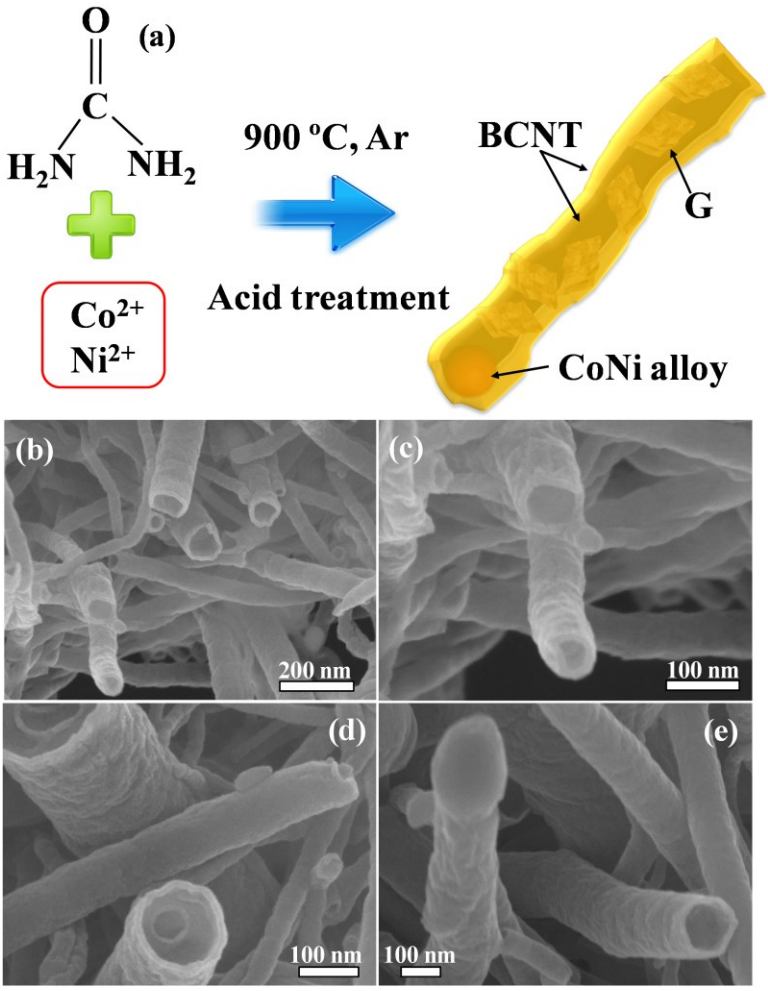

Figure 5.1 (a) Schematic illustration of the synthesis process of N-G@CoNi/BCNT. (b-e) FESEM images of N-G@CoNi/BCNT at different magnifications.

Based on the experiment results, a plausible mechanism for the growth of the N-G@CoNi/BCNT hybrid structure is proposed. During heat treatment, the nitrogen-containing polymer (e.g., polymeric carbon nitride) [323] evolved from urea can be decomposed and a large number of nitrogen-containing gases (e.g., $C_2N_2^+$, $C_3N_2^+$, $C_3N_3^+$) are released simultaneously [324], which can serve as carbon and nitrogen sources for BCNT growth and nitrogen-doping reactions. As a result, BCNT appears with visible metal nanoparticles at the end and/or the middle section by a well-known "tip-growth mechanism" [325], suggesting the growth of such carbon nanotubes is catalyzed by the CoNi alloy [91]. Dynamical observations of such BCNT growth revealed the existence of N-doping is necessary to catalyze the formation of the bamboo-like carbon structures [321]. At a low concentration of the Co/Ni source, the resulting CoNi alloy nanoparticles are small,

thus leading to the formation of nanotubes with a relatively small diameter (Figure C2). With an increasing concentration of Co/Ni, the obtained carbon nanotubes have a much larger diameter than that of nanotubes with a low concentration of the Co/Ni as the size of CoNi alloy catalyst become larger accordingly (Figure 5.2). Besides the large inner cavities of as-formed BCNT, the structural defects and broken sites formed inside the BCNT due to N-doping could contribute to the formation of graphene nanosheets [295, 326, 327], thus leading to the formation of the unique nanostructure where N-doped graphene/CoNi-alloy was encased within BCNT. It is worth noting that when only Co or Ni salt instead of Co/Ni composite salt was used as the precursor, the diameters of the resulting nanotubes are still less than 100 nm (Figure C3); no such N-G@CoNi/BCNT hybrid nanostructure was obtained. In other words, the co-existence of Co and Ni with proper concentrations and urea are important for the formation of N-G@CoNi/BCNT hybrid. The detailed mechanisms need to be further clarified in the future work.

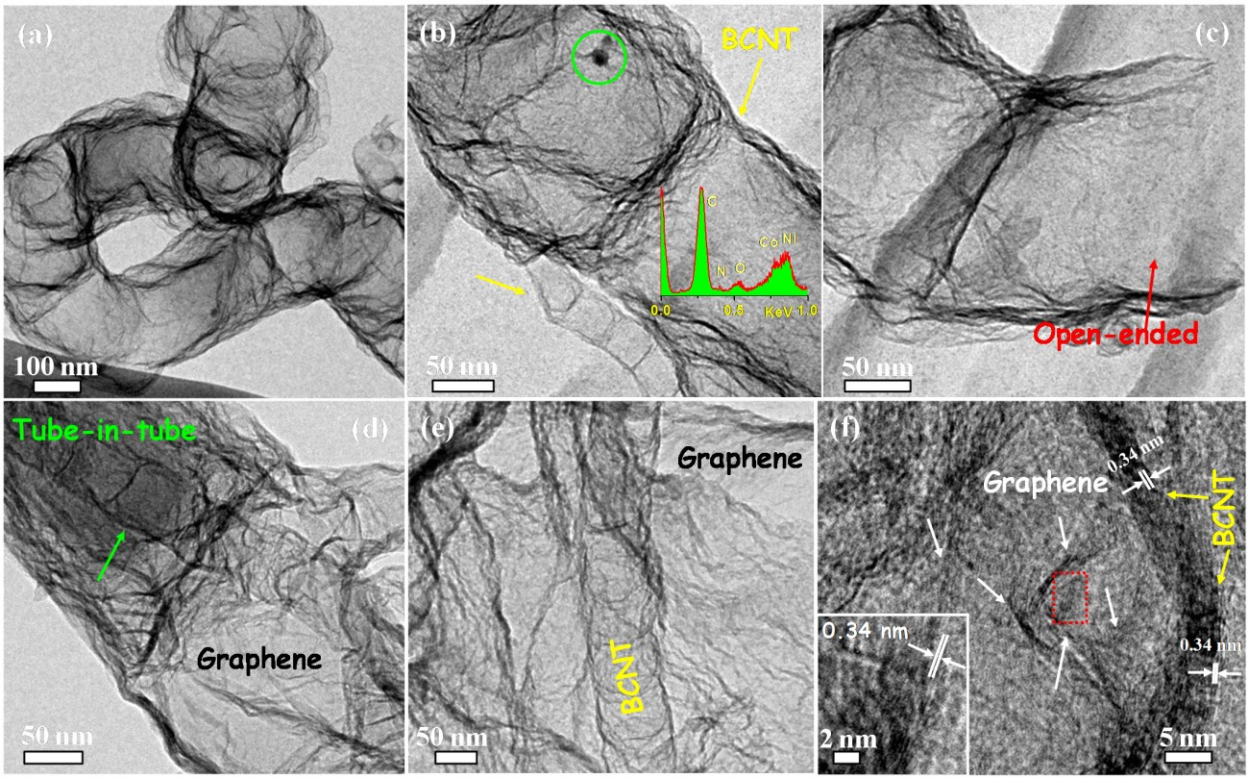

Figure 5.2 TEM images (a-e) and HRTEM image (f) of N-G@CoNi/BCNT. The inset of (b) shows the EDX spectrum from the area labeled by the circle in (b).

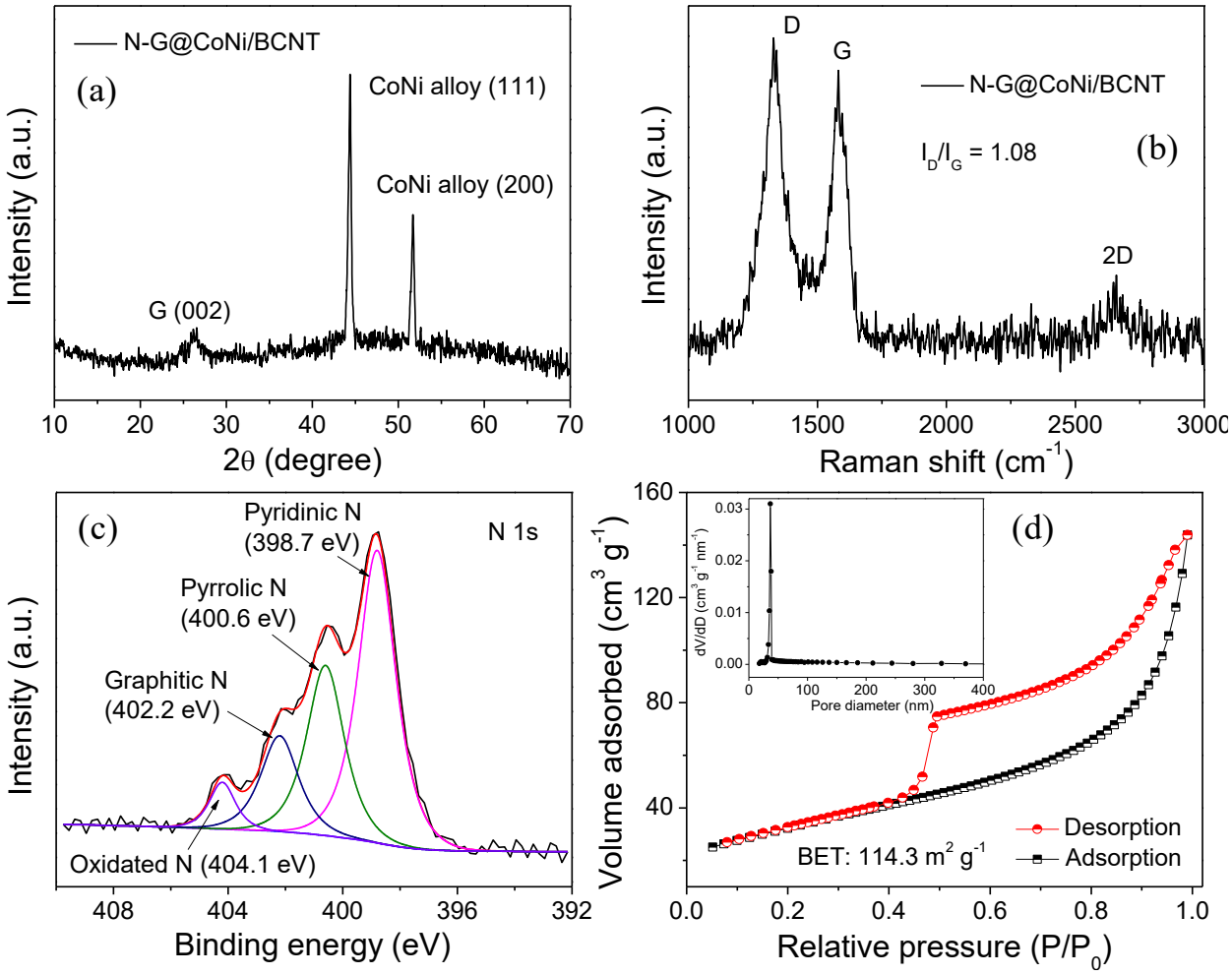

Figure 5.3 (a) XRD pattern, (b) Raman spectrum, (c) high-resolution N 1s XPS spectrum, and (d) Nitrogen adsorption-desorption isotherm curve and BJH pore size distribution derived from the adsorption branch of the isotherm (inset) of N-G@CoNi/BCNT.

The XRD pattern shows that except for the graphitic carbon and the CoNi alloy that are suggested by the graphite (002), CoNi alloy (111) and (200) planes [328], no other phases are present in the N-G@CoNi/BCNT (Figure 5.3a). The Raman spectrum of N-G@CoNi/BCNT (Figure 5.3b) shows that the hybrid exhibits intense D (1,332 cm^{-1}) and G (1,581 cm^{-1}) bands as well as a weak 2D (2,656 cm^{-1}) band. The intensity ratio of D to G band is about 1.08, which indicates the existence of substantial defects or disordered sites in the structure of N-G@CoNi/BCNT [329], presumably stemming from the presence of N dopants and the concomitant absence of C atoms in the hybrid structure [301]. X-ray photoelectron spectroscopy (XPS) analysis (Figure C4) reveals that the N-G@CoNi/BCNT is mainly composed of C, N, and O with a nitrogen content of 4.1 %,

confirming that nitrogen has been successfully doped into the nanocarbon. Although no obvious CoNi signal was detectable because of the formed carbon shells in the hybrid hindered the CoNi alloy [330], the presence of CoNi alloy was confirmed by EDX analysis and high-resolution Co 2p and Ni 2p XPS spectra (Figure C1, Figure C4, and Figure 5.2). The atomic ratio of Co/Ni in the N-G@CoNi/BCNT hybrid was found to be ~ 1:1 from ICP-OES measurements. Further, based on TGA analysis, the wt.% of CoNi alloy in the N-G@CoNi/BCNT was calculated to be 3.95% (Figure C5). A high-resolution N 1s XPS spectrum (Figure 5.3c) of N-G@CoNi/BCNT shows that there exists pyridinic (398.7 eV), pyrrolic (400.6 eV), graphitic (402.2 eV), and oxidated N (404.1 eV) [331, 332]. The evidence of N-doping in the hybrid is also provided by Fourier transform infrared spectroscopy (FTIR, Figure C6), which reveals a new band around 1,619-1,363 cm^{-1} that matches well with the stretching of the carbonyl aromatic C=C bond and the formed C–N bond [333]. As determined by N_2 sorption measurements (Figure 5.3d), the N-G@CoNi/BCNT sample possesses a high Brunauer–Emmett–Teller specific surface area of 114.3 $m^2\ g^{-1}$ with a pore volume of 0.22 $cm^3\ g^{-1}$.

5.3.2 Electrochemical performance

It has been reported that N-doped carbon can efficiently catalyze ORR due to the high specific surface area and good electrical conductivity [309, 334]. The catalytic activity of the synthesized N-G@CoNi/BCNT in the present study was thus evaluated with LSV in 1.0 M PBS. Compared to the early onset potential of the Pt/C electrode (0.2 V vs. Ag/AgCl), N-G@CoNi/BCNT started to catalyze ORR at ~ 0.06 V vs. Ag/AgCl (Figure 5.4a). This onset potential is significantly more positive than that of bare Co and Ni, indicating an enhanced ORR catalysis of the hybrid. The difference of onset potentials between Pt/C and N-G@CoNi/BCNT (0.14 V) is consistent with the previous study on N-doped graphene [335]. The catalytic activity was further confirmed by the exchange current density calculated from the corresponding Tafel slope (Table C2). According to the Butler-Volmer model, exchange current is proportional to the standard rate constant at equilibrium, and thus is an important kinetic parameter reflecting reaction rate [115]. The highest exchange current density was obtained from Pt/C (2.59×10^{-3} A m^{-2}), followed by N-G@CoNi/BCNT (1.73×10^{-3} A m^{-2}), which is several folds higher than that of the pristine Co and Ni. This suggests that the hybrid catalyzes ORR faster than Co and Ni. Similar trend was observed in the EIS results (Figure C7), in which the charge transfer resistance, characterized by the

diameter of the semicircle, was 5 Ω for Pt/C and ~ 10 Ω for N-G@CoNi/BCNT, while those for Co and Ni were noticeably higher. Because the three-electrode cell was purged with air in the headspace, the early occurrence of Warburg impedance could be attributed to the low oxygen concentration in the PBS solution.

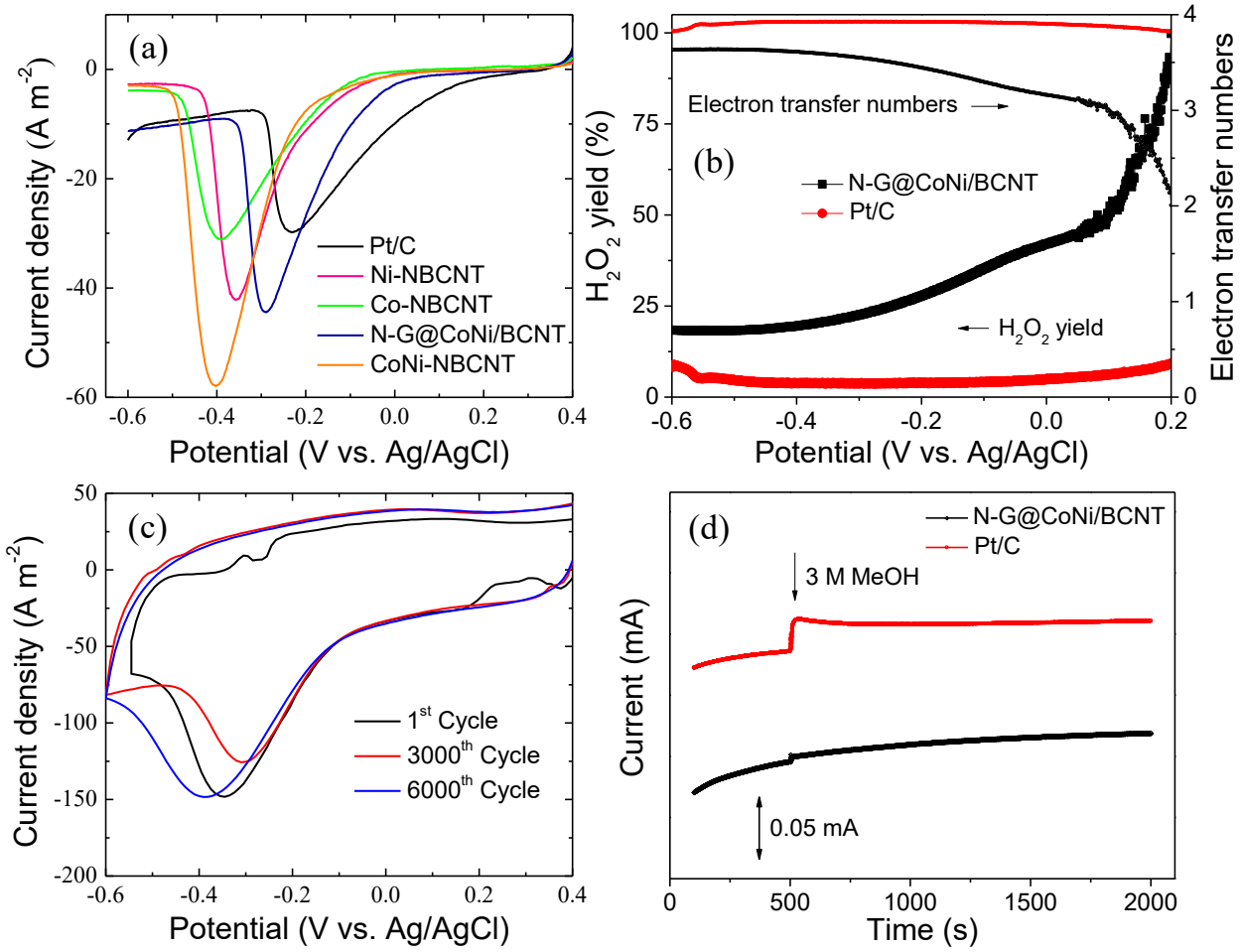

Figure 5.4 (a) LSV curves (scan rate 5 mV s−1) in 1.0 M PBS solution, (b) H2O2 yield (left y-axis, large dots) and electron transfer number (right y-axis, small dots) as a function of potential obtained from RRDE measurement at a rotating rate of 1,600 rpm, (c) CV curves in 1.0 M PBS solution for durability test (scan rate 100 mV s−1), and (d) chronoamperometric responses at -0.3 V (1,600 rpm) followed by 3.0 M methanol of N-G@CoNi/BCNT. Partial data for Ni-NBCNT, Co-NBCNT, CoNi-NBCNT, and Pt/C are also shown.

In principle, oxygen can be reduced through two mechanisms: 1) one-step four-electron pathway or 2) two-electron pathway in which O_2 is reduced to HO_2^- followed by the disproportionation of HO_2^- [336]. While the 2-e pathway generates highly reactive hydrogen peroxide that may lead to damage to membranes and electrodes, the 4-e pathway is more favorable in fuel cells applications because of the higher reduction potential. The ORR pathway was investigated with RRDE measurements in 1.0 M PBS solution (Figure C8). Calculated from Figure C8, the H_2O_2 yield at N-G@CoNi/BCNT is potential dependent, and drops from 100% at a low overpotential to 18.2% at a high overpotential (Figure 5.4b), suggesting that ORR catalyzed by N-G@CoNi/BCNT proceeds initially through the 2-e pathway, and shifts to the 4-e pathway with increasing potentials. The electron transfer number of N-G@CoNi/BCNT reached the plateau of 3.63 at -0.46 V vs. Ag/AgCl, close to the 3.9 of Pt/C, showing an efficient 4-e process. This value is also comparable to that obtained by polyelectrolyte-functionalized CNT (3.72) and N-doped graphene (3.69) [59, 337]. The ORR catalysis of the N-G@CoNi/BCNT can mainly be attributed to the introduction of three nitrogen species shown in Figure 5.3c: graphitic N can adsorb OOH and reduce O_2 to H_2O_2 via the 2-e pathway, while pyridinic and pyrrolic N are responsible for the catalysis of the 4-e pathway [61, 338]. Besides, the CoNi alloy can be stripped by nitrogen atoms to form the enclosed Co-coordinated nitrogen complex that reduced the oxygen adsorption energy of carbon surfaces and made the reduction of oxygen more easily [339, 340]. Finally, the presence of O species (Figure C4a) may help decrease active energy carrier of ORR and protects catalytic C-N groups from being degenerated by protons [335]. In a recent study, an N-doped graphene/CNT nanocomposite achieved an electron transfer number up to 3.7 at a large overpotential [341]. The synthesis of this nanocomposite started from the pre-oxidation of multi-walled CNTs and the reduction of graphene oxide with the Hummer's method, followed by the hydrothermal treatment in the presence of ammonium for 12 h. Compared to the complicated modified Hummer's method and secondary reduction to graphene reported in the previous works (Table C1), the decomposition of urea with the assistance of CoNi alloy demonstrated in the present study greatly simplifies the synthesis of N-doped nanocarbon. Another relevant parameter for practical applications is the durability of the electrode. Although the current density showed slight fluctuation possibly due to the operational error during aeration, the

onset potential of N-G@CoNi/BCNT after continuous 3,000 and 6,000 cycles remained the same as in the first cycle (Figure 5.4c), indicating that the N-G@CoNi/BCNT is stable as an ORR catalyst. Moreover, this hybrid showed a satisfactory tolerance to methanol cross-over effect, which is superior to the Pt/C catalyst and thus renders it a promising candidate catalyst for fuel cells (Figure 5.4d).

5.3.3 MFC performance

It should be noted that the electrochemical analysis in a well-defined system (i.e., a three-electrode cell) may yield results different from those in real situations, where various factors such as mass transfer and adsorption/desorption may play a dominant role in the ORR catalysis. Therefore, the prepared N-G@CoNi/BCNT was examined in an MFC to mimic real applications. It can be seen from Figure 5.5a that the current density for all testing groups gradually decreases over time due to the consumption of substrates. The sudden drop of current density at 24 h indicates the renewal of electrolyte, and the rapid recovery implies that the MFC anode is well cultivated and exerts little effects on the investigation of the cathode electrode. The MFC equipped with N-G@CoNi/BCNT yielded an average current density of 6.7 A m^{-2}, slightly lower than that with Pt/C (7.5 A m^{-2}). In comparison, the maximum current densities obtained from pristine Co and Ni were only 64.2 % and 44.8 % that of N-G@CoNi/BCNT, respectively.

The maximum power density calculated from the polarization curve (Figure 5.5b) is 2.0±0.1 W m^{-2} for N-G@CoNi/BCNT and 2.6±0.2 W m^{-2} for Pt/C, meaning that the power density of N-G@CoNi/BCNT is only 71.4% that of Pt/C. Nevertheless, to the best of our knowledge, this value of the power density for N-G@CoNi/BCNT is one of the highest reported compared to those of other top doped nanocarbons as MFC catalysts (Table C1). Interestingly, the current density of N-G@CoNi/BCNT is calculated to be 89.3% that of Pt/C. Such a discrepancy in power and current is a complicated result of catalytic activity and mass transfer. It can be seen from the polarization curve that the open circuit voltage (i.e., the intercept of y-axis) of N-G@CoNi/BCNT is 0.1 V lower than that of Pt/C, agreeing well with the findings in the electrochemical measurements. Furthermore, the polarization curve shows three typical regions representing different types of potential losses [71]. The sudden potential drop at a low current (< 0.5 A m^{-2}) indicates a high activation potential loss of N-G@CoNi/BCNT. At a high current (> 5.5 A m^{-2}) where the mass

transfer potential loss is located, the drop of N-G@CoNi/BCNT is less drastic than that of Pt/C. This implies a more efficient interaction between O_2 and the catalyst, which could be ascribed to the unique morphology and considerable specific surface area (114.3 $m^2\ g^{-1}$) of the synthesized N-G@CoNi/BCNT [315]. Collectively, the N-G@CoNi/BCNT exhibits a relatively high current density but a low power density, suggesting that this material is more suitable for applications in which a high current is desired.

Because N-G@CoNi/BCNT exhibited comparable performance to Pt/C in both electrochemical and MFC experiments, it was further studied using catholyte with different conductivity and pH. The current density of Pt/C and N-G@CoNi/BCNT with 35 g L^{-1} NaCl solution reached up to 12.7 and 11.2 A m^{-2}, respectively, but dropped below 4 A m^{-2} with tap water (Figure 5.5c), indicating that high conductivity was favorable for current generation. This was confirmed with neutral buffer (pH = 7.0, 10.0 mS cm^{-1}), whose current density was higher than that with 50 mM PBS (Figure 5.5a, pH = 7, 6.4 mS cm^{-1}) due to the increased conductivity. On the other hand, the current density of both Pt/C and N-G@CoNi/BCNT decreased with increased pH (Figure 5.5c). This is because, according to the Nernst equation, high pH (i.e. low proton concentration) leads to low reduction potential of ORR, and thus low cell voltage and current. It was worth noting that the MFC equipped with N-G@CoNi/BCNT was less susceptible to pH change and yielded comparable current density to Pt/C at the pH of 10.0, which could be attributed to the ORR mechanisms of Co and Ni under alkaline condition. A previous study on carbon supported palladium–nickel alloys showed that the alloy with high Ni content had a higher electron transfer number than commercial Pt did in alkaline media [342]. In another study, cobalt-polypyrrole catalysts were synthesized and it was proposed that the materials possessed two types of active sites: the Co-N sites adsorbed O_2 molecules and converted them via 2 e^- process to HO_2^-, which were then converted to OH^- react at the decorating cobalt oxides/Co nanoparticle sites [343]. Given that the N-G@CoNi/BCNT synthesized here is composed of different nitrogen species, Ni and Co, which may catalyze ORR individually or interact with each other and exert effects to catalysis, the ORR mechanisms of this material can be complicated and warrant further study.

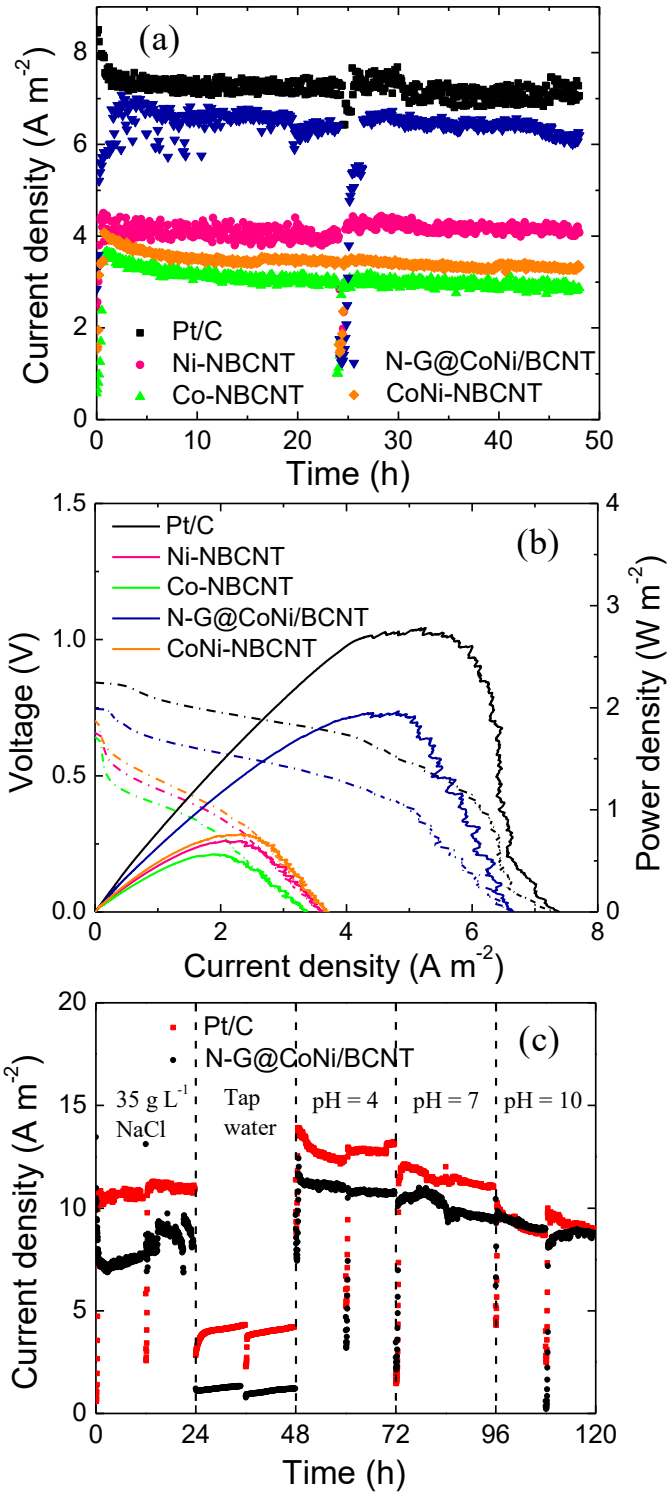

Figure 5.5 (a) Current density of the MFC equipped with different cathode electrodes, (b) the polarization curves, and (c) current density of with Pt/C and N-G@CoNi/BCNT in different catholyte.

5.4 Conclusions

The N-G@CoNi/BCN synthesized in the present work exhibited effective ORR catalysis as a result of its unique morphology and defect structures, such as CoNi/N-doping, carbon-coated alloy/graphene hybridization, considerable specific surface area, and high electron conductivity. It can be seen from the electrochemical experiments that ORR catalysis of the hybrid is comparable to that of platinum, and the MFC experiments reveal a high current density possibly due to the synergy of effective catalysis and enhanced mass transfer. Hence, it holds great promise in practical applications due to its simple synthesis procedure, high catalytic activity of ORR, and excellent durability. While the outstanding performance of N-G@CoNi/BCN at high pH remains to be understood by further studies, it is highly desirable as it can reduce the cost of pH control (e.g. buffer addition). More importantly, the N-G@CoNi/BCNT is significantly advantageous over catalysts based on noble metals in terms of material cost. Given that 1 g of N-G@CoNi/BCNT can be produced from 5 g of urea, 0.12 g of Co salt, and 0.10 g of Ni salt with the synthesis method demonstrated in this study, the cost for synthesizing 50 g N-G@CoNi/BCNT to construction 1-m^2 electrode is $ 13.3, which is 200 times less expensive than using the 10% Pt/C ($2,750 for 59 g). The fact that the prepared catalyst generates a high current but a low power implies the necessity of identifying proper application niches. For example, a high current means a rapid oxidation reaction in the anode and thus fast degradation of organic matters and short hydraulic retention time. Therefore, MFCs equipped with the N-G@CoNi/BCNT may be a competitive approach for treating domestic wastewater compared to the energy-consuming activated sludge process. In addition, previous studies on microbial desalination cells have reported enhanced desalination performance and energy efficiency at the high-current mode [310]. These results imply that the hybrid may hold great promise not only in wastewater treatment, but also for fresh water recovery.

CHAPTER 6: Enhancing Desalination and Wastewater Treatment by Coupling Microbial Desalination Cells with Forward Osmosis

(This section has been published as: Heyang Yuan, Ibrahim M. Abu-Reesh, and Zhen He. "Enhancing desalination and wastewater treatment by coupling microbial desalination cells with forward osmosis." Chemical Engineering Journal (2015): 270, 437-443.)

6.1 Introduction

Globally there are some 2.4 billion people suffering from water-borne illness due to inadequate sanitation [344]. Effective treatment of saline water and contaminated water can substantially tackle these problems in freshwater supply and wastewater treatment. However, conventional methods for desalination (e.g. reverse osmosis, multi-stage flash and electrodialysis) and wastewater treatment (e.g. activated sludge process) are energy-intensive [4, 191], posing a major challenge for addressing water issues in the areas that are short of energy supply. In addition, the separate treatment of saline water and wastewater results in high capital cost and inefficient utilization of infrastructures. Therefore, novel technologies with integrated desalination and wastewater treatment will be of great interests.

Microbial desalination cells (MDCs) are an emerging technology that can simultaneously treat wastewater and desalinate saline water by taking advantages of microbial respiration with an electrode [84]. In a typical MDC, a salt chamber is separated from an anode chamber with an anion exchange membrane (AEM), and from a cathode chamber with a cation exchange membrane (CEM) [345]. Exoelectrogens growing in the anode oxidize organic compounds in the wastewater and donate electrons to the anode electrode to accomplish extracellular respiration [15]. These electrons flow through an external circuit to reduce electron acceptors in the cathode, creating an electric field between the two electrodes. Driven by the electrostatic force, anions and cations in the saline water migrate to the anode and cathode, respectively [85]. As a result, both saline water and wastewater can be treated with low energy consumption. Both fundamental studies and large-scale tests have advanced MDC technology towards practical applications [33, 346-351]. For example, a tubular MDC with an anode liquid volume of 1.9 L was able to remove 94.3% of the NaCl at a TDS (total dissolved solids) removal rate of 11.61 g L^{-1} d^{-1} [310]. This system was further scaled up to 105 L (total liquid volume) and achieved a salt removal rate of 9.2 g L^{-1} d^{-1}

with more than 97% of the COD (chemical oxygen demand) being removed. In addition, the stacked MDCs were also widely studied and recently enlarged to a ten-liter system packed with mixed ion-exchange resins for desalinating the secondary effluent of wastewater treatment [352].

Forward osmosis (FO) is another promising technology for both desalination and wastewater treatment. An FO process refers to the movement of water molecules from a low-concentration solution (feed) through a semipermeable membrane to a high-concentration solution (draw) under an osmotic pressure gradient [353]. Because of the relatively low osmotic pressure difference, FO is advantageous over conventional membrane technologies such as reverse osmosis, nanofiltration and ultrafiltration, in terms of fouling propensity, water recovery and energy efficiency [168]. When FO is applied to treat wastewater, clean water can be extracted by osmotic pressure, thereby greatly reducing wastewater's volume [170]. For desalination application, fresh water can be recovered from the diluted draw solution by low-grade heat, membrane-based methods, or magnetic separation [184, 354-356].

The fact that FO achieves dilution instead of salt removal and MDCs are low efficient in desalinating high-salinity water provide opportunities for the combination of those two technologies for complementing each other [357]. In a previous study, an osmotic MDC (OsMDC) was developed by replacing the AEM (anion exchange membrane) with an FO membrane [178]. In addition to water extraction, the OsMDC could also remove organic matter and salts, which outperformed the FO process and regular MDCs. However, the OsMDC removed fewer salts than a regular MDC, mainly because ion transportation was blocked by the semi-permeable FO membrane. To overcome this drawback, an OsMFC (osmotic microbial fuel cell) was hydraulically coupled with a regular MDC [179]. Both desalination efficiency and COD removal were distinctly enhanced compared to regular MDCs, but at the expense of a prolonged hydraulic retention time of salt solution (HRT = 3.5 d). Moreover, energy consumption by aeration in the OsMFC was a major hindrance to the development of the OsMFC-MDC system. To achieve better integration of FO and MDCs towards practical applications, one must consider the balance in treatment capacity between the two and reduction in energy consumption.

In this study, we proposed an MDC-FO system that eliminated aeration and significantly enhanced desalination performance at a salt solution's HRT as short as 16 h. The anode effluent from two MDC batches was mixed and used as the FO feed to mimic the parallel operation of two identical MDCs (Figure 6.1). After clean water was extracted, the concentrated feed of the FO was introduced back into the anode of the MDC for further COD removal, whilst the diluted draw of the FO was desalinated in the desalination chamber of the MDC. To demonstrate the feasibility and performance of this coupled system, the effects of initial COD concentration, salt concentration and HRT were examined.

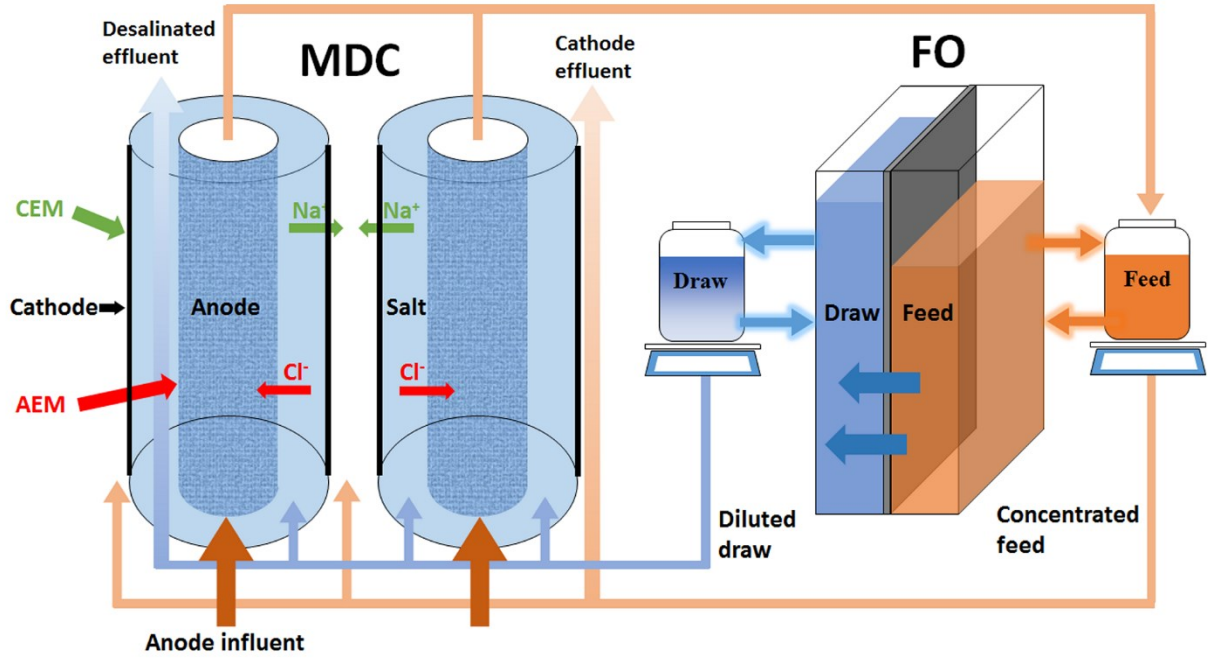

Figure 6.1 Schematic of the MDC-FO system. CEM: cation exchange membrane; AEM: anion exchange membrane.

6.2 Materials and methods

6.2.1 System setup

The tubular MDC was constructed similarly to that in a previous study [199]. Briefly, an AEM tube (AMI-7001, Membrane International, Inc., NJ, USA) and a CEM tube (cation exchange membrane, CMI-7000, Membrane International, Inc.) were made to form the anode chamber (350 mL) and salt chamber (80 mL) (Figure 6.1). A carbon brush (Gordon Brush Mfg. Co., Inc., CA,

USA) was used as the anode electrode. The cathode electrode was a piece of 150-cm^2 carbon cloth (Zoltek Companies, Inc., MO, USA) coated with 0.1 mg cm^{-2} Pt/C as previously described [88] and wrapped the CEM tube. The anode and the cathode electrodes were connected to an external circuit across a 0.1-Ω resistor using titanium wire. An FO cell (Sepa CF II Forward Osmosis Cell 316 SS, Sterlitech Corporation, WA, USA) was used for the FO tests, containing an FO membrane (HTI OsMem™ CTA-ES, Hydration Technology Innovations, OR, USA) tailored to an area of 140 cm^2.

6.2.2 System operation

The synthetic anode solution using sodium acetate as an organic substrate contained (per liter of deionized water): sodium acetate (concentration ranged from 0.5 to 2 g L^{-1} depending on the test conditions); NaCl, 0.5 g; $MgSO_4$, 0.015 g; $CaCl_2$, 0.02 g; KH_2PO_4, 5.3 g; K_2HPO_4, 10.7 g; $NaHCO_3$, 1 g; and trace element, 1 mL [200]. Saline water was prepared by dissolved sodium chloride in DI water. The MDC was inoculated with anaerobic sludge and cultivated for two months with the anode feed solution containing 750 mg L^{-1} COD and saline water containing 35 g L^{-1} NaCl. The cathode was exposed to air and rinsed with 100-mM phosphate buffered saline (PBS, 5.3 g L^{-1} KH_2PO_4 and 10.7 g L^{-1} K_2HPO_4).

The MDC was operated in two consecutive batches with an initial COD concentration of 750 mg L^{-1} and at an anode HRT of 12 h. The effluent collected from those two consecutive batches formed a 700-mL feed solution for an FO cell, in which the feed solution was recirculated between a reservoir and the FO feed chamber at a cross-flow velocity of 16.4 cm s^{-1} by a peristaltic pump (BT600-2J, Langer Instruments Corp., NJ, USA). The draw solution was 100-mL NaCl solution (35 g L^{-1}) recirculated at the same velocity. The FO cell was operated at the same HRT as that of the MDC anode. After the FO, half of the effluents of the feed and the draw solutions were introduced back to the MDC cathode and salt chambers, respectively, and operated at the same HRT as that of the MDC anode. This operation was to simulate the parallel operation of two identical MDCs linked to one FO cell, resulting in an organic solution's HRT of 36 h and saline water's HRT of 24 h (Table 6.1). The effects of initial COD concentration, initial NaCl concentration and HRT were examined with varied parameters shown in Table 6.1. All

experiments were conducted at room temperature and repeated at least 6 times, with the first three ones as the adaptation period of the new conditions and the last three for data analysis.

Table 6.1 The parameters in different experimental conditions.

Parameters	COD concentration (mg L^{-1})	NaCl concentration (g L^{-1})	$HRT_{A/F}$[a] (h)	HRT_{SW}[b] (h)	HRT_{OS}[c] (h)
COD	350 750 1000	35	12	24	36
Salt	750	10 20 35	12	24	36
HRT	750	35	8 12 16	16 24 32	24 36 48

[a] HRT in the anode or in the FO cell.
[b] Total HRT of saline water.
[c] Total HRT of organic solution.

6.2.3 Measurement and analysis

The voltage of the MDC was measured by a digital multimeter (2700, Keithley Instruments, Inc., OH, USA) every 5 min. The concentration of soluble COD was measured using a colorimeter according to the manufacturer's instruction (DR/890, Hach, CO, USA). Coulombic efficiency (CE) was calculated according to a previous study [358]. The COD removal rate in the anode was calculated based on the anode HRT, and the total removal rate was based on the total HRT of organic solution in the MDC-FO system (Table 6.1). COD loss in the FO cell (ΔCOD_{FO}) was calculated as:

$$\Delta COD_{FO} = (COD_{FO,\,in} \times V_{FO,\,in}) / V_{FO,\,eff} - actual\ COD_{FO,\,eff} \quad (6.1)$$

where $COD_{FO,\,in}$ is the FO influent COD, $V_{C,\,in}$ is the FO influent volume, $V_{C,\,eff}$ is the FO effluent volume and $actual\ COD_{FO,\,eff}$ is the actual FO effluent COD measured with the standard method. Water flux in the FO process and evaporation on the cathode was considered when calculating the total COD removal (ΔCOD_T) and removal rate:

$$\Delta COD_T = (COD_{A,\,in} \times V_{A,\,in} - COD_{C,\,eff} \times V_{C,\,eff}) / V_{C,\,eff} \quad (6.2)$$

where $COD_{A,\ in}$ is the anode influent COD, $V_{A,\ in}$ is the anode influent volume, $COD_{C,\ eff}$ is the cathode effluent COD and $V_{C,\ eff}$ is the cathode effluent volume. The conductivity was measured by a bench-top conductivity meter (FiveEasy™ conductivity, Mettler-Toledo, OH, USA). The TDS concentration (g L^{-1}) was estimated by multiplying the conductivity (mS cm^{-1}) with the empirical coefficient of 0.64. The decrease rate of TDS concentration in the FO was calculated based on the FO's HRT, and the total decrease rate was calculated based the total HRT of saline water within the MDC-FO system (Table 6.1). The weight change in the feed and the draw was monitored with digital balances (Scort Pro, Ohaus, NJ, USA) for the calculation of water flux. The current efficiency was calculated as the total amount of NaCl removed in the salt chamber divided by the amount of total coulomb [85].

6.3 Results and discussion

6.3.1 Feasibility of the coupled system

To examine the feasibility of the coupled system, the MDC-FO system was operated with a synthetic anode solution containing 750 mg L^{-1} COD and a saline solution containing 35 g L^{-1} NaCl at an MDC anode HRT of 12 h. A standalone MDC and a standalone FO cell were operated separately under the same conditions. It can be seen from Figure 6.2A that current generation in the MDC of the MDC-FO system exhibited a repeated profile affected by the consumption of substrate, while that in the standalone MDC showed noticeable fluctuation. The anode conductivity in the standalone MDC increased from 13.9±0.3 to 15.5±0.4 mS cm^{-1} after one cycle (12 h), while that in the MDC-FO increased from 13.3±0.1 to 14.9±0.2 mS cm^{-1}. The conductivity difference between the standalone MDC and the coupled system is insignificant, indicating that factors other than conductivity affected the current generation in the standalone MDC. For the MDC-FO system, 153.6 mL of water was extracted from the organic solution by the draw solution after the 12-h FO process, leading to a 62% reduction in the conductivity of the draw solution (Table 6.2). When this diluted draw solution was desalinated in the salt chamber of the MDC, the anode achieved more stable current generation and slightly higher COD removal, even though the Coulombic efficiency (CE) became lower due to the reduced conductivity (Table 6.2). These results suggest that pretreatment of saline water with an FO process can help the MDC to maintain stability, which is of great interest for large-scale and long-term applications.

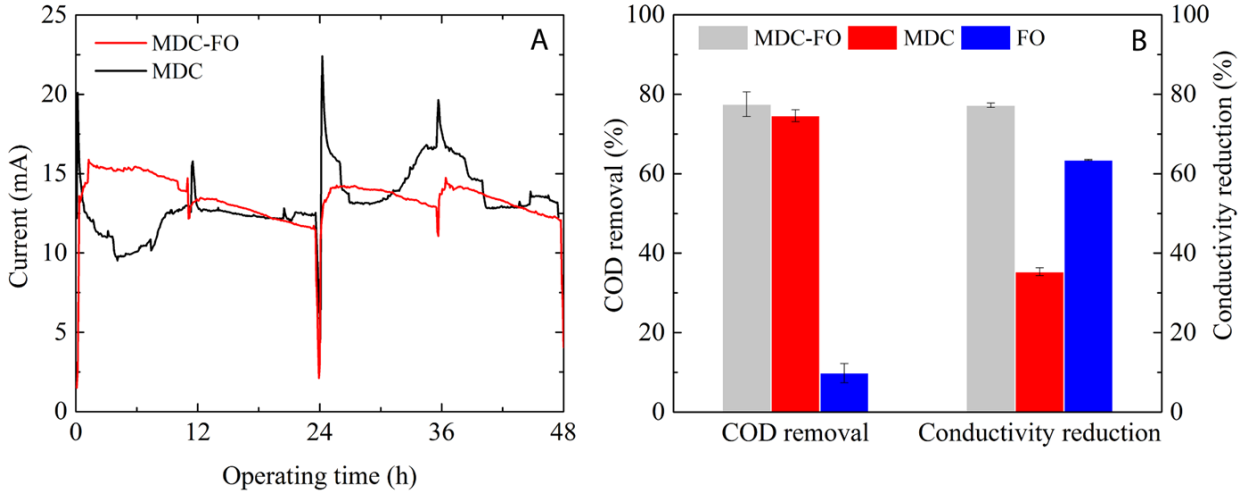

Figure 6.2 Comparison between the MDC-FO system and the standalone unit: (A) Current generation by the MDC-FO system and the standalone MDC; (B) COD removal and conductivity reduction after a complete cycle (24 h).

Table 6.2 The performance of the MDC-FO system, a standalone MDC and a standalone FO. Standard deviation is calculated with triplicate experiments.

	CE[a] (%)	**ΔCOD_A[b] (%)**	**$Rate_{COD-T}$[c] (g L^{-1} d^{-1})**	**$\Delta water$[d] (mL)**	**$\Delta conductivity_{FO}$[e] (%)**	**$Rate_{MDC}$[f] (g L^{-1} d^{-1})**
MDC-FO	83.6±5.4	43.7±1.3	0.421±0.030	153.6±6.7	61.9±0.3	22.7±5.3
MDC	90.2±0.6	40.2±2.5	0.400±0.010	0	-	11.2±0.3
FO	-	-	0.076±0.019	166.4±6.2	63.5±0.1	20.1±0.0

[a] Coulombic efficiency.
[b] COD removal efficiency in the MDC anode.
[c] Total COD removal after a complete cycle.
[d] Water Recovery
[e] Conductivity reduction in the FO cell.
[f] The rate of decrease in TDS concentration.

When the organic solution was used as the feed for the FO, water loss to the draw solution should concentrate the feed and thereby increase the COD concentration in the feed. However, Figure 6.2B shows that the standalone FO process could reduce the COD by 10% when feeding with fresh organic solution containing 750 mg L^{-1} COD, or 28% by taking water loss (166.4 mL) into account, likely because of the movement of small organic molecules through the FO membrane and/or biodegradation due to microbial contamination inside the FO cell. After each FO batch, the FO

cell was dismantled for cleaning and fouling was observed on the membrane surface facing the feed. Further experiments are warranted to characterize the fouling and reveal the mechanisms of COD loss in the FO process. Both the MDC-FO system and the standalone MDC achieved ~75% COD removal at the end of a complete cycle. The effluent volume of the MDC-FO system was reduced by 64% due to water flux in the FO and evaporation on the cathode, while the 14% reduction of the effluent volume of the standalone MDC was caused by evaporation on its cathode.

In contrast, a significant difference in desalination was observed in three systems (Figure 6.2B). The MDC-FO system reduced 80% of conductivity, twice that of the standalone MDC. The enhanced desalination of the MDC-FO system was mainly due to the dilution in the coupled FO cell, which contributed 62% of the conductivity reduction (Table 6.2). On the other hand, the standalone FO process reduced the conductivity 1.5 times more than the standalone MDC, but still lower than the MDC-FO system. In the FO process of both the standalone FO cell and the MDC-FO system, water flux declined noticeably over time due to the concentration change in the feed and the draw (data not shown), indicating that further prolonging the FO operation would help little to the conductivity reduction. It should also be noted that the standalone FO process is not able to remove salts. Desalination is accomplished when solutes in the diluted draw solution are separated by other technologies, e.g. MDCs in this study. Therefore, the combination of FO with MDC is beneficial as it can tackle post-treatment of the draw solution, enhance MDC desalination efficiency and reduce the volume of wastewater effluent.

6.3.2 Effects of the key factors on the MDC-FO system

For this coupled system, the two inputs are an organic solution and salt water; therefore, organic concentration (COD) and salinity are the key factors that affect the system performance. In addition, HRT is a key operating parameter that influences the system operation and treatment results. The following sections focus on those three factors and their effects on the coupled system.

(i) Initial COD concentration. Three COD concentrations ranging from 350 to 1000 mg L^{-1} were examined in the MDC-FO system at an MDC anode HRT of 12 h. Increasing the COD concentration linearly increased COD removal rate in the MDC anode from 0.42 g L^{-1} d^{-1} at 350 mg L^{-1} COD to 0.80 g L^{-1} d^{-1} at 1000 mg L^{-1} COD (Figure 6.3A), indicating that anode microbes

were able to develop strategies to treat excessive COD content. The lower CE of 66.7% at 1000 mg L^{-1} COD, on the other hand, implies that non-exoelectrogens might have increased contribution to the removal of the excessive COD [359, 360].

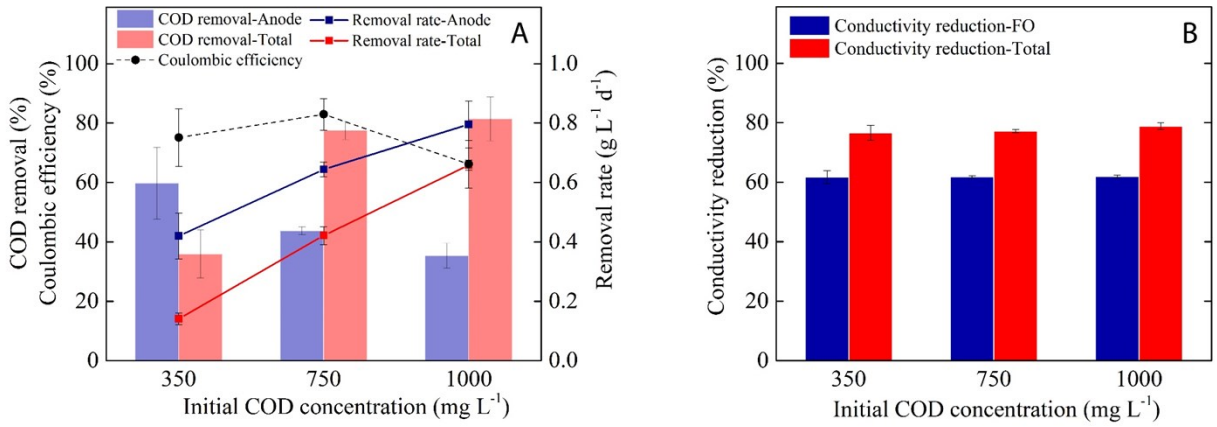

Figure 6.3 The performance of the MDC-FO system at different initial COD concentrations: (A) COD removal, removal rate and CE in the MDC anode (HRT 12 h) and the MDC-FO system (HRT 36 h); (B) Conductivity reduction and TDS decrease rate of the FO cell (HRT 12 h) and the MDC-FO system (HRT 36 h).

At 350 mg L^{-1} COD, the total COD removal (based on concentration variation) decreases from 60% after an anode batch to 35% after a complete MDC-FO cycle (Figure 6.3A), suggesting that the COD concentration increased in the FO (water loss) and cathode process (evaporation). However, the treatment performance did not seem to be affected by higher initial COD concentrations. The total COD removal of ~80% was achieved at 750 and 1000 mg L^{-1} COD, indicating that the organisms remained active at increased organic input [361]. This suggests that organic supply was not a limiting factor in the present MDC and some organic compounds were oxidized by non-exoelectrogens, which play a key role in COD removal, especially in wastewater containing a relatively high COD concentration.

Unlike the varied COD removal, the desalination performance was consistent. Figure 6.3B shows that the FO cell was not affected by the COD change and could reduce the conductivity by 60% at

all three COD conditions. When the saline water was further desalinated in the salt chamber of the MDC, the conductivity reduction reached 80% with a TDS decrease rate of ~25 g L^{-1} d^{-1}, which is 7 times faster than the removal rate of ~ 3.8 g L^{-1} d^{-1} obtained in previous studies [362, 363]. The rapid decrease in the TDS concentration in the MDC-FO system was mainly attributed to the fast dilution process in the FO. The experiment using 350 mg L^{-1} COD produced less amount of total coulomb, leading to a current efficiency of the MDC-FO system of 210.4%. The current efficiency was 124.7% at 750 mg L^{-1} COD and 126.9% at 1000 mg L^{-1} COD, both over 100%, indicating that current generation alone was not sufficient to accomplish the removal of salts measured by conductivity decrease. Meanwhile, an increase in the saline water volume in the salt chamber was observed. Therefore, the mechanisms other than electron migration, e.g. water dilution or salt diffusion, may play an important role in the conductivity reduction [364].

(ii) Effects of initial salt concentration. Three salt concentrations, 10, 20 and 35 g L^{-1} NaCl, were investigated in the MDC-FO system. When the 10-g L^{-1} NaCl solution was examined in the FO cell, the low osmotic pressure led to less water flux, which reduced the conductivity of the draw solution by only 12.8% (Table 6.3). However, with a TDS removal rate of 9.1 g L^{-1} d^{-1}, the total conductivity reduction of the system reached 99.4% after a complete MDC-FO cycle. For comparison, the experiments with 20 and 35 g L^{-1} NaCl resulted in water flux of 76.7 and 153.6 mL, and decreased the conductivity by 45.7% and 61.9% in the FO cell, respectively (Table 6.3). With the help of the FO process, the total TDS decrease rate of the MDC-FO system reached 13.8 g L^{-1} d^{-1} for 20 g L^{-1} NaCl and 25.5 g L^{-1} d^{-1} for 35 g L^{-1} NaCl, noticeably faster than the total TDS decrease rate of 9.1 g L^{-1} d^{-1} for 10 g L^{-1} NaCl. Those results demonstrate that the coupled system could well desalinate the low-salinity water such as brackish water, or pre-desalinate the high-salinity water with post-treatment.

Low conductivity in the salt chamber could increase MDC internal resistance and consequently inhibit exoelectrogenic activity. This is demonstrated by Figure 6.4, in which both anode COD removal and current generation exhibited distinct decrease when the low-concentration NaCl solution was used. However, the MDC-FO system fed with 10 g L^{-1} NaCl removed 92.6% COD after a complete cycle, significantly higher than the 74% at 35 g L^{-1} NaCl. This is likely because aerobic organisms might thrive on the cathode with less Cl^- content in the anode effluent (or

cathode influent), noticeably facilitating COD degradation. It is also possible that the high salinity in the cathode can inhibit further COD removal. When 35 g L^{-1} NaCl was examined, the catholyte conductivity was measured to be 24.9 mS cm^{-1} after a complete MDC-FO cycle, whereas that at 10 g L^{-1} NaCl was 20.2 mS cm^{-1}.

Table 6.3 Desalination performance of the MDC-FO system at varied NaCl concentrations. Standard deviation is calculated with triplicate experiments.

Salt (g L^{-1})	**Δwater[a] (mL)**	**ΔC_{FO}[b] (%)**	**ΔC_{MDC}[c] (%)**	**ΔC_{T}[d] (%)**	**$Rate_{FO}$[e] (g L^{-1} d^{-1})**	**$Rate_{MDC}$[f] (g L^{-1} d^{-1})**	**$Rate_{total}$[g] (g L^{-1} d^{-1})**
10	21.8±8.6	12.8±5.1	99.3±0.0	99.4±0.0	2.6±1.1	17.9±0.9	9.1±2.0
20	76.7±6.3	45.7±3.1	64.1±3.6	80.5±2.5	17.6±1.5	13.4±0.9	13.8±3.3
35	153.6±6.7	61.9±0.3	40.3±1.2	77.2±0.6	40.8±0.7	10.2±0.4	25.5±0.5

[a] Water Recovery from the MDC anode effluent.
[b] Conductivity reduction in the FO cell.
[c] Conductivity reduction in the MDC.
[d] Total conductivity reduction in the MDC-FO system.
[e] The rate of decrease in TDS in the FO cell.
[f] The rate of decrease in TDS in the MDC.
[g] The rate of decrease in TDS in the MDC-FO system.

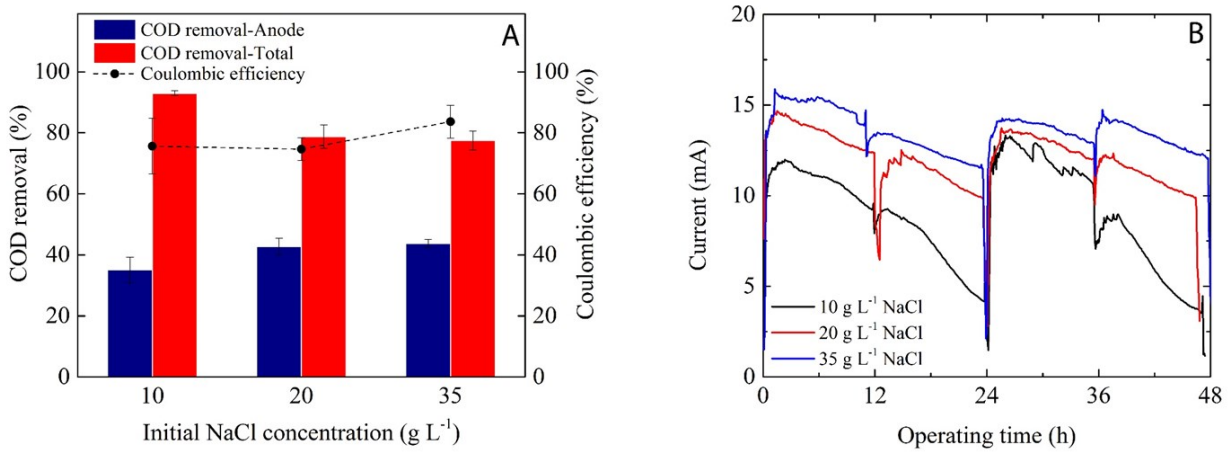

Figure 6.4 The performance of the MDC-FO system at different initial NaCl concentrations: (A) COD removal and CE in the MDC anode (HRT 12 h) and the MDC-FO system (HRT 36 h); (B) Current generation in the MDC.

(iii) Effects of HRT. The coupled system was examined at the MDC anode HRT of 8, 12, and 16 h (Table 6.1). The COD removal was ~40% in the anode and ~77% in the MDC-FO system regardless of the HRT (Figure 6.5A). The CE at 8 h (69.8%) was approximately 10% lower than that at other HRTs, because the organic loading rate was relatively higher at the lower HRT, and the growth and activities of organisms other than exoelectrogens might be encouraged. The abundant COD content was also beneficial to organisms growing on the cathode, thereby resulting in a comparable total COD removal of 75% at the low HRT of 8 h, despite a high COD loading rate. The COD removal rate in the MDC anode decreased linearly from 0.88 g L^{-1} d^{-1} at 8 h to 0.64 g L^{-1} d^{-1} at 12 h, and then to 0.43 g L^{-1} d^{-1} at 16 h. A similar trend was observed for the total COD removal rate by the whole system.

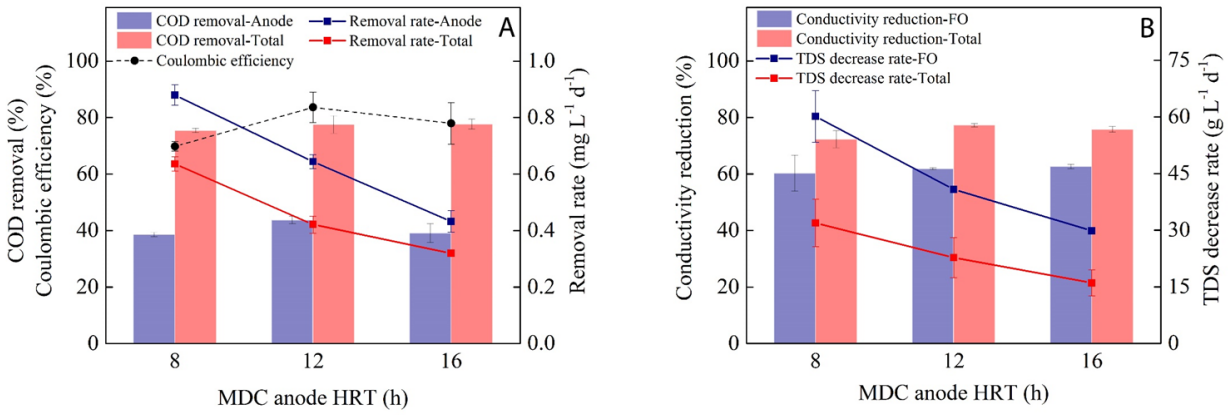

Figure 6.5 The performance of the MDC-FO system at different anode HRT: (A) COD removal, removal rate and CE in the MDC anode (HRT=8, 12, 16 h) and the MDC-FO system (HRT=24, 36, 48h); and (B) Conductivity reduction and TDS decrease rate of the FO cell (HRT=8, 12, 16 h) and the MDC-FO system (HRT=24, 36, 48h).

The desalination performance exhibited a similar trend as the COD removal: no significant difference in conductivity reduction was observed at three HRTs, but the total reduction rate decreased with increased operation time (Figure 6.5B). Conductivity reduction in the FO cell did not change with HRT because the water flux is governed by the osmotic pressure difference between the feed and draw, which was fixed with the MDC anode effluent and 35 g L^{-1} NaCl solution being used in this experiment. The water flux in the FO cell declined below 0.5 LMH (L

m^{-2} h^{-1}) in 6 h of operation, implying that the FO could yield comparable performance at a shorter HRT. For the desalination in the MDC, ion separation was related to electricity generation. Therefore, the slightly lower total conductivity reduction at the HRT of 8 h could be ascribed to the slightly lower anode COD removal and CE (Figure 6.5A). The highest COD removal rate and conductivity reduction rate, together with the comparable desalination and COD removal at the HRT of 8 h, indicating that HRT could be shortened without compromising the treatment performance.

6.3.3 Perspectives on the MDC-FO system

The synergy of MDC and FO has helped overcome their inherent limitations and thus yielded multiple benefits: (1) the FO process in the MDC-FO system can reduce wastewater's volume and recover high-quality water, thereby improving wastewater reuse; (2) conductivity reduction can be significantly accelerated by the rapid FO process; (3) the post-treatment of the diluted saline water can be more energy-efficient in MDCs than in RO [310]; and (4) the MDC-FO system can achieve comparable COD removal and more stable current generation compared to the standalone MDC.

Despite the enhanced performance and efficiency in the MDC-FO system compared to standalone MDC or FO, several challenges remain to be addressed. First, the MDC-FO system did not exhibit high COD removal at 350 mg L^{-1}, which is the typical COD concentration of domestic wastewater. Furthermore, the total COD removal of ~80% at most conditions cannot meet the requirement of practical applications. Understanding the limiting factors in COD removal, for example developing a more robust anode biofilm and improving cathode treatment, will greatly facilitate the development of the coupled system. Second, the system must be examined with actual wastewater and saline water (either seawater or brackish water). The organic solution used in this study had a higher conductivity than regular domestic wastewater; the actual wastewater may lead to more water recovery because of a larger osmotic pressure. The use of actual wastewater/saline water will also help examine membrane fouling. While fouling may improve COD removal in the FO cell because of the presence of microbes, it will hinder water recovery and conductivity reduction, thereby reducing desalination efficiency. Fouling behavior and cleaning strategy will be a focus in future studies. Third, the fast treatment of the FO process is indicative that more MDCs could be

coupled with one FO cell. For example, based on the system proposed in Figure 6.1, one FO cell could be coupled to four MDCs and continuously operated at an anode HRT of 8 h and an FO HRT of 4 h, further enhancing the efficiency of desalination and wastewater treatment. Another implication is that volume ratio between the MDC and the FO cell may play an important role in the overall system performance. Increasing the anode volume may, in theory, lead to higher biomass concentration and thus higher electricity generation. Meanwhile, increased amount of anode effluent will prolong the FO process and thereby yield higher water recovery, which means that more salt water will be desalinated in the MDC salt chamber. Previous studies revealed that enlarging the salt chamber by increasing the inter-membrane distance resulted in declined desalination efficiency [213]. Therefore, substantial experiments need to be performed to understand the synergy between the MDC and the FO cell. The successful establishment of an MDC model in a recent study [131] suggests that modeling can be a powerful tool to determine optimal configuration and operational parameters in the MDC-FO system.

6.4 Conclusions

This study has demonstrated the improved performance of both desalination and COD removal by an MDC-FO system compared to a standalone FO cell or MDC. The coupled system achieved more stable current generation and accomplished desalination more rapidly than the standalone MDC. Moreover, the MDC-FO recovered clean water and reduced the volume of wastewater. The MDC-FO system could effectively treat wastewater containing high COD content without affecting desalination performance. Low initial NaCl concentration was beneficial for COD removal and conductivity reduction, while high initial NaCl concentration increased water recovery. Therefore, the MDC-FO system can serve as either direct treatment of brackish water or pre-treatment of seawater. In addition, shortening the HRT did not exert effects on the performance, but noticeably improved the efficiency. The results of this study encourage further optimization and development of the MDC-FO system towards practical applications.

CHAPTER 7: Mathematical Modeling Assisted Investigation of Forward Osmosis as Pretreatment for Microbial Desalination Cells to Achieve Continuous Water Desalination and Wastewater Treatment

(This section has been published as: Heyang Yuan, Ibrahim M. Abu-Reesh and Zhen He. Mathematical modeling assisted investigation of forward osmosis as pretreatment for microbial desalination cells to achieve continuous water desalination and wastewater treatment. Journal of Membrane Science (2015): 502, 116-123.)

7.1 Introduction

Due to the increasing demand for clean water and the generation of wastewater whose treatment/production is associated with high energy consumption, it is urgent to develop new strategies for simultaneous seawater desalination and wastewater treatment at low energy consumption to meet the requirement of water-energy sustainability. Among various membrane-based water/wastewater treatment technologies, forward osmosis (FO) holds great promise for its low energy input and low fouling propensity [168]. FO refers to the diffusion of water from a low-salinity solution (feed) through a semipermeable membrane to a high-salinity solution (draw) [353]. When wastewater serves as a feed and saline water is used as a draw, clean water can be extracted by the draw solution and the volume of the wastewater will be greatly reduced [170]. The concentrated feed solution (wastewater) needs to be further disposed, and regeneration of draw solution in an energy-efficient way remains to be a great challenge for FO application. There have been very limited studies focusing on the post-treatment of the concentrated feed effluent [365]. Regeneration of draw solution relies on conventional methods e.g. reverse osmosis (RO), electrodialysis or membrane distillation at reduced energy consumption [354, 366, 367], although regenerable solutes such as ammonium bicarbonate, superparamagnetic nanoparticles or polymer hydrogels have also been reported [184, 368-370].

With a relatively high organic content in the concentrated wastewater after FO treatment, the feed effluent may be used for energy recovery in bioelectrochemical systems (BES), such as microbial fuel cells (MFCs), microbial electrolysis cells (MECs), and microbial desalination cells (MDCs) [7]. If seawater is used as a draw solution, the diluted seawater could be further desalinated in MDCs, thereby eliminating the need for regenerating draw solution. MDCs are an emerging

concept that can achieve desalination and wastewater treatment at the same time [84]. In a typical MDC, exoelectrogens growing in the anode consume organic compounds in wastewater and respire by releasing electrons extracellularly to an anode electrode [18]. When proper electron acceptors (e.g. oxygen) are present in the cathode and the overall redox reaction of the cell is thermodynamically favorable, the electrons flow spontaneously from the anode to the cathode, creating an electric field between the two electrodes. Driven by the electrostatic force, anions and cations in the saline water migrate to the anode and the cathode, respectively [85]. Both bench and large-scale studies have demonstrated the great potential of MDCs for the applications in wastewater treatment and desalination of both seawater and brackish water [9, 85, 192, 347, 371]. For example, a ten-liter stacked MDC packed with ion-exchange resins was constructed to desalinate secondary effluent and achieved comparable effluent quality to that of RO [352]. To improve the understanding of MDC processes, mathematical models were developed and predicted that the desalination effectiveness could be greatly enhanced by reducing the flow rate of salt solution [131]. The model also suggested that four-stage operation could reduce 14% more salinity than one-stage operation when treating brackish water [372].

Given that FO effluents require further treatment and MDCs can simultaneously remove COD and salt, the integration of FO with MDCs may create synergistic benefits [75, 171]. Examples of such synergy include an osmotic MDC with replacing the AEM (anion exchange membrane) by an FO membrane [178], and hydraulic coupling of an osmotic microbial fuel cell (OsMFC) to an MDC for enhancing desalination efficiency and COD removal [179]. We have previously developed a batch-operated MDC-FO system, in which the organic solution was first treated in an MDC anode and its effluent was used as the feed in an FO cell for water recovery; the concentrated feed solution was then reused as the catholyte and the diluted draw was desalinated in the MDC [180]. Although the coupled system was more advantageous over standalone MDC or FO cell regarding COD and salt removal and water recovery, it was concluded that the system could not generate water for direct use due to the relatively low TDS (total dissolved solids) reduction (77.2%) when desalinating 35 g L^{-1} NaCl solution; in addition, the treatment capacity between the FO and the MDC was not properly coordinated, because of faster treatment in the FO than that in the MDC.

In this study, we have developed an FO-MDC system under a continuously operated mode (Figure 7.1), and this system significantly differs from the coupled MDC-FO system in our previous study [180]: in the present system, wastewater is first treated in the FO feed chamber for water extraction and then the concentrated feed solution is treated in the MDC anode. The volume ratio of the FO cell and the MDC was properly coordinated to guarantee adequate hydraulic retention time (HRT) in the individual components, and thus the system is highly integrated in terms of water stream. Such a modification is expected to generate high-quality effluents from both the wastewater and seawater streams. The coupled system was examined with synthetic and actual domestic wastewaters (raw or amended with glucose). To understand the synergistic factors between the two units, a mathematical model was developed for the first time through integrating the FO model with the MDC model. The developed model was used to predict the system performance at varied flow rates and provide perspectives on system development.

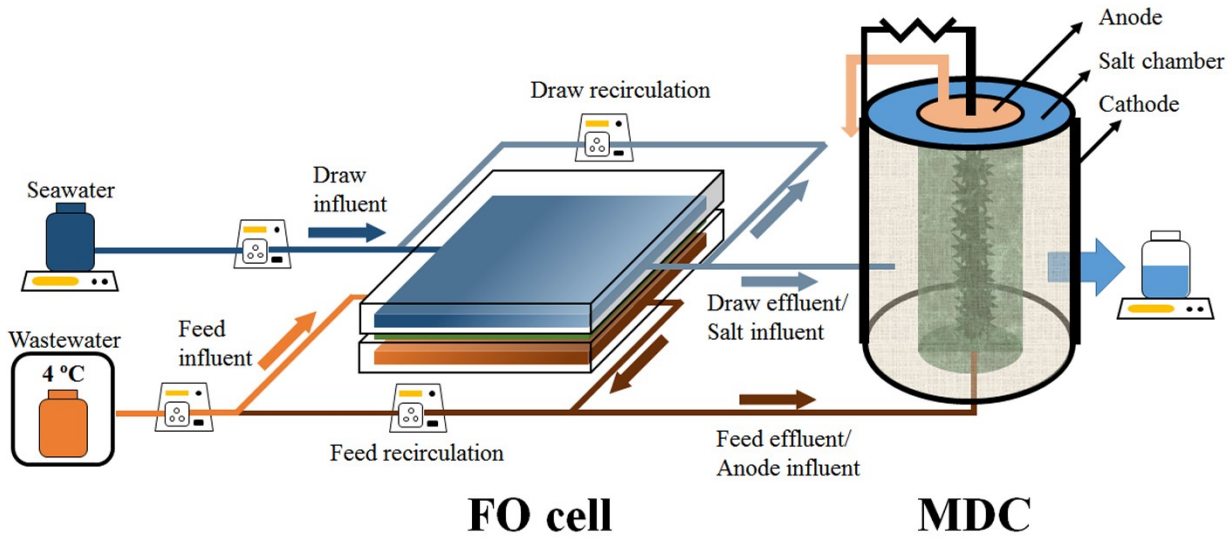

Figure 7.1 Schematic of the FO-MDC system operated continuously.

7.2 Materials and methods

7.2.1 System setup and operation

An FO cell with a membrane area of 40 cm^2 was constructed by sandwiching an FO membrane (HTI OsMem™ CTA-ES, Hydration Technology Innovations, OR, USA) between the feed and the draw chambers (40 mL/each). The active layer was placed against the feed side to minimize the effects of biofouling [373]. A tubular MDC was constructed as previously described [199]: an

AEM tube (AMI-7001, Membrane International, Inc., NJ, USA) was made to form the anode chamber (250 mL), and a CEM tube (CMI-7000, Membrane International, Inc.) with a larger diameter was made to form a compartment between the AEM and CEM tubes as the salt chamber (70 mL). A carbon brush (Gordon Brush Mfg. Co., Inc., CA, USA) was used as the anode electrode. A piece of 150-cm^2 carbon cloth (Zoltek Companies, Inc., MO, USA) was coated with 0.1 mg cm^{-2} Pt/C as a cathode catalyst [88], and wrapped the CEM tube as the cathode electrode. The anode and cathode electrode were connected with titanium wire across a 1-Ω resistor.

Table 7.1 Performance of the FO cell under different conditions.

Feed	**$Q_{F,0}$ (mL min^{-1})**	**$Q_{D,0}$ (mL min^{-1})**	**J (LMH)**	**J_{sim} (LMH)**	**$F_{effective}$ (g L^{-1})**	**$D_{effective}$ (g L^{-1})**	**HRT_F (h)**	**HRT_D (h)**
Synthetic	0.6	0.04	0.99	1.13	6.0	13.2	1.1	16.7
Synthetic	0.4	0.04	1.01	1.17	5.9	13.1	1.7	16.7
Synthetic	0.4	0.02	0.61	0.80	6.1	11.6	1.7	33.3
Synthetic	0.8	0.03	0.84	1.07	5.7	12.2	0.8	22.2
Wastewater	0.6	0.01	0.84	0.90	0.9	5.3	1.1	66.7
Wastewater + glucose	0.6	0.01	0.64	0.64	3.1	6.6	1.1	66.7

$Q_{F,0}$, influent flow rate of the feed; $Q_{D,0}$, influent flow rate of the draw; J, water flux; J_{sim}, simulated water flux; $F_{effective}$, effective feed concentration (TDS in the feed effluent); $D_{effective}$, effective draw concentration (TDS in the draw effluent); HRT_D, HRT of the draw; HRT_F, HRT of the feed.

When synthetic wastewater was used as the feed solution, it contained (per liter of deionized water): sodium acetate 0.4 g; NaCl, 0.5 g; $MgSO_4$, 0.015 g; $CaCl_2$, 0.02 g; KH_2PO_4, 0.265 g; K_2HPO_4, 0.535 g; $NaHCO_3$, 4.2 g; and trace element, 1 mL [200]. When the actual wastewater was the feed solution, the primary effluent was collected from a local wastewater treatment plant (Peppers Ferry, VA, USA), and was used either in raw or amended with 500 mg L^{-1} glucose and 50 mM $NaHCO_3$. The feed was stored with coolant in a container at 4 ºC. The draw solution was 35 g L^{-1} NaCl (to mimic seawater) with conductivity ranging from 51.6 to 53.2 mS cm^{-1}. The MDC was inoculated with anaerobic sludge and cultivated for one month with the synthetic wastewater and the NaCl solution to achieve stable current output. Then, the system was operated under a continuous mode (Figure 7.1): the feed and the draw solutions were pumped into the FO cell and recirculated at a rate of 190 mL min^{-1} (~0.08 cm s^{-1}); the feed and the draw effluents were then introduced into the MDC anode and salt chambers, respectively; finally, the anode effluent was used to rinse the cathode electrode for cathodic oxygen reduction and further COD removal. The

anolyte, the catholyte and the salt solution in the MDC were recirculated at 46 mL min^{-1}. The influent flow rates of the feed and the draw were varied, resulting in different HRT in both the FO cell and the MDC (Table 7.1). The FO membrane was washed with deionized water before changing to a new flow rate.

7.2.2 Model formulation

Because the active layer of the FO membrane was placed against the feed solution to alleviate biofouling, dilutive internal concentration polarization would occur within the porous support, and therefore water flux (J) of the FO process was simulated using a model developed by McCutcheon and Elimelech [185]:

$$J = A \cdot \left[\pi_D \, exp(-JK) - \pi_F \, exp\left(\frac{J}{k}\right)\right] \quad (7.1)$$

where A is the permeability coefficient; K is the solute resistivity for diffusion within the porous support layer; and k is the mass transfer coefficient. The osmotic pressures of the bulk draw (π_D) and feed (π_F) solution were calculated according to the van't Hoff equation:

$$\pi = iRTC \quad (7.2)$$

where i is the number of dissolved species (2 for NaCl); R is the ideal gas constant; T is the absolute temperature; and C is the molar concentration (C = conductivity × 0.64 / 58.5). The reverse salt flux (J_S) can be approximated as [374]:

$$J_S = \frac{BJ}{AiRT} \quad (7.3)$$

where B is the salt permeability coefficient. The flow rate (Q_F, Q_D) and the salt concentration (C_F, F_D) of the feed and draw and substrate concentration (S) of the FO effluent at steady state are expressed as follow:

$$Q_F = Q_{F,0} - Ja \quad (7.4)$$

$$Q_D = Q_{D,0} + Ja \quad (7.5)$$

$$C_F = \frac{Q_{F,0}C_{F,0} + J_S a}{Q_F} \quad (7.6)$$

$$C_D = \frac{Q_{D,0}C_{D,0} - J_S a}{Q_D} \quad (7.7)$$

$$S = \frac{Q_{F,0}S_0}{Q_F} \quad (7.8)$$

where $Q_{F,0}$ and $Q_{d,0}$ are the influent flow rate of the feed and draw, respectively; $C_{F,0}$ and $C_{d,0}$ are the salt concentration in the influent, respectively; S_0 is the substrate concentration in the influent; a is the membrane area. The MDC model was modified based the previous studies [131, 132]. The conversion of the substrate to acetate by the fermentative microorganisms is generalized as the conversion of glucose to acetate (Ac) [132]:

$$S \rightarrow 3Ac \quad (7.9)$$

$$D_A = \frac{Q_F}{V_A} \quad (7.10)$$

$$\frac{dS}{dt} = D_A(S - S_A) - q_{f,max}x_f \quad (7.11)$$

$$\frac{dAc}{dt} = D_A(Ac - Ac_A) - q_{e,max}\frac{S}{K_e + S}\frac{M_{OX}}{K_M + M_{OX}}x_e - q_{m,max}\frac{S}{K_m + S}x_m \quad (7.12)$$

$$\frac{dx_f}{dt} = -\mu_{f,max}\frac{S}{K_f + S}x_e - d_f x_f - D_A\frac{1 + tanh[k_{f,x}(x_f + x_e + x_m - x_{f,max})]}{2}x_f \quad (7.13)$$

$$\frac{dx_e}{dt} = -\mu_{e,max}\frac{Ac}{K_e + Ac}\frac{M_{OX}}{K_M + M_{OX}}x_e - d_e x_e - D_A\frac{1 + tanh[k_{e,x}(x_f + x_e + x_m - x_{e,max})]}{2}x_e \quad (7.14)$$

$$\frac{dx_m}{dt} = -\mu_{m,max}\frac{Ac}{K_m + Ac}x_m - d_m x_m - D_A\frac{1 + tanh[k_{m,x}(x_f + x_e + x_m - x_{m,max})]}{2}x_m \quad (7.15)$$

where D_A is the dilution rate of the anode; V_A is the anode volume; x_f, x_e and x_m are the concentrations of fermentative organisms, exoelectrogens and methanogens, respectively; $x_{f,max}$, $x_{e,max}$ and $x_{m,max}$ are the maximum attainable concentrations of fermentative organisms, exoelectrogens and methanogens, respectively; $q_{f,max}$, $q_{e,max}$ and $q_{m,max}$ are the maximum substrate consumption rates by organisms; K_f, K_e, K_m, and K_M are the half saturation concentrations for fermentative organisms, exoelectrogens, methanogens, and the redox mediators, respectively; $\mu_{f,max}$, $\mu_{e,max}$ and $\mu_{m,max}$ are the maximum growth rates of the organisms; d_f, d_e and d_m are the decay rates of the organisms; $k_{f,x}$, $k_{e,x}$ and $k_{m,x}$ are the steepness factors for fermentative organisms, exoelectrogens and methanogens for the biofilm retention. M_{OX} is the fraction of oxidized mediators per exoelectrogen, which can be described as [131]:

$$\frac{dM_{OX}}{dt} = -Y_M \frac{S}{K_e + S} \frac{M_{OX}}{K_M + M_{OX}} + \frac{\gamma}{V_A x_e} \frac{I}{F} \quad (7.16)$$

$$M_{red} = M_{tot} - M_{OX} (7.17)$$

where Y_M is the mediator yield; γ is the mediator molar mass; I is the current; M_{tot} is the total mediator fraction per microorganisms; M_{RED} is the fraction of reduced mediators per exoelectrogen and. The mass balance of the salt is expressed as follow [131]:

$$\frac{dC_S}{dt} = D_S(C_D - C_S) - d(C_S - C_A) - d(C_S - C_C) - \frac{I}{FV_S} \quad (7.18)$$

$$D_S = \frac{Q_D}{V_S} \quad (7.19)$$

$$\frac{dC_A}{dt} = d(C_S - C_A) - D_S C_A \quad (7.20)$$

$$\frac{dC_C}{dt} = d(C_S - C_A) \quad (7.21)$$

where C_S, C_A and C_S and are the salt concentrations in the salt chamber, the anode, and the cathode, respectively; D_S is the dilution rate of the salt chamber; V_S is the volume of the salt chamber; d is a membrane salt transfer coefficient that (equal to the ratio between the product of diffusion

coefficient and membrane surface area and the product of the membrane thickness and the anode volume). The internal resistance R_{in} is expressed as [375]:

$$R_{in} = R_{memebrane} + R_S + R_A + (R_{max} - R_{min})e^{-K_R x_e} \quad (7.22)$$

$$R_S = \frac{58.5C_S}{0.64}\frac{l}{\pi(r_C^2 - r_A^2)} \quad (7.23)$$

$$R_A = \frac{58.5C_A}{0.64}\frac{l}{\pi r_A^2} \quad (7.24)$$

Where $R_{membrane}$, R_S and R_A are the resistance of the AEM and CEM, the salt solution and the anolyte, respectively; r_A and r_C are the radius of the AEM and CEM tube, respectively; R_{min} and R_{max} are the lowest and highest observed internal resistance, respectively; and K_R is the constant that determines the curve steepness. The concentration overpotential η_{con} (V) in the anode is written:

$$\eta_{con} = \frac{RT}{F}\ln\frac{M_{Total}}{M_{RED}} \quad (7.25)$$

In addition, the anode potential and the cathode potential (E_A and E_C) were calculated using the Nernst equation and their difference was used as the open circuit voltage to simulate current generation (I) [182]:

$$E_A = E_A^0 - \frac{RT}{8F}\ln\frac{[Ac]}{[HCO_3^-]^2[H^+]^9} \quad (7.26)$$

$$E_C = E_C^0 - \frac{RT}{4F}\ln\frac{[OH^-]^4}{p_{O_2}} \quad (7.27)$$

$$I = \frac{E_C - E_A - \eta_{con}}{R_{ext} + R_{in}}\frac{M_{RED}}{\varepsilon + M_{RED}} \quad (7.28)$$

where E_A^0 (0.187 V vs. SHE) is the standard reduction potential of HCO_3^-/CH_3COOH^- and E_C^0 (1.23V vs. SHE) is the standard reduction potential of O_2/OH^-; both $[H^+]$ and $[OH^-]$ are fixed at 10^{-7} M because of the addition of buffer; R_{ext} is the external resistance, respectively; ε is a constant

obtained from a previous study [375]. Model fitting and parameter estimation were listed in Appendix Table D1.

7.2.3 Measurement and analysis

Conductivity was measured using a bench-top conductivity meter (FiveEasy™ conductivity, Mettler-Toledo, OH, USA). The weight change of the FO draw influent and the MDC salt chamber effluent was monitored with two digital balances (Scort Pro, Ohaus, NJ, USA) and their difference was estimated as the water flux. The effective TDS concentrations of the feed and the draw solutions (i.e. concentration in the feed and draw effluent) were calculated based on the flow rate and water flux. The current output of the MDC was monitored by measuring the voltage on the 1-Ω resistor using a digital multimeter (2700, Keithley Instruments, Inc., OH, USA) at a time interval of 2 min. The soluble COD was measured using a colorimeter according to the manufacturer's instruction (DR/890, Hach, CO, USA). Coulombic efficiency (CE) was calculated according to a previous study [358]. COD loading rate was calculated by multiplying COD concentration with the wastewater flow rate. COD removal was calculated using COD loading of the feed influent and the cathode effluent [180]. The HRT of the FO feed and draw was calculated based on the influent flow rate, and water flux was taken into account when calculating the HRT of the MDC anolyte and the salt solution. Desalination effectiveness was calculated as the percentage of conductivity reduction by the FO-MDC system. For the experiments at different flow rates, the system was operated for 12 h to reach stable current output and desalination performance before measurement.

7.3 Results and discussion

7.3.1 System performance with synthetic wastewater

The system performance was demonstrated using a synthetic wastewater and a NaCl solution at an influent flow rate of 0.6 mL min^{-1} for the feed and 0.04 mL min^{-1} for the draw (labeled as "0.6/0.04"). With water being extracted, the COD concentration in the feed increased from 325 mg L^{-1} to 368 mg L^{-1}. Figure 7.2A shows that the COD loading of the feed influent and effluent remained unchanged, indicating that the organic matters were not degraded in the feed chamber, which was different from the case of actual wastewater (in the following section), likely due to the absence of microorganisms in the synthetic wastewater. In the subsequent MDC, the COD loading

dropped to 3.5 mg h^{-1} in the anode effluent, but did not exhibit further decrease in the cathode effluent, leading to an overall COD removal of 70.6%. Meanwhile, an average current of 32.9 mA was generated with a CE of 83.6% (Figure 7.2B and Table 7.2).

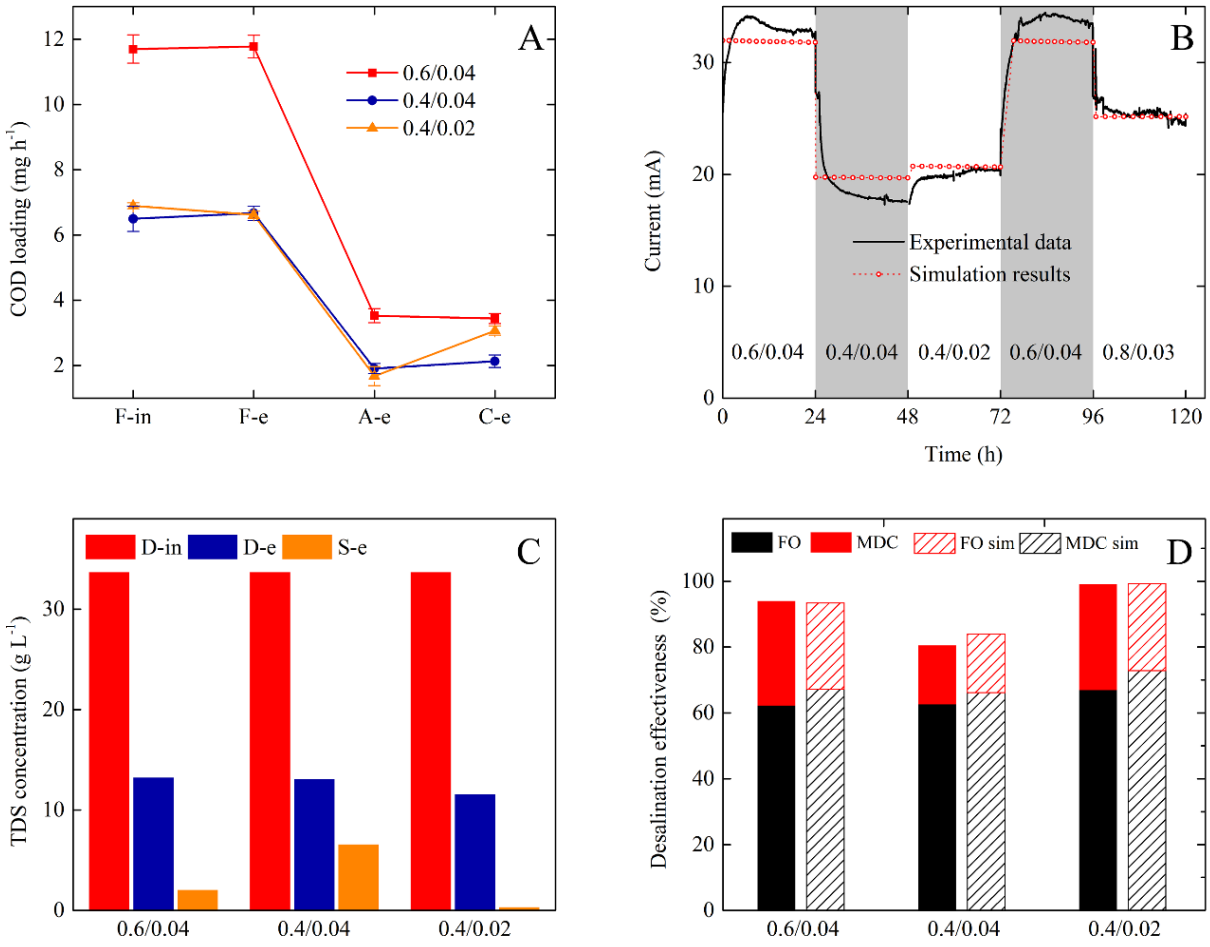

Figure 7.2 Performance of the FO-MDC system with synthetic wastewater: (A) COD loading, (B) current generation, (C) TDS concentration, and (D) desalination effectiveness at different feed/draw flow rates. D-in: FO draw influent; D-e: FO draw effluent; S-e: effluent of the MDC salt chamber; FO sim: simulated desalination effectiveness of the FO cell; and MDC sim: simulated desalination effectiveness of the MDC.

The initial TDS of the feed and the draw solution was 5.3 g L^{-1} and 35.0 g L^{-1}, respectively. Theoretically, such a salinity difference could produce a water flux up to 4 LMH (L m^{-2} h^{-1}) [376]; however, only 1 LMH was obtained in the present FO cell (Table 7.1). As described in the Model

formulation, water flux reduced salinity difference between the feed and the draw solutions, and the lower salinity difference, in turn, resulted in decreased water flux. The FO process eventually reached equilibrium where the effective concentration was 6.0 g L^{-1} for the feed and 13.2 g L^{-1} for the draw (Table 7.1 and Figure 7.2C), which explained the relatively low water flux that could also be attributed to the large chamber thickness (1 cm), inadequate mixing and the consequent concentration polarization [168]. After the MDC desalination, the TDS concentration in the effluent of the salt chamber decreased to 2.0 g L^{-1} (Figure 7.2C). The final desalination effectiveness by the FO-MDC system was estimated to be 94.0%, of which 62.3% was contributed by the FO cell (dilution effect) and 31.7% was performed by the MDC (salt removal) (Figure 7.2D). No COD was detected in the desalinated effluent from the MDC. Affected by the water flux, the flow rate of the MDC salt solution increased from 0.04 to 0.11 mL min^{-1}, resulting in an HRT in the MDC salt chamber of 11.0 h. As a result, an overall TDS reduction rate of 28.5 g L^{-1} d^{-1} was achieved (Table 7.2), which was 4 times faster than a stand-along MDC [199]. In addition to the higher desalination efficiency, the water flux increased by 40% and the COD removal was enhanced by 35% compared to that in the previous studies [179, 180], demonstrating that the FO-MDC system could effectively and efficiently treat synthetic wastewater and salt water.

Table 7.2 Performance of the MDC and the FO-MDC system under different conditions. Standard deviation is calculated with triplicate experiments.

Feed	**$Q_{F,0}$ (mL min^{-1})**	**$Q_{D,0}$ (mL min^{-1})**	**HRT_A (h)**	**HRT_S (h)**	**$Rate_{TDS}$ (g L^{-1} d^{-1})**	**COD (%)**	**I_{mean} (m)A**	**CE (%)**
Synthetic	0.6	0.04	7.8	11.0	28.5±0.0	70.5±2.2	32.9	83.6±5.1
Synthetic	0.4	0.04	12.5	10.9	24.5±0.0	67.2±1.5	18.5	81.3±3.1
Synthetic	0.4	0.02	11.6	19.3	15.8±0.0	55.5±2.6	19.9	84.6±6.8
Synthetic	0.8	0.03	5.6	13.58	22.4±0.0	81.7±2.3	24. 9	90.4±2.5
Wastewater	0.6	0.01	7.7	17.7	8.8±0.0	60.7±5.4	2.1	80.2±13.2
Wastewater + glucose	0.6	0.01	7.5	22.1	9.1±0.0	76.9±2.6	9.1	69.3±10.5

$Q_{F,0}$, influent flow rate of the feed; $Q_{D,0}$, influent flow rate of the draw; HRT_S, HRT of the salt solution in the MDC; HRT_A, HRT of the anolyte; $Rate_{TDS}$, overall TDS reduction rate of the FO-MDC system; COD%, overall COD removal by the FO-MDC system; I_{mean}, average current; CE, Coulombic efficiency.

7.3.2 Effects of the feed and draw flow rates

The influent flow rate is playing an important role in the continuous FO-MDC system because it can affect the HRT and the effluent concentration, thereby exerting effects on both COD removal and desalination. Decreasing the feed flow rate significantly decreased the COD loading of the feed influent from 11.7 mg h^{-1} (at 0.6 mL min^{-1}) to 6.5 mg h^{-1} (at 0.4 mL min^{-1}) (Figure 7.2A), and the current dropped correspondingly to around 19 mA (Figure 7.2B). As a result of the low current, the desalination effectiveness by the MDC at the feed/draw influent flow rates of 0.4/0.04 mL min^{-1} was only 17.9%, distinctly lower than the 31.7% at 0.6/0.04 mL min^{-1} (Figure 7.2D). On the other hand, decreasing the draw flow rate from 0.04 to 0.02 mL min^{-1} led to lower water flux; however, the draw solution was, in fact, more diluted and the TDS of the draw effluent (11.6 g L^{-1}) at 0.02 mL min^{-1} was lower than the 13.0 g L^{-1} at 0.04 mL min^{-1} (Figure 7.2C), because the draw HRT was twice prolonged (Table 7.1). Decreased draw flow rate also resulted in a longer HRT in the salt chamber of the MDC (19.3 h at 0.02 mL min^{-1} compared to 10.9 h at 0.04 mL min^{-1}), and consequently the desalination effectiveness of the MDC reached 32.1%, consistent with the results of a previous study that prolonged HRT favored desalination [213]. Moreover, at 0.4/0.02 mL min^{-1}, the TDS in the final effluent reached 315 mg L^{-1} (Figure 7.2C), below the maximum contaminant levels (500 mg L^{-1}) of the National Secondary Drinking Water Regulations [199].

Interestingly, with the same COD loading, the system operated at 0.4/0.02 mL min^{-1} showed slightly higher current than it did at 0.4/0.04 mL min^{-1}, which could be related to the higher catholyte conductivity. Because of the higher desalination effectiveness, the catholyte conductivity at 0.4/0.02 mL min^{-1} was measured to be 17.0±0.4 mS cm^{-1}, 23% higher than that at 0.4/0.04 mL min^{-1}. At the end of the experiments, the influent flow rates were changed to the initial 0.6/0.04 mL min^{-1}, and the current rose back to the same level, indicating that the FO-MDC system was resilient against fluctuation. These results suggest that a high feed flow rate with high COD loading is favorable for current generation, and a high draw flow rate benefits water extraction, whereas a low draw flow rate can yield satisfactory desalination performance at the expense of prolonged salt solution HRT and low TDS reduction rate.

7.3.3 Model validation and prediction

To further understand the FO-MDC system for the information that cannot be easily obtained from experiments, a mathematical model was developed based on previously developed FO and MDC

models [131, 132, 182, 185]. The model yielded slight overestimation of the water flux and underestimation of the MDC desalination. For example, at 0.6/0.04 mL min^{-1}, the model predicted a water flux of 1.13 LMH (Table 7.1), slightly higher than the experimental result (0.99 LMH). The simulation of the current generation at this flow rate was satisfactory (Figure 7.2B), and the desalination effectiveness of the MDC was 5% underestimated (Figure 7.2D). While the accuracy of the equations describing FO water flux and MDC salt removal needed to be improved, the simulation of the overall desalination effectiveness well fitted the experimental values (Figure 7.2D), demonstrating the validity of the model.

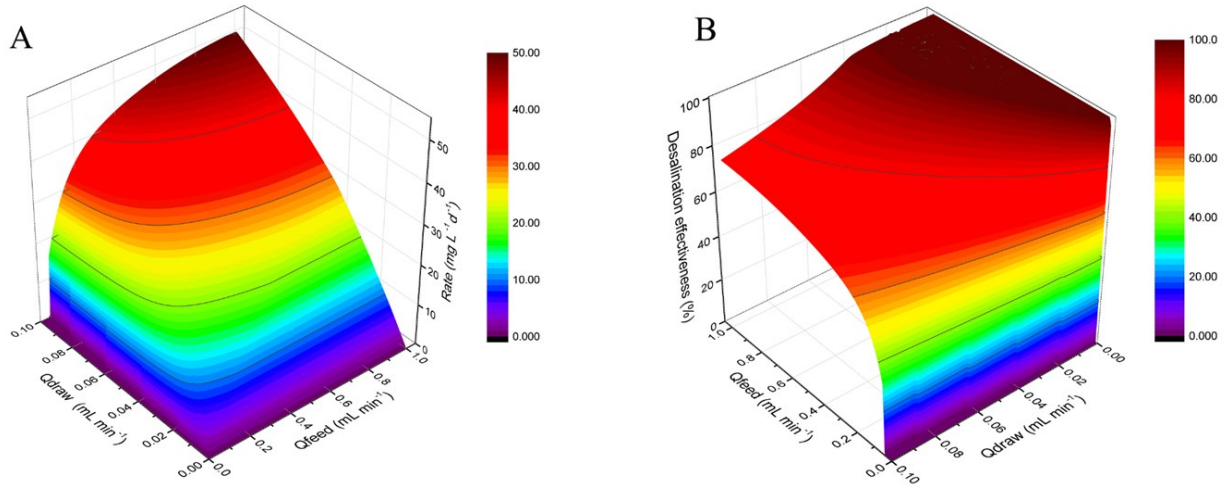

Figure 7.3 Model simulation of the FO-MDC system: (A) TDS reduction rate and (B) desalination effectiveness.

The model was used to simulate system performance at a series of feed and draw flow rates. It predicted that the TDS reduction rate could be enhanced up to 50 g L^{-1} d^{-1} at 1.0/0.1 mL min^{-1} (Figure 7.3A). Increasing the feed and draw flow rate could facilitate TDS reduction rate, but the influence of feed flow rate became less significant as it increased. These results are indicative that desalination efficiency is mainly determined by the draw flow rate. While high efficiency is desirable in practical applications, the model also predicted that TDS reduction is enhanced by increasing feed flow rate but hindered by increased draw flow rate (Figure 7.3B). The combination of the feed and draw flow rate must fall in the dark red area in order to guarantee satisfactory desalination effectiveness (Figure 7.3B). For example, at 0.6/0.06 mL min^{-1}, the effectiveness is estimated to be 83.4%, 10% lower than that at 0.6/0.04 mL min^{-1} (Figure 7.2D). This is in

agreement with the conclusion drawn from the experiments at varied flow rates that a low draw flow rate and the consequent high HRT is beneficial for overall conductivity reduction.

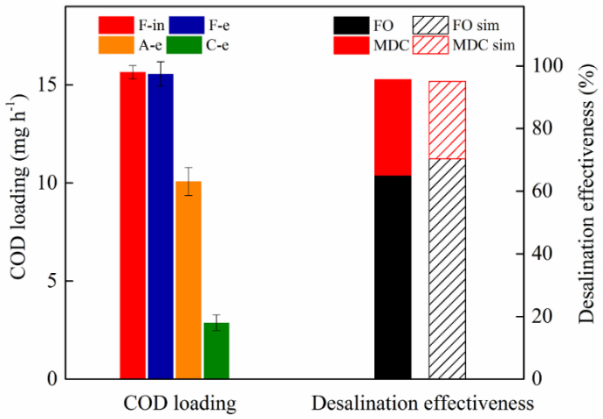

Figure 7.4 The performance of the FO-MDC system at 0.8/0.03 mL min^{-1} as a validation of the model prediction. F-in: FO feed influent; F-e: FO feed effluent; A-e: MDC anode effluent; C-e: MDC cathode effluent; FO sim: simulated desalination effectiveness of the FO cell; and MDC sim: simulated desalination effectiveness of the MDC.

To justify the prediction, the experiments and simulation at 0.8/0.03 mL min^{-1} were conducted. The COD loading of the feed influent and effluent were both 15.6 mg h^{-1}, which decreased to 10.1 mg h^{-1} in the anode effluent and further dropped to the same level at other flow rates (3 mg h^{-1}, Figure 7.4), suggesting that the excessive COD caused by the high feed flow rate could be removed by the aerobes on the cathode. Although the COD loading of the anode influent at 0.8/0.03 mL min^{-1} was high, the current was only 24.9 mA, lower than the 32.9 mA at 0.6/0.04 mL min^{-1} (Figure 7.2B). The model predicted an increased resistance of the anolyte from 8.3 Ω to 19.8 Ω when the draw flow rate is reduced from 0.04 to 0.03 mL min^{-1}, which could be the major reason of the lower simulated current. Such an increase in the anolyte resistance was because of less ion transport and accumulation from the desalination chamber into the anode chamber at higher feed flow rate and lower draw flow rate. The conductivity of the anolyte effluent at 0.8/0.03 mL min^{-1} (9.9 mS cm^{-1}) was 17% lower than that at 0.6/0.04 mL min^{-1}, consistent with the assumption. The water flux was measured to be 0.84 LMH, which was slightly overestimated by the model

simulation (Table 7.1). An overall desalination effectiveness of 95.7% and an overall TDS reduction rate of 22.4 g L^{-1} d^{-1} were achieved by the FO-MDC system, both of which were well predicted by the model. Therefore, the model can be considered reliable and may be used to predict system performance and guide the design and optimization of the FO-MDC system.

7.3.4 FO-MDC system treating domestic wastewater

According to the predicted effects of the flow rate, a relatively high feed flow rate of 0.6 mL min^{-1} and a low draw flow rate of 0.01 mL min^{-1} were used to study the treatment of actual domestic wastewater. The wastewater (primary effluent) contained an average COD concentration of 56 mg L^{-1} and thus a COD loading of the feed influent of only 2.0 mg h^{-1} (Figure 7.5A). After the FO treatment, the COD concentration increased to 66 mg L^{-1} while the COD loading remained the same, resulting in an average current of 2.1 mA and a high CE of 81.2% in the subsequent MDC (Table 7.2). With the fermentation process being included, the model predicted a current of 2.9 mA, close to the experiment. Because of the low conductivity of the wastewater (1.28±0.02 mS cm^{-1}), the draw solution (artificial seawater) was highly diluted by 10 times, leading to a TDS of 5.3 g L^{-1} in the draw effluent. Meanwhile, the wastewater's volume was reduced by approximately 10%. The simulated water flux of 0.9 LMH agreed well with the experimental result. While the water flux contributed 84.8% to the overall conductivity decrease (Figure 7.5B), which was approximately 20% high than using synthetic wastewater, the MDC removed only 3.9% of the salt, mainly attributed to the low current. The desalination effectiveness and the contribution of the individual components were well predicted by the model (Figure 7.5B).

To improve current generation and MDC desalination, the wastewater was amended with 500 mg L^{-1} glucose and 50 mM $NaHCO_3$ as the buffer. The COD loading of the feed influent increased to above 21 mg h^{-1} (Figure 7.5A), but showed 15% decrease after the FO process, indicating that organic matters were degraded during the FO treatment by the organisms that were present in the wastewater. After the anode process, 65% of the excessive COD was removed in the cathode (Figure 7.5A), consistent with the finding using synthetic wastewater at 0.8/0.03 mL min^{-1}. The average current increased to 9.1 mA (Table 7.2), but CE decreased to 69.3%, suggesting that non-exoelectrogens became more competitive at elevated COD loading. Due to the addition of bicarbonate, the influent conductivity increased to 4.54 mS cm^{-1}, and thereby reduced the water

flux to 0.64 LMH, which was precisely predicted by the model (Table 7.1). This water flux was still high given the low draw flow rate (0.01 mL min^{-1}), and the seawater was diluted to an effluent concentration of 6.6 g L^{-1}, meaning that the FO cell accounted for 81.0% of the desalination effectiveness (Figure 7.5B). Subsequently, the MDC removed 15.5% of the salt, 4 times higher than that without additional glucose. The model again yielded consistent prediction of the desalination effectiveness (Figure 7.5B). The final TDS in the salt solution effluent was about 1130 mg L^{-1}.

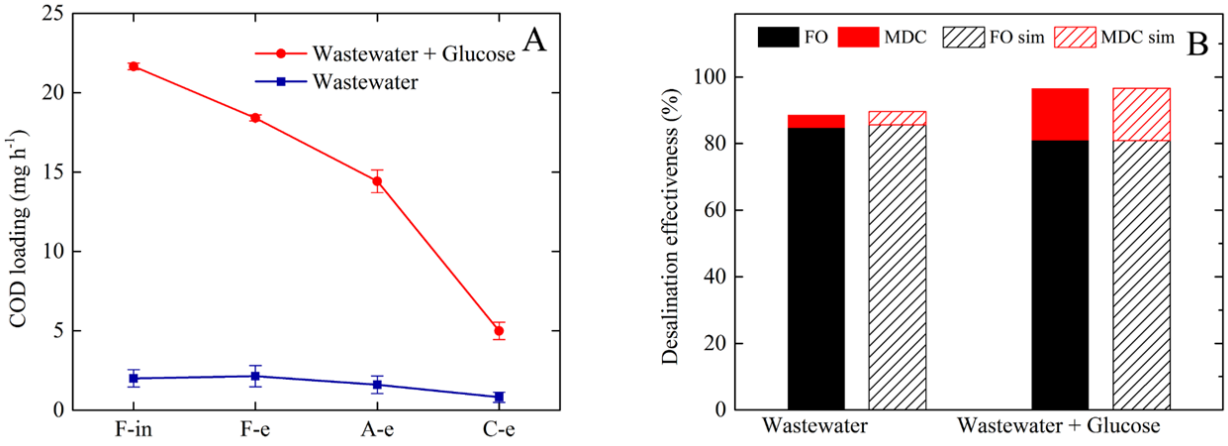

Figure 7.5 The FO-MDC system treating actual wastewater: (A) COD removal and (B) desalination effectiveness. F-in: FO feed influent; F-e: FO feed effluent; A-e: MDC anode effluent; C-e: MDC cathode effluent; FO sim: simulated desalination effectiveness of the FO cell; and MDC sim: simulated desalination effectiveness of the MDC.

3.5 Perspectives

Because water flux in the FO cell is fast and biological treatment in the MDC is slow, the HRT and the size ratio of the individual components remain a major challenge for the system integration. In a previous MDC-FO system that exhibited enhanced performance through coupling, effective cooperation between the individual component was not accomplished as the fast FO process produced more feed effluent than that the MDC could treat [180]. Its results suggest that, to guarantee adequate MDC HRT, the volume of the MDC should be significantly larger than that of the FO cell. Based on this rationale, the present study achieved proper coordination of wastewater treatment and seawater desalination between the FO cell and the MDC in a continuously-operated

mode, thereby further demonstrating the technical feasibility of this integrated system. The developed mathematical model has, for the first time, integrated FO model with MDC model for accurate prediction of system performance. The model can reveal the response of several key parameters (e.g. current and internal resistance) with varied operational conditions and thus may guide further development of the present system for optimized operation and configuration.

The present system can achieve wastewater reuse through two membrane-based processes. High-quality water is extracted from wastewater by the FO process, and salts are removed by the MDC process. Although the MDC has a slow salt removal process, the water production rate may not be negatively affected because of water recovery from wastewater. The present system recovered five volumes of clean water with one volume of seawater. In addition, reverse salt flux, which is a serious problem in the FO process, will not be a critical issue in the present system, because salts are expected to be removed from seawater into wastewater (effluent). Because of the low desalination rate, MDCs are commonly considered as a pretreatment process [310]. This study shows that the FO-MDC system can produce high-quality effluent for direct reuse at a relatively short HRT. Further improvement of the present system can be conducted from a few aspects: 1) to enhance energy efficiency, the FO cell can be operated at PRO (pressure retarded osmosis) mode, in which energy can be generated by pressurizing the diluted draw solution through a hydroturbine [377], and such energy may be used to drive organic removal and energy production in bioelectrochemical treatment [182]; 2) desalination performance of the MDC can be improved by applying an external voltage, which can also result in hydrogen production [378]; 3) membrane fouling, though not being studied here, is always a critical issue in membrane-based treatment systems and will be studied for long-term operation of the present system with actual wastewater and seawater; 4) the MDC cathode effluent contains relatively high salinity and low biomass [11], and thus may be discharged to where saline water comes from, but its potential environmental impacts warrant further investigation; and 5) when modified wastewater was used, glucose were degraded in the feed chamber and $NaHCO_3$ decreased water flux, and thus they should be added after the FO process in future studies.

7.4 Conclusions

A continuously-operated FO-MDC system was developed for simultaneous wastewater treatment and seawater desalination. The system has exhibited satisfactory COD removal and high desalination effectiveness. A high feed flow rate led to high COD loading, which was favorable for current generation and salt removal. A high draw flow rate was beneficial for water flux and TDS reduction by the FO cell, whereas a low draw flow rate prolonged salt solution HRT and thus resulted in high overall desalination effectiveness. The integrated mathematical model was used to simulate system performance at varied flow rates and the results agreed well with the experiments. The system was further demonstrated with real wastewater and artificial seawater. The results have collectively demonstrated that the present FO-MDC system has a potential for reducing wastewater discharge and improving reuse through combined water recovery and desalination.

CHAPTER 8: Bioelectrochemical Production of Hydrogen in an Innovative Pressure Retarded Osmosis – Microbial Electrolysis Cell System: Experiments and Modeling

(This section has been published as: Heyang Yuan, Yaobin Lu, Ibrahim M. Abu-Reesh, and Zhen He. "Bioelectrochemical production of hydrogen in an innovative pressure retarded osmosis/microbial electrolysis cell system: experiments and modeling." Biotechnology for Biofuels (2015): 8, 1-12.)

8.1 Introduction

Microbial electrolysis cells (MECs) is an attractive technology that can simultaneously remove organics and produce hydrogen gas. In MECs, exoelectrogens growing on the anode respire by releasing electrons extracellularly; driven by an external voltage > 0.2 V, those electrons flow to the cathode to reduce protons into hydrogen gas [86]. MECs are of strong interests to hydrogen production because its energy consumption could be significantly lower than that of conventional methods such as water-splitting and steam reforming [379, 380]. Life cycle assessment suggested that MECs might outperform the prevailing wastewater treatment methods (i.e. activated sludge process and anaerobic digester) in terms of energy requirement, greenhouse gas effect and other environmental impacts [13, 381]. However, the requirement of additional energy, which is mostly from fossil fuels, should be further addressed to make MECs more sustainable.

Researchers have explored alternative energy sources to drive hydrogen production in MECs. For example, a microbial fuel cell (MFC) was used to replace the external power supply and provided a voltage to achieve a hydrogen production rate of 0.015 m^3 m^{-3} d^{-1} in an MFC-MEC coupled system [382]. It was found that the hydrogen yield was relatively low and also unstable in this coupled system, possibly due to cell voltage reversal between the two bioelectrochemical systems (BES). To avoid voltage reversal, a capacitor circuit was installed between MFCs and an MEC, and helped achieve 38% higher hydrogen production rate compared to the directly coupled system [383]. In another study, solar energy was harvested by a dye-sensitized solar cell and then applied on an MEC, which achieved a hydrogen production rate of 0.07 m^3 m^{-3} d^{-1} [384]. The entropic energy stored in a salinity gradient between seawater and fresh water is estimated to be 0.8 kW m^{-3} [181, 385], which could be captured by reverse electrodialysis and then used to drive MECs [386-388].

Unlike salinity energy that relies on salt movement, osmotic energy can be produced through water interaction between saline water and fresh water, and can be harvested by using pressure retarded osmosis (PRO). In a PRO system, water is driven by the salinity gradient and diffuses from a low-salinity solution (feed) to a high-salinity solution (draw) through a semi-permeable membrane; consequently, electrical energy is generated by pressurizing the diluted draw (whose volume becomes larger after water extraction) through a hydroturbine [377]. As a forward osmosis (FO) process, PRO shows low fouling propensity compared to reverse osmosis because of relatively low water flux and hydraulic pressure [170]. The capital cost of PRO is estimated to be competitive with other renewable energy sources, benefited from the advances in membrane technology in recent years [389]. The highest power density produced by PRO was reported to be 10.6 W m^{-2} with 1 M NaCl solution as draw [390].

We have previously integrated osmotic processes with BES to assist with bioelectricity generation in MFCs or desalination in microbial desalination cells (MDCs) [391]. For example, the first osmotic microbial fuel cell (OsMFC) was developed by replacing the ion exchange membrane with an FO membrane, and accomplished simultaneous wastewater treatment, water extraction, and bioenergy production [172]. The performance of an OsMFC was affected by its draw solution, membrane condition, anode substrates, and cathode reactions [138, 173, 174]. The osmotic process was integrated with MDCs in several ways: replacement of anion exchange membrane with an FO membrane to create an osmotic MDC, linking an OsMFC with an MDC, or connecting an FO to an MDC [178-180]. Those prior studies have demonstrated the synergy between BES and FO, and provided a foundation for the present study.

Given the fact that PRO can generate electric energy and MECs need additional energy for hydrogen production, a PRO-MEC system is proposed here: wastewater (feed) and seawater (draw) flow into a PRO unit for water extraction and energy generation; then, the energy is applied to an MEC for organic removal and hydrogen production, with the PRO feed and draw effluents serving as the anolyte and the catholyte of the MEC, respectively (Figure 8.1). This is the first time that the PRO energy (osmotic-to-electricity) is studied to drive the conversion of organic compounds to hydrogen in an MEC; in addition to the electrical interaction between the two

components, this system also contains hydraulic linkage between the two for wastewater treatment and reuse and saline water desalination. After further desalination, the produced water (diluted draw solution) could be useful for non-potable applications such as agricultural irrigation and landscaping. The system may have application niches in a location with seawater and a high demand for wastewater reuse.

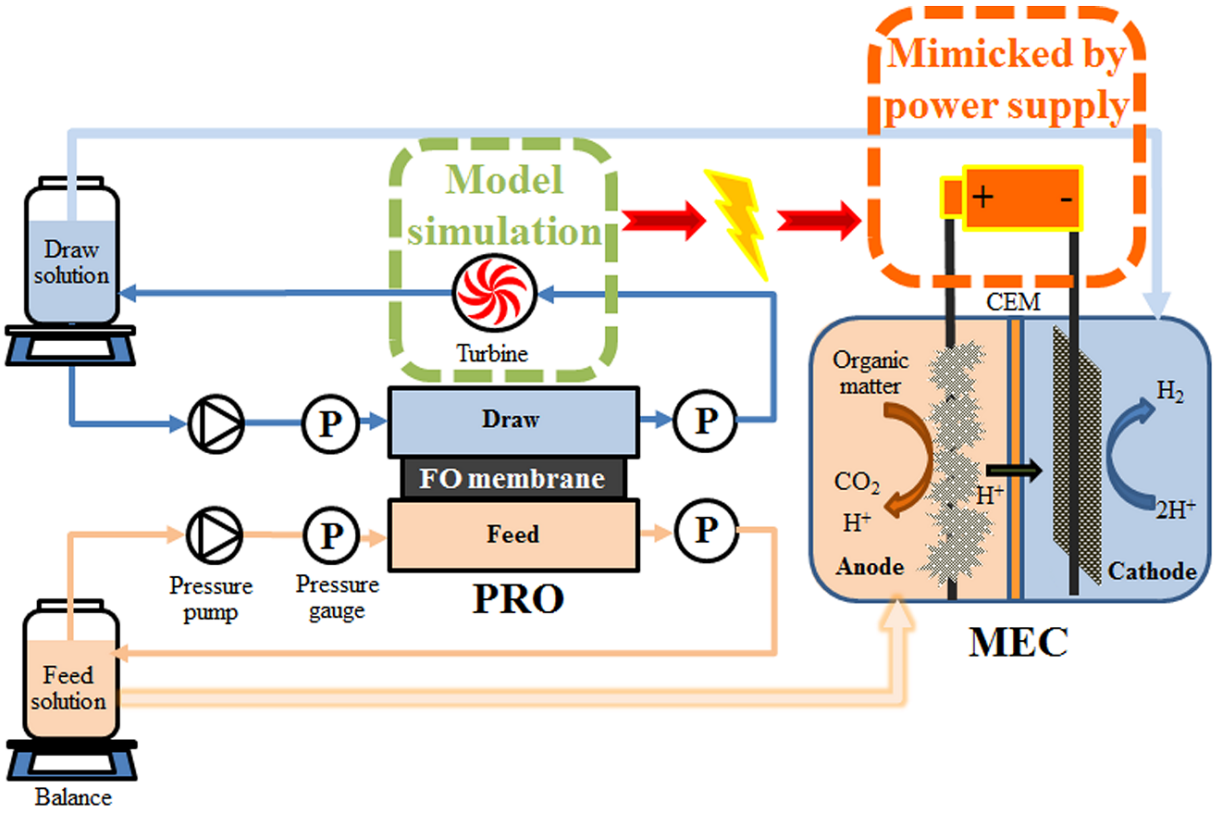

Figure 8.1 Schematic of the proposed system consisting of a PRO unit and an MEC through the hydraulic connection.

To examine the proposed system, we first developed a time-dependent PRO model and a batch-model MEC model. According to the simulated water flux obtained from the PRO model, the anolyte and the catholyte were prepared for an MEC that was operated experimentally using a power supply to mimic the energy supply process. The system feasibility was demonstrated by comparing the simulated PRO energy production and the experimental MEC energy consumption, together with other parameters such as water extraction, organics removal and hydrogen

production. Finally, the PRO and MEC models were used to predict the system performance at varied influent volume, draw concentration and external voltage.

8.2 Materials and methods

8.2.1 System setup and operation

The experimental system consisted of a PRO unit and an MEC, as shown in Figure 8.1. A forward osmosis (FO) cell (Sepa CF II Forward Osmosis Cell 316 SS, Sterlitech Corporation, USA) was used as the PRO unit, containing an FO membrane (HTI OsMem™ CTA-ES, Hydration Technology Innovations, USA) tailored to an area of 0.014 m^2. The feed solution contained (per liter of deionized water): sodium acetate, 193 mg; NaCl, 0.5 g; $MgSO_4$, 0.015 g; $CaCl_2$, 0.02 g; KH_2PO_4, 1.06 g; K_2HPO_4, 2.14 g; $NaHCO_3$, 1 g; and trace element, 1 mL. A synthetic organic solution was used because it could be better controlled for organic concentrations and other parameters. The feed solution (600 mL, $\pi_{F,0}$ = 2.4 bar) was recirculated between a reservoir and the PRO feed chamber by a peristaltic pump (Langer Instruments Corp., USA) at a cross-flow velocity of 16.4 cm s^{-1}. The NaCl solution (0.8 M, 600 mL, $\pi_{D,0}$ = 48.8 bar) was used as a draw and recirculated between a reservoir and the PRO draw chamber by a high-pressure water pump (Estone 12V DC 5L/min 60W, China) at a cross-flow velocity of 85.9 cm s^{-1}. Low hydraulic pressures (1, 2 and 3 bars) were applied on the draw chamber of the PRO cell using a pressure valve at the outlet and monitored with two gauges at both inlet and outlet. The PRO unit was operated for 6.0 h as a batch, and the weight change in both feed and draw solutions was monitored by using digital balances (Scort Pro, Ohaus, USA).

A two-chamber MEC was built as previously described [88], with a carbon-brush anode electrode and a carbon-cloth cathode electrode that contained 5 mg cm^{-2} of Pt/C and a surface area of 10 cm^2. The anode was inoculated with anaerobic sludge from a local wastewater treatment plant (Peppers Ferry, Radford, VA, USA). The liquid volumes of the anode compartment and the cathode compartment of the MEC were equal at 140 mL/each. Those electrolytes were recirculated between the MEC and the external reservoirs. An external voltage of 0.8 V was applied on the MEC with a power supply (3644A, Circuit Specialists, Inc., USA) to mimic the utilization of the energy from the PRO unit. The electrolytes were prepared as shown in Table 8.1 and purged with nitrogen gas for 15 min prior to each test. The MEC was operated under a batch mode at room

temperature. The operation time of the MEC was determined by equating the PRO energy production with the MEC energy consumption by assuming no energy loss during energy conversion process. In both the PRO and MEC experiments, triplicate experiments were conducted for each test condition. The system at different PRO influent volumes, NaCl concentrations and external voltages was evaluated with the time-dependent PRO model and the batch-mode MEC model.

8.2.2 Measurement and analysis

Weight change of the feed and draw solutions was recorded by an auto logging software (Scort Pro, Ohous, USA) at a timer interval of 2 min. Water flux was calculated as derivative of the volume change. Conductivity was measured by using a bench-top conductivity meter (Mettler-Toledo, USA). The voltage (U) of the MEC on a resistor (R = 1 Ω, HARS-X-3_0.001, USA) was recorded by a digital multimeter (2700, Keithley Instruments, Inc., USA) at a time interval of 5 min. The current was calculated according to the Ohm's law: $i = U/R$. Hydrogen produced by the MEC was collected using water displacement method and the volume was measured with a syringe. COD was measured using a DR/890 colorimeter (HACH Co., Ltd., USA) according to manufacturer's instruction. Organics (acetate) concentration in the effluent was calculated by dividing the COD by the empirical coefficient of 0.78. The pH was measured by a benchtop pH meter (Oakton Instruments, USA). Important MEC parameters were calculated as previously described [88]. Hydrogen production rate was calculated based on the catholyte volume, which was obtained from the PRO simulation.

8.2.3 Time-dependent PRO model

The time-dependent water flux was simulated based on the PRO model developed by Yip, Tiraferri [392]:

$$J_t = A\left\{\frac{\pi_{D,t}\exp\left(-\frac{J_t}{k}\right) - \pi_{F,t}\exp\left(\frac{J_t S}{D}\right)}{1+\frac{B}{J_t}\left[\exp\left(\frac{J_t S}{D}\right) - \exp\left(-\frac{J_t}{k}\right)\right]} - P_t\right\} \quad (8.1)$$

where J_t (m^3 m^{-2} s^{-1}) is the instantaneous water flux at time t, $\pi_{D,t}$ and $\pi_{F,t}$ (bar) are the osmotic pressure of the bulk draw and feed solution at time t, respectively, A (m^3 m^{-2} s^{-1} bar^{-1}) is the permeability coefficient, B (m^3 m^{-2} s^{-1}) is the salt permeability coefficient, S (m) is the support layer structural parameter, D (m^2 s^{-1}) is the diffusion coefficient of NaCl in the membrane substrate, k (m^3 m^{-2} s^{-1}) is the mass transfer coefficient, and P_t (bar)is the hydraulic pressure applied to the draw chamber at time t. The real-time volume of the feed ($V_{F,t}$) and draw ($V_{D,t}$) are thus:

$$V_{F,t} = V_{F,0} - \int J_t dt \quad (8.2)$$

$$V_{D,t} = V_{D,0} + \int J_t dt \quad (8.3)$$

where $V_{F,0}$ and $V_{D,0}$ (L) are the initial feed and draw volume. The reverse salt flux $J_{S,t}$ (mol m^{-2} s^{-1}) can be approximated as [374]:

$$J_{S,t} = \frac{BJ_t}{AiRT} \quad (8.4)$$

where i is the number of dissolved species (2 for NaCl), R (8.3145 J mol^{-1} K^{-1}) is the ideal gas constant, and T (298.15 K) is the absolute temperature. According to the van't Hoff equation: $\pi = iRTC$, where C (M) is the molar concentration, the real-time osmotic pressure is obtained by combining Equation 8.1-8.4:

$$\pi_{F,t} = iRT\left(\frac{V_{F,0}C_{F,0} + a\int J_{S,t}dt}{V_{F,t}}\right) \quad (8.5)$$

$$\pi_{D,t} = iRT\left(\frac{V_{D,0}C_{D,0} - a\int J_{S,t}dt}{V_{D,t}}\right) \quad (8.6)$$

where a (0.014 m^2) is the membrane area, $C_{F,0}$ (M) is the initial salt concentration in the feed solution obtained by multiplying the conductivity (mS cm^{-1}) by the empirical coefficient of 0.64 ppm and dividing the result by the molecular weight of NaCl (58.5 g mol^{-1}), and $C_{D,0}$ (M) is the initial NaCl concentration. It can be derived from the expression of power density and ideal water

flux that the maximum power is generated when $P = (\pi_D - \pi_F)/2$ [389]. In order to maintain the maximum energy production Q_{PRO} (joule) during the PRO process, the instantaneous hydraulic pressure applied on the draw chamber in Equation 8.1 is calculated as:

$$P_t = \frac{(\pi_{D,t} - \pi_{F,t})}{2} \quad (8.7)$$

$$Q_{PRO} = a \int P_t J_t dt \quad (8.8)$$

8.2.4 Batch-mode MEC model

The batch-mode MEC model was modified based on previously reported multi-population MEC model and MDC model [131, 132, 375]. Because acetate was used as the substrate and the cathode chamber is abiotic, it was assumed that the anode biofilm was composed of acetoclastic methanogens and exoelectrogens. Moreover, the MEC was operated under a batch mode and thus the dilution rate used in the previous study is not applicable [131]. The mass balance for the substrate and the growth of the organisms can be written:

$$\frac{dS}{dt} = -q_{e,max} \frac{S}{K_e + S} \frac{M_{OX}}{K_M + M_{OX}} x_e - q_{m,max} \frac{S}{K_m + S} x_m \quad (8.9)$$

$$\frac{dx_e}{dt} = -\mu_{e,max} \frac{S}{K_e + S} \frac{M_{OX}}{K_M + M_{OX}} x_e - d_e x_e \quad (8.10)$$

$$\frac{dx_m}{dt} = -\mu_{m,max} \frac{S}{K_m + S} x_m - d_m x_m \quad (8.11)$$

$$\frac{dM_{OX}}{dt} = -Y_M \frac{S}{K_e + S} \frac{M_{OX}}{K_M + M_{OX}} + \frac{\gamma}{V_a x_e} \frac{I}{nF} \quad (8.12)$$

where S (mg-S L^{-1}) is the acetate concentration, x_e and x_m (mg-x L^{-1}) are the concentrations of exoelectrogens and methanogens, respectively, $q_{e,max}$ and $q_{m,max}$ (mg-S mg-x^{-1} day^{-1}) are the maximum substrate consumption rates by organisms, K_e, K_m, and K_M (mg-S L^{-1}, mg-S L^{-1}, and mg-M mg-x^{-1}) are the half saturation concentrations for exoelectrogens, methanogens, and the redox mediators, respectively, $\mu_{e,max}$ and $\mu_{m,max}$ (day^{-1}) are the maximum growth rates by the organisms,

d_e and d_m (day^{-1}) are the decay rates of the organisms, M_{OX} (mg-M mg-x^{-1}) is the fraction of oxidized mediators per exoelectrogen, Y_M (mg-M mg-S^{-1}) is the mediator yield, γ (mg-M mole-M^{-1}) is the mediator molar mass, I (A) is the current through the circuit of the MEC, F (96485 C mol^{-1}) is the Faraday constant, n (2) is number of electrons transferred per mole of mediator, V_a (L) is the anolyte volume. The anode and cathode potential E_A and E_C (V) are calculated with the Nernst equation [113]:

$$E_A = E_A^0 - \frac{RT}{8F}\ln\frac{S}{[HCO_3^-]^2[H^+]^9} \quad (8.13)$$

$$[HCO_3^-] = [HCO_3^-]_0\frac{V_{F,0}}{V_F} + \frac{2(S_0 - S)}{m_S} \quad (8.14)$$

$$\frac{d[H^+]}{dt} = \frac{\beta}{m_S}\frac{dS}{dt}(9 - 8\cdot CE\cdot Y_{H2}) \quad (8.15)$$

$$E_C = E_C^0 - \frac{RT}{2F}\ln\frac{1}{(10^{-11})^2} \quad (8.16)$$

where E_A^0 (0.187 V) is the standard reduction potential of HCO_3^-/CH_3COOH^- and E_C^0 (0V) is the standard reduction potential of H^+/H_2, $[HCO_3^-]_0$ (0.00012 M) is the initial bicarbonate concentration in the feed influent, $V_{F,0}$ and V_F (L) are the initial and final volume of the PRO feed, S_0 and S (mg L^{-1}) are the initial and final acetate concentration in the PRO feed, m_S (82 g mol^{-1}) is the molar weight of acetate, β (%) is the buffer efficiency of the anolyte, CE (%) is the coulombic efficiency and Y_{H2} (%) is the cathodic efficiency. The rationale of Equation 8.15 is that every mole of the acetate produces 9 moles of protons and 8 moles of electrons. With $8\cdot CE$ moles of electrons being transferred to the cathode, $8\cdot CE\cdot Y_{H2}$ moles of protons migrate and diffuse to the cathode and are reduced to H_2, leaving the residual protons to affect the anolyte pH. The cathode potential is assumed to be stable and calculated with a pH value of 11 (10^{-11} in Equation 8.16 as proton concentration) because no buffer is added in the draw solution/catholyte, and the pH increased from neutral to 11.64±0.02 in the first three hours and remained stable throughout the MEC experiments. At batch mode, the concentration overpotential η_{con} (V) in the anode is determined by both the mediator concentration and the substrate concentration, and thus can be written:

$$\eta_{con} = \frac{RT}{F} \ln \frac{M_{Total}}{M_{Total} - M_{OX}} \frac{S_0}{S} \quad (8.17)$$

where M_{total} (mg-M mg-x^{-1}) is the total mediator fraction per exoelectrogen. Combining Equation 8.13-8.17 yields the MEC current, the energy consumption Q_{MEC} (joule) and the hydrogen production V_{H2} (mL):

$$I = \frac{(E_C - E_A) + E_{ext} - \eta_{con}}{R_{ext} + R_{in}} \frac{M_{Total} - M_{OX}}{\varepsilon + M_{Total} - M_{OX}} \quad (8.18)$$

$$Q_{MEC} = E_{ext} \int I dt \quad (8.19)$$

$$V_{H2} = Y_{H2} \frac{I}{2F} \frac{RT}{P} \quad (8.20)$$

where E_{ext} (V) is the external voltage applied on the MEC, R_{ext} (Ω) is the external resistance, ε (0.0001 mg-M mg-x^{-1}) is a constant from a previous study [375], P (1 atm) is the air pressure in the cathode and R_{in} (Ω) is the internal resistance [375]:

$$R_{in} = R_{min} + (R_{max} - R_{min}) e^{-K_R x_e} \quad (8.21)$$

where R_{min} (Ω) is the lowest observed internal resistance, R_{max} (Ω) is the highest observed internal resistance, and K_R (L mg-x^{-1}) is the constant that determines the curve steepness.

8.2.5 Parameter estimation

The parameters were estimated as previously described and listed in the Table E1 [131]. The relative root-mean square error (RMSE) as a measure of the discrepancy between the experimental data and the simulation results was calculated:

$$RMSE = \frac{\sqrt{\frac{\sum_{i=1}^{N} (y_i - \hat{y}_i)^2}{N}}}{\hat{y}_{i,max}} \quad (8.22)$$

where N is the total sampling time points in the simulation; $\hat{y}_i$ and y_i are experimental data and model predicted values at t, respectively; and $\hat{y}_{i,max}$ is the maximum value of the experimental data. The RMSE of the PRO model was calculated using the feed volume, and that of the MEC model was calculated using electricity.

8.3 Results and discussion

8.3.1 Model Validation

Mathematical modeling can help understand the key factors in the PRO-MEC system and predict the behaviors that cannot be easily investigated by experiments. Previous PRO studies focused on achieving instantaneous maximum energy production, and it was not necessary to take the concentration change of the feed and the draw into account because of the constant replenishment of fresh solutions to maintain high osmotic pressure difference [392, 393]. However, that is not applicable to a PRO-MEC system, because that the relatively fast PRO process will generate an excessive amount of effluent that can exceed the treating capacity of bench-scale MECs. In this regard, the PRO unit must be operated in a batch mode and the time variable must be introduced in the PRO model to predict the water flux and energy production. To examine that hypothesis, the PRO unit was operated for 6.0 h at different hydraulic pressures (1, 2 and 3 bars) with the initial conditions listed in Table 8.1. At 1 bar, the feed solution decreased from 600 mL to 138 mL (462 mL of water recovery) with a significant decrease in water flux (Figure E1). The experiments at 2 and 3 bar showed similar trends, but with slightly lower water recovery due to the higher hydraulic pressure (Figure E1). With the PRO parameters listed in the Table E1, the time-dependent PRO model successfully predicted the volume profile with RMSE less than 2.5% (Table 8.2). The experiments with different NaCl concentrations (0.5 and 2.0 M) at 1 bar were conducted to further validate the model. After 5.0-h operation, the feed volume decreased from 600 mL to 452 mL with 0.5 M (148 L water recovery, Figure E2), 65% lower than that with 0.8 M at the same operation time because of the lower osmotic pressure difference between the feed and the draw. On the other hand, water recovery rapidly reached 315 mL in 2.0 h with 2.0-M NaCl solution (Figure E2). The results collectively demonstrated that the time-dependent PRO simulation agreed well with the experimental data (Table 8.2).

Based on the method presented in previous studies of MDC and MEC modeling [131, 132], a batch-mode MEC model was implemented with independent experiments of varied substrate and external resistance. The introduction of [HCO_3^-] and [H^+] into the anode potential (Equation 8.14 and Equation 8.15) and the substrate change in the concentration overpotential (Equation 8.17) helped achieve satisfactory agreement between the experimental and simulation results. The RMSE for the MEC model (Table 8.2) was relatively high mainly due to the overestimation of organics removal (99.9% removal) at the end of the MEC process. Consequently, at 0.8 V, the model yielded slightly higher energy consumption (488 joules) and hydrogen production (36.7 mL) compared to the experiments (470 joules and 32.8 mL). The MEC's operation time was prolonged from 19.2 h at 357 mg L^{-1} acetate to 96.1 h at 2,007 mg L^{-1} acetate (Figure E3). When the external voltage was increased, the current was improved from 2.7 mA at 0.6 V to 6.6 mA at 1.0 V (Figure E3) with 60% increase in Coulombic efficiency and 40% increase in cathodic efficiency (Table 8.3). As a result, both hydrogen production and energy consumption increased by two times. The experimental results are consistent with previous studies [394]. In summary, the simulated current generation under different conditions could match the experimental data, with slight overestimation of organics removal, energy consumption and hydrogen production.

Table 8.1 Initial conditions for the PRO experiments and simulation in different studies.

Experiment	**V_{PRO}** (mL)	**S_{PRO}** (mg L^{-1})	**$NaCl_{In}$** (M)	**P** (bar)	**V_A** (mL)	**V_C** (mL)	**S_A** (mg L^{-1})	**V** (V)
Exp1-System feasibility	600	193	0.8	P_t	115	1085	1007	0.8
Exp2-Model validation	600	193	0.5, 0.8 and 2.0	1, 2 and 3	115	1085	357, 1006 and 2007	0.6, 0.8 and 1
Exp3-PRO influent volume	100-2000	193	0.8	P_t	Obtained from the time-dependent			0.8
Exp4-NaCl concentration	600	193	0.1 - 2.0	P_t	PRO model			0.8
Exp5-External voltage	600	193	0.8	P_t	115	1085	1007	0.5-1.1

V_{PRO}, Volume of PRO feed and draw influent; S_{PRO}, Substrate concentration in the PRO feed influent; $NaCl_{In}$, NaCl concentration in the PRO draw influent; P, Hydraulic pressure applied on the PRO draw chamber; V_A, Volume of MEC anolyte influent; V_C, Volume of MEC catholyte influent; S_A, Substrate concentration in the MEC anolyte influent; V, External voltage applied on the MEC.

Table 8.3 The MEC performance at three different external voltages. The standrad deviation was calculated with triplicate experiments.

Voltage (V)	**S_{In}** (mg L^{-1})	**C_{In}** mS cm^{-1}	**V_{H2}** (mL)	**$Rate_{H2}$** m^3 m^{-3} d^{-1}	**ΔS** (%)	**R_{CE}** (%)	**R_{cat}** (%)	**Energy** (joule)	**HRT** (h)
0.6	1009±31	19.5±0.8	18.4±0.9	0.008±0.001	95.6±0.0	36.1±0.0	42.9±0.0	221±7	54.4±2.3
0.8	1009±8	18.3±0.1	32.8±0.6	0.016±0.001	93.7±0.0	57.5±0.0	48.1±0.0	470±2	46.9±1.4
1.0	987±53	19.9±1.5	40.8±2.8	0.030±0.005	94.7±0.0	58.3±0.0	60.7±0.1	581±22	30.9±3.2

S_{In}, Substrate concentration in the MEC influent; C_{In}, Conductivity of the MEC influent; V_{H2}, Total H_2 production; ΔS, organics removal; R_{CE}, Coulombic efficiency; R_{cat}, Cathodic efficiency.

Table 8.2. RMSE for the PRO and MEC simulation. The standrad deviation was calculated with triplicate experiments.

		RMSE
PRO	1 bar-feed	1.8±0.3%
	1 bar draw	0.8±0.0%
	2 bar-feed	1.9±0.6%
	2 bar draw	0.8±0.0%
	3 bar-feed	0.9±0.1%
	3 bar draw	2.4±0.6%
	0.5 M feed	1.90±0.2%
	0.5 M draw	0.94±0.0%
	2.0 M feed	1.40±0.3%
	2.0 M draw	0.78±0.0%
MEC	0.6 V	16.5+5.6%
	0.8 V	13.0±2.3%
	1.0 V	23.6+1.3%
	357 mg L^{-1}	12.1%
	2007 mg L^{-1}	21.6%

8.3.2 System Feasibility

The feasibility of the PRO-MEC system was demonstrated by estimating energy production in the PRO unit using the models and applying the energy (mimicked by a power supply) to the MEC for hydrogen production and organic removal. It should be noted that, because of the difficulty in generating real energy from bench-scale PRO units at a high hydraulic pressure, the majority of the PRO studies or publications adopted theoretical estimate of energy production [395-398]. The results showed that the PRO unit could theoretically generate sufficient energy to drive the MEC, which successfully produced hydrogen gas and removed more than 90% of organic compounds. In more details, the PRO simulation was performed at the hydraulic pressure of $P_t = (\pi_{D,t} - \pi_{F,t})/2$ (Equation 8.7, at the maximum energy mode), and was stopped when water flux dropped below 0.5 LMH (L m^{-2} h^{-1}). This is because that after 14.5 h of simulation, P_t decreased to 2.4 bars and both the volume and the energy production reached a plateau (Figure 8.2A). At the end of the simulation, the volume of the feed solution decreased from the initial 600 mL to 115 mL and the draw volume increased to 1085 mL, suggesting that 485 mL of clean water was extracted from the feed solution. Meanwhile, the PRO unit could produce a feed effluent containing 1007 mg L^{-1} acetate, a draw effluent with 0.46 M NaCl, and 579 joules of energy (Table 8.1 and Figure 8.2A).

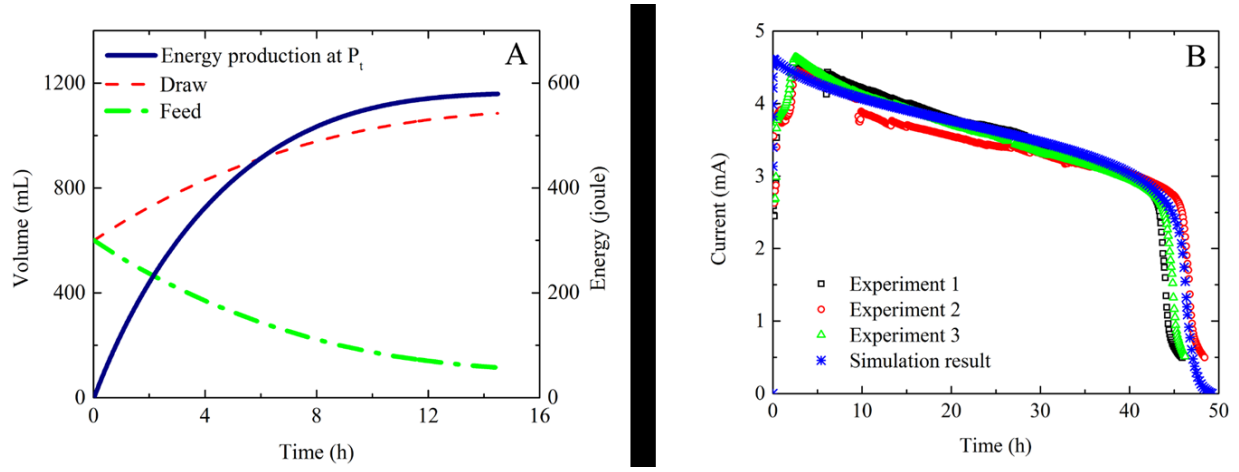

Figure 8.2 (A) Volume profile and energy production in the PRO unit at the hydraulic pressure $P_t = (\pi_{D,t} - \pi_{F,t})/2$; (B) experimental data and simulation result of the current generation in the MEC at 0.8 V using electrolyte and energy produced by the PRO unit.

Based on those results obtained from the PRO simulation, 115 mL of anolyte with 1009±8 mg L^{-1} acetate and 1085 mL of the catholyte with the 0.46 M NaCl were prepared and supplied to the MEC (Table 8.1). An external voltage of 0.8 V was applied to the MEC to mimic the utilization of the energy produced by the PRO unit. The MEC operating time was determined by equating the PRO energy production with the MEC energy consumption (Equation 8.8 and Equation 8.19). The MEC current decreased steadily over time (Figure 8.2B), mainly due to the consumption of organic compounds. At the end of the experiment, the MEC removed 93.7% of the organics and produced 32.8 mL of H_2 at the expense of 470 joules of energy after 46.9 h (Table 8.3), indicating that the energy produced by the PRO unit (579 joules) was sufficient to drive the MEC. The relatively low hydrogen production rate (0.016 m^3 m^{-3} d^{-1}) and cathodic efficiency (48.1%) was probably because no buffer was added in the catholyte (the pH increased from neutral to 11.6 after 3.0 h of operation). Coulombic efficiency (57.5%) was comparable with other MECs, likely benefited from a relatively high organics concentration and conductivity of the anolyte, which was the concentrated feed solution from the PRO unit. Similar to the substrate concentration, the conductivity in the feed was concentrated by 5.2 times due to water extraction in the PRO unit, resulting in an initial conductivity of 18.3 mS cm^{-1} in the MEC anolyte. All those results have demonstrated that it is possible to harvest osmotic energy in the PRO unit and use it to convert chemical energy into

hydrogen gas in the MEC from the same organic solution. In addition, the coupling of PRO and MEC can simultaneously recover clean water and reduce the volume of the organic solution.

8.3.3 Model Prediction

Effects of PRO influent volume. In theory, the osmotic pressure difference will be less affected by the water flux at larger volumes of the feed and the draw solutions, leading to a prolonged PRO process and more energy available for driving the MEC. This hypothesis was examined with the PRO influent volume varied from 100 to 2000 mL (simultaneous change in both the feed and the draw volumes), with other parameters listed in Table 8.1 and 0.5 LMH as a simulation end-point. The PRO simulation shows that both water recovery and energy production are enhanced by increasing the PRO influent volume, while the substrate concentration in the feed effluent remains stable (Figure 8.3A and 8.3B). At the PRO influent of 1,000 mL, 794 mL of clean water is recovered and 949 joules of energy is produced. These values are increased by 2 times with 2,000 mL of PRO influent. As the initial substrate concentration in the PRO feed influent remains unchanged (193 mg L^{-1}), increasing the PRO influent volume leads to a higher total organic content in the MEC anolyte, which prolongs the MEC's HRT but does not exert effects on the maximum current (4.5 mA, Figure 8.3C). As a result of the increased organics and HRT, hydrogen production is improved consistently. It is predicted that the PRO-MEC system produces 59 mL of H_2 in 77.7 h with 1,000 mL of the PRO influent, and 92 mL of H_2 in 121.2 h with 2,000 mL of the PRO influent (Figure 8.3D). Interestingly, the energy consumption by the MEC increases non-linearly with increased PRO influent volume, resulting in an enlarged energy surplus between PRO unit and MEC (Figure 8.3B). This is indicative that one PRO unit can drive multiple MECs at large volume loading, and thereby further enhance the overall treating capacity of the PRO-MEC system.

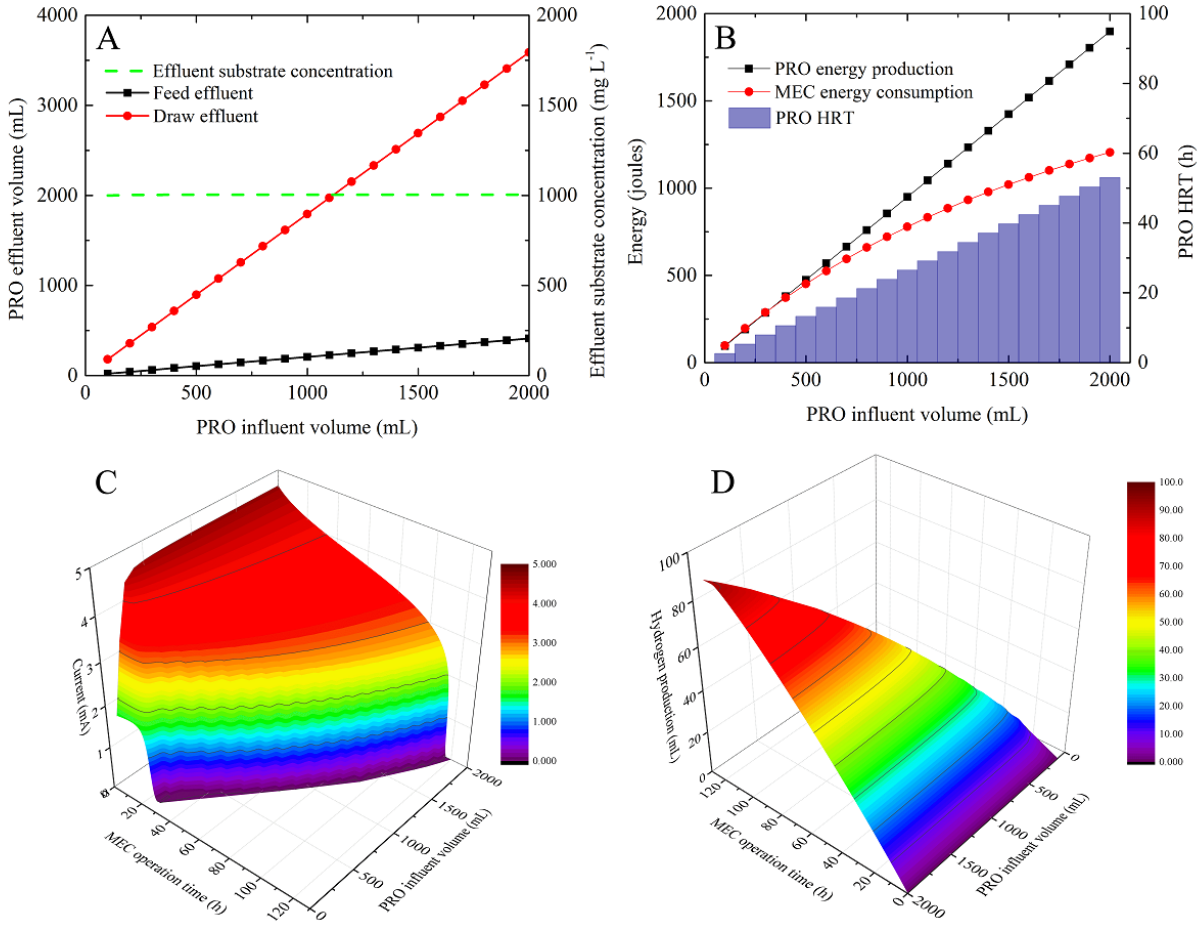

Figure 8.3 Effects of varied PRO influent volume on (A) PRO effluent volume and substrate concentration, (B) PRO energy production, PRO's HRT and MEC energy consumption, (C) current generation in the MEC and (D) hydrogen production in the MEC.

Effects of NaCl concentration in the PRO draw influent. The NaCl concentration ranging from 0.1 to 2.0 M is input in the time-dependent PRO model with other parameters summarized in Table 8.1 and 0.5 LMH as simulation end-point. It is predicted that the water recovery is enhanced significantly when the NaCl concentration increases from 0.1 to 0.7 M, and a further increase in the NaCl concentration does not result in continuing improvement of water recovery (Figure 8.4A). On the other hand, both the energy production and the effluent substrate concentration increase linearly with the increased NaCl concentration (Figure 8.4A and 8.4B). The PRO's HRT reaches the maximum of 20.8 h at 0.4 M, and then decreases readily to 9.2 h at 2.0 M (Figure 8.4B), likely because high water flux at higher draw concentration causes a faster decline in the osmotic pressure

difference as described by Equation 8.5 and Equation 8.6. When the NaCl concentration is lower than 0.7 M, the PRO energy production is predicted to be lower than the MEC energy consumption if the substrate is completely degraded (Figure 8.4B). Therefore, the MEC performance is limited by the energy supply with low NaCl concentrations, and both the organics removal and hydrogen production cannot be performed effectively (below 93.0% and 34.2 mL, respectively, Figure 8.4C). When the NaCl concentration is higher than 0.8 M, sufficient electrical energy is generated in the PRO unit to support a complete MEC cycle with organics removal >99%. Consequently, the MEC's operating time is prolonged to over 50.7 h, and the hydrogen production reaches 37.6 mL. Further increase in the NaCl concentration beyond 1.5 M does not noticeably enhance the hydrogen production, suggesting that the total organic content may have become a limiting factor for the MEC performance.

Effects of external voltage on the MEC. The energy consumption by the MEC is affected by the externally applied voltage according to Equation 8.18 and Equation 8.19. MEC simulation is therefore performed with the external voltage varying from 0.5 to 1.1 V. The initial conditions for the MEC simulation are listed in Table 8.1. The results show that at 0.5 V, the MEC needs 89 joules of energy to remove organics, but generates only 10.7 mL H_2 in 68.8 h (Figure 8.5). The hydrogen production reaches the maximum value of 38.1 mL in 42.9 h at 0.9 V, and declines at a higher external voltage. That is because the MEC energy consumption exceeds the PRO energy production: the PRO energy production with given input parameters is fixed (i.e. 579 joules, Figure 8.5 inset, red dash line), and at 1.0 V (or 1.1 V), the MEC simulation is stopped once the energy consumption reaches 579 joules; as a result, the MEC cannot accomplish a complete cycle and hydrogen production would decrease because of a shorter operating time. The organic removal is predicted to be 92.7% at 1.0 V and only 80.3% at 1.1 V. Meanwhile, the MEC's HRT is significantly shortened at a higher external voltage. These results indicate that the coupled system is versatile towards different purposes, and the treating capacity of the PRO and MEC can be balanced through varying external voltage.

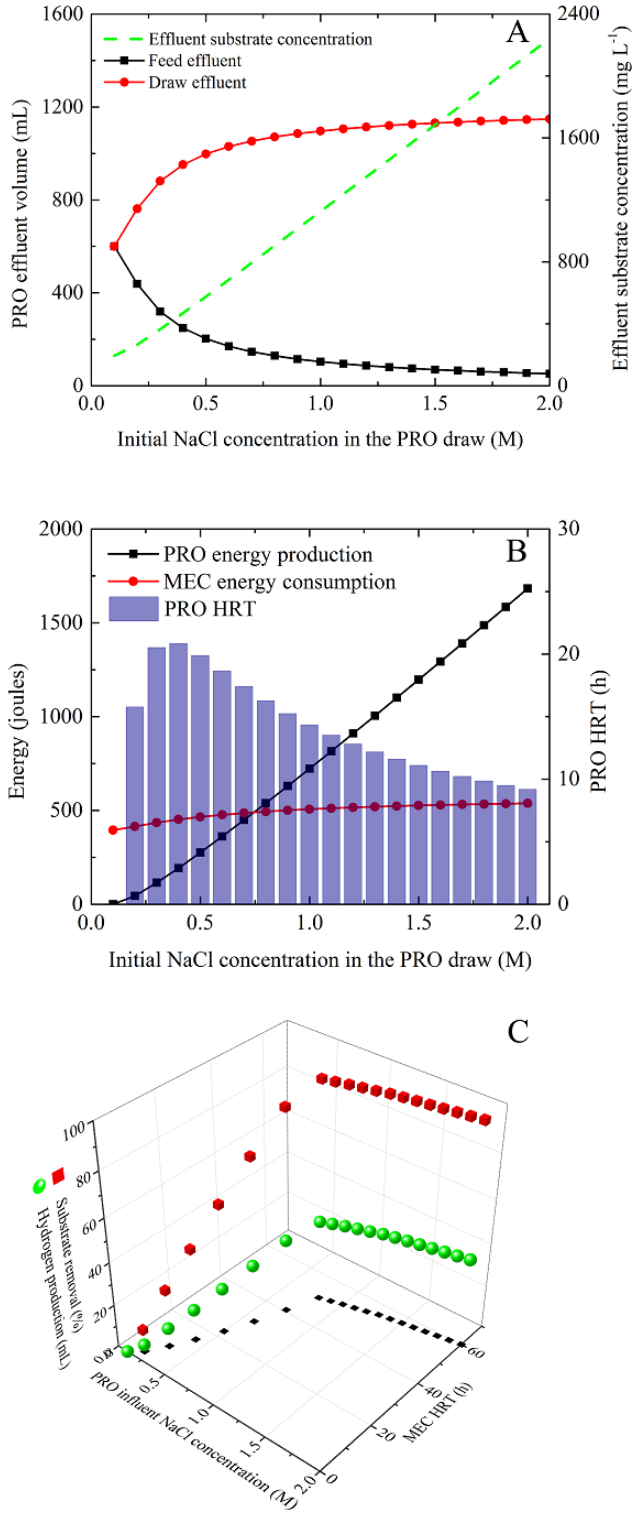

Figure 8.4 Effects of varied NaCl concentration on (A) PRO effluent volume and substrate concentration, (B) PRO energy production, PRO's HRT and MEC energy consumption and (C) substrate removal and hydrogen production in the MEC.

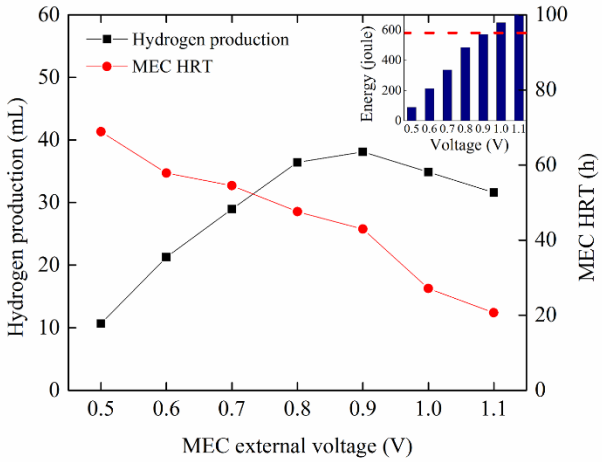

Figure 8.5 Hydrogen production and MEC's HRT predicted by the batch-mode MEC model with external voltage ranging from 0.5 to 1.1 V. The inset shows the MEC energy consumption at different voltage and the red line indicates the PRO energy production.

8.3.4 Perspectives

The coupled PRO-MEC system can achieve multiple benefits. Firstly, the PRO unit can serve as pre-treatment of organic solutions (e.g. wastewater), substantially reducing its volume and extracting clean water [170]. The draw solution for the PRO unit could be brine from RO desalination (91.3% of water recovery predicted by the model) or seawater (71.7% water recovery). Secondly, the PRO process can generate a high-conductivity feed solution as the MEC anolyte, which decrease the electrolyte resistance and thus is beneficial for bioelectrochemical processes [14, 247]. Thirdly, the osmotic energy harvested by the PRO process at certain influent volume and draw concentration is sufficient for a complete MEC cycle, making organic removal and hydrogen production more sustainable. Fourthly, compared with other approaches (e.g., MFC or solar energy) for driving hydrogen production in MECs, the present system can reduce the volume of the treated wastewater and produce a stream (diluted draw solution) for further desalination. For example, when seawater serves as a draw solution, its conductivity can be decreased from 76.2 to 44.4 mS cm^{-1} after the PRO process. Our previous study suggests that such a dilution can significantly enhance the rate of conductivity reduction in a microbial desalination cell [180].

Despite the great promise, several challenges must be addressed to move the PRO-MEC system towards practice. First, the robustness of the batch-mode MEC model should be improved by introducing endogenous respiration and more accurate pH variables [399, 400]. Because buffer was added in the feed/anolyte, the equilibrium between [HCO_3^-] and [H_2CO_3] as a function of pH was not taken into account in this study. When real wastewater is used as a feed/anolyte, the equilibrium constant should be introduced in Equation 8.14 and Equation 8.15. Moreover, the cathode potential in Equation 8.16 could be modified by relating pH change to hydrogen production and the Fick's law of diffusion. Another critical issue for practical applications is to balance the treating capacity of PRO and MEC. The simulation results with a high PRO influent volume and a high draw concentration suggest that one PRO unit is able to generate surplus energy to drive multiple MECs. In addition, the disparity in HRTs between the PRO unit and the MEC should also be addressed with caution to optimize the efficiency when one PRO unit is coupled to several MECs. Finally, the proposed system needs to be further demonstrated with actual energy generated from a PRO unit, which was reported in only a few studies [401, 402].

8.4 Conclusions

This work has demonstrated a proof-of-concept PRO-MEC system for simultaneous bioelectrochemical hydrogen production, organic removal, and water extraction driven by two forms of energy generated from (theoretically) the same liquid stream. It also presents the first attempt to introduce time variable into a PRO model, and has modified the previous single-chamber MEC model into a two-chamber batch-mode MEC model. Multiple benefits can be achieved through the synergy between PRO and MEC, including sustainable hydrogen production, clean water recovery and reduced wastewater volume. A high influent volume and a high draw concentration are predicted to enhance the performance of the coupled system, and the optimal external voltage is determined to be 0.9 V by the models. The PRO-MEC system may hold great promise in addressing water-energy nexus.

CHAPTER 9: Effects of Electron Acceptors on Removal of Antibiotic Resistant Escherichia coli, Resistance Genes and Class 1 Integrons under Anaerobic Conditions

(This section has been published as: Heyang Yuan, Jennifer H. Miller, Ibrahim M. Abu-Reesh, Amy Pruden, and Zhen He. "Effects of electron acceptors on removal of antibiotic resistant Escherichia coli, resistance genes and class 1 integrons under anaerobic conditions." Science of The Total Environment (2016): 569, 1587-1594.)

9.1 Introduction

Antibiotic resistant bacteria (ARB) and antibiotic resistance genes (ARGs) are emerging environmental contaminants posing a serious concern for public health [186]. Bacterial pathogens carrying ARGs can survive in the presence of antibiotics through several mechanisms [403], thereby enriching resistant strains and lowering drug efficacy. A major concern is that ARGs can be shared among different species through horizontal gene transfer [404], which appears to be a rare, but important event in the spread of antibiotic resistance [405-407]. The rise in percentages of resistant bacteria has steadily followed the rise in antibiotic use in humans and agriculture. Both human and livestock excrete antibiotics, antibiotic metabolites, ARBs and ARGs into agricultural waste and domestic wastewater, treatment processes for which are not intentionally designed for their removal, with eventual impact on receiving environments [408-410]. The activated sludge process in conventional wastewater treatment plants (WWTPs) may create a suitable environment for the proliferation of ARBs and horizontal transfer of ARGs [165, 411-413]. An elevated level of ARGs has been observed in WWTP effluent after mixed-media filtration and hypochlorite disinfection [414]. The New Delhi metallo-β-lactamase (NDM-1) genetic element, which imparts resistance to a wide variety of antibiotics, has recently been found in WWTP effluent in China, and was able to be propagated to indigenous bacteria in the receiving environment [415]. Given the environmental impacts and persistence of ARBs and ARGs, there is an urgent need to understand removal mechanisms and take steps towards the formulation of effective removal strategies.

The fate of ARBs and ARGs in anaerobic treatment processes, which represent an approach for energy efficient wastewater treatment, is of great interest. It has been reported that a two-stage thermophilic/mesophilic anaerobic digestion system can efficiently remove ARGs associated with

tetracycline resistance [187]. In another study, both the mesophilic and thermophilic anaerobic digesters showed approximately 1 log removal of nine ARGs, while a longer solids retention time and elevated temperature were suspected to play an important role in their fate [416]. The removal rate and efficiency of ARGs encoding tetracycline resistance could be increased with increased temperature of the digester [417]. Anaerobic digestion was also used as pre-treatment for aerobic stirred tank reactors and noticeably enhanced the removal of a variety of ARGs [188]. While these prior studies demonstrated that ARBs and ARGs can be reduced under some circumstances by anaerobic digesters, there remains a knowledge gap with respect to the removal mechanisms.

Bioelectrochemical systems (BES), such as microbial fuel cells (MFCs) and microbial electrolysis cells (MECs), are novel anaerobic biotechnologies for water and wastewater treatment with simultaneous energy recovery [8, 9, 171]. Electrochemically active microorganisms (i.e., exoelectrogens) consume organics in wastewater and respire by releasing electrons extracellularly, and the anode electrode serves as the main electron acceptor [15]. The fact that oxidation and reduction reactions are separate and controllable makes BES a versatile research platform for various functions, such as the removal of nutrients, organic pollutants and heavy metals [7, 87, 418, 419]. However, the fate of ARBs and ARGs in BES has not yet been reported to our knowledge.

The objective of this study was to investigate the fate of a native tetracycline and sulfonamide-resistant *E. coli* strain and its ARGs in BES, and to study the possible effects of electron acceptors on removal. The *E. coli* strain was isolated from primary WWTP effluent and confirmed to carry the sulfonamide-resistant gene *sulI*, the tetracycline-resistant gene *tet*(E) and class 1 integrase gene *intI1*. The *E. coli* was spiked into a tubular BES anode, which was operated in either an MFC or an MEC mode, and was subject to a range of currents by adjusting the external resistance. Synthetic wastewater with acetate as the carbon source and without any electron acceptor was used as the substrate. The removal of the *E. coli* and the target ARGs were tracked before and after treatment using real-time quantitative polymerase chain reaction (qPCR). To further examine the effects of the electrode and electron shuttles as the electron acceptors on removal, pure-culture tetracycline and sulfonamide-resistant *E. coli* were incubated in a two-chamber MEC, or in serum bottles amended with autoclaved effluent from the tubular BES.

9.2 Materials and methods

9.2.1 Preparation of Antibiotic Resistant E. coli

Primary effluent collected from a local WWTP (Peppers Ferry, VA, USA) was diluted 1:50 in LB broth that was amended with 50 mg L^{-1} tetracycline and sulfamethoxazole (above the minimum inhibitory concentrations for *E. coli*) [420]. The selection of pure-culture antibiotic resistant *E. coli* was performed as follow: the broth was incubated aerobically at room temperature overnight and spread on HiCrome™ m-TEC agar (Sigma-Aldrich, MO, USA); the agar was incubated according to the manufacturer's instruction and a single colony was transferred into antibiotic-amended LB broth. The broth-agar incubation was repeated three times. The obtained pure culture was then incubated aerobically at room temperature with constant stirring, and bacterial growth was monitored by measuring the optical density at 600 nm. After 12 h of incubation, the growth reached mid-log phase. The culture (20 mL) was collected and washed with 10 mM PBS (phosphate buffer saline). The PBS was discarded after centrifugation and the pellet was ready for use. After the collection step, 1 mL of the culture was transferred into 24 mL of fresh antibiotic-amended LB broth for next batch of incubation and the culture was collected every 12 h.

9.2.2 BES Construction and Operation

A tubular BES was constructed as previously described [180]. Briefly, a cation exchange membrane (CMI-7000, Membrane International, Inc., NJ, USA) tube was made to form the anode chamber (~250 mL) containing a carbon brush (Gordon Brush Mfg. Co., Inc., CA, USA) as the anode electrode. A piece of 300-cm^2 carbon cloth (Zoltek, MO, USA) was coated with 0.1 mg cm^{-2} Pt/C and wrapped around the cation exchange membrane tube as the cathode electrode. The BES was placed in a tubular PVC container, which served as the cathode chamber (~1000 mL). The anode and cathode electrodes were connected by titanium wire across a resistance decade box. Synthetic wastewater was used as the anolyte (per liter of deionized water): sodium acetate 1.2 g; NaCl, 0.5 g; $MgSO_4$, 0.015 g; $CaCl_2$, 0.02 g; KH_2PO_4, 0.265 g; K_2HPO_4, 0.535 g; $NaHCO_3$, 8.4 g; and trace element, 1 mL [200]. The catholyte was 100 mM PBS (KH_2PO_4, 5.3 g L^{-1}; and K_2HPO_4, 10.7 g L^{-1}). A peristaltic pump (BT600-2J, Langer Instruments, NJ, USA) was used to recirculate the electrolyte at a flow rate of ~96 mL min^{-1}.

The BES was inoculated with anaerobic sludge and operated under MFC mode by aerating the catholyte at room temperature. After a one month of start-up period, stable current generation was obtained, indicating the BES was well acclimated. No colonies formed when the BES effluent was spread on m-TEC agar, suggesting that the number of background *E. coli* was negligible. The previously prepared tetracycline and sulfonamide-resistant *E. coli* pellet was then resuspended in the synthetic wastewater and fed in the BES anode. The BES was batch-operated, and the substrate was replaced every 24 h. The anode influent and effluent (1 mL) were collected and stored at -80 ºC for DNA analysis. The fate of the *E. coli* and ARGs was studied for the effect of current generation (Table 9.1). The experiments were conducted at room temperature in triplicate.

Table 9.1 Performance of the tubular BES under MFC or MEC mode and different current, DO and pH of the anode effluent. H: high current; M: medium current; L: low current; O: open circuit (zero current). CE: Coulombic efficiency. DO: dissolved oxygen. The standard deviation was calculated with triplicate reactor runs.

		Current mA	CE %	DO mg L^{-1}	pH
MFC	H	20.2±1.0	79.9±0.5	2.01±0.05	6.34±0.06
	M	9.6±0.0	69.9±2.3	1.25±0.07	7.27±0.04
	O	-	-	0.50±0.01	7.45±0.11
MEC	H	19.4±0.3	74.1±0.9	0.35±0.07	6.19±0.04
	M	9.3±0.3	71.8±5.2	0.36±0.01	6.75±0.04
	L	1.1±0.1	56.7±4.3	0.37±0.00	7.11±0.17
	O	-	-	0.32±0.06	7.97±0.21

After the MFC experiments, the BES was operated under the MEC mode to exclude the effects of oxygen diffusion. The aeration in the cathode was stopped, the cathode chamber was sealed and an external voltage of 0.8 V was applied (3644A, Circuit Specialists, AZ, USA). The fate of the *E. coli* and ARGs in the MEC was examined following the same experimental procedures as that under the MFC mode.

9.2.3 Tracking the Fate of Pure-culture Antibiotic Resistant E. coli

To study the effects of electron shuttles excreted from exoelectrogens on the survival of the *E. coli* and its ARGs, the tetracycline and sulfonamide-resistant *E. coli* isolate was anaerobically incubated in synthetic wastewater amended with the BES effluent (which was expected to contain

oxidized electron shuttles). To obtain such an effluent, the tubular BES was operated under the MEC mode without dosing antibiotic resistant *E. coli* for two weeks. The colony-forming units of tetracycline and sulfonamide-resistant bacteria decreased to within one log of the baseline level that was measured prior to dosing antibiotic resistant *E. coli* (Figure F1). The anode effluent was then collected and filtered through a 0.22-µm filter membrane. Synthetic wastewater and 100 mL of the filtered effluent were autoclaved at 121 ºC for 20 min. Filtered riboflavin solution (1 mM) was used as the electron acceptor in positive control groups. The tetracycline and sulfonamide-resistant *E. coli* pellet was resuspended in 24 mL of the autoclaved synthetic wastewater and transferred to the autoclaved serum bottles. The culture was amended with either 1 mL of autoclaved synthetic wastewater (blank), filtered anode effluent, filtered/autoclaved anode effluent, or riboflavin solution (positive control). The serum bottles were sparged with nitrogen gas for 5 min, sealed and incubated with constant stirring. After 23 h of incubation, stirring was stopped for 1 h to allow dead cells settle, and 1-mL sample was collected and stored at -80 ºC for molecular analysis.

To determine the effects of the anode electrode on the removal of the ARB and it ARGs, the *E. coli* strain was incubated in the anode of a two-chamber MEC. This MEC was built by sandwiching a cation exchange membrane between two glass bottles [88]. The anode electrode was a carbon brush and the cathode electrode was two pieces of 20-cm^2 carbon cloth coated with 0.5 mg cm^{-2} Pt/C. The liquid volume of the anode and cathode chamber were 130 and 140 mL, respectively. The anolyte and catholyte were the same as those of the tubular BES. Before experiments, both the MEC reactor and the electrolyte were autoclaved at 121 ºC for 20 min. The *E. coli* pellet was resuspended in the anolyte and used to inoculate the MEC anode. An external voltage of 0.8 V was applied on the MEC across the external resistance of 1 Ω. The MEC was operated in batch mode for 24 h with constant stirring. An MEC operated under open circuit condition served as the blank control. After 23 h of incubation, stirring in the anode was stopped for 1 h and 1-mL sample was collected and stored at -80 ºC for molecular analysis. Both the serum bottle and MEC experiments were conducted at room temperature in triplicate.

9.2.4 Molecular Analyses

DNA in the synthetic wastewater before and after treatment was exacted using PureLink® Genomic DNA Mini Kit (Thermo Fisher Scientific, MA, USA). PCR assays were performed with GoTaq® Green Master Mix (Promega, WI, USA) on a thermal cycler (Mastercycler® nexus gradient, Eppendorf, NY, USA). The culture isolated with HiCrome™ m-TEC agar was confirmed to be *E. coli* by detecting the *E. coli* specific gene *uid*A [421]. A series of PCR assays served to detect ARGs [416]. The presence of *sulI*, *tet*(E) and *intI1* was confirmed to be of the expected size using gel electrophoresis (Figure F2). PCR was also used to amplify bacterial 16S rRNA genes as an indicator of the total number of bacteria. Details of the primers can be found in Table F1.

PCR products of those genes were cloned with TOPA TA Cloning Kit (Invitrogen, CA, USA) and plasmids were isolated using QIAprep Spin Miniprep Kit (Qiagen, CA, USA). Six-point standard curves were constructed from 10-fold serial dilutions of plasmid ranging from 10^9 to 10^3 gene copies μL^{-1}. The highest concentration of the plasmid standard for *sul*I was excluded, making it a five-point standard curve to maintain the linear range. Quantitative PCR was performed on a Real Time PCR System (7300, Applied Biosystems, CA, USA) with SsoFast Evagreen Supermix (Bio-Rad Laboratories, CA, USA) to quantify bacterial 16S rRNA gene, *uid*A, *intI1* and *sulI*, *tet*(E). The qPCR protocols have been validated and reported in a previous study [416]. A dilution series was performed and 1:20 was selected and applied to DNA extracts to minimize inhibitory effects. Samples were quantified in triplicate with standards and a negative control included in every run. The average slope of all qPCR assays was -3.32 ± 0.00 with $R^2 > 0.98$.

9.2.5 Measurement and Statistics

The concentration of the plasmid (ng μL^{-1}) was measured using a spectrophotometer (NanoDrop Lite, Thermo Fisher Scientific, DE, USA) and converted to gene copies μL^{-1} as previously described [422]. Because the tubular BES was a mixed-culture system, the concentrations of target genes were normalized to that of 16S rRNA gene to minimize the variance in total bacterial population size and to gain insight into the possibility of horizontal gene transfer [423, 424]. The serum bottles and two-chamber MEC contained only pure-culture *E. coli*, and thus the copy concentrations from those experiments were normalized to the sample volume (1 mL). Removal of the *E. coli* and ARGs was calculated as the log difference of the copy concentrations between the influent and effluent. One-way ANOVA (analysis of variance), two-sample t-test and linear

correlation with log removal were performed using OriginPro 9. A p-value of <0.05 was considered to indicate statistical significance. The current generation was monitored by measuring the voltage on the external resistance using a digital multimeter (2700, Keithley Instruments, OH, USA) at a time interval of 2 min. Soluble COD (chemical oxygen demand) was measured using a colorimeter according to the manufacturer's instruction (DR/890, Hach Company, CO, USA). Coulombic efficiency was calculated according to a previous study [358]. Dissolved oxygen (DO) was measured using a benchtop DO meter (Orion Star™ A213, Thermo Fisher Scientific, MA, USA).

9.3 Results and discussion

9.3.1 Fate of antibiotic resistant *E. coli and ARGs under MFC mode*

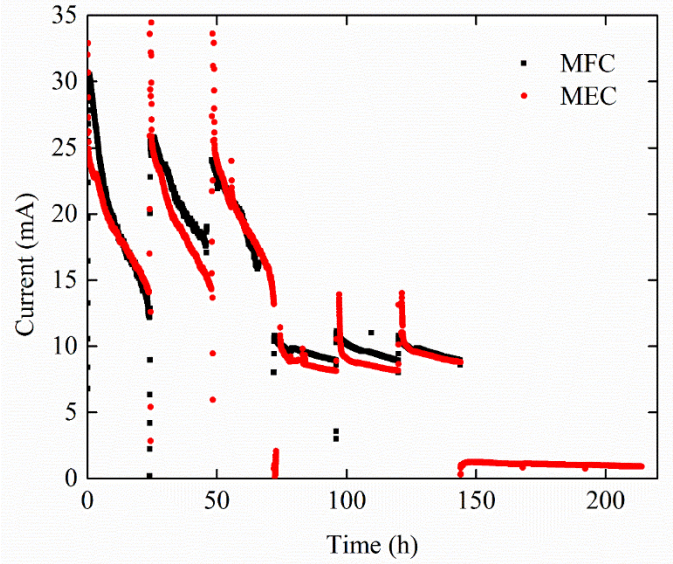

Figure 9.1 Current generation of the BES operated under MEC or MFC mode with different external resistance.

Before dosing the tetracycline and sulfonamide-resistant *E. coli*, background *E. coli* in the BES were confirmed to be below detection using m-TEC agar, indicating that indigenous strains were not likely to interfere with tracking of the spiked strain. The tubular BES was first operated as an MFC with consistent current generation. The current dropped constantly in one cycle due to the consumption of substrate, and rose back to the initial level rapidly after the anolyte was refreshed (Figure 9.1), indicating a well-acclimated anode [212]. The average peak current reached 20.2 mA

with a coulombic efficiency of 88.1% when operated under the high current mode, and decreased to 9.6 mA when higher external resistance was applied (Table 9.1). Meanwhile, the DO of the BES anode effluent significantly decreased from 2.01 mg L^{-1} under the high current condition to 0.50 mg L^{-1} under the open circuit condition ($p<0.05$).

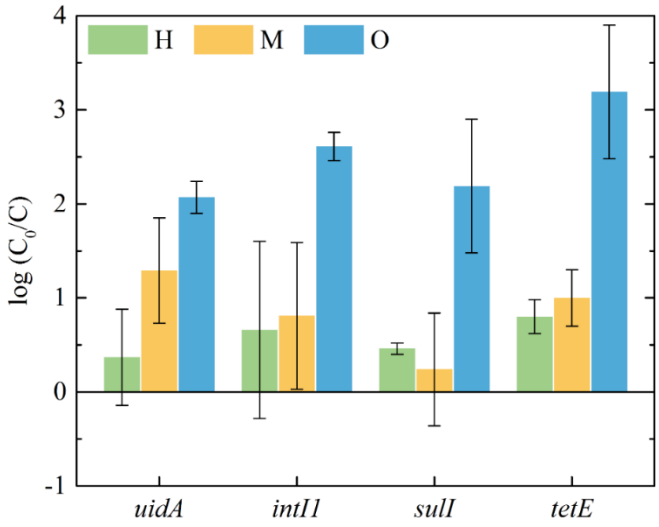

Figure 9.2 Removal of tetracycline and sulfonamide-resistant *E. coli* (*uid*A), *intI1*, *sulI* and *tet*(E) by the BES operated as an MFC under different current conditions. H: high current; M: medium current; O: open circuit (zero current). The standard deviation was calculated with triplicate reactor runs.

Figure 9.2 shows that the average removal of the *E. coli* (according to *uid*A gene copies) was significantly enhanced from 0.37 log to 2.07 log when the BES operation was switched from high current to open circuit mode (t-test, $p<0.05$). The large standard deviation may be due to the variance of sample collection associated with rapid recirculation (96 mL min^{-1}). Similarly, the average removal of *intI1*, *sulI* and *tet*(E) was improved by ~2 log when the circuit was disconnected (Figure 9.2). The BES anode essentially functioned as an anaerobic digester under the open circuit condition, but the log removal of ARGs achieved (ranging from 2.16 to 3.19 log reduction) here was higher than that reported for mesophilic and thermophilic anaerobic digesters [416]. This higher removal could be related to the highly specific environment (acetate as the sole carbon source) and limited electron acceptors in the BES anode (no electron acceptors were added in the substrate). *E. coli* is a facultative organism that can use various chemicals, including nitrate,

fumarate and dimethyl sulfoxide as electron acceptors under anaerobic conditions [425]. However, these substances were absent in the synthetic wastewater, making either the oxygen diffused from the cathode or the anode electrode the possible electron acceptor available to the *E. coli*. The lower removal of ARGs under the condition of high DO together with high current mode was also in agreement with the previous finding that high DO concentrations was beneficial for the persistence of tetracycline resistance plasmids in *E. coli* [426].

9.3.2 Fate of antibiotic resistant *E. coli and ARGs under MEC mode*

To exclude the possible effects of oxygen diffusion on the removal of the *E. coli* and ARGs, the BES was operated as an MEC. As a consequence, the DO in the anode effluent was maintained at 0.32 - 0.37 mg L^{-1} (Table 9.1). The current output was adjusted to the same level as the MFC mode through varying external resistance (Figure 9.1 and Table 9.1). The comparable coulombic efficiency suggested that the microbial community did not noticeably change [24, 427].

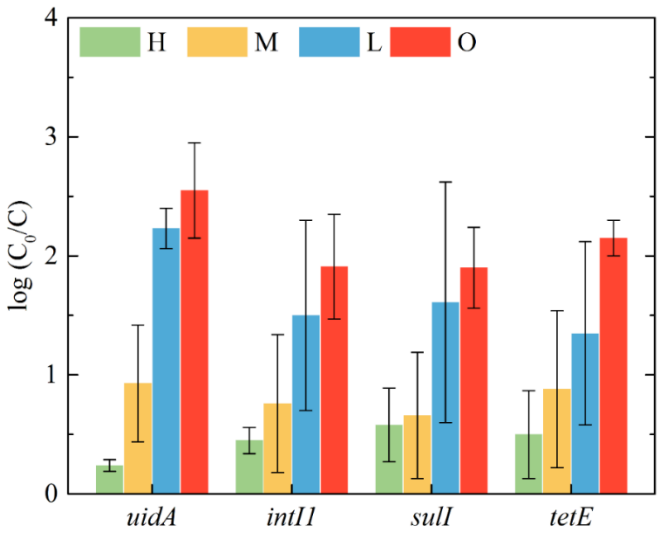

Figure 9.3 Removal of tetracycline and sulfonamide-resistant *E. coli* (*uidA*), *intI1*, *sulI* and *tet*(E) by the BES operated as an MEC under different current conditions. H: high current; M: medium current; L: low current; O: open circuit (zero current). The standard deviation was calculated with triplicate reactor runs.

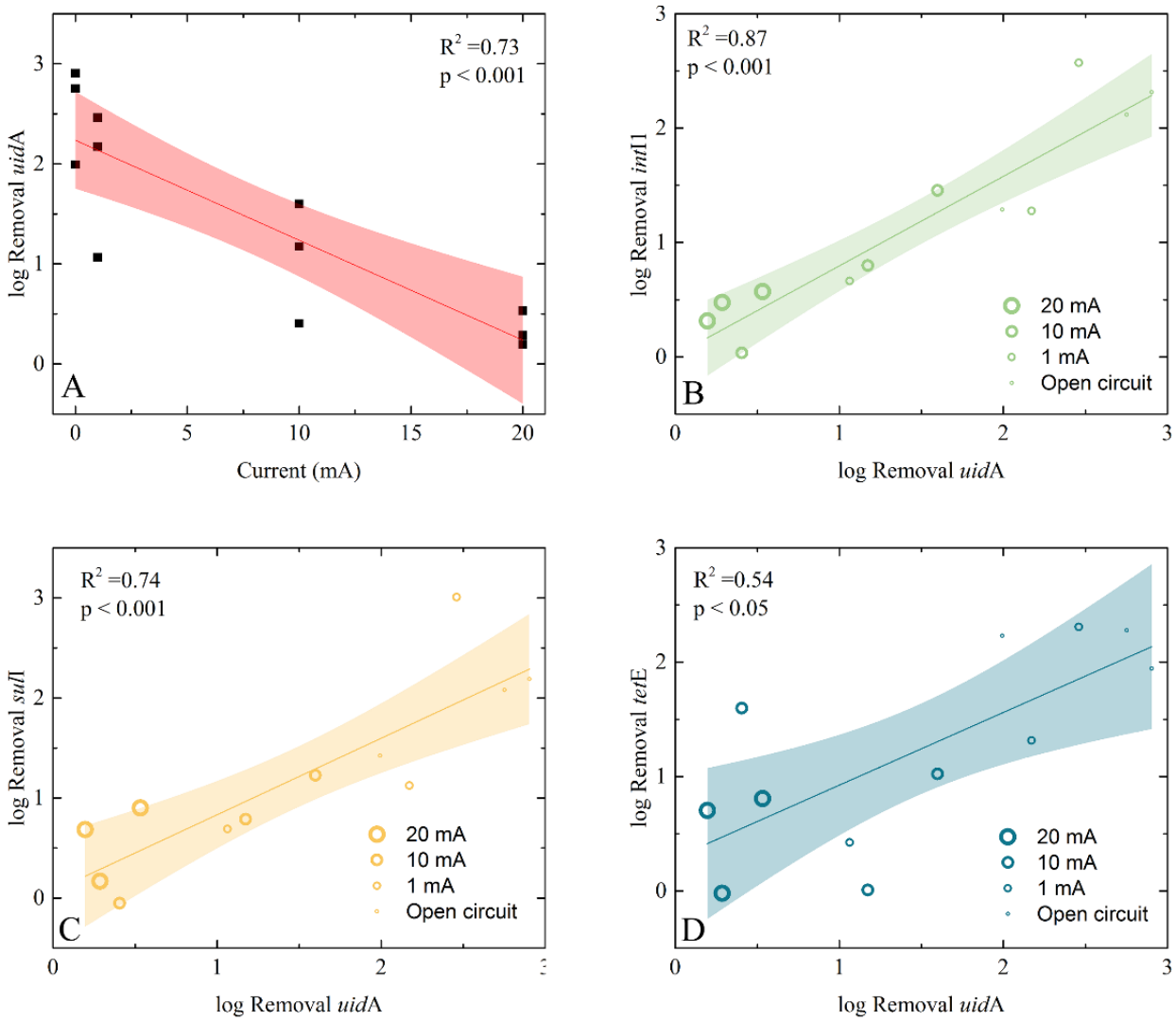

Figure 9.4 Linear fitting and Pearson's correlation of (A) *uidA* vs. current, (B) *intI1* vs. *uidA*, (C) *sulI* vs. *uidA* and (D) *tet*(E) vs. *uidA*. Shadow area represents 95% confidence interval.

Similar to the results obtained with the MFC mode, more *E. coli* were removed with decreased current (Figure 9.3). The reduction of *E. coli* (*uid*A) reached 2.23 log under low current conditions, considerably more than the 0.24 log removal observed with high current, and was further enhanced to 2.55 log removal under the open circuit condition. One-way ANOVA supported the conclusion that the removal of *E. coli* was significantly different across the different current conditions ($p<0.05$). The removal of ARGs followed the same pattern and was enhanced when the current was decreased. For example, *tet*(E) was reduced by 1.27 log more under the open circuit condition relative to the high current condition. The pH of the anolyte varied as a function of current, but it

was maintained within the optimal range for *E. coli* growth (pH 6-8) [428], and thus was not likely a significant factor in this study. Therefore, as previously discussed, the availability of electron acceptors was likely an important factor accounting for the abundance change of the *E. coli* and ARGs.

Correlation analyses of *E. coli* vs. current and ARGs vs. *E. coli* were conducted to further understand potential removal mechanisms. The log removal of *uid*A was found to negatively correlate with the current ($p<0.001$) (Figure 9.4A), implying that current production is beneficial for the survival of antibiotic resistant *E. coli*, likely because they have the opportunity to respire the anode electrode during electricity generation. Previous studies have demonstrated that *E. coli* release electron shuttles to the anode electrode for extracellular electron transfer [429, 430]. Moreover, prior research indicates that *E. coli* are likely capable of using electron shuttles released by exoelectrogens (e.g., riboflavin) for respiration [431, 432]. Strong correlations between the reduction of ARGs and the reduction of *E. coli* were observed in this study (Figure 9.4B-9.4D, $p<0.05$), indicating that the survival of the host *E. coli* is an overarching factor in the persistence of ARGs.

9.3.3 Effects of Anode Electrode

Based on the aforementioned results, we hypothesized that the survival of antibiotic resistant *E. coli* and the persistence of ARGs could be determined by the availability of an anode electrode as the electron acceptor. To examine this hypothesis, a two-chamber MEC was inoculated with the tetracycline and sulfonamide-resistant *E. coli*. Under closed circuit conditions, the MEC achieved an average current of 0.70 mA with DO below detection in the anode chamber. The log difference between the copy concentration of *uid*A in the influent and the effluent was negative (Figure 9.5), meaning growth occurred and the abundance of *E. coli* increased by 0.24 log. Consistent with the fate of the host, the abundance of *intI1*, *sulI* and *tet*(E) increased by 0.28, 0.26 and 0.21 log, respectively. In contrast, the abundance of *E. coli* was reduced by 0.13 log under open circuit conditions. The removal of ARGs was slightly higher, ranging from 0.23 to 0.25 log. It should be noted that the removal of the *E. coli* and ARGs under open circuit conditions in the two-chamber MEC was noticeably less than that in the tubular at MEC mode (~ 2 log, Figure 9.3), which could be attributed to the amplification of DNA that persisted from dead cells during qPCR assays [433].

The tubular BES contained a mixed-culture that could survive under the open circuit conditions and potentially be transformed by naked DNA from lysed *E. coli*, whereas DNA accumulated in the pure-culture two-chamber MEC may result in false-positive in qPCR measurement. While the reason of the lower removal in the two-chamber MEC warrants further studies, the significant difference in abundance change between the closed and open circuit conditions was in agreement with the proposed removal mechanism.

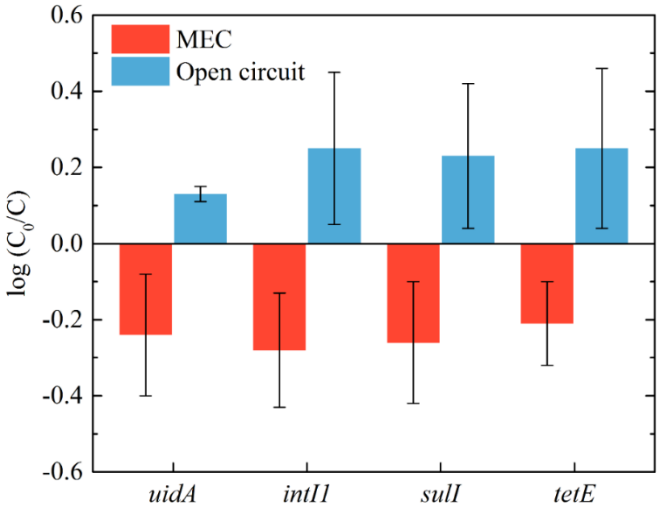

Figure 9.5 Abundance change of *uid*A, *intI1*, *sulI* and *tet*(E) in a two-chamber MEC inoculated with pure culture *E. coli*. The standard deviation was calculated with triplicate reactor runs.

9.3.4 Effects of Electron Shuttles

It was also hypothesized that the electron shuttles released by exoelectrogens in the BES anode may serve as electron acceptors after being oxidized by the anode electrode, thereby leading to the survival of antibiotic resistant *E. coli* and persistence of ARGs. To examine this, the effluent from the tubular BES anode containing oxidized electron shuttles was added in serum bottles to incubate the tetracycline and sulfonamide-resistant *E. coli* under an anaerobic condition. Similar to the results in the two-chamber MEC, the serum bottles amended with the filtered BES effluent showed negative log difference (i.e., increased abundance) of *E. coli* and ARGs ranging from -0.12 to -0.28 log (Figure 9.6). The abundance increase was slightly higher in the experiments using filtered and autoclaved BES effluent, which did not significantly differ from the results with the filtered effluent ($p>0.05$). Riboflavin as a positive control yielded similar abundance increase as the BES effluent did. On the other hand, the blank group without amendment showed reduced *E. coli* and

ARGs by approximately 0.3 log, comparable to the results in the two-chamber MEC under the open circuit condition. It has been reported that the addition of riboflavin could enhance electricity generation by *E. coli* in a pure-culture MFC [434]. A recent study also revealed the symbiosis of *E. coli* and exoelectrogen *Shewanella oneidensis* on flavin-mediated extracellular electron transfer [432]. Thus, the results of this study provide evidence that interspecies interactions related to the utilization of electron acceptors could be playing a critical role in the fate of ARB and ARGs under an anaerobic condition.

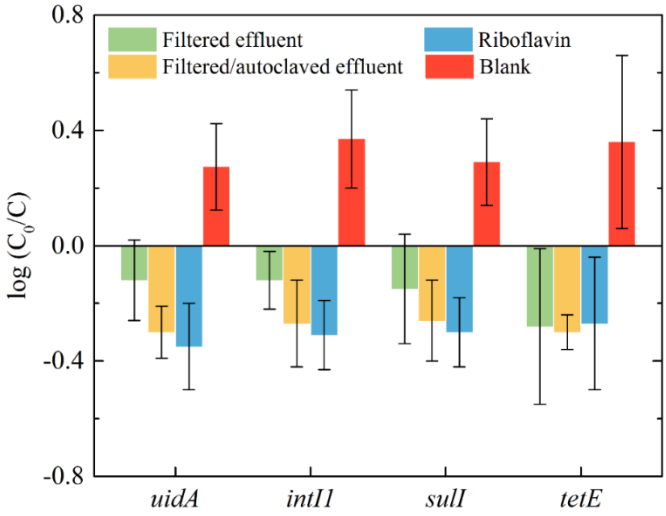

Figure 9.6 Abundance change of *uid*A, *int*I1, *sul*I and *tet*E in serum bottles amended with BES effluent or riboflavin. The standard deviation was calculated with triplicate reactor runs.

9.3.5 Perspectives

The present study, for the first time, used a BES as a research platform and *E. coli* as a model organism to gain insight into the removal mechanisms of ARB and ARGs under anaerobic conditions. The removal of exogenously introduced ARBs was significantly enhanced with decreased electrical current ($p<0.05$), and ARG removal was significantly correlated with ARB removal ($p<0.05$). It was therefore hypothesized that ARGs persisted as their host ARB survived, and the survival of ARB was affected by the availability of electron acceptors. Both the anode electrode and the electron shuttles excreted by exoelectrogens were available to ARB for respiration and could have benefitted their survival (Figure 9.7A). In the absence of those electron acceptors (i.e., under the open circuit condition), ARB death was likely the main mechanism of ARG removal (Figure 9.7B). Further examination of the proposed mechanisms with a two-

chamber MEC and serum bottle experiments produced results that agreed well with this explanation. These findings collectively demonstrated that electron acceptor was a key factor affecting the fate of ARBs and ARGs during biological treatment.

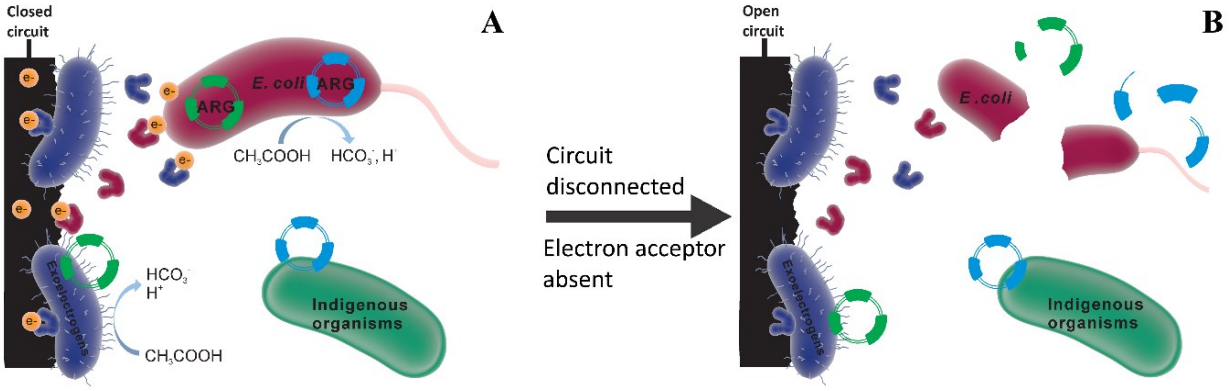

Figure 9.7 Proposed mechanisms for anaerobic removal of tetracycline and sulfonamide-resistant *E. coli* and ARGs in a BES. (A) Under closed circuit conditions, the *E. coli* survive by using the anode electrode and electron shuttles from exoelectrogens as electron acceptors, ARGs persist and horizontal gene transfer occurs. (B) Under open circuit conditions, when the electron acceptors are absent, the *E. coli* dies and ARGs are removed, horizontal gene transfer may also occur.

ARGs are typically carried on mobile genetic elements, such as plasmids and integrons, which are readily transferred across species through horizontal gene transfer, leading to the persistence of ARGs [189]. ARGs are therefore considered the primary contaminants of interest in minimizing the potential to spread antibiotic resistance [186]. The persistence and selective increase of ARGs resulting from horizontal gene transfer is a major challenge for biological treatment processes [435, 436]. The slopes in Figure 9.4B-9.4D (0.64-0.78) were lower than 1, implying that the removal of ARGs was at a slower rate than that of *E. coli*. This may be an indication of the persistence of extracellular ARGs and/or horizontal gene transfer of ARGs to new hosts. In addition, the slope of *sulI* vs. *E. coli* (0.74, Figure 9.4C) is distinct from that of *tet*(E) vs. *E. coli* (0.64, Figure 9.4D). Given the similar lengths of those two amplicons (Table F1), the varied slopes suggest that *sulI* and *tet*(E) decreased at different rates, which is suggestive of gene transfer. While the identification of horizontal gene transfer based on the correlation of ARGs and their host organism is qualitative, quantitative measurement in mixed-cultures is technically difficult. Metagenomics has emerged as a powerful tool to comprehensively understand horizontal gene

transfer in environment samples [437], and can be used to demonstrate horizontal gene transfer in digesters and BES in future studies.

One of the advantages of BES is energy production. However, the lower removal of *E. coli* and ARGs under high current operating conditions may present a new challenge if the removal of antibiotic resistance becomes one of the key criteria for wastewater treatment. The enhanced removal at low current suggests that, in order to maintain effluent quality, it may be more suitable to operate BES in high power mode (i.e., the external resistance is adjusted to equal to the internal resistance for achieving the maximum power output) [310]. In addition to the anode treatment, ARBs and ARGs may also be removed in the BES cathode. The anode effluent is commonly used as the catholyte for further COD removal and cathodic reduction reactions. The intermediate products, such as hydroxyl radical and hydrogen peroxide produced by inefficient catalysis of oxygen reduction reactions [98], may cause oxidative stress of ARBs and damage of ARGs. It has recently been reported that the combination of anaerobic and aerobic treatment remove more ARGs than an anaerobic process alone [188]. Moreover, the fate of ARBs and ARGs in other types of BES that focus on biosynthesis or water recovery may differ from that in MFCs and MECs. For example, it will be interesting to explore in a forward osmosis-microbial desalination cell [130] whether ARGs can be transported across the forward osmosis membrane and ion exchange membranes to contaminate the desalinated water.

While new insights were gained into the fate of the antibiotic resistant *E. coli* and its ARGs in BES, several challenges still remain to be addressed. First, the effects of anode substrate on the fate of ARBs and ARGs remained to be understood. Real wastewater may contain a trace amount of antibiotics and exert a selective pressure for ARBs. Second, BES is a unique system that has a stable biofilm with dominant species growing on the electrode. Once exogenous ARGs are horizontally transferred into the exoelectrogens on the electrode, the transformed exoelectrogens may reproduce and slough off the biofilm, thereby releasing ARBs and associated ARGs in the effluent. The interplay of exoelectrogens, ARBs, and horizontal gene transfer of ARGs warrants further studies.

9.4 Conclusions

The present study, for the first time, used a BES as a research platform to gain insight into the fate of a native tetracycline and sulfonamide-resistant *E. coli* strain and its ARGs under anaerobic conditions. When the BES was operated under MFC mode, the removal of the tetracycline and sulfonamide-resistant *E. coli* and its ARGs was enhanced with decreased electrical current. The fate of the tetracycline and sulfonamide-resistant *E. coli* and its ARGs in BES operated under MEC mode was similar to that under MFC mode. Both the anode electrode and the electron shuttles excreted by exoelectrogens could be used as electron acceptors by the antibiotic resistant *E. coli* for respiration and thus benefit their survival. The ARGs persisted as the *E. coli* survived, and was removed when the *E. coli* died.

CHAPTER 10: Perspectives

The studies in this dissertation, including understanding the fundamentals, optimizing the processes and explore the application niches, have collectively demonstrated that BES may hold great promise for energy-efficient water and wastewater treatment.

It has been shown in Chapter 2 that the anode can be operated under certain conditions (e.g., high salinity) to enrich electrochemically active microorganisms and maximize energy production. The current production of the MDC reached the maximum of current density of 300 A m^{-3} with 4 M NaCl, which was one of the highest reported in the literature. Electrochemically active bacteria *Pseudomonas* and *Acinetobacter* took advantage of shuttle-mediated EET and created optimal anode salinities for their dominance. Predictive functional dynamics and Bayesian networks suggested that the taxa putatively not capable of EET (e.g., Bacteroidales and Clostridiales) might indirectly contribute to bioelectrochemical desalination. By combining Bayesian network with logistic regression, current production was for the first time predicted from taxonomic data. This study has developed a novel statistical model to understand and predict the nexus of microbial ecology and system performance, towards the development of bioelectrochemical desalination to address water-energy challenges.

In Chapter 3, 4 and 5, three materials, i.e., N- and S- co-doped porous carbon nanosheets, N-doped bamboo-like CNTs and MoS_2 coated on CNTs, were studies as the cathode catalysts for ORR and HER catalysis in BES. The catalysts were synthesized through facile procedures and could meet the requirement for large-scale applications. Moreover, the catalysts exhibited outstanding physical and electrochemical properties, including high specific surface area, low resistance, favorable electron transfer mechanisms, which resulted in effective catalysis of ORR/HER and efficient BES performance. The costs of the catalysts were significantly lower than Pt/C, indicating their potential in practical applications.

Chapter 6, 7 and 8 have demonstrated the process engineering of combining BES with FO. Initially, the organic solution was treated in the MDC anode and its effluent was sent to the FO for water recovery. The diluted draw solution from the FO was desalinated in the MDC and the concentrated feed solution served as the catholyte. The MDC-FO system achieved relatively low

TDS reduction and could not generate water for direct use. To coordinate the treatment capacity between the FO and the MDC, an FO-MDC system under a continuous mode was developed: wastewater was first treated in the FO feed chamber for water extraction and then the concentrated feed solution was treated in the MDC anode. The volume ratio of the FO cell and the MDC was properly balanced to guarantee adequate HRT in the individual components, and thus the system is highly integrated in terms of water stream. A mathematical model developed based on previous models predicted that both desalination efficiency and effectiveness were mainly determined by the draw flow rate. Based on the rationale that FO can operated PRO mode to extract osmotic energy, a proof-of-concept PRO-MEC system was developed. The PRO-MEC system can achieve synergetic benefits as the PRO unit can reduce the volume of wastewater and extract clean water, the PRO effluents can be further treated by the MEC and the osmotic energy harvested from the PRO unit can be applied to the MEC for sustainable bioelectrochemical hydrogen production. The feasibility of the system was proven valid using simulated PRO performance (in terms of energy production and effluent quality) and experimental MEC results (e.g., hydrogen production and organic removal).

In Chapter 9, BES were employed as a platform to investigate the fate of a native tetracycline and sulfonamide-resistant *Escherichia coli* strain and its ARGs. The *E. coli* strain carrying *intI1*, *sulI* and *tet*(E) was isolated from domestic wastewater and dosed into a tubular BES. The BES was first operated as an MFC with aeration in the cathode, which resulted in enhanced removal of *E. coli* and ARGs by ~2 log when switched from high current to open circuit operation mode. The BES was then operated as an MEC to exclude the effects of oxygen diffusion, and the removal of *E. coli* and ARGs during the open circuit configuration was again 1-2 log higher than that at high current mode. Subsequent experiments with pure-culture tetracycline and sulfonamide-resistant *E. coli* being incubated in a two-chamber MEC and serum bottles demonstrated that the *E. coli* could survive by respiring anode electrode and/or electron shuttles released by exoelectrogens, and ARGs persisted with their host *E. coli*.

Despite the great advance in BES, there still remain many challenges to be addressed. First, the microbial community and functional dynamics need to be better understood. Several taxa, including Erysipelotrichales, Synergistales, Acholeplasmatales and Bacteroidales, were dominant

at low current conditions and their roles in the community warrant further studies with "omics" methods. It was also proposed that Clostridiales recycled the electrons and bicarbonate produced by the electrochemically active microorganisms, and the hypothesis remained to be examined. In addition, the robustness of the statistical model needs to be tested with more BES experiments, for example, MFC with different carbon sources and different external resistance. If the model is tested valid in BES, it may be applied to other biological systems such as anammox and anaerobic digesters. Another possibility is that the statistical model can be integrated with well-developed engineering models to simulate microbial parameters such as grow and decay rate, which are normally empirical values and present the major reason of inconsistent prediction.

Second, cost-effective and bifunctional cathode catalysts need be developed. As reviewed in Chapter 1, metal-nitrogen-carbon complexes are promising cathode catalysts for BES applications. Metal-organic frameworks (MOFs) have abundant metal-nitrogen-carbon sites, making them ideal candidates for ORR and HER catalysis. MOFs are highly defined 3D-structured materials composed of metal centers and organic ligands. Owing to the high BET surface area (theoretically up to 10,000 m^2 g^{-1}), uniform open cavities and tunable microstructures, MOFs have gained growing interests in a variety of applications [438]. There have been a few pioneering studies using MOFs as the precursor to synthesize ORR catalysts in the past five years [324, 439-443]. The applications of MOF-based ORR catalysts in MFCs has been reported by two recent studies [74, 444]. MOFs have also been used to derive HER catalysts and shown interesting chemistry and excellent catalytic activity [445-447]. One recent study has synthesized bifunctional catalysts for ORR and HER using Zn−Fe-MOFs and Au nanoparticles as the precursors [92]. The catalysts achieved comparable ORR catalysis and slightly inferior HER catalysts to Pt/C, demonstrating the feasibility of MOFs-derived bifunctional catalysts. However, the practicality of the catalysts (e.g., durability) remained to be examined in BES.

Last but not least, the fate of ARGs in the cathode remains to be studied and removal of ARG by BES needs to be improved from an engineering perspective. It was previously reported that an anaerobic-aerobic system reduced ARG level [188]. Similarly, the anode-cathode treatment of BES is an anaerobic-aerobic process. Based on literature and the study shown in Chapter 9, it is hypothesized that ARGs may be removed by the combination of anode/cathode treatment of BES.

Antibiotic-resistant organisms are likely to be outcompeted in the anode because of the lack of electron acceptors, and the ARGs they carry will be released to the anode environment and degrade. When the anode effluent is further treated in the cathode, antibiotic resistant bacteria and ARGs may be attacked by hydrogen peroxide, which is a common product of 2-electron-pathway ORR in the cathode. Because horizontal gene transfer occurs only in specific species, the fate of ARGs may closely related to their host organisms, and thus the relationship of ARGs and microbial community should also be studied.

References

1. UNESCO, *The United Nations World Water Development Report 2014: Water and Energy*. 2014, UNESCO, Paris, France.
2. Briefing, U.S., *International Energy Outlook 2013.* US Energy Information Administration, 2013.
3. Fritzmann, C., et al., *State-of-the-art of reverse osmosis desalination.* Desalination, 2007. **216**(1–3): p. 1-76.
4. McCarty, P.L., J. Bae, and J. Kim, *Domestic Wastewater Treatment as a Net Energy Producer–Can This be Achieved?* Environmental Science & Technology, 2011. **45**(17): p. 7100-7106.
5. Goldstein, R. and W. Smith, *Water & Sustainability (Volume 4): US Electricity Consumption for Water Supply & Treatment-The Next Half Century*. 2002: Electric Power Research Institute.
6. Smith, A.L., S.J. Skerlos, and L. Raskin, *Psychrophilic anaerobic membrane bioreactor treatment of domestic wastewater.* Water research, 2013. **47**(4): p. 1655-1665.
7. Wang, H. and Z.J. Ren, *A comprehensive review of microbial electrochemical systems as a platform technology.* Biotechnology Advances, 2013. **31**(8): p. 1796-1807.
8. Logan, B.E. and K. Rabaey, *Conversion of Wastes into Bioelectricity and Chemicals by Using Microbial Electrochemical Technologies.* Science, 2012. **337**(6095): p. 686-690.
9. Sevda, S., et al., *Microbial desalination cells as a versatile technology: Functions, optimization and prospective.* Desalination, 2015. **371**: p. 9-17.
10. Ge, Z., et al., *Recovery of Electrical Energy in Microbial Fuel Cells: a Brief Review.* Environmental Science & Technology Letters, 2014. **1**(2): p. 137–141.
11. Zhang, F., et al., *Long-term performance of liter-scale microbial fuel cells treating primary effluent installed in a municipal wastewater treatment facility.* Environmental Science & Technology, 2013. **47**(9): p. 4941-8.
12. Li, W.-W., H.-Q. Yu, and Z. He, *Towards sustainable wastewater treatment by using microbial fuel cells-centered technologies.* Energy & Environmental Science, 2014. **7**(3): p. 911-924.
13. Foley, J.M., et al., *Life Cycle Assessment of High-Rate Anaerobic Treatment, Microbial Fuel Cells, and Microbial Electrolysis Cells.* Environmental Science & Technology, 2010. **44**(9): p. 3629-3637.
14. Rozendal, R.A., et al., *Towards practical implementation of bioelectrochemical wastewater treatment.* Trends in Biotechnology, 2008. **26**(8): p. 450-459.
15. Lovley, D.R., *Electromicrobiology.* Annual Review of Microbiology, 2012. **66**: p. 391-409.
16. Kracke, F., I. Vassilev, and J.O. Krömer, *Microbial electron transport and energy conservation – the foundation for optimizing bioelectrochemical systems.* Frontiers in Microbiology, 2015. **6**: p. 575.
17. Kouzuma, A., et al., *Catabolic and regulatory systems in Shewanella oneidensis MR-1 involved in electricity generation in microbial fuel cells.* Frontiers in Microbiology, 2015. **6**.
18. Logan, B.E., *Exoelectrogenic bacteria that power microbial fuel cells.* Nature Reviews Microbiology, 2009. **7**(5): p. 375-381.

19. Boon, N., et al., *Use of Pseudomonas species producing phenazine-based metabolites in the anodes of microbial fuel cells to improve electricity generation.* Applied microbiology and biotechnology, 2008. **80**(6): p. 985-993.
20. Zhi, W., et al., *Methods for understanding microbial community structures and functions in microbial fuel cells: A review.* Bioresource Technology, 2014. **171**(0): p. 461-468.
21. Ishii, S.i., et al., *A novel metatranscriptomic approach to identify gene expression dynamics during extracellular electron transfer.* Nature Communications, 2013. **4**: p. 1601.
22. Ishii, S.i., et al., *Microbial metabolic networks in a complex electrogenic biofilm recovered from a stimulus-induced metatranscriptomics approach.* Scientific Reports, 2015. **5**: p. 14840.
23. Yates, M.D., et al., *Convergent development of anodic bacterial communities in microbial fuel cells.* The ISME journal, 2012. **6**(11): p. 2002-2013.
24. Zhu, X., et al., *Microbial Community Composition Is Unaffected by Anode Potential.* Environmental Science & Technology, 2014. **48**(2): p. 1352-1358.
25. Shehab, N., et al., *Characterization of bacterial and archaeal communities in air-cathode microbial fuel cells, open circuit and sealed-off reactors.* Applied Microbiology and Biotechnology, 2013. **97**(22): p. 9885-9895.
26. Ishii, S.i., et al., *Microbial population and functional dynamics associated with surface potential and carbon metabolism.* The ISME Journal, 2014. **8**(5): p. 963-978.
27. Zhang, H., et al., *Phylogenetic and Metagenomic Analyses of Substrate-Dependent Bacterial Temporal Dynamics in Microbial Fuel Cells.* PLoS ONE, 2014. **9**(9): p. e107460.
28. Lefebvre, O., et al., *Effect of increasing anodic NaCl concentration on microbial fuel cell performance.* Bioresource Technology, 2012. **112**: p. 336-340.
29. Monzon, O., et al., *Microbial fuel cells under extreme salinity: performance and microbial analysis.* Environmental Chemistry, 2015. **12**(3): p. 293-299.
30. Mehanna, M., et al., *Microbial Electrodialysis Cell for Simultaneous Water Desalination and Hydrogen Gas Production.* Environmental Science & Technology, 2010. **44**(24): p. 9578-9583.
31. Luo, H., et al., *Microbial desalination cells for improved performance in wastewater treatment, electricity production, and desalination.* Bioresource Technology, 2012. **105**(0): p. 60-66.
32. Luo, H., P. Xu, and Z. Ren, *Long-term performance and characterization of microbial desalination cells in treating domestic wastewater.* Bioresource Technology, 2012. **120**(0): p. 187-193.
33. Qu, Y., et al., *Salt removal using multiple microbial desalination cells under continuous flow conditions.* Desalination, 2013. **317**(0): p. 17-22.
34. Logan, B.E., *Scaling up microbial fuel cells and other bioelectrochemical systems.* Applied Microbiology and Biotechnology, 2010. **85**(6): p. 1665-1671.
35. Qiao, Y., S.-J. Bao, and C.M. Li, *Electrocatalysis in microbial fuel cells-from electrode material to direct electrochemistry.* Energy & Environmental Science, 2010. **3**(5): p. 544-553.
36. Zhou, M., et al., *An overview of electrode materials in microbial fuel cells.* Journal of Power Sources, 2011. **196**(10): p. 4427-4435.

37. Novoselov, K.S., et al., *Electric field effect in atomically thin carbon films.* Science, 2004. **306**(5696): p. 666-669.
38. Lee, C., et al., *Measurement of the Elastic Properties and Intrinsic Strength of Monolayer Graphene.* Science, 2008. **321**(5887): p. 385-388.
39. Balandin, A.A., et al., *Superior Thermal Conductivity of Single-Layer Graphene.* Nano Letters, 2008. **8**(3): p. 902-907.
40. Kim, K.S., et al., *Large-scale pattern growth of graphene films for stretchable transparent electrodes.* Nature, 2009. **457**(7230): p. 706-710.
41. Stoller, M.D., et al., *Graphene-Based Ultracapacitors.* Nano Letters, 2008. **8**(10): p. 3498-3502.
42. Bolotin, K.I., et al., *Ultrahigh electron mobility in suspended graphene.* Solid State Communications, 2008. **146**(9–10): p. 351-355.
43. Du, X., et al., *Approaching ballistic transport in suspended graphene.* Nature Nanotechnology 2008. **3**(8): p. 491-495.
44. Edwards, R.S. and K.S. Coleman, *Graphene synthesis: relationship to applications.* Nanoscale, 2013. **5**(1): p. 38-51.
45. Huang, X., et al., *Graphene-Based Materials: Synthesis, Characterization, Properties, and Applications.* Small, 2011. **7**(14): p. 1876-1902.
46. Zhao, C., et al., *High biocurrent generation in Shewanella-inoculated microbial fuel cells using ionic liquid functionalized graphene nanosheets as an anode.* Chemical Communications, 2013. **49**(59): p. 6668-6670.
47. Zhu, Y., et al., *Conductive multilayered polyelectrolyte films improved performance in microbial fuel cells (MFCs).* Colloids and Surfaces A: Physicochemical and Engineering Aspects, 2014. **455**(0): p. 92-96.
48. Yuan, H. and Z. He, *Graphene-modified electrodes for enhancing the performance of microbial fuel cells.* Nanoscale, 2015. **7**(16): p. 7022-7029.
49. Zhang, Y., et al., *Iron tetrasulfophthalocyanine functionalized graphene as a platinum-free cathodic catalyst for efficient oxygen reduction in microbial fuel cells.* Journal of Power Sources, 2012. **197**: p. 93-96.
50. Xie, X., et al., *Graphene-sponges as high-performance low-cost anodes for microbial fuel cells.* Energy & Environmental Science, 2012. **5**(5): p. 6862-6866.
51. Wang, H., et al., *High power density microbial fuel cell with flexible 3D graphene-nickel foam as anode.* Nanoscale, 2013. **5**(21): p. 10283-10290.
52. Qiao, Y., et al., *A hierarchical porous graphene/nickel anode that simultaneously boosts the bio- and electro-catalysis for high-performance microbial fuel cells.* RSC Advances, 2014. **4**(42): p. 21788-21793.
53. Zhao, C.-e., et al., *Nanostructured Graphene/TiO2 Hybrids as High-Performance Anodes for Microbial Fuel Cells.* Chemistry – A European Journal, 2014. **20**(23): p. 7091-7097.
54. He, Z., et al., *Architecture Engineering of Hierarchically Porous Chitosan/Vacuum-Stripped Graphene Scaffold as Bioanode for High Performance Microbial Fuel Cell.* Nano Letters, 2012. **12**(9): p. 4738-4741.
55. Feng, L., et al., *Enhancing Electrocatalytic Oxygen Reduction on Nitrogen-Doped Graphene by Active Sites Implantation.* Scientific Reports, 2013. **3**.
56. Chua, C.K. and M. Pumera, *Chemical reduction of graphene oxide: a synthetic chemistry viewpoint.* Chemical Society Reviews, 2014. **43**(1): p. 291-312.

57. Huang, Y.-X., et al., *Graphene oxide nanoribbons greatly enhance extracellular electron transfer in bio-electrochemical systems.* Chemical Communications, 2011. **47**(20): p. 5795-5797.
58. Yong, Y.-C., et al., *Macroporous and Monolithic Anode Based on Polyaniline Hybridized Three-Dimensional Graphene for High-Performance Microbial Fuel Cells.* ACS Nano, 2012. **6**(3): p. 2394-2400.
59. Feng, L., Y. Chen, and L. Chen, *Easy-to-Operate and Low-Temperature Synthesis of Gram-Scale Nitrogen-Doped Graphene and Its Application as Cathode Catalyst in Microbial Fuel Cells.* ACS Nano, 2011. **5**(12): p. 9611-9618.
60. Agharkar, M., et al., *Trends in green reduction of graphene oxides, issues and challenges: A review.* Materials Research Bulletin, 2014. **59**(0): p. 323-328.
61. Wang, H., T. Maiyalagan, and X. Wang, *Review on Recent Progress in Nitrogen-Doped Graphene: Synthesis, Characterization, and Its Potential Applications.* ACS Catalysis, 2012. **2**(5): p. 781-794.
62. Hou, Y., et al., *A 3D hybrid of layered MoS2/nitrogen-doped graphene nanosheet aerogels: an effective catalyst for hydrogen evolution in microbial electrolysis cells.* Journal of Materials Chemistry A, 2014. **2**(34): p. 13795-13800.
63. Schmidt, T., et al., *The oxygen reduction reaction on a Pt/carbon fuel cell catalyst in the presence of chloride anions.* Journal of Electroanalytical Chemistry, 2001. **508**(1): p. 41-47.
64. Harnisch, F., S. Wirth, and U. Schröder, *Effects of substrate and metabolite crossover on the cathodic oxygen reduction reaction in microbial fuel cells: Platinum vs. iron(II) phthalocyanine based electrodes.* Electrochemistry Communications, 2009. **11**(11): p. 2253-2256.
65. Liu, B., et al., *Cobalt porphyrin-based material as methanol tolerant cathode in single chamber microbial fuel cells (SCMFCs).* Journal of Power Sources, 2014. **257**: p. 246-253.
66. Kiely, P.D., et al., *Long-term cathode performance and the microbial communities that develop in microbial fuel cells fed different fermentation endproducts.* Bioresource Technology, 2011. **102**(1): p. 361-366.
67. Yuan, Y., S. Zhou, and J. Tang, *In Situ Investigation of Cathode and Local Biofilm Microenvironments Reveals Important Roles of OH– and Oxygen Transport in Microbial Fuel Cells.* Environmental Science & Technology, 2013. **47**(9): p. 4911-4917.
68. He, Z. and L.T. Angenent, *Application of Bacterial Biocathodes in Microbial Fuel Cells.* Electroanalysis, 2006. **18**(19-20): p. 2009-2015.
69. Jung, S. and J.M. Regan, *Influence of external resistance on electrogenesis, methanogenesis, and anode prokaryotic communities in microbial fuel cells.* Applied and Environmental Microbiology, 2011. **77**(2): p. 564-571.
70. He, Z. and F. Mansfeld, *Exploring the use of electrochemical impedance spectroscopy (EIS) in microbial fuel cell studies.* Energy & Environmental Science, 2009. **2**(2): p. 215.
71. Zhao, F., R.C. Slade, and J.R. Varcoe, *Techniques for the study and development of microbial fuel cells: an electrochemical perspective.* Chemical Society Reviews 2009. **38**(7): p. 1926-39.
72. Feng, Y., et al., *Effects of sulfide on microbial fuel cells with platinum and nitrogen-doped carbon powder cathodes.* Biosensors and Bioelectronics, 2012. **35**(1): p. 413-415.

73. Gong, X.-B., et al., *Silver–tungsten carbide nanohybrid for efficient electrocatalysis of oxygen reduction reaction in microbial fuel cell.* Journal of Power Sources, 2013. **225**: p. 330-337.
74. You, S., et al., *Enhanced Cathodic Oxygen Reduction and Power Production of Microbial Fuel Cell Based on Noble-Metal-Free Electrocatalyst Derived from Metal-Organic Frameworks.* Advanced Energy Materials, 2016. **6**(1): p. n/a-n/a.
75. Yuan, H. and Z. He, *Integrating membrane filtration into bioelectrochemical systems as next generation energy-efficient wastewater treatment technologies for water reclamation: A review.* Bioresource Technology, 2015. **195**: p. 202-209.
76. Malaeb, L., et al., *A Hybrid Microbial Fuel Cell Membrane Bioreactor with a Conductive Ultrafiltration Membrane Biocathode for Wastewater Treatment.* Environmental Science & Technology, 2013. **47**(20): p. 11821-11828.
77. Li, Y., et al., *Performance of carbon fiber cathode membrane with C–Mn–Fe–O catalyst in MBR–MFC for wastewater treatment.* Journal of Membrane Science, 2015. **484**: p. 27-34.
78. Liu, J., et al., *Integration of microbial fuel cell with independent membrane cathode bioreactor for power generation, membrane fouling mitigation and wastewater treatment.* International Journal of Hydrogen Energy, 2014. **39**(31): p. 17865-17872.
79. Li, Y., L. Liu, and F. Yang, *High flux carbon fiber cloth membrane with thin catalyst coating integrates bio-electricity generation in wastewater treatment.* Journal of Membrane Science, 2016. **505**: p. 130-137.
80. Wang, Y.-K., et al., *In-situ utilization of generated electricity in an electrochemical membrane bioreactor to mitigate membrane fouling.* Water Research, 2013. **47**(15): p. 5794-5800.
81. Yu, T., et al., *Catalytic and filterable polyester-filter membrane electrode with a high performance carbon foam-Fe-Co catalyst improved electricity generation and waste-water treatment in MBR-MFC.* RSC Advances, 2015. **5**(60): p. 48946-48953.
82. Ahmed, J., H.J. Kim, and S. Kim, *Embedded cobalt oxide nano particles on carbon could potentially improve oxygen reduction activity of cobalt phthalocyanine and its application in microbial fuel cells.* RSC Advances, 2014. **4**(83): p. 44065-44072.
83. Chen, J.-y., N. Li, and L. Zhao, *Three-dimensional electrode microbial fuel cell for hydrogen peroxide synthesis coupled to wastewater treatment.* Journal of Power Sources, 2014. **254**: p. 316-322.
84. Cao, X., et al., *A New Method for Water Desalination Using Microbial Desalination Cells.* Environmental Science & Technology, 2009. **43**(18): p. 7148-7152.
85. Kim, Y. and B.E. Logan, *Microbial desalination cells for energy production and desalination.* Desalination, 2013. **308**: p. 122-130.
86. Liu, H., S. Grot, and B.E. Logan, *Electrochemically assisted microbial production of hydrogen from acetate.* Environmental Science & Technology, 2005. **39**(11): p. 4317-4320.
87. Zhang, Y. and I. Angelidaki, *Microbial electrolysis cells turning to be versatile technology: Recent advances and future challenges.* Water Research, 2014. **56**: p. 11-25.
88. Yuan, H., et al., *Facile Synthesis of MoS2@CNT as an Effective Catalyst for Hydrogen Production in Microbial Electrolysis Cells.* ChemElectroChem, 2014. **1**(11): p. 1828-1833.

89. Fan, X., et al., *M3C (M: Fe, Co, Ni) nanocrystals encased in graphene nanoribbons: An active and stable bifunctional electrocatalyst for oxygen reduction and hydrogen evolution reactions.* ACS nano, 2015. **9**(7): p. 7407-7418.
90. Hou, Y., et al., *Strongly Coupled 3D Hybrids of N-doped Porous Carbon Nanosheet/CoNi Alloy-Encapsulated Carbon Nanotubes for Enhanced Electrocatalysis.* Small, 2015. **11**(44): p. 5940-5948.
91. Hou, Y., et al., *An Advanced Nitrogen-Doped Graphene/Cobalt-Embedded Porous Carbon Polyhedron Hybrid for Efficient Catalysis of Oxygen Reduction and Water Splitting.* Advanced Functional Materials, 2015. **25**(6): p. 872-882.
92. Lu, J., et al., *Core–Shell Nanocomposites Based on Gold Nanoparticle@Zinc–Iron-Embedded Porous Carbons Derived from Metal–Organic Frameworks as Efficient Dual Catalysts for Oxygen Reduction and Hydrogen Evolution Reactions.* ACS Catalysis, 2016. **6**(2): p. 1045-1053.
93. Hou, Y., et al., *Vertically oriented cobalt selenide/NiFe layered-double-hydroxide nanosheets supported on exfoliated graphene foil: an efficient 3D electrode for overall water splitting.* Energy & Environmental Science, 2016. **9**(2): p. 478-483.
94. Yuan, Y., S. Zhou, and L. Zhuang, *Polypyrrole/carbon black composite as a novel oxygen reduction catalyst for microbial fuel cells.* Journal of Power Sources, 2010. **195**(11): p. 3490-3493.
95. Zhang, X., et al., *Long-Term Performance of Chemically and Physically Modified Activated Carbons in Air Cathodes of Microbial Fuel Cells.* ChemElectroChem, 2014. **1**(11): p. 1859-1866.
96. Ghasemi, M., et al., *Activated carbon nanofibers as an alternative cathode catalyst to platinum in a two-chamber microbial fuel cell.* International Journal of Hydrogen Energy, 2011. **36**(21): p. 13746-13752.
97. Jiang, Y., et al., *Power generation using polyaniline/multi-walled carbon nanotubes as an alternative cathode catalyst in microbial fuel cells.* International Journal of Energy Research, 2014. **38**(11): p. 1416-1423.
98. Yuan, H., et al., *Porous Carbon Nanosheets Codoped with Nitrogen and Sulfur for Oxygen Reduction Reaction in Microbial Fuel Cells.* ACS Applied Materials & Interfaces, 2015. **7**(33): p. 18672-18678.
99. Liu, Q., et al., *Cellulose-derived nitrogen and phosphorus dual-doped carbon as high performance oxygen reduction catalyst in microbial fuel cell.* Journal of Power Sources, 2015. **273**: p. 1189-1193.
100. Park, H.I., et al., *Effective and Low-Cost Platinum Electrodes for Microbial Fuel Cells Deposited by Electron Beam Evaporation.* Energy & Fuels, 2007. **21**(5): p. 2984-2990.
101. An, J., et al., *Bifunctional Silver Nanoparticle Cathode in Microbial Fuel Cells for Microbial Growth Inhibition with Comparable Oxygen Reduction Reaction Activity.* Environmental Science & Technology, 2011. **45**(12): p. 5441-5446.
102. Dong, H., et al., *Carbon-supported perovskite oxides as oxygen reduction reaction catalyst in single chambered microbial fuel cells.* Journal of Chemical Technology & Biotechnology, 2013. **88**(5): p. 774-778.
103. Xia, X., et al., *Use of Pyrolyzed Iron Ethylenediaminetetraacetic Acid Modified Activated Carbon as Air–Cathode Catalyst in Microbial Fuel Cells.* ACS Applied Materials & Interfaces, 2013. **5**(16): p. 7862-7866.

104. Huang, J., et al., *Nickel oxide and carbon nanotube composite (NiO/CNT) as a novel cathode non-precious metal catalyst in microbial fuel cells.* Biosensors and Bioelectronics, 2015. **72**: p. 332-339.
105. Ma, M., et al., *Silver/iron oxide/graphitic carbon composites as bacteriostatic catalysts for enhancing oxygen reduction in microbial fuel cells.* Journal of Power Sources, 2015. **283**: p. 74-83.
106. Hou, Y., et al., *Nitrogen-doped graphene/CoNi alloy encased within bamboo-like carbon nanotube hybrids as cathode catalysts in microbial fuel cells.* Journal of Power Sources, 2016. **307**: p. 561-568.
107. Ahmed, J., et al., *Carbon supported cobalt oxide nanoparticles–iron phthalocyanine as alternative cathode catalyst for oxygen reduction in microbial fuel cells.* Journal of Power Sources, 2012. **208**: p. 170-175.
108. Wen, Z., et al., *Nitrogen-Enriched Core-Shell Structured Fe/Fe3C-C Nanorods as Advanced Electrocatalysts for Oxygen Reduction Reaction.* Advanced Materials, 2012. **24**(11): p. 1399-1404.
109. Xia, X., et al., *Oxygen-Reducing Biocathodes Operating with Passive Oxygen Transfer in Microbial Fuel Cells.* Environmental Science & Technology, 2013. **47**(4): p. 2085-2091.
110. Higgins, S.R., et al., *Hybrid Biofuel Cell: Microbial Fuel Cell with an Enzymatic Air-Breathing Cathode.* ACS Catalysis, 2011. **1**(9): p. 994-997.
111. Laursen, A.B., et al., *Molybdenum sulfides-efficient and viable materials for electro - and photoelectrocatalytic hydrogen evolution.* Energy & Environmental Science, 2012. **5**(2): p. 5577-5591.
112. Nørskov, J.K., et al., *Trends in the exchange current for hydrogen evolution.* Journal of The Electrochemical Society, 2005. **152**(3): p. J23-J26.
113. Logan, B.E., et al., *Microbial fuel cells: methodology and technology.* Environmental Science & Technology, 2006. **40**(17): p. 5181-5192.
114. Benck, J.D., et al., *Catalyzing the Hydrogen Evolution Reaction (HER) with Molybdenum Sulfide Nanomaterials.* ACS Catalysis, 2014. **4**(11): p. 3957-3971.
115. Bard, A.J. and L.R. Faulkner, *Electrochemical methods: fundamentals and applications*. Vol. 2. 1980: Wiley New York.
116. Hou, Y., et al., *Improved Hydrogen Production in the Microbial Electrolysis Cell by Inhibiting Methanogenesis Using Ultraviolet Irradiation.* Environmental Science & Technology, 2014. **48**(17): p. 10482-10488.
117. Cusick, R.D., et al., *Performance of a pilot-scale continuous flow microbial electrolysis cell fed winery wastewater.* Applied Microbiology and Biotechnology, 2011. **89**(6): p. 2053-2063.
118. Pasupuleti, S.B., et al., *Development of exoelectrogenic bioanode and study on feasibility of hydrogen production using abiotic VITO-CoRE™ and VITO-CASE™ electrodes in a single chamber microbial electrolysis cell (MEC) at low current densities.* Bioresource Technology, 2015. **195**: p. 131-138.
119. Dai, H., et al., *Electrochemical evaluation of nano-Mg(OH)2/graphene as a catalyst for hydrogen evolution in microbial electrolysis cell.* Fuel, 2016. **174**: p. 251-256.
120. Katuri, K.P., et al., *A Novel Anaerobic Electrochemical Membrane Bioreactor (AnEMBR) with Conductive Hollow-fiber Membrane for Treatment of Low-Organic Strength Solutions.* Environmental Science & Technology, 2014. **48**(21): p. 12833-12841.

121. Werner, C.M., et al., *Graphene-Coated Hollow Fiber Membrane as the Cathode in Anaerobic Electrochemical Membrane Bioreactors – Effect of Configuration and Applied Voltage on Performance and Membrane Fouling.* Environmental Science & Technology, 2016. **50**(8): p. 4439-4447.
122. Selembo, P.A., M.D. Merrill, and B.E. Logan, *Hydrogen production with nickel powder cathode catalysts in microbial electrolysis cells.* International Journal of Hydrogen Energy, 2010. **35**(2): p. 428-437.
123. Tenca, A., et al., *Evaluation of low cost cathode materials for treatment of industrial and food processing wastewater using microbial electrolysis cells.* International Journal of Hydrogen Energy, 2013. **38**(4): p. 1859-1865.
124. Lu, L., et al., *Nickel based catalysts for highly efficient H2 evolution from wastewater in microbial electrolysis cells.* Electrochimica Acta, 2016. **206**: p. 381-387.
125. Croese, E., et al., *Analysis of the microbial community of the biocathode of a hydrogen-producing microbial electrolysis cell.* Applied Microbiology and Biotechnology, 2011. **92**(5): p. 1083-1093.
126. Wang, Y., et al., *Hydrogen production using biocathode single-chamber microbial electrolysis cells fed by molasses wastewater at low temperature.* International Journal of Hydrogen Energy, 2014. **39**(33): p. 19369-19375.
127. Liu, Q., et al., *Multiple syntrophic interactions drive biohythane production from waste sludge in microbial electrolysis cells.* Biotechnology for Biofuels, 2016. **9**(1): p. 162.
128. Parameswaran, P., et al., *Syntrophic interactions among anode respiring bacteria (ARB) and Non-ARB in a biofilm anode: electron balances.* Biotechnology and Bioengineering, 2009. **103**(3): p. 513-523.
129. Rago, L., et al., *Microbial community analysis in a long-term membrane-less microbial electrolysis cell with hydrogen and methane production.* Bioelectrochemistry, 2015. **106, Part B**: p. 359-368.
130. Yuan, H., I.M. Abu-Reesh, and Z. He, *Mathematical Modeling Assisted Investigation of Forward Osmosis as Pretreatment for Microbial Desalination Cells to Achieve Continuous Water Desalination and Wastewater Treatment.* Journal of Membrane Science, 2016. **502**: p. 116–123.
131. Ping, Q., et al., *Mathematical Model of Dynamic Behavior of Microbial Desalination Cells for Simultaneous Wastewater Treatment and Water Desalination.* Environmental Science & Technology, 2014. **48**(21): p. 13010-13019.
132. Pinto, R.P., et al., *Multi-Population Model of a Microbial Electrolysis Cell.* Environmental Science & Technology, 2011. **45**(11): p. 5039-5046.
133. Ruiz, Y., J.A. Baeza, and A. Guisasola, *Revealing the proliferation of hydrogen scavengers in a single-chamber microbial electrolysis cell using electron balances.* International Journal of Hydrogen Energy, 2013. **38**(36): p. 15917-15927.
134. Santos, A., W. Ma, and S.J. Judd, *Membrane bioreactors: Two decades of research and implementation.* Desalination, 2011. **273**(1): p. 148-154.
135. Ozgun, H., et al., *A review of anaerobic membrane bioreactors for municipal wastewater treatment: Integration options, limitations and expectations.* Separation and Purification Technology, 2013. **118**(0): p. 89-104.
136. Wang, Y.-K., et al., *Development of a Novel Bioelectrochemical Membrane Reactor for Wastewater Treatment.* Environmental Science & Technology, 2011. **45**(21): p. 9256-9261.

137. Li, J., Z. Ge, and Z. He, *A fluidized bed membrane bioelectrochemical reactor for energy-efficient wastewater treatment.* Bioresource Technology, 2014. **167**(0): p. 310-315.
138. Ge, Z., et al., *Reducing effluent discharge and recovering bioenergy in an osmotic microbial fuel cell treating domestic wastewater.* Desalination, 2013. **312**: p. 52-59.
139. Kim, K.-Y., et al., *Polydopamine coating effects on ultrafiltration membrane to enhance power density and mitigate biofouling of ultrafiltration microbial fuel cells (UF-MFCs).* Water Research, 2014. **54**(0): p. 62-68.
140. Xu, L., et al., *Anti-fouling performance and mechanism of anthraquinone/polypyrrole composite modified membrane cathode in a novel MFC-aerobic MBR coupled system.* RSC Advances, 2015. **5**(29): p. 22533-22543.
141. Zuo, K., et al., *Carbon filtration cathode in microbial fuel cell to enhance wastewater treatment.* Bioresource technology, 2015. **185**: p. 426-430.
142. Ng, A.N.L. and A.S. Kim, *A mini-review of modeling studies on membrane bioreactor (MBR) treatment for municipal wastewaters.* Desalination, 2007. **212**(1–3): p. 261-281.
143. Wang, Y.-P., et al., *A microbial fuel cell–membrane bioreactor integrated system for cost-effective wastewater treatment.* Applied Energy, 2012. **98**(0): p. 230-235.
144. Liu, J., et al., *Integration of bio-electrochemical cell in membrane bioreactor for membrane cathode fouling reduction through electricity generation.* Journal of Membrane Science, 2013. **430**(0): p. 196-202.
145. Wang, Z., et al., *A Bioelectrochemically-Assisted Membrane Bioreactor for Simultaneous Wastewater Treatment and Energy Production.* Chemical Engineering & Technology, 2013. **36**(12): p. 2044-2050.
146. Zhang, G., et al., *Membrane filtration biocathode microbial fuel cell for nitrogen removal and electricity generation.* Enzyme and Microbial Technology, 2014. **60**(0): p. 56-63.
147. Tang, X., et al., *Microfiltration membrane performance in two-chamber microbial fuel cells.* Biochemical Engineering Journal, 2010. **52**(2–3): p. 194-198.
148. Kim, J.R., et al., *Power Generation Using Different Cation, Anion, and Ultrafiltration Membranes in Microbial Fuel Cells.* Environmental Science & Technology, 2007. **41**(3): p. 1004-1009.
149. Hou, B., J. Sun, and Y.-y. Hu, *Simultaneous Congo red decolorization and electricity generation in air-cathode single-chamber microbial fuel cell with different microfiltration, ultrafiltration and proton exchange membranes.* Bioresource Technology, 2011. **102**(6): p. 4433-4438.
150. Ge, Z., Q. Ping, and Z. He, *Hollow-fiber membrane bioelectrochemical reactor for domestic wastewater treatment.* Journal of Chemical Technology & Biotechnology, 2013. **88**(8): p. 1584-1590.
151. Kim, K.-Y., et al., *High-quality effluent and electricity production from non-CEM based flow-through type microbial fuel cell.* Chemical Engineering Journal, 2013. **218**(0): p. 19-23.
152. Li, J., Z. Ge, and Z. He, *Advancing membrane bioelectrochemical reactor (MBER) with hollow-fiber membranes installed in the cathode compartment.* Journal of Chemical Technology & Biotechnology, 2013. **89**(9): p. 1330-1336.
153. Su, X., et al., *Performance of a combined system of microbial fuel cell and membrane bioreactor: Wastewater treatment, sludge reduction, energy recovery and membrane fouling.* Biosensors and Bioelectronics, 2013. **49**(0): p. 92-98.

154. Wang, J., et al., *In situ investigation of processing property in combination with integration of microbial fuel cell and tubular membrane bioreactor.* Bioresource Technology, 2013. **149**(0): p. 163-168.
155. Wang, J., et al., *Bioelectricity generation in an integrated system combining microbial fuel cell and tubular membrane reactor: Effects of operation parameters performing a microbial fuel cell-based biosensor for tubular membrane bioreactor.* Bioresource Technology, 2014. **170**(0): p. 483-490.
156. Kim, K.-Y., et al., *Anode direct contact for enhancing power generation and biofouling reduction in ultrafiltration microbial fuel cells.* Journal of Chemical Technology & Biotechnology, 2014. **89**(11): p. 1767-1771.
157. Köroğlu, E.O., et al., *Novel design of a multitube microbial fuel cell (UM2FC) for energy recovery and treatment of membrane concentrates.* Biomass and Bioenergy, 2014. **69**(0): p. 58-65.
158. Ren, L., Y. Ahn, and B.E. Logan, *A Two-Stage Microbial Fuel Cell and Anaerobic Fluidized Bed Membrane Bioreactor (MFC-AFMBR) System for Effective Domestic Wastewater Treatment.* Environmental Science & Technology, 2014. **48**(7): p. 4199-4206.
159. Tian, Y., et al., *Assessment of an anaerobic membrane bio-electrochemical reactor (AnMBER) for wastewater treatment and energy recovery.* Journal of Membrane Science, 2014. **450**(0): p. 242-248.
160. Kim, K.-Y., et al., *Influence of pressurized anode chamber on ion transports and power generation of UF membrane microbial fuel cells (UF-MFCs).* Journal of Power Sources, 2015. **279**(0): p. 731-736.
161. Li, J. and Z. He, *Optimizing the Performance of a Membrane Bio-electrochemical Reactor Using Anion Exchange Membrane for Wastewater Treatment.* Environmental Science: Water Research & Technology, 2015. **1**: p. 355-362.
162. Tian, Y., et al., *In-situ integration of microbial fuel cell with hollow-fiber membrane bioreactor for wastewater treatment and membrane fouling mitigation.* Biosensors and Bioelectronics, 2015. **64**(0): p. 189-195.
163. Jones, O., N. Voulvoulis, and J. Lester, *Potential ecological and human health risks associated with the presence of pharmaceutically active compounds in the aquatic environment.* Critical Reviews in Toxicology, 2004. **34**(4): p. 335-350.
164. Yuan, H., et al., *Determination of optimal conditions for 5-methyl-benzotriazole biodegradation with activated sludge communities by dilution of the inoculum.* Science of The Total Environment, 2014. **487**(0): p. 756-762.
165. Pruden, A., *Balancing Water Sustainability and Public Health Goals in the Face of Growing Concerns about Antibiotic Resistance.* Environmental Science & Technology, 2013. **48**(1): p. 5-14.
166. Tran, N.H., et al., *Insight into metabolic and cometabolic activities of autotrophic and heterotrophic microorganisms in the biodegradation of emerging trace organic contaminants.* Bioresource Technology, 2013. **146**(0): p. 721-731.
167. Feng, H., et al., *Enhanced removal of p-fluoronitrobenzene using bioelectrochemical system.* Water Research, 2014. **60**(0): p. 54-63.
168. Zhao, S., et al., *Recent developments in forward osmosis: Opportunities and challenges.* Journal of Membrane Science, 2012. **396**: p. 1-21.

169. Fang, Y., et al., *Evaluation of the pore size distribution of a forward osmosis membrane in three different ways.* Journal of Membrane Science, 2014. **454**(0): p. 390-397.
170. Lutchmiah, K., et al., *Forward osmosis for application in wastewater treatment: A review.* Water Research, 2014. **58**: p. 179-197.
171. Lu, Y., et al., *When Bioelectrochemical Systems Meet Forward Osmosis: Accomplishing Wastewater Treatment and Reuse through Synergy.* Water, 2015. **7**(1): p. 38-50.
172. Zhang, F., K.S. Brastad, and Z. He, *Integrating forward osmosis into microbial fuel cells for wastewater treatment, water extraction and bioelectricity generation.* Environmental Science & Technology, 2011. **45**(15): p. 6690-6.
173. Ge, Z. and Z. He, *Effects of draw solutions and membrane conditions on electricity generation and water flux in osmotic microbial fuel cells.* Bioresource Technology, 2012. **109**: p. 70-6.
174. Werner, C.M., et al., *Wastewater treatment, energy recovery and desalination using a forward osmosis membrane in an air-cathode microbial osmotic fuel cell.* Journal of Membrane Science, 2013. **428**: p. 116-122.
175. Pardeshi, P. and A. Mungray, *High Flux Layer by Layer Polyelectrolyte FO Membrane: Toward Enhanced Performance for Osmotic Microbial Fuel Cell.* International Journal of Polymeric Materials and Polymeric Biomaterials, 2014. **63**(12): p. 595-601.
176. Lee, M.-Y., et al., *Evaluation of hydrogen production and internal resistance in forward osmosis membrane integrated microbial electrolysis cells.* Bioresource Technology, 2015. **184**: p. 106-112.
177. Rabaey, K. and R.A. Rozendal, *Microbial electrosynthesis - revisiting the electrical route for microbial production.* Nature Reviews Microbiology, 2010. **8**(10): p. 706-16.
178. Zhang, B. and Z. He, *Integrated salinity reduction and water recovery in an osmotic microbial desalination cell.* RSC Advances, 2012. **2**(8): p. 3265-3269.
179. Zhang, B. and Z. He, *Improving water desalination by hydraulically coupling an osmotic microbial fuel cell with a microbial desalination cell.* Journal of Membrane Science, 2013. **441**: p. 18-24.
180. Yuan, H., I.M. Abu-Reesh, and Z. He, *Enhancing Desalination and Wastewater Treatment by Coupling Microbial Desalination Cells with Forward Osmosis.* Chemical Engineering Journal, 2015. **270**: p. 437-443.
181. Logan, B.E. and M. Elimelech, *Membrane-based processes for sustainable power generation using water.* Nature, 2012. **488**(7411): p. 313-319.
182. Yuan, H., et al., *Bioelectrochemical production of hydrogen in an innovative pressure-retarded osmosis/microbial electrolysis cell system: experiments and modeling.* Biotechnology for Biofuels, 2015. **8**(116): p. 1-12.
183. McCutcheon, J.R., R.L. McGinnis, and M. Elimelech, *A novel ammonia—carbon dioxide forward (direct) osmosis desalination process.* Desalination, 2005. **174**(1): p. 1-11.
184. Qin, M. and Z. He, *Self-Supplied Ammonium Bicarbonate Draw Solute for Achieving Wastewater Treatment and Recovery in a Microbial Electrolysis Cell-Forward Osmosis-Coupled System.* Environmental Science & Technology Letters, 2014. **1**(10): p. 437-441.
185. McCutcheon, J.R. and M. Elimelech, *Influence of concentrative and dilutive internal concentration polarization on flux behavior in forward osmosis.* Journal of Membrane Science, 2006. **284**(1): p. 237-247.
186. Pruden, A., et al., *Antibiotic Resistance Genes as Emerging Contaminants: Studies in Northern Colorado†.* Environmental Science & Technology, 2006. **40**(23): p. 7445-7450.

187. Ghosh, S., S.J. Ramsden, and T.M. LaPara, *The role of anaerobic digestion in controlling the release of tetracycline resistance genes and class 1 integrons from municipal wastewater treatment plants.* Applied Microbiology and Biotechnology, 2009. **84**(4): p. 791-796.
188. Christgen, B., et al., *Metagenomics Shows That Low-Energy Anaerobic−Aerobic Treatment Reactors Reduce Antibiotic Resistance Gene Levels from Domestic Wastewater.* Environmental Science & Technology, 2015. **49**(4): p. 2577-2584.
189. Andersson, D.I. and D. Hughes, *Persistence of antibiotic resistance in bacterial populations.* FEMS microbiology reviews, 2011. **35**(5): p. 901-911.
190. UNESCO, *The United Nations world water development report 2014: water and energy*. 2014.
191. Semiat, R., *Energy Issues in Desalination Processes.* Environmental Science & Technology, 2008. **42**(22): p. 8193-8201.
192. Zhang, F. and Z. He, *Scaling up microbial desalination cell system with a post-aerobic process for simultaneous wastewater treatment and seawater desalination.* Desalination, 2015. **360**(0): p. 28-34.
193. Rabaey, K., et al., *Microbial ecology meets electrochemistry: electricity-driven and driving communities.* The ISME journal, 2007. **1**(1): p. 9-18.
194. Sun, D., et al., *Geobacter sp. SD-1 with enhanced electrochemical activity in high-salt concentration solutions.* Environmental Microbiology Reports, 2014: p. n/a-n/a.
195. Oren, A., *Thermodynamic limits to microbial life at high salt concentrations.* Environmental Microbiology, 2011. **13**(8): p. 1908-1923.
196. Widder, S., et al., *Challenges in microbial ecology: building predictive understanding of community function and dynamics.* The ISME journal, 2016. **10**(11): p. 2557-2568.
197. Larsen, P.E., D. Field, and J.A. Gilbert, *Predicting bacterial community assemblages using an artificial neural network approach.* Nature Methods, 2012. **9**(6): p. 621-625.
198. Kuang, J., et al., *Predicting taxonomic and functional structure of microbial communities in acid mine drainage.* The ISME Journal, 2016. **10**(6): p. 1527-1539.
199. Jacobson, K.S., D.M. Drew, and Z. He, *Efficient salt removal in a continuously operated upflow microbial desalination cell with an air cathode.* Bioresource Technology, 2011. **102**(1): p. 376-80.
200. He, Z., et al., *An upflow microbial fuel cell with an interior cathode: assessment of the internal resistance by impedance spectroscopy.* Environmental Science & Technology, 2006. **40**(17): p. 5212-5217.
201. Miyahara, M., A. Kouzuma, and K. Watanabe, *Sodium chloride concentration determines exoelectrogens in anode biofilms occurring from mangrove-grown brackish sediment.* Bioresource Technology, 2016. **218**: p. 674-679.
202. Xiao, Y., et al., *Pyrosequencing reveals a core community of anodic bacterial biofilms in bioelectrochemical systems from China.* Frontiers in Microbiology, 2015. **6**.
203. Caporaso, J.G., et al., *Ultra-high-throughput microbial community analysis on the Illumina HiSeq and MiSeq platforms.* The ISME journal, 2012. **6**(8): p. 1621-1624.
204. Edgar, R.C., *Search and clustering orders of magnitude faster than BLAST.* Bioinformatics, 2010. **26**(19): p. 2460-2461.
205. Wang, Q., et al., *Naive Bayesian classifier for rapid assignment of rRNA sequences into the new bacterial taxonomy.* Applied and environmental microbiology, 2007. **73**(16): p. 5261-5267.

206. Quast, C., et al., *The SILVA ribosomal RNA gene database project: improved data processing and web-based tools.* Nucleic Acids Research, 2013. **41**(D1): p. D590-D596.
207. Langille, M.G.I., et al., *Predictive functional profiling of microbial communities using 16S rRNA marker gene sequences.* Nature Biotechnology, 2013. **31**(9): p. 814-821.
208. Caporaso, J.G., et al., *QIIME allows analysis of high-throughput community sequencing data.* Nature methods, 2010. **7**(5): p. 335-336.
209. Krzywinski, M., et al., *Circos: an information aesthetic for comparative genomics.* Genome research, 2009. **19**(9): p. 1639-1645.
210. Bro, R., et al., *Cross-validation of component models: a critical look at current methods.* Analytical and bioanalytical chemistry, 2008. **390**(5): p. 1241-1251.
211. Koseki, S. and J. Nonaka, *Alternative approach to modeling bacterial lag time, using logistic regression as a function of time, temperature, pH, and sodium chloride concentration.* Applied and Environmental Microbiology, 2012. **78**(17): p. 6103-6112.
212. Logan, B.E. and J.M. Regan, *Electricity-producing bacterial communities in microbial fuel cells.* Trends in Microbiology, 2006. **14**(12): p. 512-518.
213. Ping, Q. and Z. He, *Effects of inter-membrane distance and hydraulic retention time on the desalination performance of microbial desalination cells.* Desalination and Water Treatment, 2013. **52**: p. 1324-1331.
214. Oren, A., *Life at High Salt Concentrations*, in *The Prokaryotes: Prokaryotic Communities and Ecophysiology*, E. Rosenberg, et al., Editors. 2013, Springer Berlin Heidelberg: Berlin, Heidelberg. p. 421-440.
215. Herlemann, D.P.R., et al., *Transitions in bacterial communities along the 2000[thinsp]km salinity gradient of the Baltic Sea.* The ISME journal, 2011. **5**(10): p. 1571-1579.
216. Rabaey, K., et al., *Biofuel cells select for microbial consortia that self-mediate electron transfer.* Applied and Environmental Microbiology, 2004. **70**(9): p. 5373-5382.
217. Venkataraman, A., et al., *Quorum sensing regulates electric current generation of Pseudomonas aeruginosa PA14 in bioelectrochemical systems.* Electrochemistry Communications, 2010. **12**(3): p. 459-462.
218. Whiteson, K.L., et al., *Breath gas metabolites and bacterial metagenomes from cystic fibrosis airways indicate active pH neutral 2,3-butanedione fermentation.* The ISME journal, 2014. **8**(6): p. 1247-1258.
219. Dietrich, L.E.P., et al., *Redox-Active Antibiotics Control Gene Expression and Community Behavior in Divergent Bacteria.* Science, 2008. **321**(5893): p. 1203-1206.
220. Zhang, H.-K., et al., *Cr(VI) Reduction and Cr(III) Immobilization by Acinetobacter sp. HK-1 with the Assistance of a Novel Quinone/Graphene Oxide Composite.* Environmental Science & Technology, 2014. **48**(21): p. 12876-12885.
221. Li, Y., *The Current Response of a Mediated Biological Fuel Cell with Acinetobacter calcoaceticus: The Role of Mediator Adsorption and Reduction Kinetics*. 2013.
222. Liu, H., et al., *Extracellular Electron Transfer of a Highly Adhesive and Metabolically Versatile Bacterium.* ChemPhysChem, 2013. **14**(11): p. 2407-2412.
223. Pham, T.H., et al., *Metabolites produced by Pseudomonas sp. enable a Gram-positive bacterium to achieve extracellular electron transfer.* Applied Microbiology and Biotechnology, 2008. **77**(5): p. 1119-1129.
224. Venkataraman, A., et al., *Metabolite-based mutualism between Pseudomonas aeruginosa PA14 and Enterobacter aerogenes enhances current generation in bioelectrochemical systems.* Energy & Environmental Science, 2011. **4**(11): p. 4550.

225. Grabowski, A., et al., *Petrimonas sulfuriphila gen. nov., sp. nov., a mesophilic fermentative bacterium isolated from a biodegraded oil reservoir.* International Journal of Systematic and Evolutionary Microbiology, 2005. **55**(3): p. 1113-1121.
226. Kim, N.-K., S. Oh, and W.-T. Liu, *Enrichment and characterization of microbial consortia degrading soluble microbial products discharged from anaerobic methanogenic bioreactors.* Water Research, 2016. **90**: p. 395-404.
227. Zhang, K., L. Song, and X. Dong, *Proteiniclasticum ruminis gen. nov., sp. nov., a strictly anaerobic proteolytic bacterium isolated from yak rumen.* International Journal of Systematic and Evolutionary Microbiology, 2010. **60**(9): p. 2221-2225.
228. Sleat, R., R.A. Mah, and R. Robinson, *Acetoanaerobium noterae gen. nov., sp. nov.: an Anaerobic Bacterium That Forms Acetate from H2 and CO2.* International Journal of Systematic and Evolutionary Microbiology, 1985. **35**(1): p. 10-15.
229. Vandieken, V., et al., *Three manganese oxide-rich marine sediments harbor similar communities of acetate-oxidizing manganese-reducing bacteria.* The ISME journal, 2012. **6**(11): p. 2078-2090.
230. VanEngelen, M.R., et al., *Fe(III), Cr(VI), and Fe(III) mediated Cr(VI) reduction in alkaline media using a Halomonas isolate from Soap Lake, Washington.* Biodegradation, 2008. **19**(6): p. 841-850.
231. Fedorovich, V., et al., *Novel electrochemically active bacterium phylogenetically related to Arcobacter butzleri, isolated from a microbial fuel cell.* Applied and Environmental Microbiology, 2009. **75**(23): p. 7326-7334.
232. Hugenholtz, P., S.D. Hooper, and N.C. Kyrpides, *Focus: Synergistetes.* Environmental Microbiology, 2009. **11**(6): p. 1327-1329.
233. Shi, L., et al., *Extracellular electron transfer mechanisms between microorganisms and minerals.* Nature Reviews Microbiology, 2016. **14**(10): p. 651-662.
234. Harnisch, F. and S. Freguia, *A Basic Tutorial on Cyclic Voltammetry for the Investigation of Electroactive Microbial Biofilms.* Chemistry – An Asian Journal, 2012. **7**(3): p. 466-475.
235. Bellin, D.L., et al., *Integrated circuit-based electrochemical sensor for spatially resolved detection of redox-active metabolites in biofilms.* Nature Communications, 2014. **5**: p. 3256.
236. Tremblay, P.-L., et al., *A genetic system for Geobacter metallireducens: role of the flagellin and pilin in the reduction of Fe(III) oxide.* Environmental Microbiology Reports, 2012. **4**(1): p. 82-88.
237. Berg, I.A., *Ecological aspects of the distribution of different autotrophic CO2 fixation pathways.* Applied and Environmental Microbiology, 2011. **77**(6): p. 1925-1936.
238. D'Souza-Ault, M., L. Smith, and G. Smith, *Roles of N-acetylglutaminylglutamine amide and glycine betaine in adaptation of Pseudomonas aeruginosa to osmotic stress.* Applied and environmental microbiology, 1993. **59**(2): p. 473-478.
239. Allison, S.D. and J.B.H. Martiny, *Resistance, resilience, and redundancy in microbial communities.* Proceedings of the National Academy of Sciences, 2008. **105**(Supplement 1): p. 11512-11519.
240. Ben Hania, W., et al., *Characterization of the first cultured representative of a Bacteroidetes clade specialized on the scavenging of cyanobacteria.* Environmental Microbiology, 2017. **19**(3): p. 1134-1148.

241. Nevin, K.P., et al., *Electrosynthesis of organic compounds from carbon dioxide is catalyzed by a diversity of acetogenic microorganisms.* Applied and Environmental Microbiology, 2011. **77**(9): p. 2882-2886.
242. Metcalf, J.L., et al., *Microbial community assembly and metabolic function during mammalian corpse decomposition.* Science, 2016. **351**(6269): p. 158-162.
243. Luo, S., et al., *A review of modeling bioelectrochemical systems: engineering and statistical aspects.* Energies, 2016. **9**(2): p. 111.
244. Crabtree, G.W., M.S. Dresselhaus, and M.V. Buchanan, *The hydrogen economy.* Physics Today, 2004. **57**(12): p. 39-44.
245. Christopher, K. and R. Dimitrios, *A review on exergy comparison of hydrogen production methods from renewable energy sources.* Energy & Environmental Science, 2012. **5**(5): p. 6640-6651.
246. Logan, B.E., et al., *Microbial Electrolysis Cells for High Yield Hydrogen Gas Production from Organic Matter.* Environmental Science & Technology, 2008. **42**(23): p. 8630-8640.
247. Yossan, S., et al., *Hydrogen production in microbial electrolysis cells: Choice of catholyte.* International Journal of Hydrogen Energy, 2013. **38**(23): p. 9619-9624.
248. Zhang, Y. and I. Angelidaki, *Microbial electrolysis cells turning to be versatile technology: recent advances and future challenges.* Water Research, 2014(0).
249. Wang, H., et al., *Self-Biased Solar-Microbial Device for Sustainable Hydrogen Generation.* ACS Nano, 2013. **7**(10): p. 8728-8735.
250. Call, D. and B.E. Logan, *Hydrogen Production in a Single Chamber Microbial Electrolysis Cell Lacking a Membrane.* Environmental Science & Technology, 2008. **42**(9): p. 3401-3406.
251. Rozendal, R.A., et al., *Hydrogen Production with a Microbial Biocathode.* Environmental Science & Technology, 2007. **42**(2): p. 629-634.
252. Jeremiasse, A.W., et al., *Ni foam cathode enables high volumetric H< sub> 2</sub> production in a microbial electrolysis cell.* International Journal of Hydrogen Energy, 2010. **35**(23): p. 12716-12723.
253. Hu, H., Y. Fan, and H. Liu, *Hydrogen production in single-chamber tubular microbial electrolysis cells using non-precious-metal catalysts.* International Journal of Hydrogen Energy, 2009. **34**(20): p. 8535-8542.
254. Mitov, M., et al., *Novel nanostructured electrocatalysts for hydrogen evolution reaction in neutral and weak acidic solutions.* International Journal of Hydrogen Energy, 2012. **37**(21): p. 16522-16526.
255. Huang, Y.-X., et al., *A new cathodic electrode deposit with palladium nanoparticles for cost-effective hydrogen production in a microbial electrolysis cell.* International Journal of Hydrogen Energy, 2011. **36**(4): p. 2773-2776.
256. Xiao, L., et al., *Carbon/iron-based nanorod catalysts for hydrogen production in microbial electrolysis cells.* Nano Energy, 2012. **1**(5): p. 751-756.
257. Hinnemann, B., et al., *Biomimetic Hydrogen Evolution: MoS2 Nanoparticles as Catalyst for Hydrogen Evolution.* Journal of the American Chemical Society, 2005. **127**(15): p. 5308-5309.
258. Jaramillo, T.F., et al., *Identification of active edge sites for electrochemical H2 evolution from MoS2 nanocatalysts.* Science, 2007. **317**(5834): p. 100-102.

259. Wang, H., et al., *Electrochemical tuning of vertically aligned MoS2 nanofilms and its application in improving hydrogen evolution reaction.* Proceedings of the National Academy of Sciences, 2013. **110**(49): p. 19701-19706.
260. Lukowski, M.A., et al., *Enhanced Hydrogen Evolution Catalysis from Chemically Exfoliated Metallic MoS2 Nanosheets.* Journal of the American Chemical Society, 2013.
261. Li, Y., et al., *MoS2 Nanoparticles Grown on Graphene: An Advanced Catalyst for the Hydrogen Evolution Reaction.* Journal of the American Chemical Society, 2011. **133**(19): p. 7296-7299.
262. Tokash, J.C. and B.E. Logan, *Electrochemical evaluation of molybdenum disulfide as a catalyst for hydrogen evolution in microbial electrolysis cells.* International Journal of Hydrogen Energy, 2011. **36**(16): p. 9439-9445.
263. Kong, D., et al., *Synthesis of MoS2 and MoSe2 Films with Vertically Aligned Layers.* Nano Letters, 2013. **13**(3): p. 1341-1347.
264. Kibsgaard, J., et al., *Engineering the surface structure of MoS2 to preferentially expose active edge sites for electrocatalysis.* Nature Materials, 2012. **11**(11): p. 963-969.
265. Wen, Z., et al., *Nitrogen-enriched core-shell structured Fe/Fe(3)C-C nanorods as advanced electrocatalysts for oxygen reduction reaction.* Advanced Materials, 2012. **24**(11): p. 1399-404.
266. Chung, D.Y., et al., *Edge-exposed MoS2 nano-assembled structures as efficient electrocatalysts for hydrogen evolution reaction.* Nanoscale, 2014.
267. Ge, X., et al., *Nanoporous Metal Enhanced Catalytic Activities of Amorphous Molybdenum Sulfide for High-Efficiency Hydrogen Production.* Advanced Materials, 2014: p. n/a-n/a.
268. Chen, Z., et al., *Core–shell MoO3–MoS2 Nanowires for Hydrogen Evolution: A Functional Design for Electrocatalytic Materials.* Nano Letters, 2011. **11**(10): p. 4168-4175.
269. Yan, Y., et al., *Facile synthesis of low crystalline MoS 2 nanosheet-coated CNTs for enhanced hydrogen evolution reaction.* Nanoscale, 2013. **5**(17): p. 7768-7771.
270. Bindumadhavan, K., S.K. Srivastava, and S. Mahanty, *MoS2-MWCNT hybrids as a superior anode in lithium-ion batteries.* Chemical Communications, 2013. **49**(18): p. 1823-1825.
271. Li, D.J., et al., *Molybdenum Sulfide/N-Doped CNT Forest Hybrid Catalysts for High-Performance Hydrogen Evolution Reaction.* Nano Letters, 2014. **14**(3): p. 1228-1233.
272. Lee, K., L. Zhang, and J. Zhang, *PEM Fuel Cell Electrocatalysts and Catalyst Layers*. 2008: Springer London.
273. Cao, Y.L., et al., *The mechanism of oxygen reduction on MnO2-catalyzed air cathode in alkaline solution.* Journal of Electroanalytical Chemistry, 2003. **557**(0): p. 127-134.
274. Zhao, F., et al., *Application of pyrolysed iron(II) phthalocyanine and CoTMPP based oxygen reduction catalysts as cathode materials in microbial fuel cells.* Electrochemistry Communications, 2005. **7**(12): p. 1405-1410.
275. Lota, G., K. Fic, and E. Frackowiak, *Carbon nanotubes and their composites in electrochemical applications.* Energy & Environmental Science, 2011. **4**(5): p. 1592-1605.
276. De Volder, M.F., et al., *Carbon nanotubes: present and future commercial applications.* Science, 2013. **339**(6119): p. 535-539.

277. Yang, B., et al., *N-doped carbon xerogels as adsorbents for the removal of heavy metal ions from aqueous solution.* RSC Advances, 2015. **5**(10): p. 7182-7191.
278. Ghasemi, M., et al., *Nano-structured carbon as electrode material in microbial fuel cells: A comprehensive review.* Journal of Alloys and Compounds, 2013. **580**(0): p. 245-255.
279. Xiao, L., et al., *Crumpled graphene particles for microbial fuel cell electrodes.* Journal of Power Sources, 2012. **208**: p. 187-192.
280. Paraknowitsch, J.P. and A. Thomas, *Doping carbons beyond nitrogen: an overview of advanced heteroatom doped carbons with boron, sulphur and phosphorus for energy applications.* Energy & Environmental Science, 2013. **6**(10): p. 2839-2855.
281. Yang, Z., et al., *Sulfur-Doped Graphene as an Efficient Metal-free Cathode Catalyst for Oxygen Reduction.* ACS Nano, 2012. **6**(1): p. 205-211.
282. Wohlgemuth, S.-A., et al., *A one-pot hydrothermal synthesis of sulfur and nitrogen doped carbon aerogels with enhanced electrocatalytic activity in the oxygen reduction reaction.* Green Chemistry, 2012. **14**(5): p. 1515-1523.
283. Liang, J., et al., *Sulfur and Nitrogen Dual-Doped Mesoporous Graphene Electrocatalyst for Oxygen Reduction with Synergistically Enhanced Performance.* Angewandte Chemie International Edition, 2012. **51**(46): p. 11496-11500.
284. Liu, Z., et al., *Sulfur-nitrogen co-doped three-dimensional carbon foams with hierarchical pore structures as efficient metal-free electrocatalysts for oxygen reduction reactions.* Nanoscale, 2013. **5**(8): p. 3283-3288.
285. Li, W.-W., H.-q. Yu, and Z. He, *Towards sustainable wastewater treatment by using microbial fuel cells-centered technologies.* Energy & Environmental Science, 2013. **7**(3): p. 911-924.
286. Dong, H., H. Yu, and X. Wang, *Catalysis Kinetics and Porous Analysis of Rolling Activated Carbon-PTFE Air-Cathode in Microbial Fuel Cells.* Environmental Science & Technology, 2012. **46**(23): p. 13009-13015.
287. Zhang, B., et al., *Synthesizing Nitrogen-Doped Activated Carbon and Probing its Active Sites for Oxygen Reduction Reaction in Microbial Fuel Cells.* ACS Applied Materials & Interfaces, 2014. **6**(10): p. 7464-7470.
288. Wang, X., et al., *Accelerated OH– Transport in Activated Carbon Air Cathode by Modification of Quaternary Ammonium for Microbial Fuel Cells.* Environmental Science & Technology, 2014. **48**(7): p. 4191-4198.
289. Sevilla, M. and A.B. Fuertes, *Direct Synthesis of Highly Porous Interconnected Carbon Nanosheets and Their Application as High-Performance Supercapacitors.* ACS Nano, 2014. **8**(5): p. 5069-5078.
290. Phillips, S.L., *Potentiostatic Determination of Diffusion Coefficient of Oxygen in Absence and Presence of Surfactants.* Analytical Chemistry, 1966. **38**(12): p. 1714-1719.
291. Yang, S., et al., *Efficient Synthesis of Heteroatom (N or S)-Doped Graphene Based on Ultrathin Graphene Oxide-Porous Silica Sheets for Oxygen Reduction Reactions.* Advanced Functional Materials, 2012. **22**(17): p. 3634-3640.
292. Hou, Y., et al., *Co3O4 nanoparticles embedded in nitrogen-doped porous carbon dodecahedrons with enhanced electrochemical properties for lithium storage and water splitting.* Nano Energy, 2015. **12**(0): p. 1-8.
293. Hou, Y., et al., *Visible Light-Driven α-Fe2O3 Nanorod/Graphene/BiV1–xMoxO4 Core/Shell Heterojunction Array for Efficient Photoelectrochemical Water Splitting.* Nano Letters, 2012. **12**(12): p. 6464-6473.

294. Yang, W., et al., *Bamboo-like Carbon Nanotube/Fe3C Nanoparticle Hybrids and Their Highly Efficient Catalysis for Oxygen Reduction.* Journal of the American Chemical Society, 2015. **137**(4): p. 1436-1439.
295. Wen, Z., et al., *Facile One-Pot, One-Step Synthesis of a Carbon Nanoarchitecture for an Advanced Multifunctonal Electrocatalyst.* Angewandte Chemie International Edition, 2014. **53**(25): p. 6496-6500.
296. Jin, Z.-Y., et al., *Ionic Liquid-Assisted Synthesis of Microporous Carbon Nanosheets for Use in High Rate and Long Cycle Life Supercapacitors.* Advanced Materials, 2014. **26**(22): p. 3700-3705.
297. Niu, W., et al., *Mesoporous N-Doped Carbons Prepared with Thermally Removable Nanoparticle Templates: An Efficient Electrocatalyst for Oxygen Reduction Reaction.* Journal of the American Chemical Society, 2015. **137**(16): p. 5555-5562.
298. Gao, S., et al., *Honeysuckles-derived porous nitrogen, sulfur, dual-doped carbon as high-performance metal-free oxygen electroreduction catalyst.* Nano Energy, 2015. **12**(0): p. 785-793.
299. Ito, Y., et al., *High Catalytic Activity of Nitrogen and Sulfur Co-Doped Nanoporous Graphene in the Hydrogen Evolution Reaction.* Angewandte Chemie International Edition, 2015. **54**(7): p. 2131-2136.
300. Ma, X., et al., *High capacity Li storage in sulfur and nitrogen dual-doped graphene networks.* Carbon, 2014. **79**(0): p. 310-320.
301. Wen, Z., et al., *Crumpled Nitrogen-Doped Graphene Nanosheets with Ultrahigh Pore Volume for High-Performance Supercapacitor.* Advanced Materials, 2012. **24**(41): p. 5610-5616.
302. Xu, J., et al., *High-Performance Sodium Ion Batteries Based on a 3D Anode from Nitrogen-Doped Graphene Foams.* Advanced Materials, 2015. **27**(12): p. 2042-2048.
303. Lee, K.R., et al., *Electrochemical oxygen reduction on nitrogen doped graphene sheets in acid media.* Electrochemistry Communications, 2010. **12**(8): p. 1052-1055.
304. Su, Y., et al., *Low-temperature synthesis of nitrogen/sulfur co-doped three-dimensional graphene frameworks as efficient metal-free electrocatalyst for oxygen reduction reaction.* Carbon, 2013. **62**(0): p. 296-301.
305. Xiao, M., et al., *Meso/Macroporous Nitrogen-Doped Carbon Architectures with Iron Carbide Encapsulated in Graphitic Layers as an Efficient and Robust Catalyst for the Oxygen Reduction Reaction in Both Acidic and Alkaline Solutions.* Advanced Materials, 2015. **27**(15): p. 2521-2527.
306. Hou, Y., et al., *Metal−Organic Framework-Derived Nitrogen-Doped Core-Shell-Structured Porous Fe/Fe3C@C Nanoboxes Supported on Graphene Sheets for Efficient Oxygen Reduction Reactions.* Advanced Energy Materials, 2014. **4**(11).
307. Wang, X., et al., *One-pot synthesis of nitrogen and sulfur co-doped graphene as efficient metal-free electrocatalysts for the oxygen reduction reaction.* Chemical Communications, 2014. **50**(37): p. 4839-4842.
308. You, C., et al., *Uniform nitrogen and sulfur co-doped carbon nanospheres as catalysts for the oxygen reduction reaction.* Carbon, 2014. **69**(0): p. 294-301.
309. Gong, K., et al., *Nitrogen-doped carbon nanotube arrays with high electrocatalytic activity for oxygen reduction.* Science, 2009. **323**(5915): p. 760-764.

310. Jacobson, K.S., D.M. Drew, and Z. He, *Use of a liter-scale microbial desalination cell as a platform to study bioelectrochemical desalination with salt solution or artificial seawater.* Environmental Science & Technology, 2011. **45**(10): p. 4652-7.
311. Zhu, H., et al., *Lightweight, conductive hollow fibers from nature as sustainable electrode materials for microbial energy harvesting.* Nano Energy, 2014. **10**(0): p. 268-276.
312. Tiwari, J.N., et al., *Recent progress in the development of anode and cathode catalysts for direct methanol fuel cells.* Nano Energy, 2013. **2**(5): p. 553-578.
313. Gao, S. and K. Geng, *Facile construction of Mn3O4 nanorods coated by a layer of nitrogen-doped carbon with high activity for oxygen reduction reaction.* Nano Energy, 2014. **6**(0): p. 44-50.
314. Wu, Z.-Y., et al., *Co/Co3O4/C–N, a novel nanostructure and excellent catalytic system for the oxygen reduction reaction.* Nano Energy, 2014. **8**(0): p. 118-125.
315. Yuan, H. and Z. He, *Graphene-modified Electrodes for Enhancing the Performance of Microbial Fuel Cells.* Nanoscale, 2014.
316. Li, S., et al., *Iron- and nitrogen-functionalized graphene as a non-precious metal catalyst for enhanced oxygen reduction in an air-cathode microbial fuel cell.* Journal of Power Sources, 2012. **213**(0): p. 265-269.
317. Wen, Q., et al., *MnO2–graphene hybrid as an alternative cathodic catalyst to platinum in microbial fuel cells.* Journal of Power Sources, 2012. **216**(0): p. 187-191.
318. Su, Y., et al., *A Highly Efficient Catalyst toward Oxygen Reduction Reaction in Neutral Media for Microbial Fuel Cells.* Industrial & Engineering Chemistry Research, 2013. **52**(18): p. 6076-6082.
319. Xing, W., G. Yin, and J. Zhang, *Rotating Electrode Methods and Oxygen Reduction Electrocatalysts*. 2014: Elsevier.
320. Tang, Y., et al., *Electrocatalytic Activity of Nitrogen-Doped Carbon Nanotube Cups.* Journal of the American Chemical Society, 2009. **131**(37): p. 13200-13201.
321. Lin, M., et al., *Dynamical Observation of Bamboo-like Carbon Nanotube Growth.* Nano Letters, 2007. **7**(8): p. 2234-2238.
322. Hou, Y., et al., *Metal−Organic Framework-Derived Nitrogen-Doped Core-Shell-Structured Porous Fe/Fe3C@C Nanoboxes Supported on Graphene Sheets for Efficient Oxygen Reduction Reactions.* Advanced Energy Materials, 2014. **4**(11): p. n/a-n/a.
323. Hou, Y., et al., *Constructing 2D Porous Graphitic C3N4 Nanosheets/Nitrogen-Doped Graphene/Layered MoS2 Ternary Nanojunction with Enhanced Photoelectrochemical Activity.* Advanced Materials, 2013. **25**(43): p. 6291-6297.
324. Li, Q., et al., *Graphene/Graphene-Tube Nanocomposites Templated from Cage-Containing Metal-Organic Frameworks for Oxygen Reduction in Li–O2 Batteries.* Advanced Materials, 2014. **26**(9): p. 1378-1386.
325. Baker, R.T.K., et al., *Nucleation and growth of carbon deposits from the nickel catalyzed decomposition of acetylene.* Journal of Catalysis, 1972. **26**(1): p. 51-62.
326. Ning, G., et al., *MgO-catalyzed growth of N-doped wrinkled carbon nanotubes.* Carbon, 2013. **56**: p. 38-44.
327. Lv, R., et al., *Open-Ended, N-Doped Carbon Nanotube–Graphene Hybrid Nanostructures as High-Performance Catalyst Support.* Advanced Functional Materials, 2011. **21**(5): p. 999-1006.

328. Deng, J., et al., *Enhanced Electron Penetration through an Ultrathin Graphene Layer for Highly Efficient Catalysis of the Hydrogen Evolution Reaction.* Angewandte Chemie International Edition, 2015. **54**(7): p. 2100-2104.
329. Zou, X., et al., *Cobalt-Embedded Nitrogen-Rich Carbon Nanotubes Efficiently Catalyze Hydrogen Evolution Reaction at All pH Values.* Angewandte Chemie, 2014. **126**(17): p. 4461-4465.
330. Xiao, M., et al., *Meso/Macroporous Nitrogen-Doped Carbon Architectures with Iron Carbide Encapsulated in Graphitic Layers as an Efficient and Robust Catalyst for the Oxygen Reduction Reaction in Both Acidic and Alkaline Solutions.* Advanced Materials, 2015: p. n/a-n/a.
331. Van Khai, T., et al., *Significant enhancement of blue emission and electrical conductivity of N-doped graphene.* Journal of Materials Chemistry, 2012. **22**(34): p. 17992-18003.
332. Hassan, F.M., et al., *Pyrrolic-structure enriched nitrogen doped graphene for highly efficient next generation supercapacitors.* Journal of Materials Chemistry A, 2013. **1**(8): p. 2904-2912.
333. Duan, J., et al., *Shape Control of Mn3O4 Nanoparticles on Nitrogen-Doped Graphene for Enhanced Oxygen Reduction Activity.* Advanced Functional Materials, 2014. **24**(14): p. 2072-2078.
334. Qu, L., et al., *Nitrogen-Doped Graphene as Efficient Metal-Free Electrocatalyst for Oxygen Reduction in Fuel Cells.* ACS Nano, 2010. **4**(3): p. 1321-1326.
335. Liu, Y., et al., *Sustainable Energy Recovery in Wastewater Treatment by Microbial Fuel Cells: Stable Power Generation with Nitrogen-doped Graphene Cathode.* Environmental Science & Technology, 2013. **47**(23): p. 13889-13895.
336. Maldonado, S. and K.J. Stevenson, *Influence of nitrogen doping on oxygen reduction electrocatalysis at carbon nanofiber electrodes.* The Journal of Physical Chemistry B, 2005. **109**(10): p. 4707-4716.
337. Wang, S., D. Yu, and L. Dai, *Polyelectrolyte Functionalized Carbon Nanotubes as Efficient Metal-free Electrocatalysts for Oxygen Reduction.* Journal of the American Chemical Society, 2011. **133**(14): p. 5182-5185.
338. Lai, L., et al., *Exploration of the active center structure of nitrogen-doped graphene-based catalysts for oxygen reduction reaction.* Energy & Environmental Science, 2012. **5**(7): p. 7936-7942.
339. Wu, G., et al., *High-Performance Electrocatalysts for Oxygen Reduction Derived from Polyaniline, Iron, and Cobalt.* Science, 2011. **332**(6028): p. 443-447.
340. Chen, X., et al., *Mechanism of oxygen reduction reaction catalyzed by Fe(Co)-Nx/C.* Physical Chemistry Chemical Physics, 2013. **15**(44): p. 19330-19336.
341. Chen, P., et al., *A Nitrogen-Doped Graphene/Carbon Nanotube Nanocomposite with Synergistically Enhanced Electrochemical Activity.* Advanced Materials, 2013. **25**(23): p. 3192-3196.
342. Li, B. and J. Prakash, *Oxygen reduction reaction on carbon supported Palladium–Nickel alloys in alkaline media.* Electrochemistry Communications, 2009. **11**(6): p. 1162-1165.
343. Olson, T.S., et al., *Anion-Exchange Membrane Fuel Cells: Dual-Site Mechanism of Oxygen Reduction Reaction in Alkaline Media on Cobalt−Polypyrrole Electrocatalysts.* The Journal of Physical Chemistry C, 2010. **114**(11): p. 5049-5059.
344. Watkins, K., et al., *Human Development Report 2006: beyond scarcity: power, poverty and the global water crisis*. 2006: United Nations Development Programme (UNDP).

345. Kokabian, B. and V.G. Gude, *Sustainable photosynthetic biocathode in microbial desalination cells.* Chemical Engineering Journal, 2015. **262**(0): p. 958-965.
346. Chen, X., et al., *Stacked microbial desalination cells to enhance water desalination efficiency.* Environmental Science & Technology, 2011. **45**(6): p. 2465-70.
347. Ping, Q. and Z. He, *Improving the flexibility of microbial desalination cells through spatially decoupling anode and cathode.* Bioresource Technology, 2013. **144**: p. 304-10.
348. Forrestal, C., P. Xu, and Z. Ren, *Sustainable desalination using a microbial capacitive desalination cell.* Energy & Environmental Science, 2012. **5**(5): p. 7161-7167.
349. Kim, Y. and B.E. Logan, *Series assembly of microbial desalination cells containing stacked electrodialysis cells for partial or complete seawater desalination.* Environmental Science & Technology, 2011. **45**(13): p. 5840-5.
350. Liu, G., et al., *Tetramethylammonium hydroxide production using the microbial electrolysis desalination and chemical-production cell.* Chemical Engineering Journal, 2014. **258**(0): p. 157-162.
351. Zhang, Y. and I. Angelidaki, *A new method for in situ nitrate removal from groundwater using submerged microbial desalination–denitrification cell (SMDDC).* Water Research, 2013. **47**(5): p. 1827-1836.
352. Zuo, K., et al., *A Ten Liter Stacked Microbial Desalination Cell Packed With Mixed Ion-Exchange Resins for Secondary Effluent Desalination.* Environmental Science & Technology, 2014. **48**(16): p. 9917-9924.
353. Cath, T., A. Childress, and M. Elimelech, *Forward osmosis: Principles, applications, and recent developments.* Journal of Membrane Science, 2006. **281**(1-2): p. 70-87.
354. Zhang, Y., et al., *A Natural Driven Membrane Process for Brackish and Wastewater Treatment: Photovoltaic Powered ED and FO Hybrid System.* Environmental Science & Technology, 2013. **47**(18): p. 10548-10555.
355. McGinnis, R.L., et al., *Pilot demonstration of the NH3/CO2 forward osmosis desalination process on high salinity brines.* Desalination, 2013. **312**: p. 67-74.
356. Liu, Z., et al., *A low-energy forward osmosis process to produce drinking water.* Energy & Environmental Science, 2011. **4**(7): p. 2582.
357. Lu, Y., et al., *When Bioelectrochemical Systems Meet Forward Osmosis: Accomplishing Wastewater Treatment and Reuse through Synergy.* Water, 2015. **In Press**.
358. Logan, B.E., et al., *Microbial fuel cells: methodology and technology.* Environmental Science and Technology, 2006. **40**(17): p. 5181-5192.
359. He, Z., S.D. Minteer, and L.T. Angenent, *Electricity generation from artificial wastewater using an upflow microbial fuel cell.* Environmental Science & Technology, 2005. **39**(14): p. 5262-5267.
360. Kiely, P.D., J.M. Regan, and B.E. Logan, *The electric picnic: synergistic requirements for exoelectrogenic microbial communities.* Current Opinion in Biotechnology, 2011. **22**(3): p. 378-85.
361. Yuan, H., et al., *Determination of optimal conditions for 5-methyl-benzotriazole biodegradation with activated sludge communities by dilution of the inoculum.* Science of The Total Environment, 2013. **487** p. 756-762.
362. Morel, A., et al., *Microbial desalination cells packed with ion-exchange resin to enhance water desalination rate.* Bioresource Technology, 2012. **118**(0): p. 43-48.
363. Yuan, L., et al., *Capacitive deionization coupled with microbial fuel cells to desalinate low-concentration salt water.* Bioresource Technology, 2012. **110**(0): p. 735-738.

364. Ping, Q., et al., *Long-term investigation of fouling of cation and anion exchange membranes in microbial desalination cells.* Desalination, 2013. **325**: p. 48-55.
365. Achilli, A., et al., *The forward osmosis membrane bioreactor: A low fouling alternative to MBR processes.* Desalination, 2009. **239**(1): p. 10-21.
366. Xie, M., et al., *A Forward Osmosis–Membrane Distillation Hybrid Process for Direct Sewer Mining: System Performance and Limitations.* Environmental Science & Technology, 2013. **47**(23): p. 13486-13493.
367. Bamaga, O.A., et al., *Hybrid FO/RO desalination system: Preliminary assessment of osmotic energy recovery and designs of new FO membrane module configurations.* Desalination, 2011. **268**(1–3): p. 163-169.
368. Ge, Q., et al., *Hydrophilic superparamagnetic nanoparticles: synthesis, characterization, and performance in forward osmosis processes.* Industrial & Engineering Chemistry Research, 2010. **50**(1): p. 382-388.
369. McCutcheon, J.R., R.L. McGinnis, and M. Elimelech, *Desalination by ammonia–carbon dioxide forward osmosis: influence of draw and feed solution concentrations on process performance.* Journal of Membrane Science, 2006. **278**(1): p. 114-123.
370. Li, D., et al., *Forward osmosis desalination using polymer hydrogels as a draw agent: influence of draw agent, feed solution and membrane on process performance.* Water Research, 2013. **47**(1): p. 209-215.
371. Ping, Q., et al., *Bioelectricity inhibits back diffusion from the anolyte into the desalinated stream in microbial desalination cells.* Water Research, 2016. **88**: p. 266-273.
372. Ping, Q., et al., *Integrated experimental investigation and mathematical modeling of brackish water desalination and wastewater treatment in microbial desalination cells.* Water Research, 2015. **77**(0): p. 13-23.
373. Tang, C.Y., et al., *Coupled effects of internal concentration polarization and fouling on flux behavior of forward osmosis membranes during humic acid filtration.* Journal of Membrane Science, 2010. **354**(1-2): p. 123-133.
374. Phillip, W.A., J.S. Yong, and M. Elimelech, *Reverse Draw Solute Permeation in Forward Osmosis: Modeling and Experiments.* Environmental Science & Technology, 2010. **44**(13): p. 5170-5176.
375. Pinto, R.P., et al., *A two-population bio-electrochemical model of a microbial fuel cell.* Bioresource Technology, 2010. **101**(14): p. 5256-5265.
376. Xu, Y., et al., *Effect of draw solution concentration and operating conditions on forward osmosis and pressure retarded osmosis performance in a spiral wound module.* Journal of Membrane Science, 2010. **348**(1–2): p. 298-309.
377. Achilli, A. and A.E. Childress, *Pressure retarded osmosis: From the vision of Sidney Loeb to the first prototype installation — Review.* Desalination, 2010. **261**(3): p. 205-211.
378. Ge, Z., C.G. Dosoretz, and Z. He, *Effects of number of cell pairs on the performance of microbial desalination cells.* Desalination, 2014. **341**: p. 101-106.
379. Ni, M., et al., *A review and recent developments in photocatalytic water-splitting using for hydrogen production.* Renewable & Sustainable Energy Reviews, 2007. **11**(3): p. 401-425.
380. Haryanto, A., et al., *Current Status of Hydrogen Production Techniques by Steam Reforming of Ethanol: A Review.* Energy Fuels, 2005. **19**(5): p. 2098-2106.

381. Heidrich, E.S., et al., *Production of hydrogen from domestic wastewater in a pilot-scale microbial electrolysis cell.* Applied Microbiology and Biotechnology, 2013. **97**(15): p. 6979-6989.
382. Sun, M., et al., *An MEC-MFC-Coupled System for Biohydrogen Production from Acetate.* Environmental Science & Technology, 2008. **42**(21): p. 8095-8100.
383. Hatzell, M.C., Y. Kim, and B.E. Logan, *Powering microbial electrolysis cells by capacitor circuits charged using microbial fuel cell.* Journal of Power Sources, 2013. **229**: p. 198-202.
384. Chae, K.-J., et al., *A Solar-Powered Microbial Electrolysis Cell with a Platinum Catalyst-Free Cathode To Produce Hydrogen.* Environmental Science & Technology, 2009. **43**(24): p. 9525-9530.
385. Yip, N.Y. and M. Elimelech, *Thermodynamic and Energy Efficiency Analysis of Power Generation from Natural Salinity Gradients by Pressure Retarded Osmosis.* Environmental Science & Technology, 2012. **46**(9): p. 5230-5239.
386. Kim, Y. and B.E. Logan, *Hydrogen production from inexhaustible supplies of fresh and salt water using microbial reverse-electrodialysis electrolysis cells.* Proceedings of the National Academy of Sciences, 2011. **108**(39): p. 16176-16181.
387. Cusick, R.D., Y. Kim, and B.E. Logan, *Energy capture from thermolytic solutions in microbial reverse-electrodialysis cells.* Science, 2012. **335**(6075): p. 1474-1477.
388. Nam, J.-Y., et al., *Hydrogen Generation in Microbial Reverse-Electrodialysis Electrolysis Cells Using a Heat-Regenerated Salt Solution.* Environmental Science & Technology, 2012. **46**(9): p. 5240-5246.
389. Helfer, F., C. Lemckert, and Y.G. Anissimov, *Osmotic power with Pressure Retarded Osmosis: Theory, performance and trends – A review.* Journal of Membrane Science, 2014. **453**(0): p. 337-358.
390. Chou, S., et al., *Thin-film composite hollow fiber membranes for pressure retarded osmosis (PRO) process with high power density.* Journal of Membrane Science, 2012. **389**(0): p. 25-33.
391. Lu, Y., et al., *When Bioelectrochemical Systems Meet Forward Osmosis: Accomplishing Wastewater Treatment and Reuse through Synergy.* Water, 2015. **7**(1): p. 38-50.
392. Yip, N.Y., et al., *Thin-Film Composite Pressure Retarded Osmosis Membranes for Sustainable Power Generation from Salinity Gradients.* Environmental Science & Technology, 2011. **45**(10): p. 4360-4369.
393. She, Q., X. Jin, and C.Y. Tang, *Osmotic power production from salinity gradient resource by pressure retarded osmosis: Effects of operating conditions and reverse solute diffusion.* Journal of Membrane Science, 2012. **401-402**: p. 262-273.
394. Tartakovsky, B., et al., *High rate membrane-less microbial electrolysis cell for continuous hydrogen production.* International Journal of Hydrogen Energy, 2009. **34**(2): p. 672-677.
395. Song, X., Z. Liu, and D.D. Sun, *Energy recovery from concentrated seawater brine by thin-film nanofiber composite pressure retarded osmosis membranes with high power density.* Energy & Environmental Science, 2013. **6**(4): p. 1199-1210.
396. Yip, N.Y. and M. Elimelech, *Comparison of Energy Efficiency and Power Density in Pressure Retarded Osmosis and Reverse Electrodialysis.* Environmental Science & Technology, 2014. **48**(18): p. 11002-11012.

397. Straub, A.P., S. Lin, and M. Elimelech, *Module-Scale Analysis of Pressure Retarded Osmosis: Performance Limitations and Implications for Full-Scale Operation.* Environmental Science & Technology, 2014. **48**(20): p. 12435-12444.
398. Prante, J.L., et al., *RO-PRO desalination: An integrated low-energy approach to seawater desalination.* Applied Energy, 2014. **120**(0): p. 104-114.
399. Torres, C., A. Kato Marcus, and B. Rittmann, *Kinetics of consumption of fermentation products by anode-respiring bacteria.* Applied Microbiology and Biotechnology, 2007. **77**(3): p. 689-697.
400. Popat, S.C., et al., *Buffer pKa and Transport Govern the Concentration Overpotential in Electrochemical Oxygen Reduction at Neutral pH.* ChemElectroChem, 2014: p. n/a-n/a.
401. Achilli, A., et al., *Experimental Results from RO-PRO: A Next Generation System for Low-Energy Desalination.* Environmental Science & Technology, 2014. **48**(11): p. 6437-6443.
402. Straub, A.P., N.Y. Yip, and M. Elimelech, *Raising the Bar: Increased Hydraulic Pressure Allows Unprecedented High Power Densities in Pressure-Retarded Osmosis.* Environmental Science & Technology Letters, 2014. **1**(1): p. 55-59.
403. Wright, G.D., *Antibiotic resistome: A framework linking the clinic and the environment*. 2012: John Wiley & Sons, Inc., Hoboken, New Jersey.
404. Stokes, H.W. and M.R. Gillings, *Gene flow, mobile genetic elements and the recruitment of antibiotic resistance genes into Gram-negative pathogens.* FEMS microbiology reviews, 2011. **35**(5): p. 790-819.
405. Durso, L.M., D.N. Miller, and B.J. Wienhold, *Distribution and quantification of antibiotic resistant genes and bacteria across agricultural and non-agricultural metagenomes.* PLoS One, 2012. **7**(11): p. e48325.
406. Stalder, T., et al., *Integron involvement in environmental spread of antibiotic resistance.* Frontiers in microbiology, 2012. **3**.
407. Forsberg, K.J., et al., *Bacterial phylogeny structures soil resistomes across habitats.* Nature, 2014. **509**(7502): p. 612-616.
408. Storteboom, H., et al., *Identification of Antibiotic-Resistance-Gene Molecular Signatures Suitable as Tracers of Pristine River, Urban, and Agricultural Sources.* Environmental Science & Technology, 2010. **44**(6): p. 1947-1953.
409. Hong, P.-Y., et al., *Environmental and public health implications of water reuse: Antibiotics, antibiotic resistant bacteria, and antibiotic resistance genes.* Antibiotics, 2013. **2**(3): p. 367-399.
410. Storteboom, H., et al., *Tracking Antibiotic Resistance Genes in the South Platte River Basin Using Molecular Signatures of Urban, Agricultural, And Pristine Sources.* Environmental Science & Technology, 2010. **44**(19): p. 7397-7404.
411. Schlüter, A., et al., *Genomics of IncP-1 antibiotic resistance plasmids isolated from wastewater treatment plants provides evidence for a widely accessible drug resistance gene pool.* FEMS Microbiology Reviews, 2007. **31**(4): p. 449-477.
412. Moura, A., et al., *Broad diversity of conjugative plasmids in integron-carrying bacteria from wastewater environments.* FEMS microbiology letters, 2012. **330**(2): p. 157-164.
413. Szczepanowski, R., et al., *Detection of 140 clinically relevant antibiotic-resistance genes in the plasmid metagenome of wastewater treatment plant bacteria showing reduced susceptibility to selected antibiotics.* Microbiology, 2009. **155**(7): p. 2306-2319.

414. LaPara, T.M., et al., *Tertiary-treated municipal wastewater is a significant point source of antibiotic resistance genes into Duluth-Superior Harbor.* Environmental science & technology, 2011. **45**(22): p. 9543-9549.
415. Luo, Y., et al., *Proliferation of Multidrug-Resistant New Delhi Metallo-β-lactamase Genes in Municipal Wastewater Treatment Plants in Northern China.* Environmental Science & Technology Letters, 2014. **1**(1): p. 26-30.
416. Ma, Y., et al., *Effect of Various Sludge Digestion Conditions on Sulfonamide, Macrolide, and Tetracycline Resistance Genes and Class I Integrons.* Environmental Science & Technology, 2011. **45**(18): p. 7855-7861.
417. Diehl, D.L. and T.M. LaPara, *Effect of Temperature on the Fate of Genes Encoding Tetracycline Resistance and the Integrase of Class 1 Integrons within Anaerobic and Aerobic Digesters Treating Municipal Wastewater Solids.* Environmental Science & Technology, 2010. **44**(23): p. 9128-9133.
418. Kelly, P.T. and Z. He, *Nutrients removal and recovery in bioelectrochemical systems: A review.* Bioresource Technology, 2014. **153**: p. 351-360.
419. Zeng, X., A.P. Borole, and S.G. Pavlostathis, *Biotransformation of Furanic and Phenolic Compounds with Hydrogen Gas Production in a Microbial Electrolysis Cell.* Environmental Science & Technology, 2015. **49**(22): p. 13667-13675.
420. Andrews, J.M., *Determination of minimum inhibitory concentrations.* Journal of antimicrobial Chemotherapy, 2001. **48**(suppl 1): p. 5-16.
421. Maheux, A.F., et al., *Analytical comparison of nine PCR primer sets designed to detect the presence of Escherichia coli/Shigella in water samples.* water research, 2009. **43**(12): p. 3019-3028.
422. Pei, R., et al., *Effect of River Landscape on the sediment concentrations of antibiotics and corresponding antibiotic resistance genes (ARG).* Water Research, 2006. **40**(12): p. 2427-2435.
423. Knapp, C.W., et al., *Indirect Evidence of Transposon-Mediated Selection of Antibiotic Resistance Genes in Aquatic Systems at Low-Level Oxytetracycline Exposures.* Environmental Science & Technology, 2008. **42**(14): p. 5348-5353.
424. Liu, M., et al., *Abundance and Distribution of Tetracycline Resistance Genes and Mobile Elements in an Oxytetracycline Production Wastewater Treatment System.* Environmental Science & Technology, 2012. **46**(14): p. 7551-7557.
425. Unden, G. and J. Bongaerts, *Alternative respiratory pathways of Escherichia coli: energetics and transcriptional regulation in response to electron acceptors.* Biochimica et Biophysica Acta (BBA) - Bioenergetics, 1997. **1320**(3): p. 217-234.
426. Rysz, M., et al., *Tetracycline resistance gene maintenance under varying bacterial growth rate, substrate and oxygen availability, and tetracycline concentration.* Environmental science & technology, 2013. **47**(13): p. 6995-7001.
427. Kiely, P.D., et al., *Anode microbial communities produced by changing from microbial fuel cell to microbial electrolysis cell operation using two different wastewaters.* Bioresource Technology, 2011. **102**(1): p. 388-394.
428. Presser, K.A., D.A. Ratkowsky, and T. Ross, *Modelling the growth rate of Escherichia coli as a function of pH and lactic acid concentration.* Applied and Environmental Microbiology, 1997. **63**(6): p. 2355-2360.

429. Zhang, T., et al., *The direct electrocatalysis of Escherichia coli through electroactivated excretion in microbial fuel cell.* Electrochemistry Communications, 2008. **10**(2): p. 293-297.
430. Zhang, T., et al., *A novel mediatorless microbial fuel cell based on direct biocatalysis of Escherichia coli.* Chemical Communications, 2006. **21**: p. 2257-2259.
431. Wang, V.B., et al., *Synergistic Microbial Consortium for Bioenergy Generation from Complex Natural Energy Sources.* The Scientific World Journal, 2014. **2014**.
432. Wang, V.B., et al., *Metabolite-enabled mutualistic interaction between Shewanella oneidensis and Escherichia coli in a co-culture using an electrode as electron acceptor.* Scientific reports, 2015. **5**.
433. Rudi, K., et al., *Use of ethidium monoazide and PCR in combination for quantification of viable and dead cells in complex samples.* Applied and Environmental Microbiology, 2005. **71**(2): p. 1018-1024.
434. Yong, Y.-C., et al., *Enhancement of extracellular electron transfer and bioelectricity output by synthetic porin.* Biotechnology and Bioengineering, 2013. **110**(2): p. 408-416.
435. McKinney, C.W., et al., *tet and sul Antibiotic Resistance Genes in Livestock Lagoons of Various Operation Type, Configuration, and Antibiotic Occurrence.* Environmental Science & Technology, 2010. **44**(16): p. 6102-6109.
436. Miller, J.H., et al., *Antibiotic resistant bacteria survival and horizontal gene transfer control antibiotic resistance gene content of anaerobic digesters.* Frontiers in Microbiology, 2016. **7**.
437. Fang, H., et al., *Prevalence of Antibiotic Resistance Genes and Bacterial Pathogens in Long-Term Manured Greenhouse Soils As Revealed by Metagenomic Survey.* Environmental Science & Technology, 2015. **49**(2): p. 1095-1104.
438. Furukawa, H., et al., *The chemistry and applications of metal-organic frameworks.* Science, 2013. **341**(6149): p. 1230444.
439. Goenaga, G., et al., *New approaches to non-PGM electrocatalysts using porous framework materials.* ECS Transactions, 2010. **33**(1): p. 579-586.
440. Proietti, E., et al., *Iron-based cathode catalyst with enhanced power density in polymer electrolyte membrane fuel cells.* Nature Communications, 2011. **2**: p. 416.
441. Morozan, A. and F. Jaouen, *Metal organic frameworks for electrochemical applications.* Energy & Environmental Science, 2012. **5**(11): p. 9269-9290.
442. Xia, W., et al., *Metal-organic frameworks and their derived nanostructures for electrochemical energy storage and conversion.* Energy & Environmental Science, 2015. **8**(7): p. 1837-1866.
443. Miner, E.M., et al., *Electrochemical oxygen reduction catalysed by Ni3(hexaiminotriphenylene)2.* Nat Commun, 2016. **7**.
444. Tang, H., et al., *Metal–Organic-Framework-Derived Dual Metal- and Nitrogen-Doped Carbon as Efficient and Robust Oxygen Reduction Reaction Catalysts for Microbial Fuel Cells.* Advanced Science, 2016. **3**(2): p. 1500265.
445. Nohra, B., et al., *Polyoxometalate-Based Metal Organic Frameworks (POMOFs): Structural Trends, Energetics, and High Electrocatalytic Efficiency for Hydrogen Evolution Reaction.* Journal of the American Chemical Society, 2011. **133**(34): p. 13363-13374.

446. Gong, Y., et al., *Octamolybdate-Based Metal–Organic Framework with Unsaturated Coordinated Metal Center As Electrocatalyst for Generating Hydrogen from Water.* Inorganic Chemistry, 2013. **52**(2): p. 777-784.
447. Li, J.-S., et al., *Polyoxometalate-based metal-organic framework-derived hybrid electrocatalysts for highly efficient hydrogen evolution reaction.* Journal of Materials Chemistry A, 2016. **4**(4): p. 1202-1207.
448. Feng, L., et al., *Nitrogen-doped carbon nanotubes as efficient and durable metal-free cathodic catalysts for oxygen reduction in microbial fuel cells.* Energy & Environmental Science, 2011. **4**(5): p. 1892-1899.
449. Zhuang, L., et al., *In situ formation of graphene/biofilm composites for enhanced oxygen reduction in biocathode microbial fuel cells.* Electrochemistry Communications, 2012. **21**(0): p. 69-72.
450. Ren, Y., et al., *Effect of polyaniline-graphene nanosheets modified cathode on the performance of sediment microbial fuel cell.* Journal of Chemical Technology & Biotechnology, 2013. **88**(10): p. 1946-1950.
451. Khilari, S., et al., *Graphene supported α-MnO2 nanotubes as a cathode catalyst for improved power generation and wastewater treatment in single-chambered microbial fuel cells.* RSC Advances, 2013. **3**(21): p. 7902-7911.
452. Yan, Z., et al., *Graphene Supported Pt-Co Alloy Nanoparticles as Cathode Catalyst for Microbial Fuel Cells.* International Journal of Electrochemical Science, 2013. **8**(1): p. 149-158.
453. Hongliang, S., et al., *Graphene-Supported Silver Nanoparticles for pH-Neutral Electrocatalytic Oxygen Reduction.* IEEE Transactions on Nanotechnology, 2014. **13**(4): p. 789-794.
454. Jayaprakash, V., et al. *Graphene electrodes enhance performance for microliter scale microbial fuel cells*. in *Micro Electro Mechanical Systems (MEMS), 2014 IEEE 27th International Conference on*. 2014.
455. Gnana kumar, G., et al., *Nanotubular MnO2/graphene oxide composites for the application of open air-breathing cathode microbial fuel cells.* Biosensors and Bioelectronics, 2014. **53**(0): p. 528-534.
456. Wen, Q., et al., *Porous nitrogen-doped carbon nanosheet on graphene as metal-free catalyst for oxygen reduction reaction in air-cathode microbial fuel cells.* Bioelectrochemistry, 2014. **95**(0): p. 23-28.
457. Ansari, M.O., et al., *pTSA doped conducting graphene/polyaniline nanocomposite fibers: Thermoelectric behavior and electrode analysis.* Chemical Engineering Journal, 2014. **242**(0): p. 155-161.
458. Qi, G.H., X.Q. Li, and J. Cao, *Research on the Phenol Degradation in Microbial Fuel Cells with Fe3O4-Reduced Graphene Oxide Cathodic Catalyst.* Advanced Materials Research, 2014. **881**: p. 310-314.
459. Yuan, H., et al., *Porous carbon nanosheets co-doped with nitrogen and sulfur for oxygen reduction reaction in microbial fuel cells.* ACS Applied Materials & Interfaces, 2015.
460. Liu, Y., et al., *Homogeneous deposition-assisted synthesis of iron–nitrogen composites on graphene as highly efficient non-precious metal electrocatalysts for microbial fuel cell power generation.* Journal of Power Sources, 2015. **278**: p. 773-781.

461. Suzuki, M.T., L.T. Taylor, and E.F. DeLong, *Quantitative analysis of small-subunit rRNA genes in mixed microbial populations via 5′-nuclease assays.* Applied and Environmental Microbiology, 2000. **66**(11): p. 4605-4614.
462. Heijnen, L. and G. Medema, *Quantitative detection of E. coli, E. coli O157 and other shiga toxin producing E. coli in water samples using a culture method combined with real-time PCR.* Journal of Water and Health, 2006. **4**(4): p. 487-498.
463. Hardwick, S.A., et al., *Quantification of class 1 integron abundance in natural environments using real-time quantitative PCR.* FEMS microbiology letters, 2008. **278**(2): p. 207-212.
464. Aminov, R., et al., *Development, validation, and application of PCR primers for detection of tetracycline efflux genes of gram-negative bacteria.* Applied and Environmental Microbiology, 2002. **68**(4): p. 1786-1793.

Appendices

Appendix A Supplemental Information for Chapter 2

Table A1 The permillages of the 27 major functions of the biofilm communities predicted using PICRUSt. The highlighted two values were the highest and were visualized using Circos. Standard deviation was calculated from triplicate data.

	4 M	2 M	1 M	0.6 M	0.2 M	0.05 M
Chemotaxis	7.39±0.14	6.43±0.24	7.04±0.43	4.88±0.71	3.27±1.84	4.97±0.42
Motility	17.44±0.30	16.35±0.32	17.71±1.68	11.58±1.90	11.61±2.95	11.97±0.54
Flagellar	6.36±0.04	5.71±0.36	6.64±1.41	4.02±0.74	2.67±1.96	3.76±0.36
Amino	10.14±0.12	9.24±0.29	10.68±0.39	10.98±0.43	9.88±0.68	10.95±0.40
Butanoate	7.99±0.16	10.58±0.37	8.59±0.63	7.77±0.67	6.60±1.04	8.23±0.43
Fructose/Mannose	5.92±0.08	5.85±0.16	6.49±0.07	6.79±0.19	5.90±0.39	6.61±0.37
Glycolysis/Gluconeogenesis	10.44±0.09	10.70±0.22	11.61±0.11	11.29±0.23	10.55±0.03	10.97±0.20
PPP	6.73±0.07	6.46±0.14	7.47±0.43	7.53±0.09	6.67±0.31	6.95±0.14
Propanoate	7.55±0.06	9.20±0.38	7.91±0.14	7.19±0.82	5.78±1.09	7.60±0.41
Pyruvate	10.60±0.08	11.44±0.03	11.53±0.16	10.82±0.06	10.48±0.40	10.83±0.15
Starch/Sucrose	5.57±0.11	4.79±0.05	5.46±0.38	6.36±0.29	6.21±0.05	6.06±0.06
Carbon fixation	11.75±0.07	12.13±0.16	12.91±0.82	10.78±0.73	10.01±1.01	11.37±0.37
Methane	11.21±0.17	11.76±0.25	12.24±0.32	11.03±0.44	9.45±1.27	10.69±0.60
Nitrogen	8.79±0.17	7.73±0.02	7.94±0.13	7.14±0.27	6.21±1.18	7.90±0.32
Oxidative phosphorylation	12.95±0.04	13.13±0.20	15.45±2.54	12.86±1.05	17.76±2.53	13.03±1.11
Fatty acid	4.79±0.13	6.77±0.43	4.75±0.44	4.82±0.89	4.34±0.49	5.18±0.25
Glycerolipid	3.01±0.07	3.28±0.06	3.24±0.05	3.20±0.06	2.99±0.17	3.19±0.08
Glycerophospholipid	5.52±0.07	5.43±0.08	5.66±0.12	5.16±0.22	5.14±0.16	5.30±0.13
Unsaturated fatty acids	2.03±0.02	2.42±0.10	2.01±0.14	1.82±0.23	1.97±0.09	1.92±0.19
ABC	25.25±1.23	32.26±2.15	26.80±2.70	29.84±4.84	29.57±1.13	25.91±0.45
PTS	1.58±0.03	1.44±0.10	1.71±0.14	2.40±0.67	0.90±0.64	2.56±0.67
Secretion	17.66±0.35	17.50±0.22	17.12±0.69	13.83±1.55	17.78±0.82	15.40±0.60
Transporters	41.48±1.75	50.33±2.96	44.01±3.24	51.39±5.39	48.99±1.89	44.91±0.52
Electron transfer carriers	0.23±0.02	0.26±0.01	0.31±0.01	0.21±0.09	0.23±0.01	0.17±0.02
Inorganic ion transport	3.08±0.05	2.79±0.12	2.73±0.57	2.41±0.16	2.10±0.51	2.72±0.11
Ion channels	5.92±0.14	5.36±0.17	5.14±0.36	5.33±0.36	5.33±0.60	5.70±0.49
Membrane	7.61±0.17	6.75±0.07	6.37±0.34	6.19±0.18	6.65±0.61	7.06±0.20

Table A2 The permillages of the 27 major functions of the suspended communities predicted using PICRUSt. The highlighted two values were the highest and were visualized using Circos. Standard deviation was calculated from triplicate data.

	4 M	2 M	1 M	0.6 M	0.2 M	0.05 M
Chemotaxis	7.21±0.21	6.35±1.18	6.13±0.03	5.49±0.21	4.12±0.06	4.60±0.01
Motility	16.53±1.05	15.22±4.27	14.12±0.05	12.23±0.57	8.68±0.20	9.61±0.07
Flagellar	6.17±0.44	5.62±1.39	5.15±0.07	4.16±0.21	2.89±0.09	3.12±0.05
Amino	9.47±0.45	10.98±1.11	11.37±0.13	12.83±0.36	14.39±0.30	13.59±0.19
Butanoate	9.90±1.00	8.59±1.38	8.44±0.09	7.53±0.22	7.03±0.05	7.48±0.09
Fructose/Mannose	6.16±0.14	6.42±0.44	7.18±0.12	8.32±0.28	9.51±0.20	8.81±0.20
Glycolysis/Gluconeogenesis	10.22±0.09	10.50±0.14	11.31±0.06	11.98±0.11	12.80±0.10	12.22±0.08
PPP	6.28±0.13	6.50±0.23	7.35±0.06	8.20±0.14	8.84±0.08	8.17±0.10
Propanoate	9.52±0.70	7.74±1.23	7.72±0.06	6.82±0.20	6.14±0.06	6.83±0.08
Pyruvate	11.34±0.18	11.17±0.44	11.00±0.05	10.58±0.04	10.61±0.06	10.79±0.01
Starch/Sucrose	5.00±0.27	5.74±0.83	5.92±0.04	6.39±0.15	7.08±0.09	6.64±0.04
Carbon fixation	11.34±0.09	12.31±0.17	11.42±0.10	10.89±0.11	11.14±0.04	11.38±0.09
Methane	10.03±0.32	11.58±0.26	11.59±0.13	11.94±0.01	12.77±0.05	12.34±0.16
Nitrogen	8.79±0.08	8.35±0.18	7.76±0.09	7.46±0.10	6.94±0.05	7.56±0.09
Oxidative phosphorylation	11.95±0.29	14.33±0.53	12.59±0.13	12.52±0.06	12.11±0.20	12.10±0.13
Fatty acid	7.10±0.76	4.98±1.22	5.05±0.04	4.01±0.26	3.12±0.06	3.79±0.09
Glycerolipid	3.20±0.02	3.24±0.03	3.30±0.01	3.47±0.03	3.38±0.01	3.30±0.04
Glycerophospholipid	5.36±0.03	5.61±0.15	5.53±0.04	5.70±0.01	5.65±0.05	5.46±0.04
Unsaturated fatty acids	2.43±0.14	1.93±0.41	1.80±0.01	1.46±0.08	1.05±0.01	1.30±0.02
ABC	26.21±1.66	25.54±4.25	27.63±0.70	27.46±0.60	25.06±0.11	25.24±0.63
PTS	2.54±0.47	2.05±0.30	3.65±0.19	5.60±0.50	7.32±0.41	6.44±0.35
Secretion	16.17±0.77	16.81±3.27	15.37±0.07	14.91±0.32	11.92±0.19	12.70±0.04
Transporters	44.02±1.31	43.24±4.32	48.26±1.32	50.91±0.86	50.14±0.38	48.87±1.22
Electron transfer carriers	0.12±0.05	0.17±0.06	0.18±0.01	0.16±0.01	0.13±0.00	0.16±0.01
Inorganic ion transport	3.30±0.05	2.82±0.20	2.64±0.05	2.31±0.05	2.01±0.03	2.32±0.03
Ion channels	6.02±0.36	6.28±0.12	5.36±0.10	5.00±0.09	4.29±0.04	4.85±0.11
Membrane	7.61±0.11	8.15±0.37	6.85±0.09	6.44±0.08	5.81±0.13	6.23±0.09

Table S3 Relative root-mean square error (RMSE) between the experimental data and the predicted values using Bayesian network at different taxonomic levels. NA, not applicable.

	$RMSE_{phylum}$	**$RMSE_{order}$**	**$RMSE_{OTU}$**
4	11.8%	3.3%	5.3%
2	13.2%	1.8%	3.3%
1	18.3%	11.6%	14.5%
0.6	12.8%	14.1%	23.7%
0.2	40.1%	10.6%	20.8%
0.05	NA	9.1%	NA

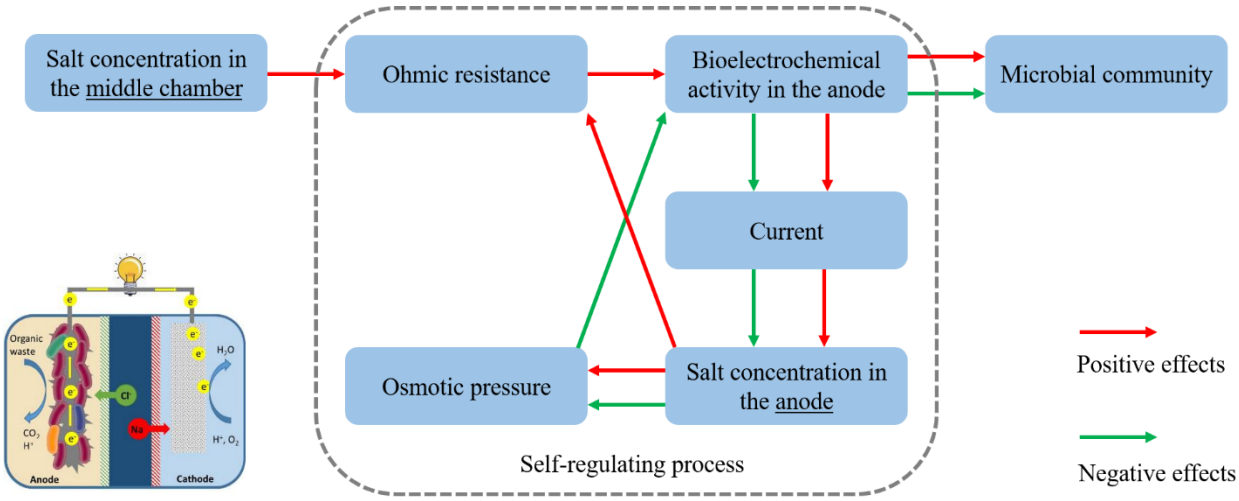

Figure A1 The microbial community in MDC anode may be self-regulated by interacting with the salt solution in the desalination chamber, and thus significantly different from that in other BES anode.

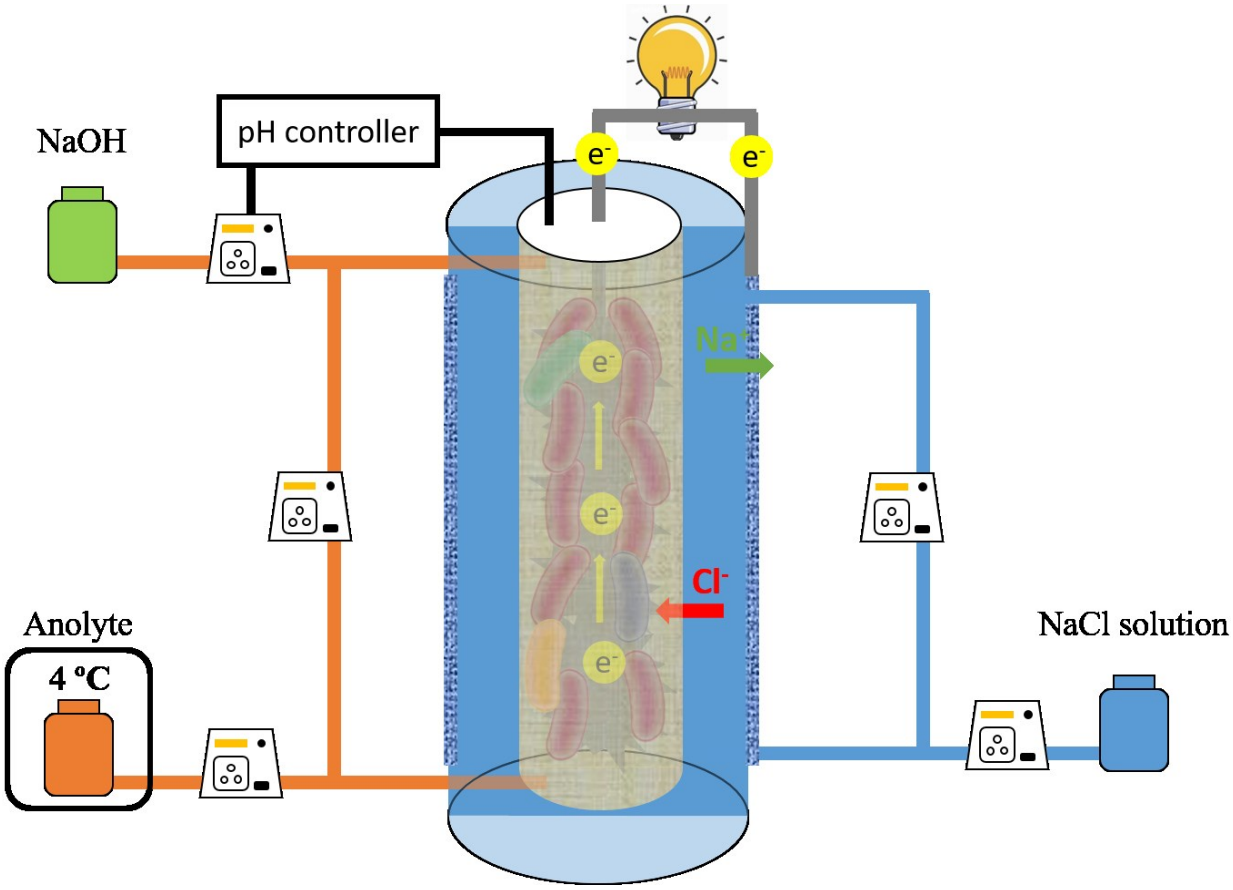

Figure A2 The schematic of the tubular MDC operated under a continuous mode.

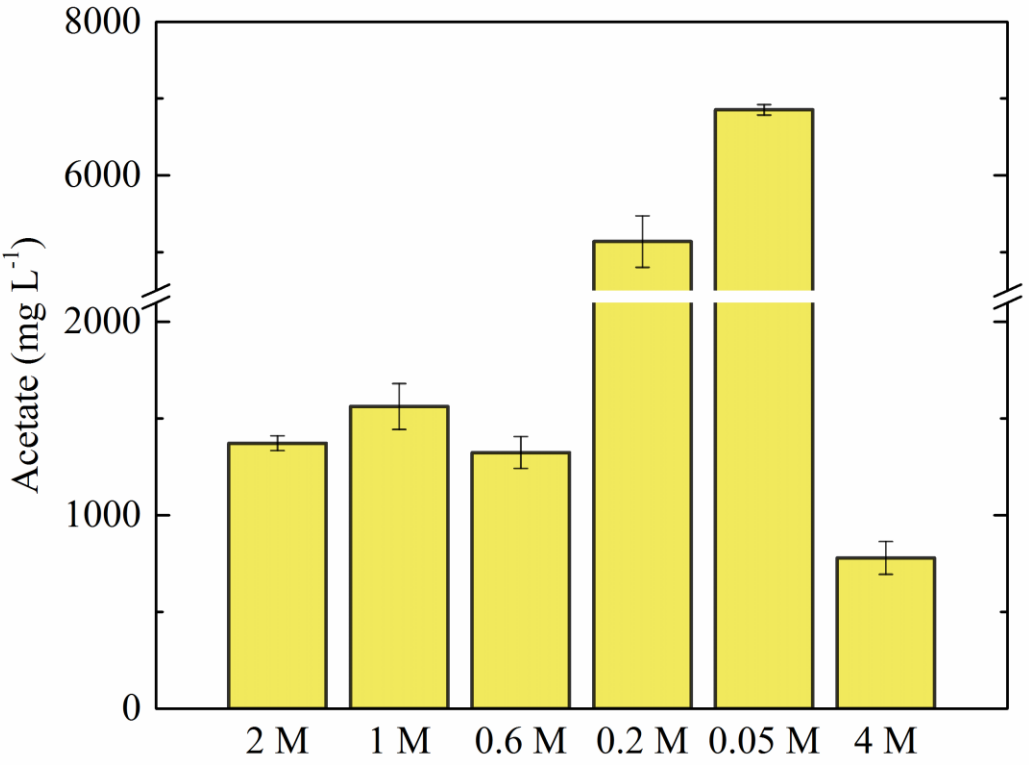

Figure A3 Acetate concentration in the MDC anode effluent. Error bars were calculated from triplicate data.

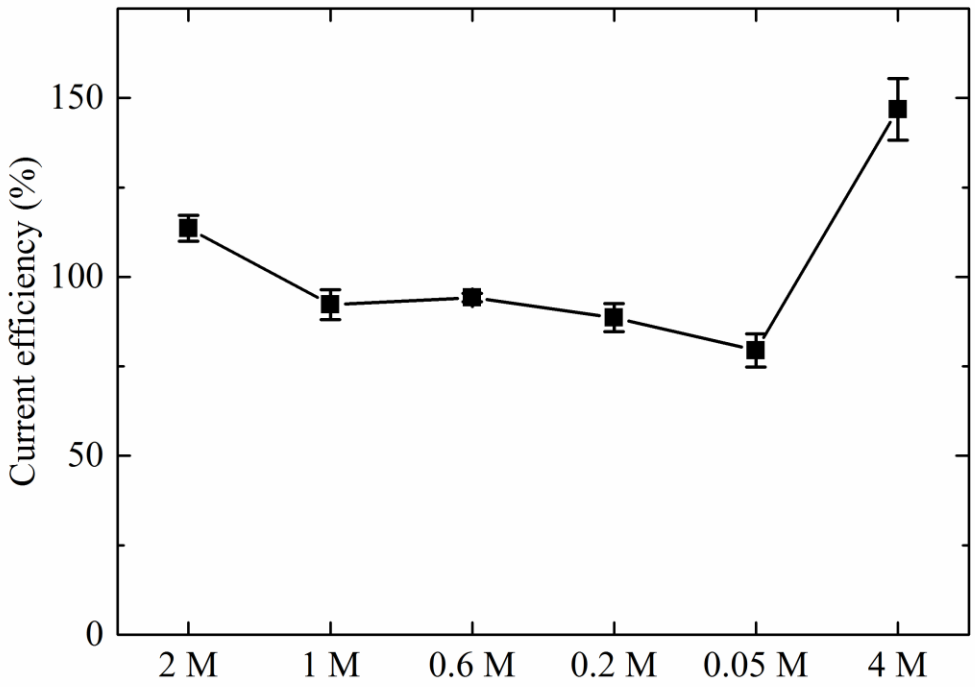

Figure A4 Current efficiency of the MDC under different NaCl concentrations. Error bars were calculated from triplicate data.

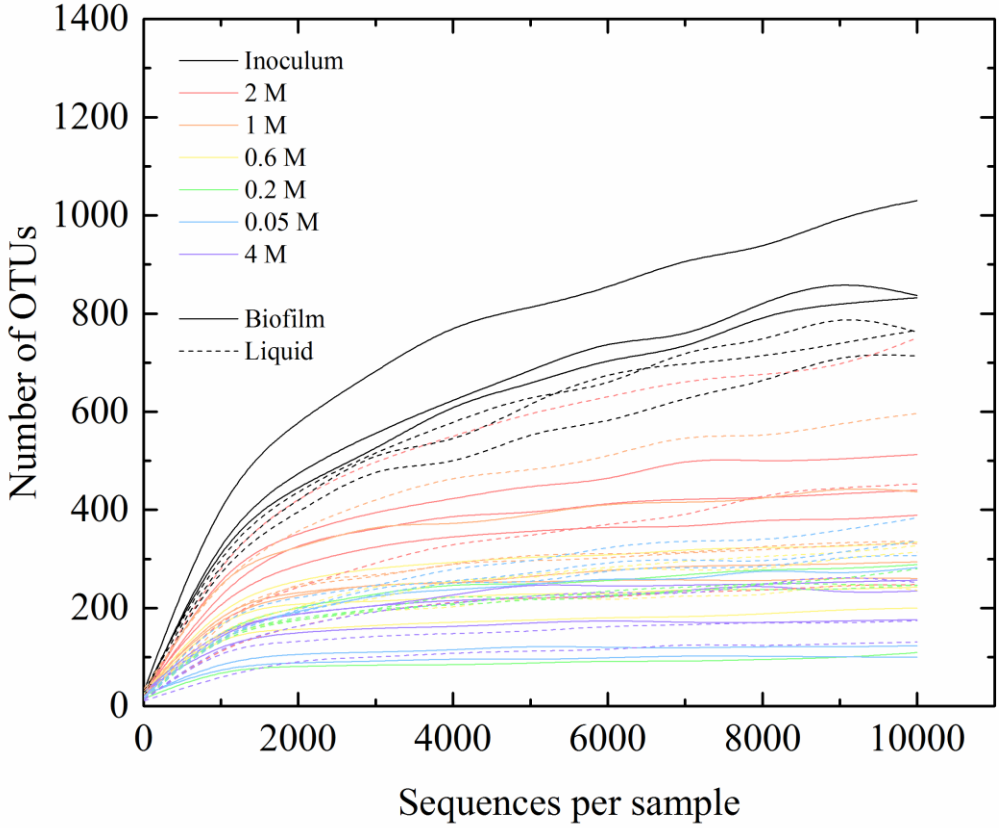

Figure A5 Rarefaction curve of the sequencing results.

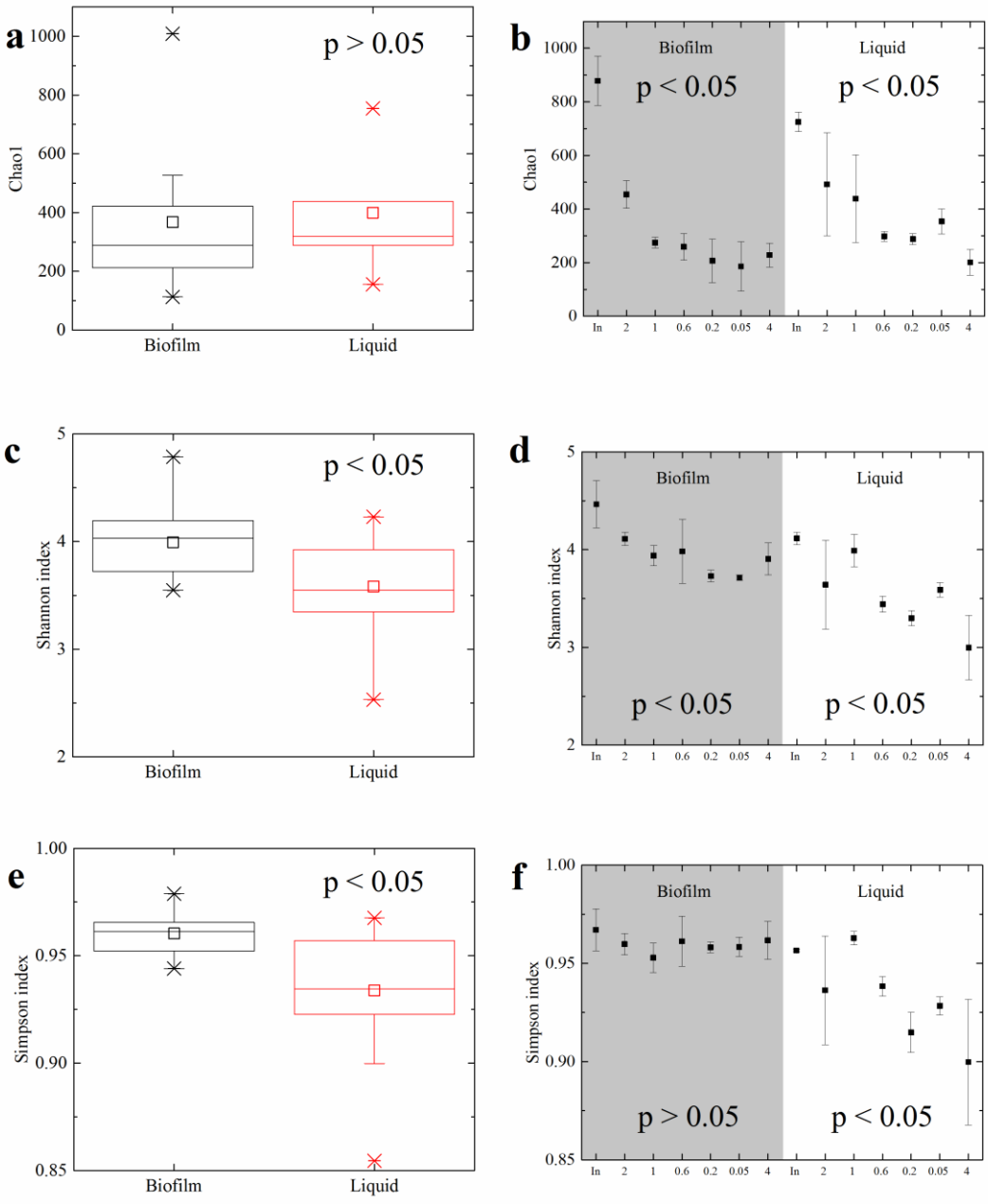

Figure A6 (a), (c) and (e) The average α-diversity indices of the biofilm and liquid samples, p-values are obtained with two-sample t-test. (b), (d) and (f) The average α-diversity indices of the anode communities cultivated under different NaCl concentrations, "In" indicates inoculum, p-values are obtained with ANOVA. Error bars were calculated from triplicate data.

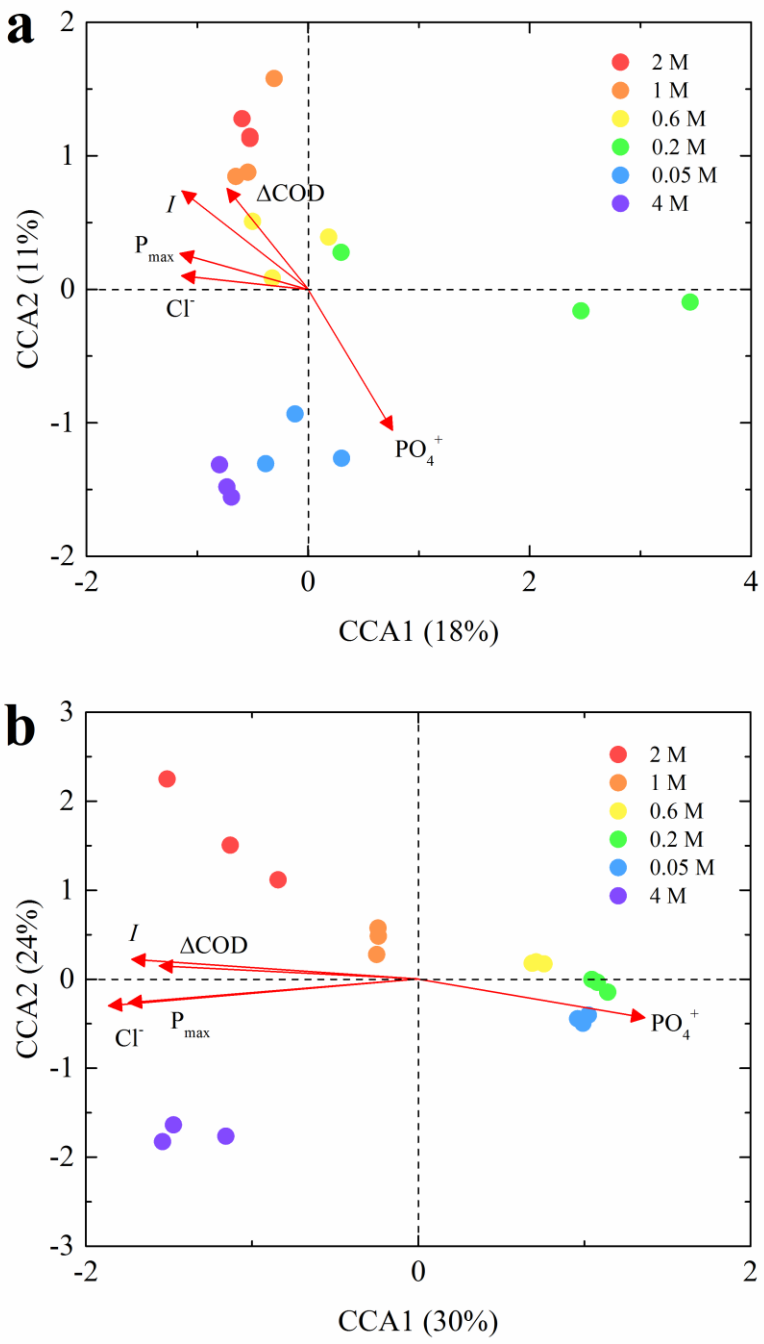

Figure A7 CCA of the microbial communities of the biofilm and liquid samples and reactor performance (I, current; ΔCOD, COD removal; P_{max}, maximum power density).

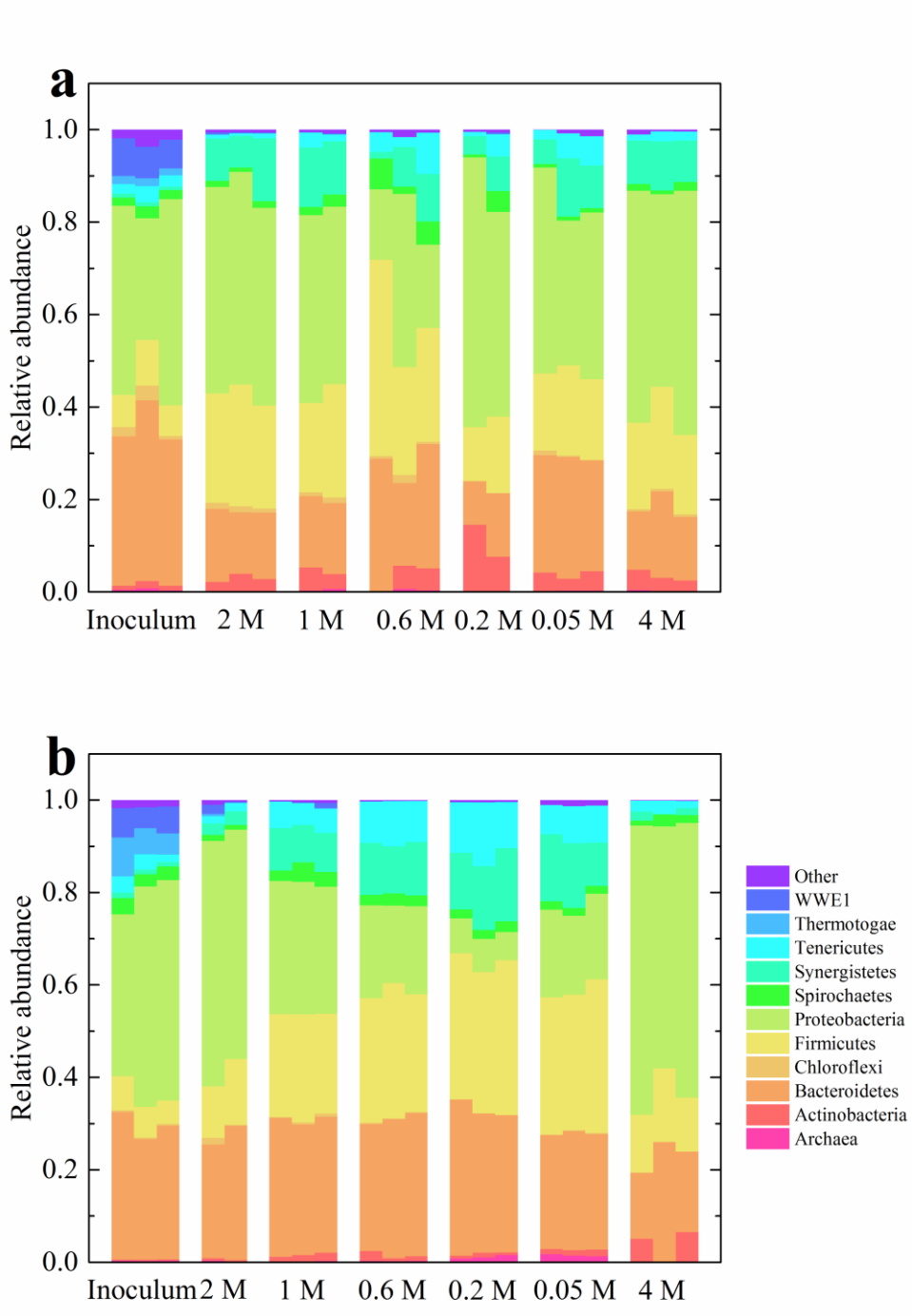

Figure A8 Relative abundance of the biofilm and liquid communities at the phylum level.

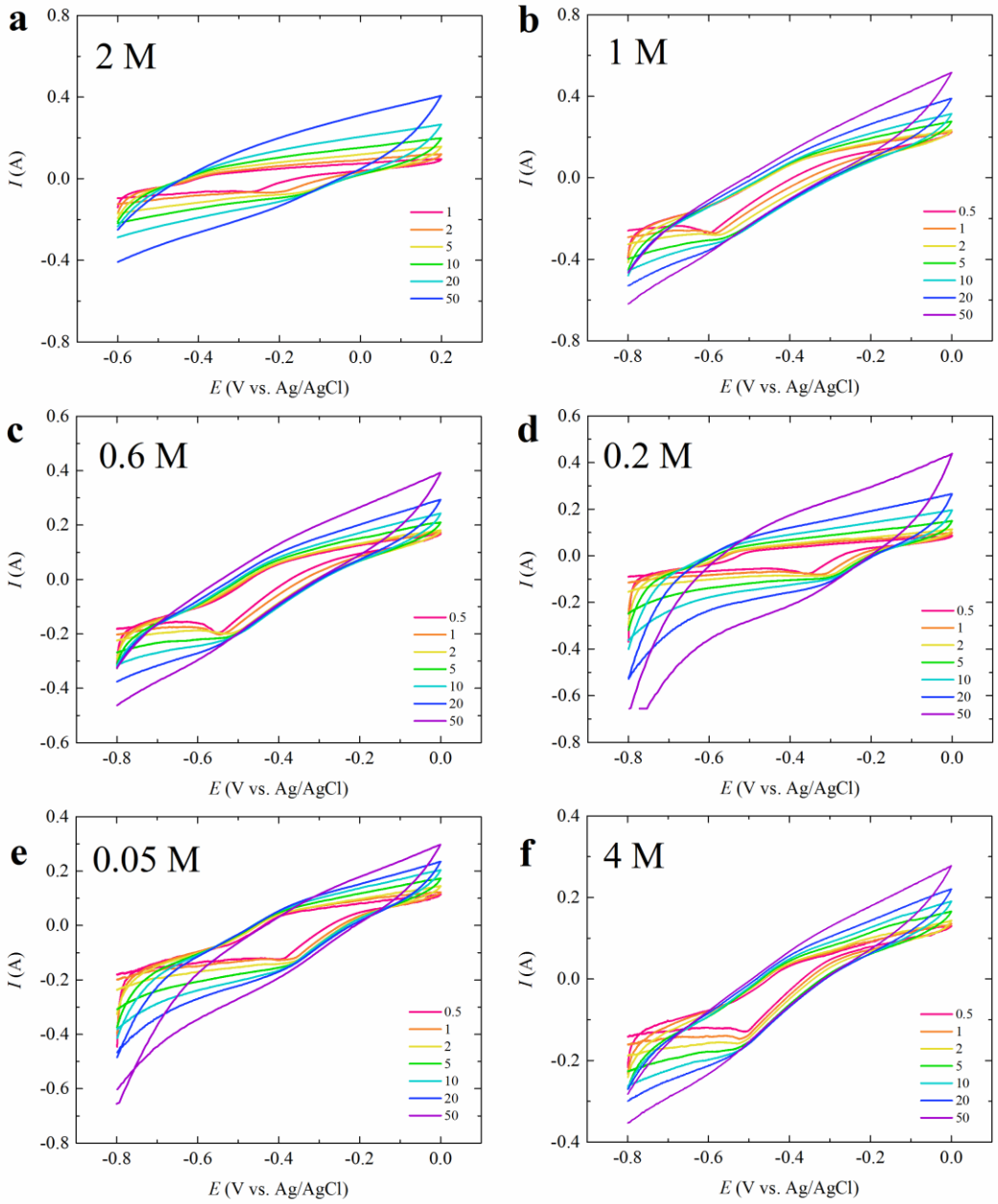

Figure A9 Cyclic voltammetry with the scan rate ranging from 0.5 to 50 mV s^{-1}.

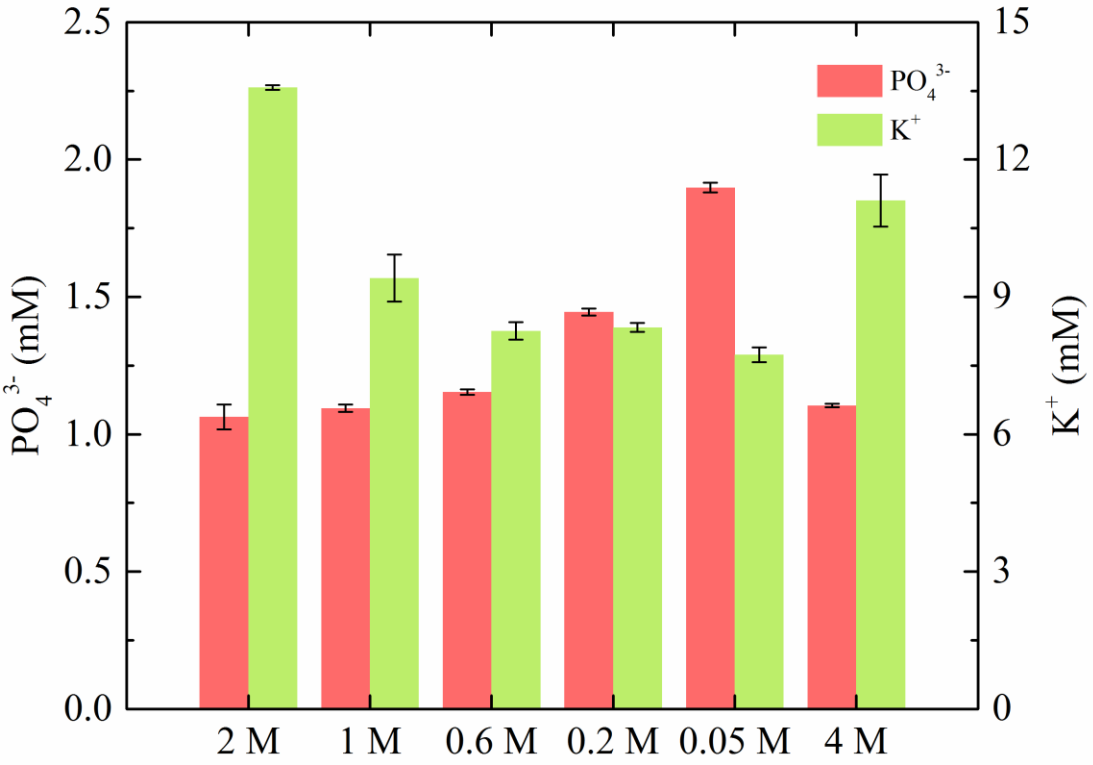

Figure A10 The concentration of PO_4^{3-} and K^+ in the anode effluent with different NaCl concentrations in the desalination chamber. Error bars were calculated from triplicate data.

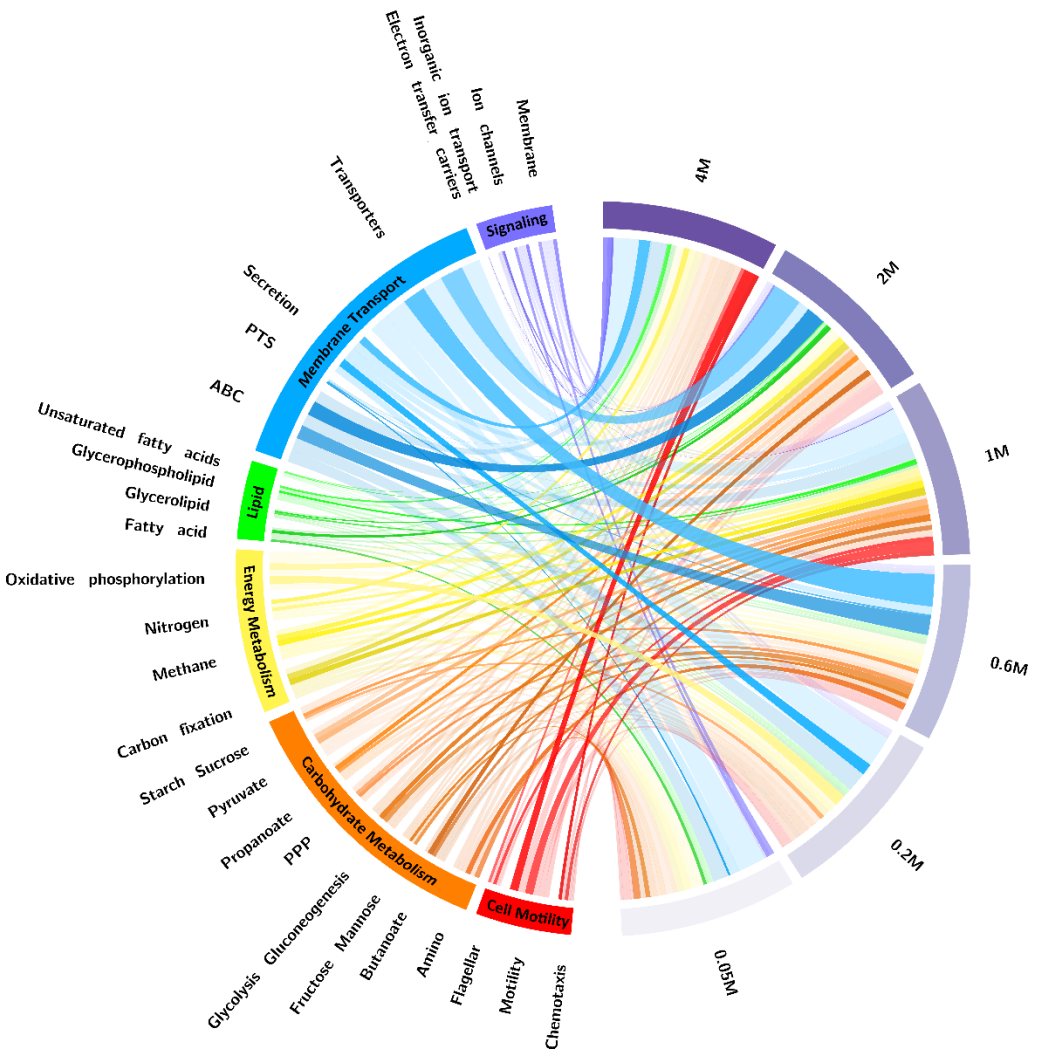

Figure A11 Major functions of the anode biofilm community predicted using PICRUSt and visualized using Circos. The thickness of the band represents the permillage of the function in the predicted data. For each function, there are six bands associated with the six NaCl concentrations, and the two highest permillages were highlighted. Amino, Amino sugar and nucleotide sugar metabolism; PPP, pentose phosphate pathway; ABC, ATP-binding cassette transporters; PTS, phosphotransferase system.

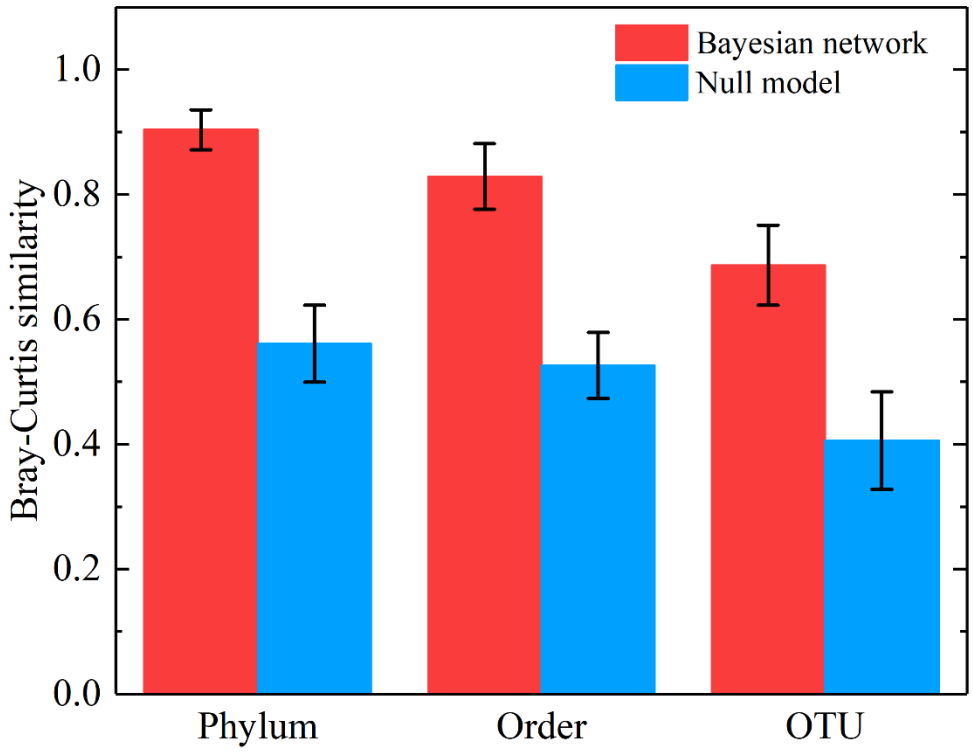

Figure A12 Bray-Curtis similarities between the actual values and the predicted values by the Bayesian networks and the null model at phylum, order and OUT level. Error bars were calculated from 16 datasets.

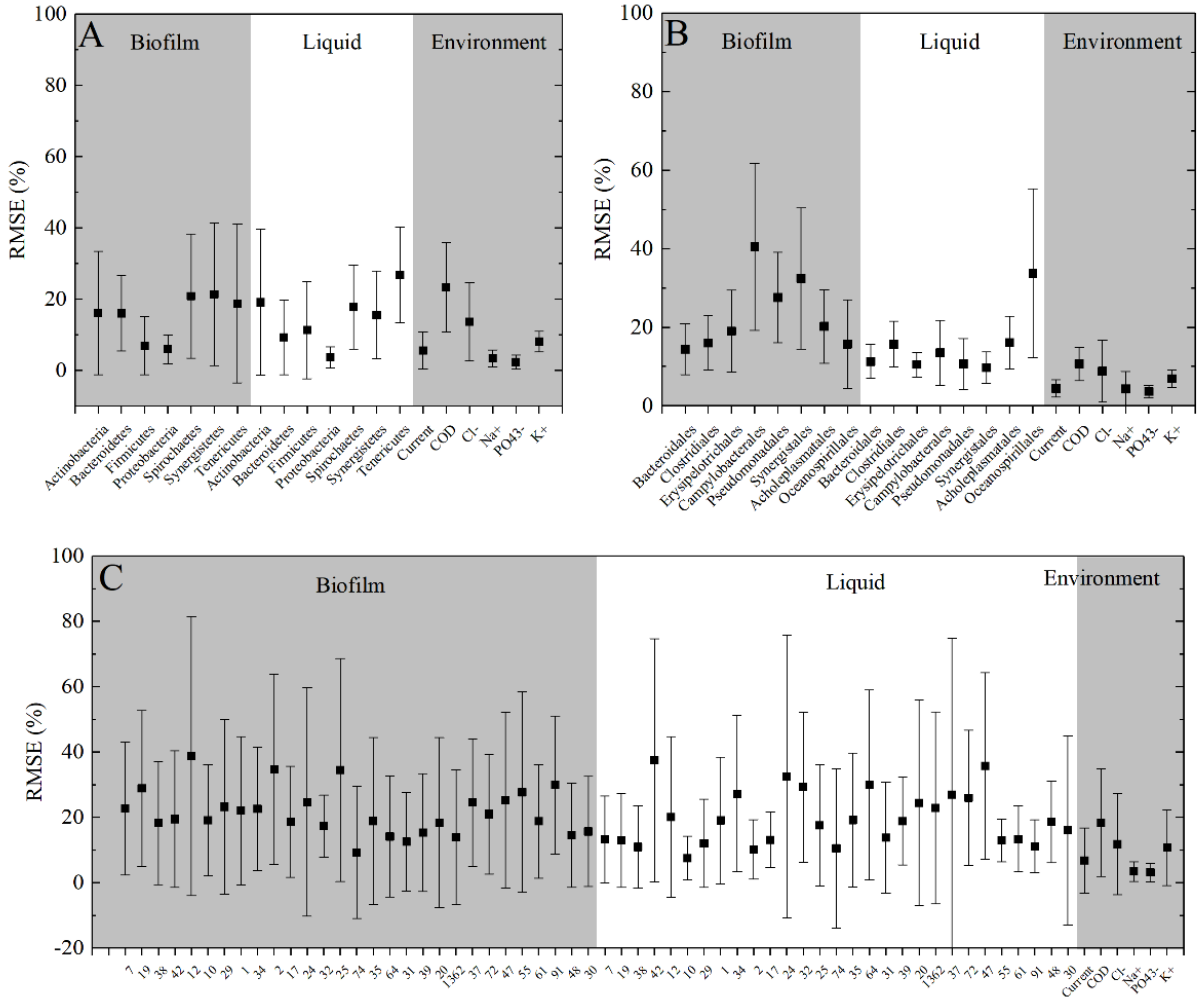

Figure A13 The RMSE between the actual and predicted values at (A) phylum level, (B) order level and (C) OUT level. Error bars were calculated from 16 datasets.

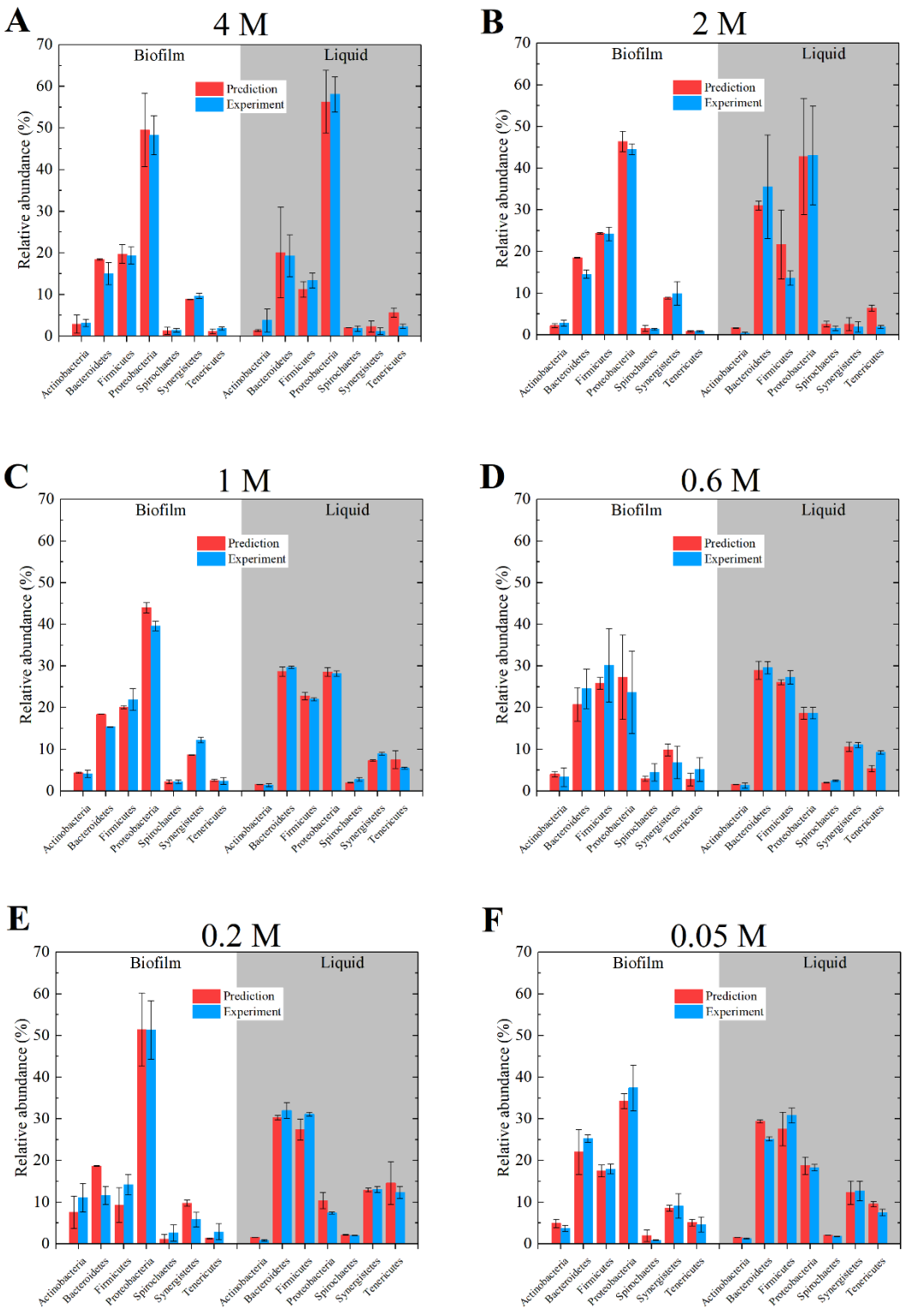

Figure A14 The actual and predicted abundance by Bayesian networks at the phylum level. Error bars were calculated from triplicate data.

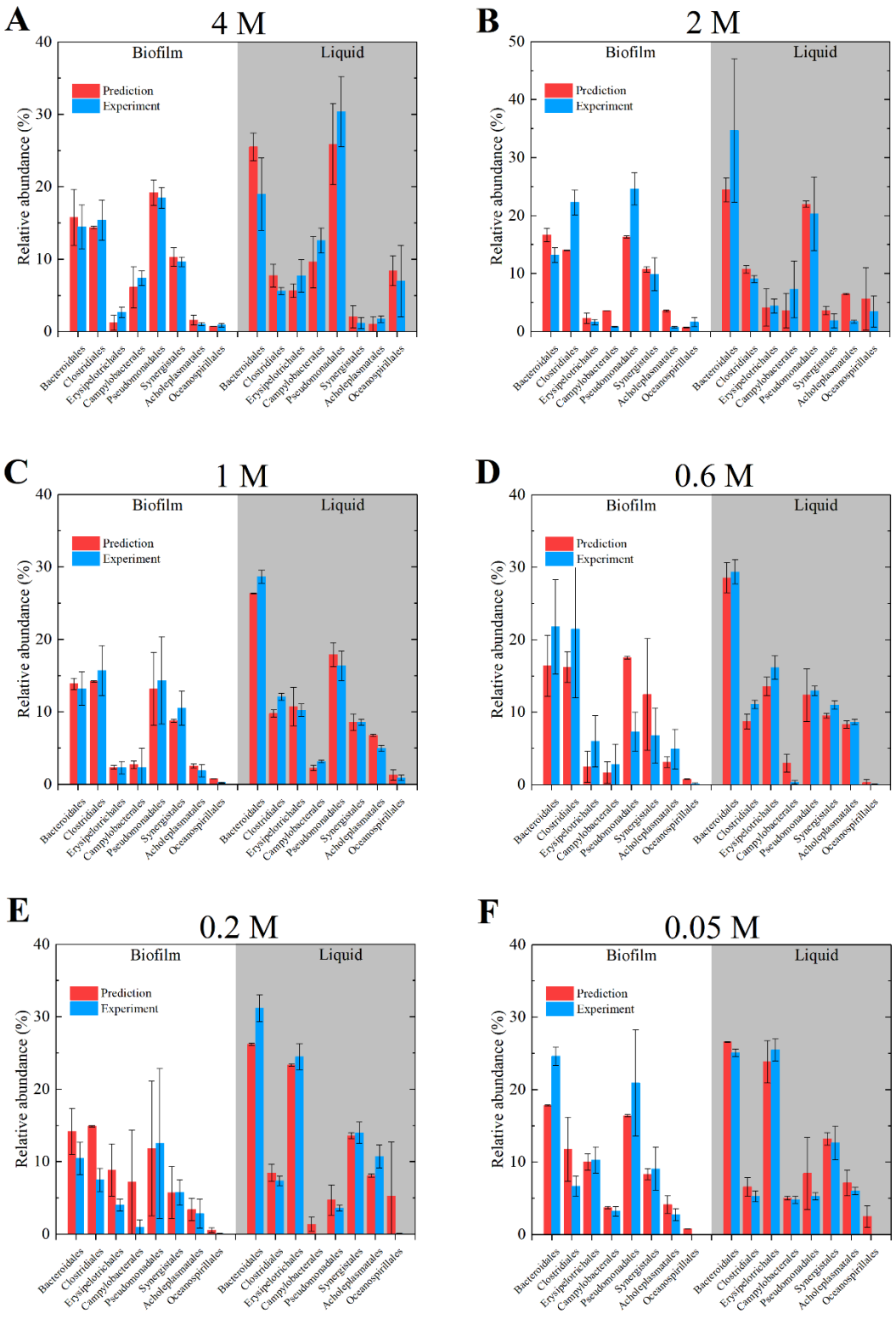

Figure A15 The actual and predicted abundance by Bayesian networks at the order level. Error bars were calculated from triplicate data.

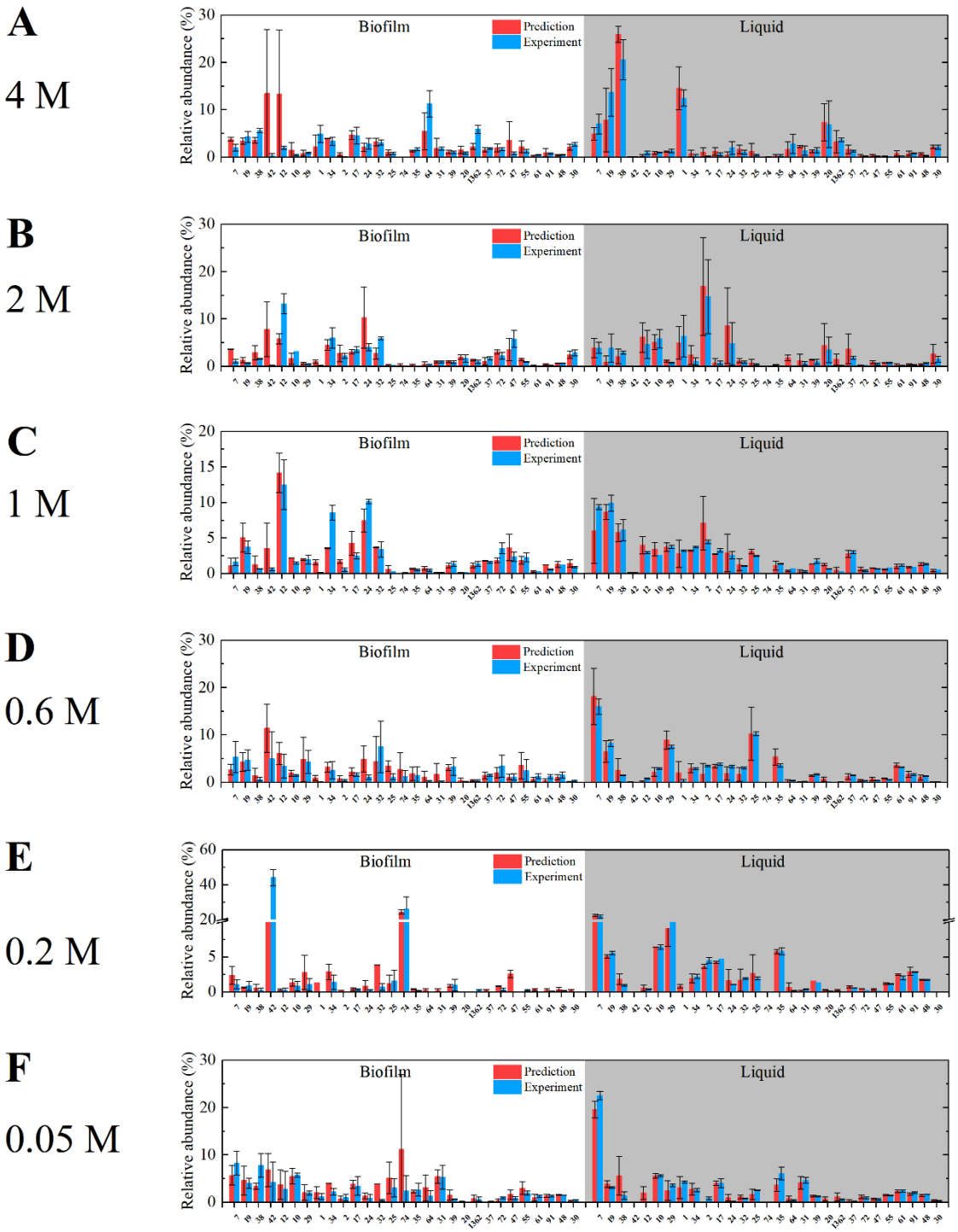

Figure A16 The actual and predicted abundance by Bayesian networks at the OTU level. Error bars were calculated from triplicate data.

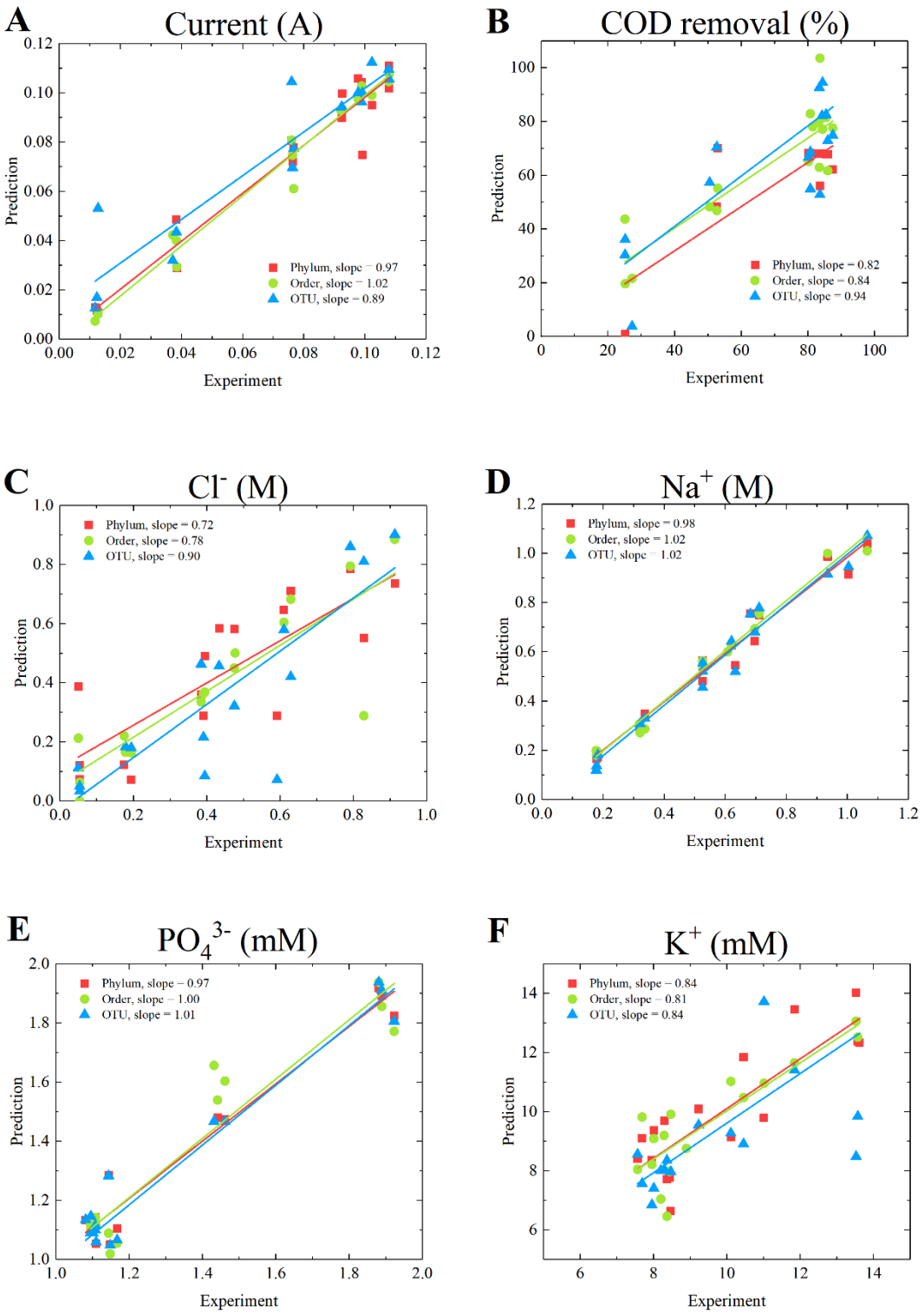

Figure A17 Comparison of predicted and experimental environmental parameters.

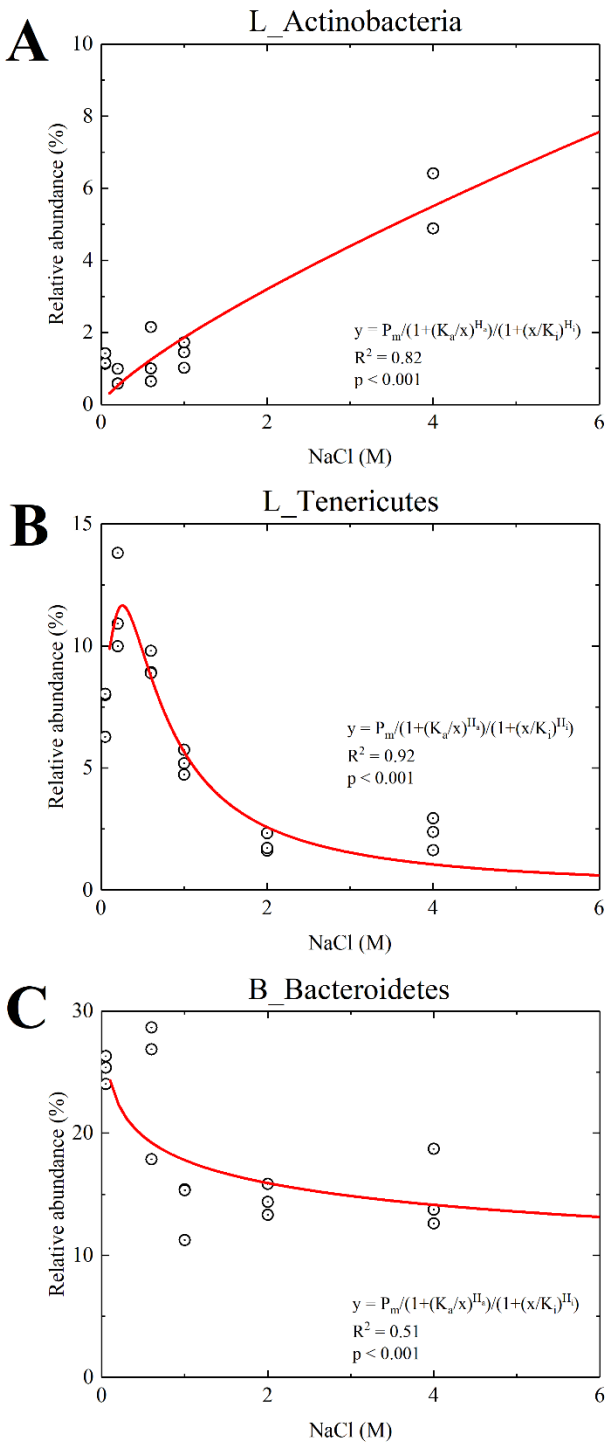

Figure A18 Logistic regression of the relative abundance of the major phyla as a function of NaCl concentration. The prefix "B_" before each phylum indicates the taxa in the biofilm and "L_" indicates the taxa in the liquid samples.

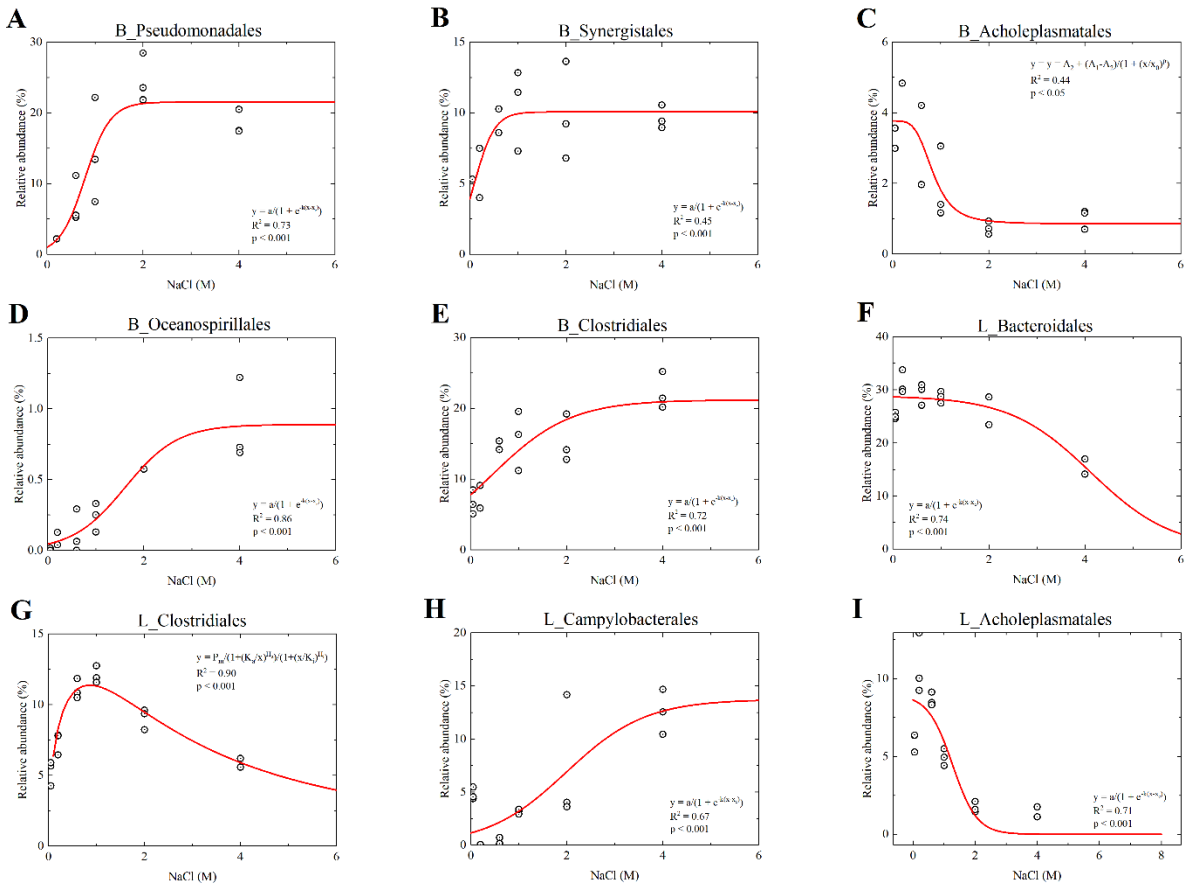

Figure A19 Logistic regressions of the relative abundance of the major orders as a function of NaCl concentration. The prefix "B_" before each order indicates the taxa in the biofilm and "L_" indicates the taxa in the liquid samples.

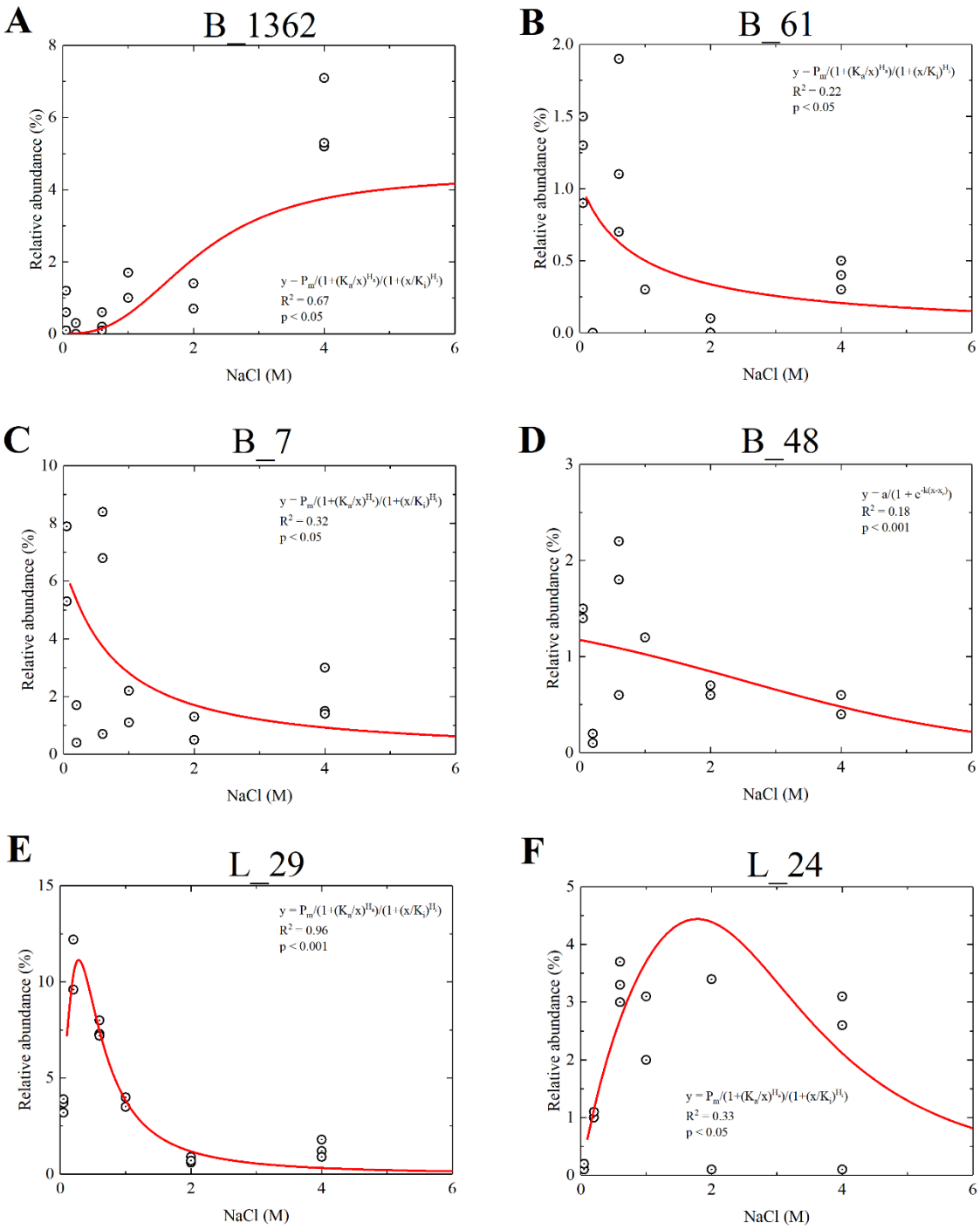

Figure A20 Logistic regressions of the relative abundance of the major OTUs as a function of NaCl concentration. The prefix "B_" before each OTU indicates the taxa in the biofilm and "L_" indicates the taxa in the liquid samples.

Appendix B Supplemental Information for Chapter 3

Table B1 Comparison of BET surface area and pore volume

Sample	S_{BET} (m^2 g^{-1})	V_{p1} (cm^3 g^{-1})
CNT	266	0.927
MoS_2	15	0.084
MoS_2/CNT-90	205	0.856
MoS_2/CNT-60	156	0.886
MoS_2/CNT-30	119	0.669

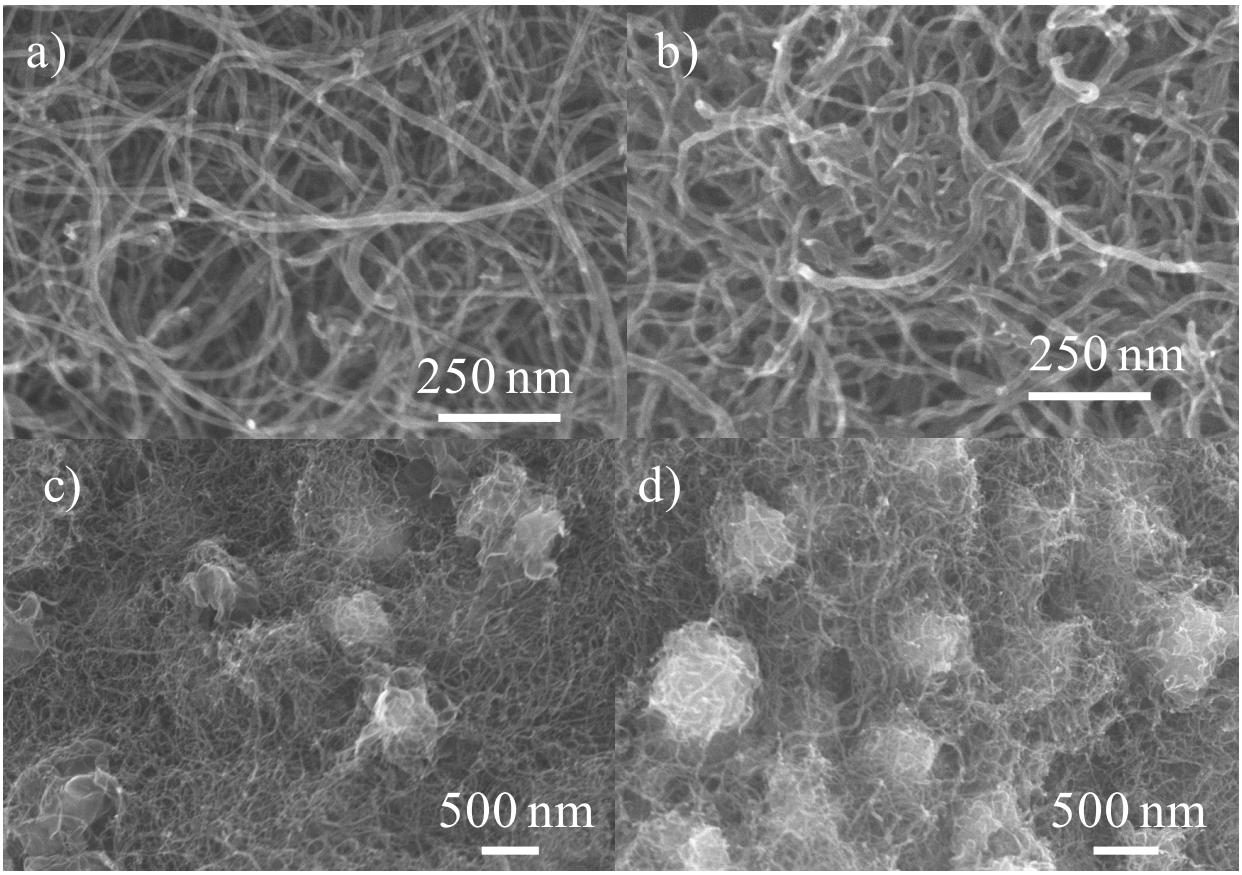

Figure B1 FESEM images of (a) CNTs, (b) MoS_2/CNT-90, (c) MoS_2/CNT-60, (d) MoS_2/CNT-30.

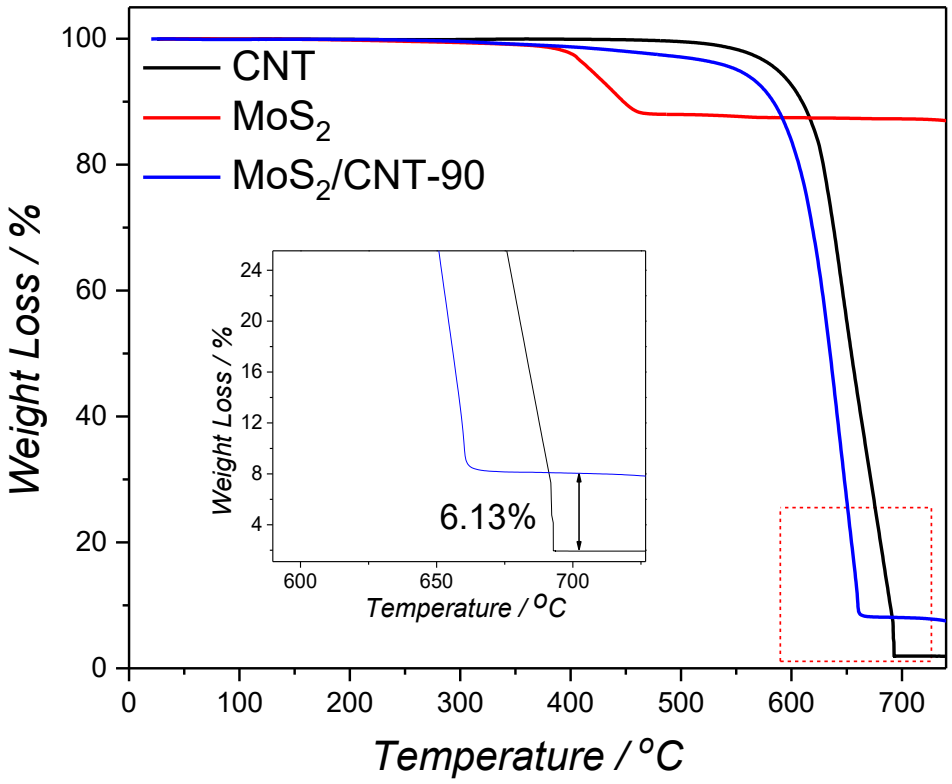

Figure B2 TGA curves of CNT, MoS_2, and MoS_2/CNT-90.

Appendix C Supplemental Information for Chapter 5

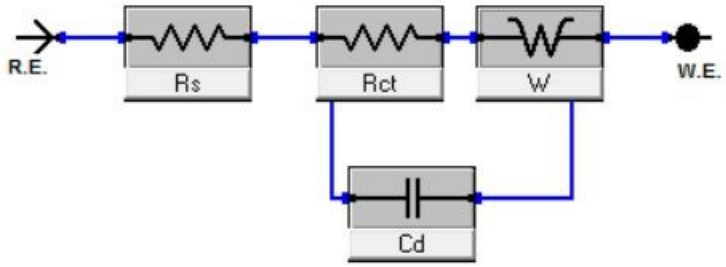

Scheme C1 Equivalent circuit for EIS fitting.

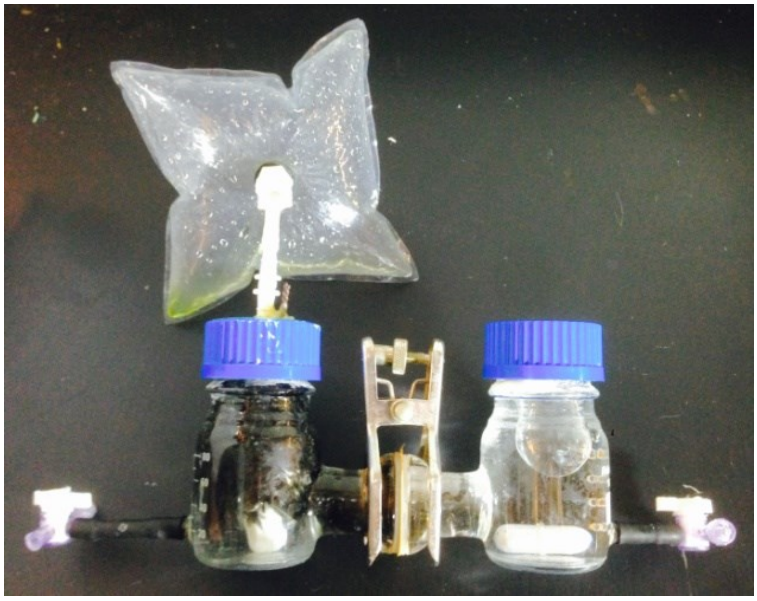

Scheme C2 Photograph of ORR from the MFC experiment.

Table C1 Synthesis and performance of graphene-based cathode catalysts in MFCs.

Material	Precursor	Synthesis	Power density	Ref.
N-G@CoNi/BCNT	**Urea, $Co(NO_3)_2$, and $NiCl_2$**	**One-pot pyrolysis**	**2000 mW m^{-2}**	**This work**
N-carbon nanotube	Ethylenediamine	Chemical vapor deposition	1600 mW m^{-2}	[448]
N-graphene films	Cyanuric chloride, trinitropheno	Detonation at 320 ℃ and 60 MPa	1350 mW m^{-2}	[59]
Crumpled GO	GO	Modified Hummer's method Capillary compression	3300 mW m^{-3}	[279]
Biofilm/graphene	GO	Modified Hummer's method Microbial reduction	323.2 mW m^{-2}	[449]
Fe/N-graphene powder	GO, g-C_3N_4, $FeCl_3$	Modified Hummer's method Hydrazine reduction	1149.8 mW m^{-2}	[316]
FeTsPc-graphene particles	rGO, FeTsPc	Staudenmaier method Hydrazine reduction Ultrasonication	817 mW m^{-2}	[49]
MnO_2-graphene nanosheets	rGO, $KMnO_4$	Modified Hummer's method Hydrazine reduction Microwave irradiation	2083 mW m^{-2}	[317]
Co_3O_4/N-graphene	GO, $Co(Ac)_2$	Modified Hummer's method Hydrothermal reduction	1340 mW m^{-2}	[318]
PANI-graphene nanosheets	rGO, PANI	Modified Hummer's method Hydrazine reduction Situ-polymerization	99 mW m^{-2}	[450]
mpg-C_3N_4/N-graphene nanosheets	N-graphene, mesoporous graphitic C_3N_4	Modified Hummer's method One-pot solvothermal process Implantation of nitrogen active sites	1618 mW m^{-2}	[55]
MnO_2-NTs/graphene	GO, MnO_2-NTs	Modified Hummer's method $NaBH_4$ reduction	4680 mW m^{-3}	[451]
Pt-Co/graphene	GO, $H_2PtCl_6 \cdot 6H_2O$, $Co(NO_3)_2 \cdot 6H_2O$	Modified Hummer's method Ethylene glycol reduction	1378 mW m^{-2}	[452]
N-graphene films	rGO, cyanamide	Modified Hummer's method Hydrazine reduction Pyrolysis	776 mW m^{-2}	[335]
AgNPs/rGO	GO, $AgNO_3$	Modified Hummer's method $NaBH_4$ reduction	474.5 mW m^{-2}	[453]
graphene	GO	High intensity laser exposure	1820 W m^{-3}	[454]
α-MnO_2/GO nanocomposites	GO, $KMnO_4$	Modified Hummer's method Hydrothermal method	3359 mW m^{-2}	[455]
Porous N-carbon nanosheet on graphene	GO-PANI, NCN	Modified Hummer's method Rapid-mixture polymerization Carbonization	1159.34 mW m^{-2}	[456]

pTSA-doped graphene@PANI	Graphene, aniline, pTSA	Oxidative polymerization and mixing	17.95 mW m^{-2}	[457]
Fe_3O_4-rGO	GO, $FeSO_4 \cdot 7H_2O$	Modified Hummer's method Fe^{2+} reduction	283 mW m^{-2}	[458]
N/S-CNS	Potassium citrate, diphenyl disulfide, NH_3	High temperature annealing	1500 mW m^{-2}	[459]
FeN/graphene	GO, $FeCl_3$, urea, cyanimide,	Modified Hummers' method Homogeneous deposition	865 mW m^{-2}	[460]

Table C2 Exchange current density calculated from Tafel plot.

Catalyst	j_0 (A m^{-2})
Pt/C	2.59×10^{-3}
Ni-NBCNT	6.01×10^{-4}
Co-NBCNT	7.98×10^{-5}
N-G@CoNi/BCNT	1.73×10^{-3}
CoNi-NBCNT	1.17×10^{-3}

j_0: exchange current density.

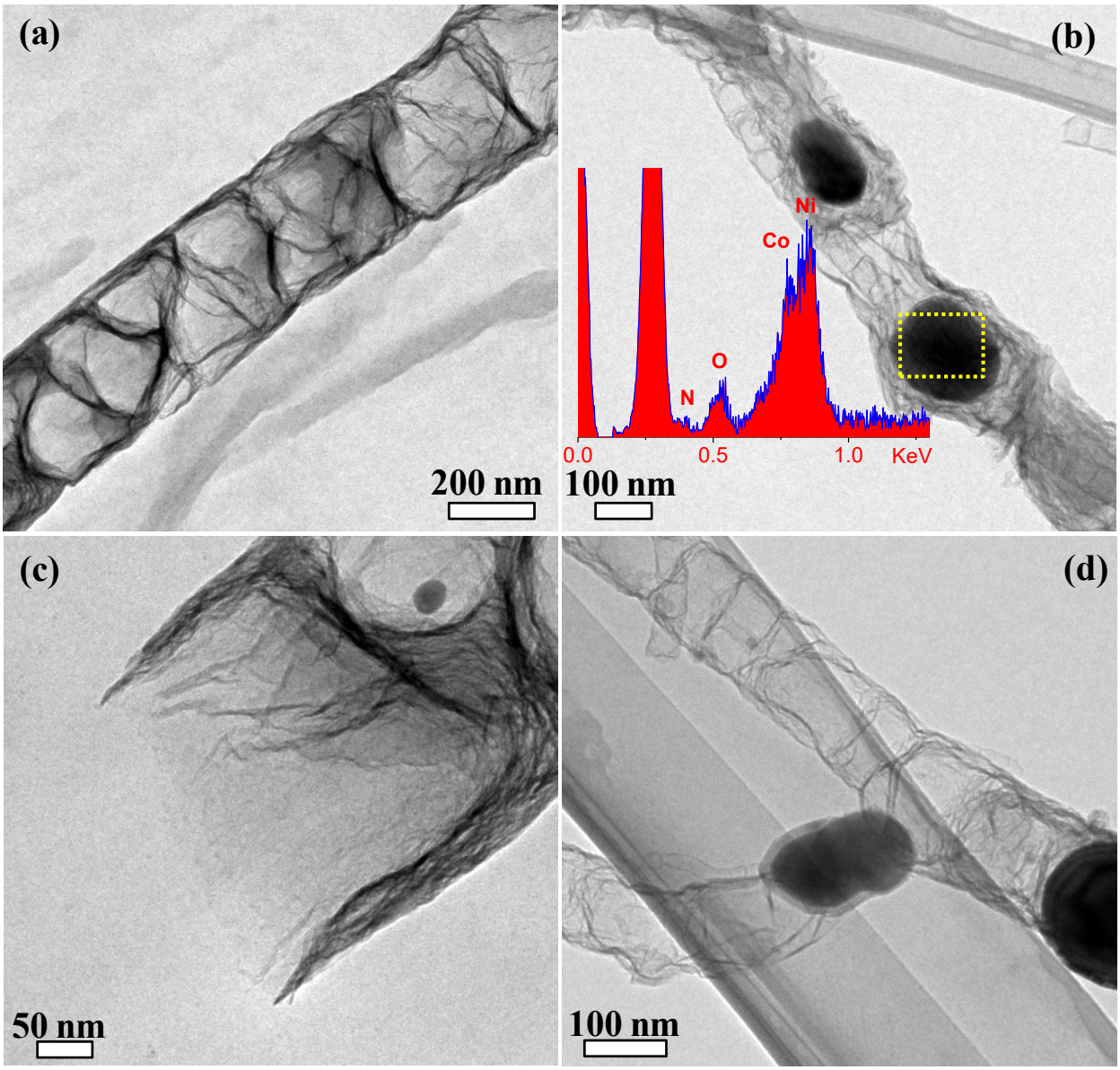

Figure C1 (a-d) TEM images of N-G@CoNi/BCNT at different magnifications. The inset of (b) shows the EDX spectrum from the area labeled by the rectangular box in (b).

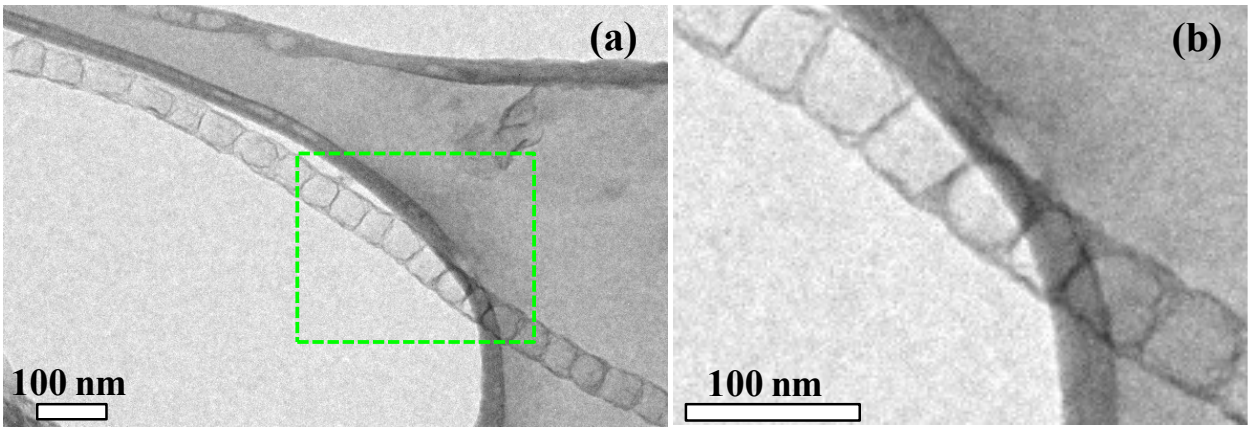

Figure C2 TEM images of CoNi-NBCNT.

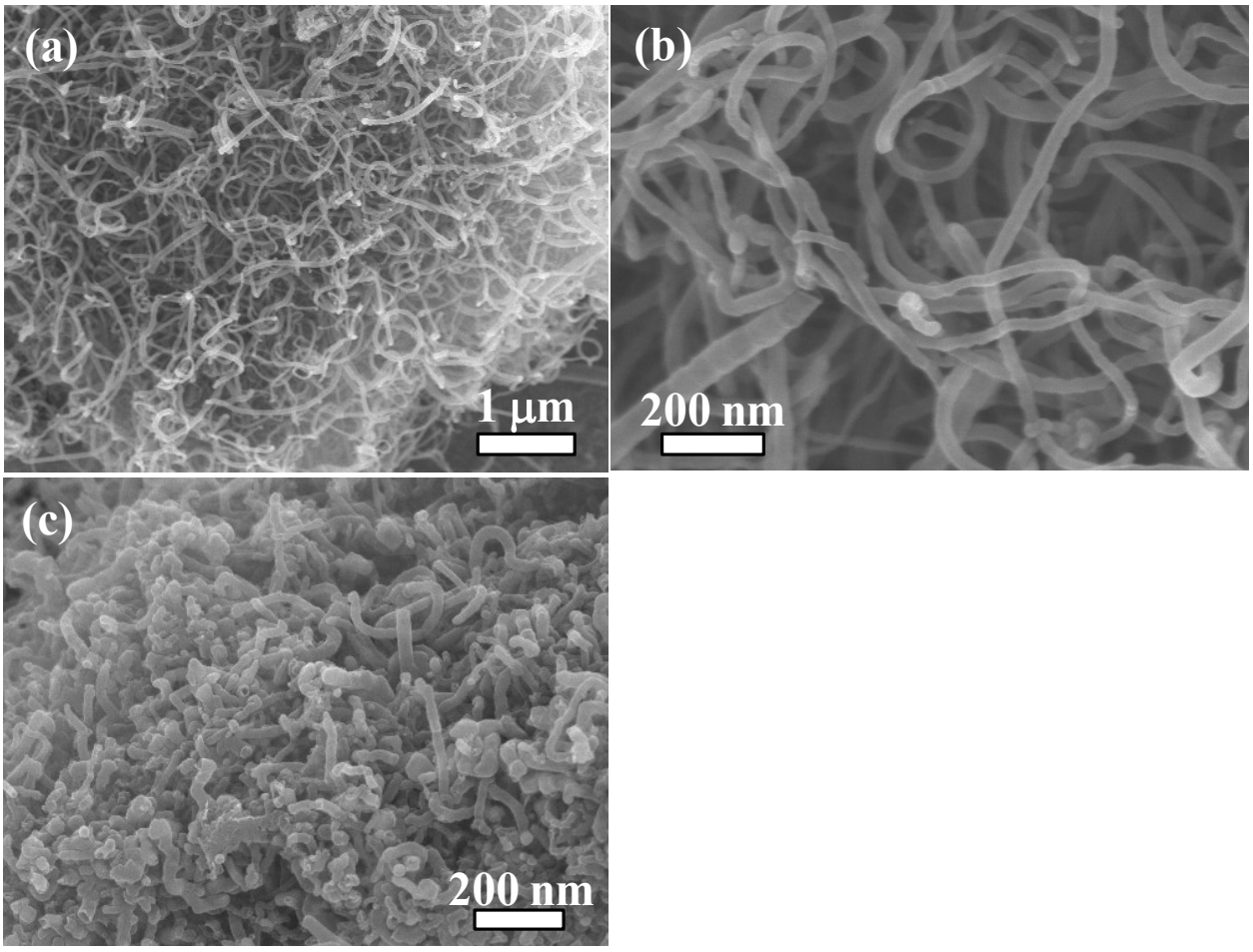

Figure C3 FESEM images of Co-NBCNT (a-b) and Ni-NBCNT (c).

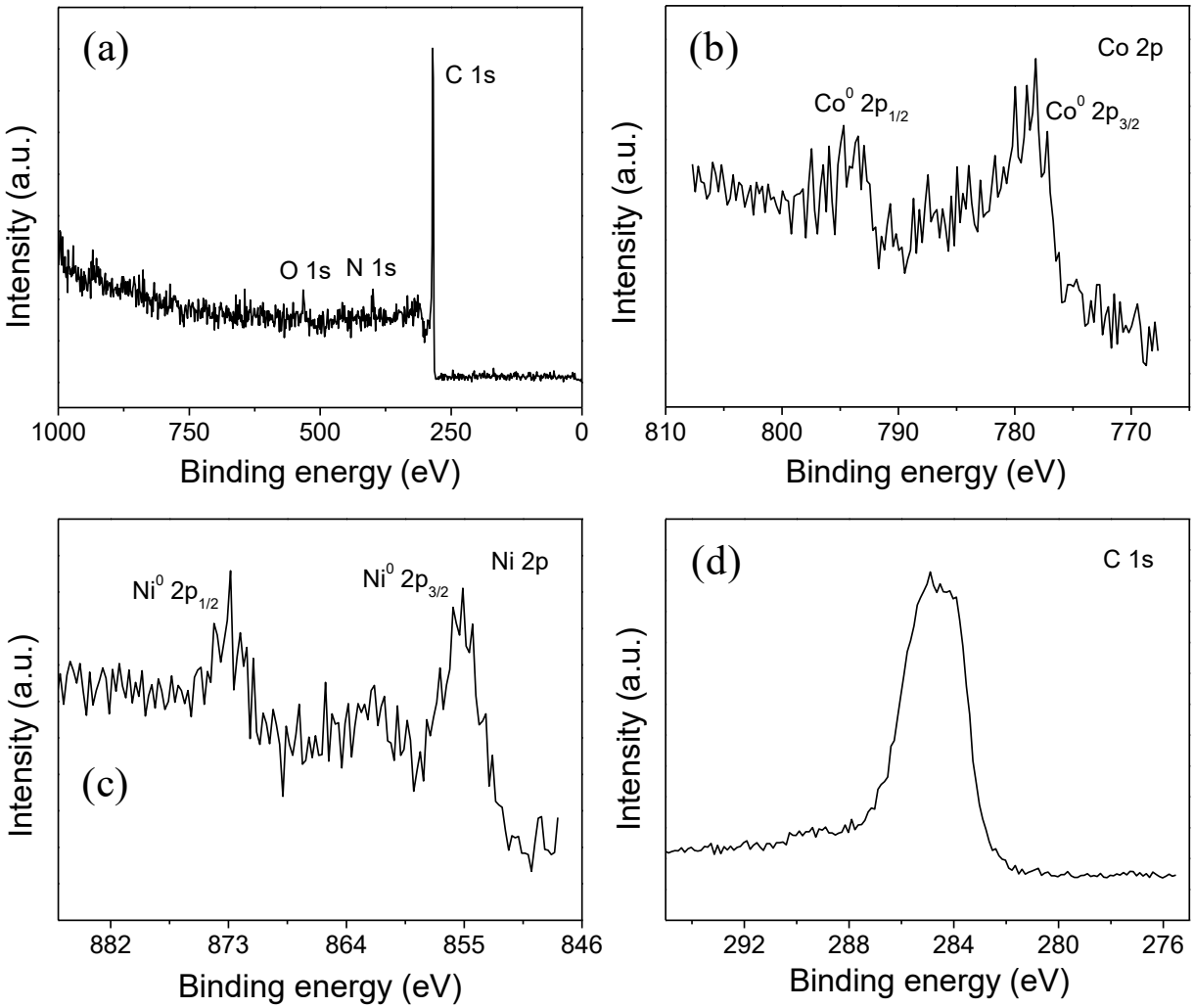

Figure C4 The survey XPS spectrum (a), high-resolution Co 2p and Ni 2p XPS spectra (b-c), and high-resolution C 1s XPS spectrum (d) of N-G@CoNi/BCNT.

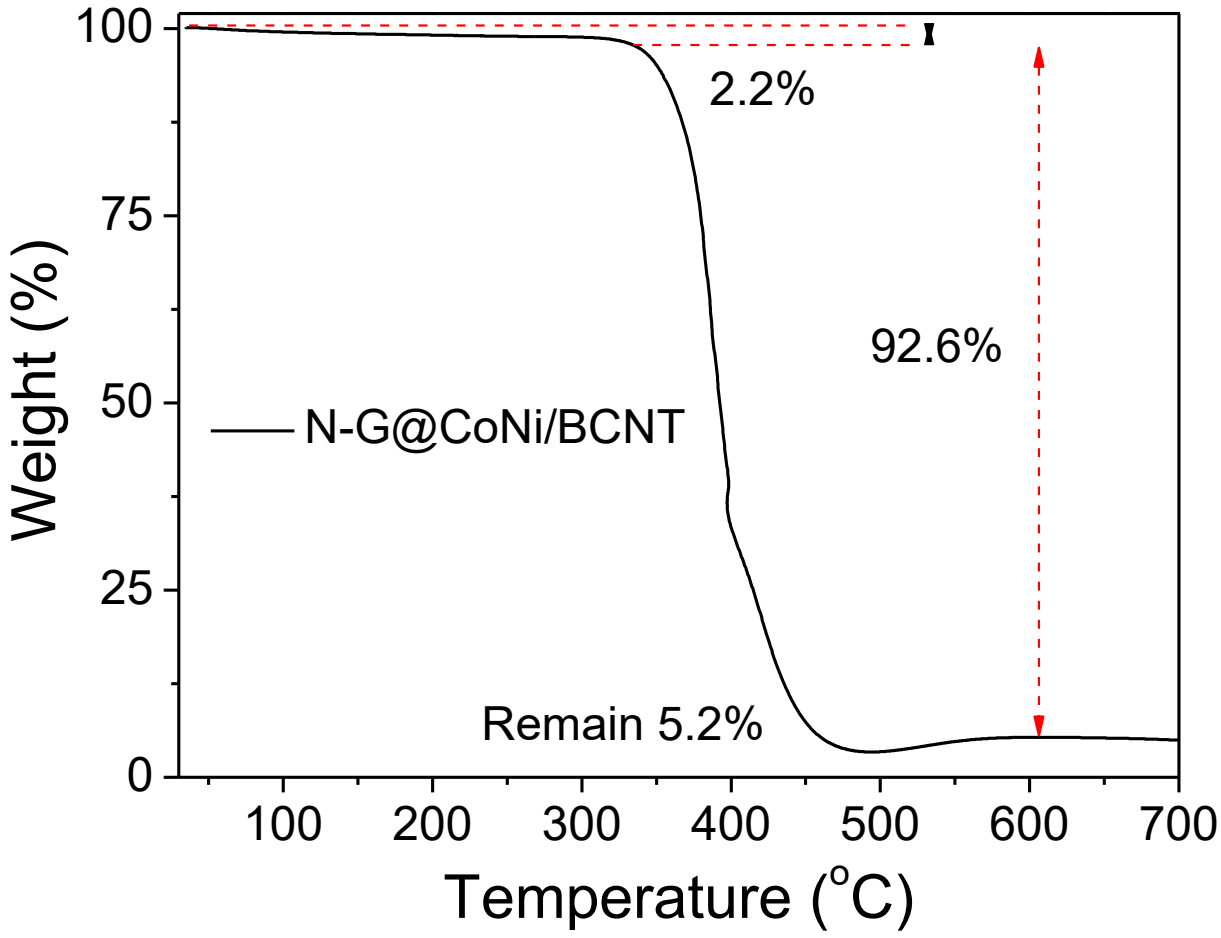

Figure C5 TGA curve of N-G@CoNi/BCNT under flowing Air.

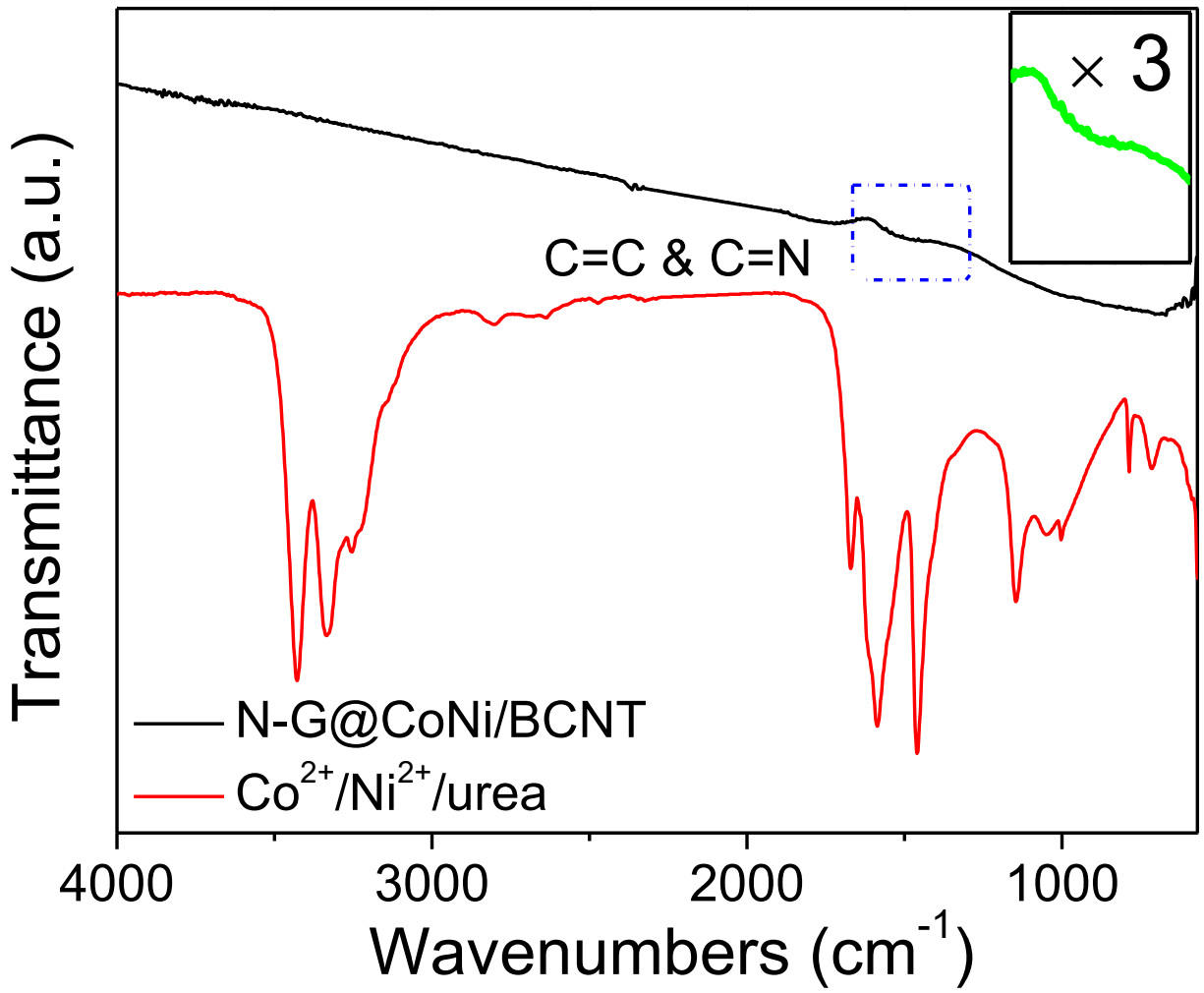

Figure C6 FTIR spectra of Co^{2+}/Ni^{2+}/urea and N-G@CoNi/BCNT.

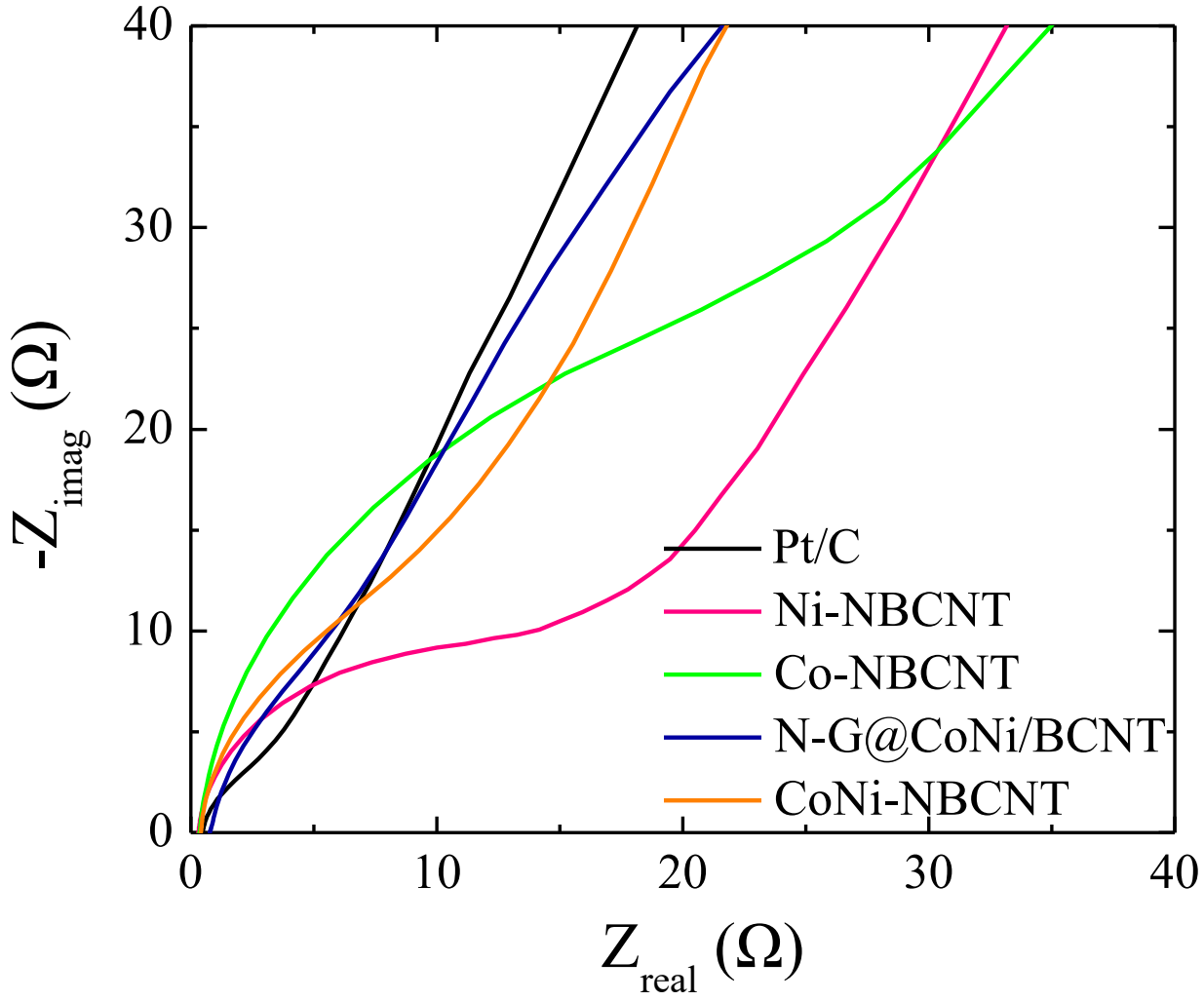

Figure C7 EIS Nyquist plots of Ni-NBCNT, Co-NBCNT, CoNi-NBCNT, N-G@CoNi/BCNT, and Pt/C at a bias of 0 V.

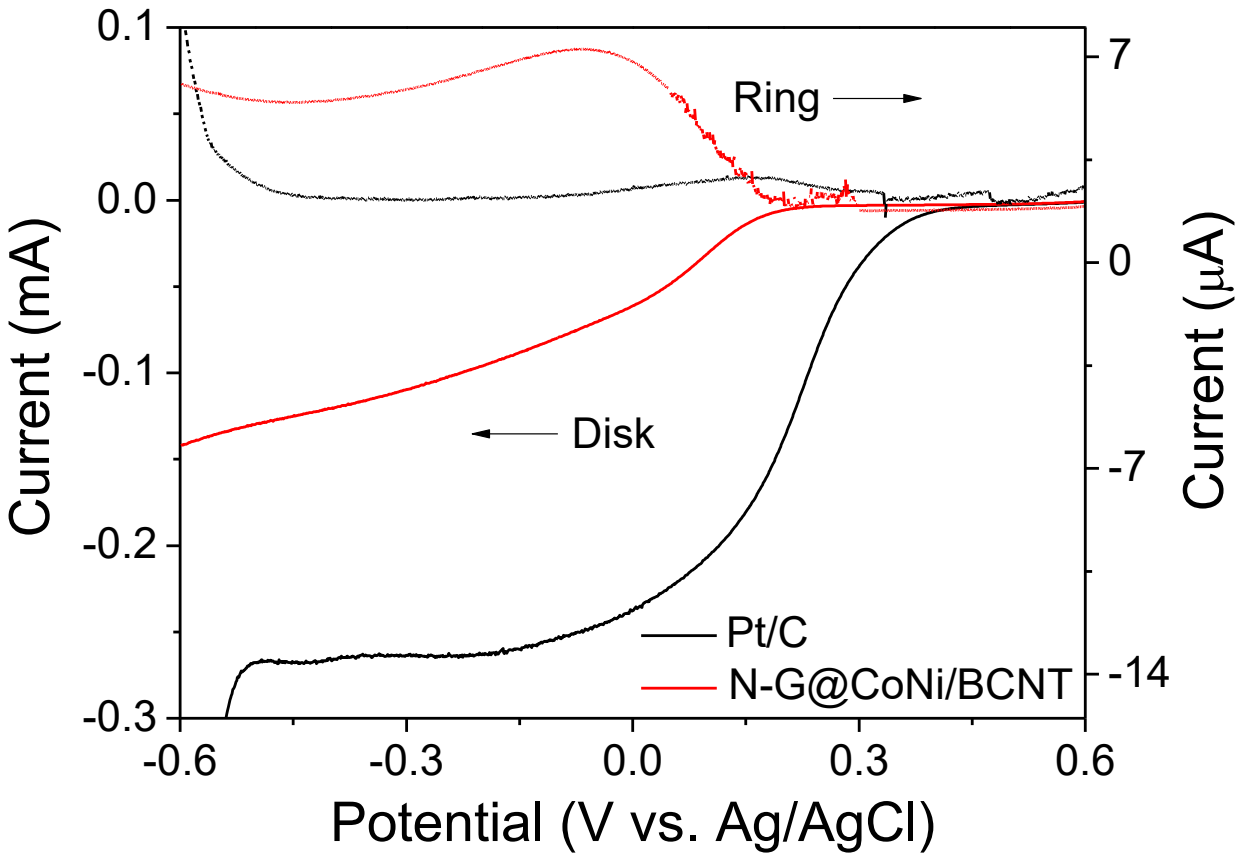

Figure C8 LSV curves on RRDE for N-G@CoNi/BCNT and Pt/C in O_2-saturated 1.0 M PBS solution at 1,600 rpm. The disk potential was scanned at 5 mV s^{-1} and the ring potential was fixed at 0.5 V.

Appendix D Supplemental Information for Chapter 7

Table D1 Values of the Parameters

Parameters		Description	Value
PRO	A	permeability coefficient	1.0×10^{-7} m^3 m^{-2} s^{-1} bar^{-1}
	K	solute resistivity	2.5×10^{-5} s m
	k	mass transfer coefficient	1.48×10^{-5} m^3 m^{-2} s^{-1}
	i	number of dissolved species	2
	R	ideal gas constant	8.3145 J mol^{-1} K^{-1}
	T	absolute temperature	298.15 K
	B	salt permeability coefficient	1.5×10^{-7} m^3 m^{-2} s^{-1}
	a	membrane area	0.014 m^2
MEC	$x_{f,max}$	maximum concentrations of fermentative organisms	500 mg-x L^{-1}
	$x_{e,max}$	maximum concentrations of exoelectrogens	500 mg-x L^{-1}
	$x_{m,max}$	maximum concentrations of methanogens	25 mg-x L^{-1}
	$q_{f,max}$	maximum substrate consumption rates by fermentative organisms	39 mg-S mg-x^{-1} day^{-1}
	$q_{e,max}$	maximum substrate consumption rates by exoelectrogens	3 mg-A mg-x^{-1} day^{-1}
	$q_{m,max}$	maximum substrate consumption rates by methanogens	10 mg-A mg-x^{-1} day^{-1}
	K_f	half saturation concentrations for fermentative organisms	100 mg-S L^{-1}
	K_e	half saturation concentrations for exoelectrogens	35 mg-S L^{-1}
	K_m	half saturation concentrations for methanogens	80 mg-S L^{-1}
	K_M	half saturation concentrations for redox mediators	0.01 mg-M mg-x^{-1}
	$\mu_{f,max}$	maximum growth rates by the fermentative organisms	0.2 day^{-1}
	$\mu_{e,max}$	maximum growth rates by the exoelectrogens	0.197 day^{-1}
	$\mu_{m,max}$	maximum growth rates by the methanogens	0.1 day^{-1}
	d_f	decay rates of the fermentative organisms	0.04 day^{-1}
	d_e	decay rates of the exoelectrogens	0. 394 day^{-1}
	d_m	decay rates of the methanogens	0.2 day^{-1}
	M_{total}	total mediator fraction per exoelectrogen	0.05 mg-M mg-x^{-1}

Y_M	mediator yield	22 mg-M mg-S^{-1}
γ	mediator molar mass	663400 mg-M mole-M^{-1}
ε	a constant that affects the current	0.0001 mg-M mg-x^{-1}
K_R	A constant that determines the curve steepness	0.0818
R_{mem}	the resistance of the AEM and CEM	2 Ω
R_{min}	the lowest observed internal resistance	15 Ω
R_{max}	the highest observed internal resistance	2000 Ω
r_C	radius of the CEM	0.00163 m
r_A	radius of the AEM	0.00184 m

Appendix E Supplemental Information for Chapter 8

Table E1 Parameters used in the time-dependent PRO model and batch-mode MEC model.

Parameters		Description	Value
PRO	A	permeability coefficient	1.20×10^{-7} m^3 m^{-2} s^{-1} bar^{-1}
	B	salt permeability coefficient	1.39×10^{-7} m^3 m^{-2} s^{-1}
	S	support layer structural parameter	0.0005 m
	D	diffusion coefficient of NaCl in the membrane substrate	1.48×10^{-9} m^2 s^{-1}
	k	mass transfer coefficient	1.48×10^{-5} m^3 m^{-2} s^{-1}
	i	number of dissolved species	2
	R	ideal gas constant	8.3145 J mol^{-1} K^{-1}
	a	membrane area	0.014 m^2
MEC	$x_{e,max}$	maximum concentrations of exoelectrogens	438.9 mg-x L^{-1}
	$x_{m,max}$	maximum concentrations of methanogens	10 mg-x L^{-1}
	$q_{e,max}$	maximum substrate consumption rates by exoelectrogens	3 mg-S mg-x^{-1} day^{-1}
	$q_{m,max}$	maximum substrate consumption rates by methanogens	10 mg-S mg-x^{-1} day^{-1}
	K_e	half saturation concentrations for exoelectrogens	35 mg-S L^{-1}
	K_m	half saturation concentrations for methanogens	80 mg-S L^{-1}
	K_M	half saturation concentrations for redox mediators	0.01 mg-M mg-x^{-1}
	$\mu_{e,max}$	maximum growth rates by the exoelectrogens	0.197 day^{-1}
	$\mu_{m,max}$	maximum growth rates by the methanogens	0.1 day^{-1}
	M_{total}	total mediator fraction per exoelectrogen	0.05 mg-M mg-x^{-1}
	Y_M	mediator yield	22 mg-M mg-S^{-1}
	γ	mediator molar mass	663400 mg-M mole-M^{-1}
	F	Faraday constant	96485 C mol^{-1}
	β	buffer efficiency of the anolyte	9.2730711×10^{-7}
	CE	coulombic efficiency	0.5731
	Y_{H2}	cathodic efficiency	0.4748
	R_{min}	the lowest observed internal resistance	90 Ω
	R_{max}	the highest observed internal resistance	2000 Ω
	K_R	a constant that determines the curve steepness	0.0818 L mg-x^{-1}
	ε	a constant that affects the current	0.0001 mg-M mg-x^{-1}

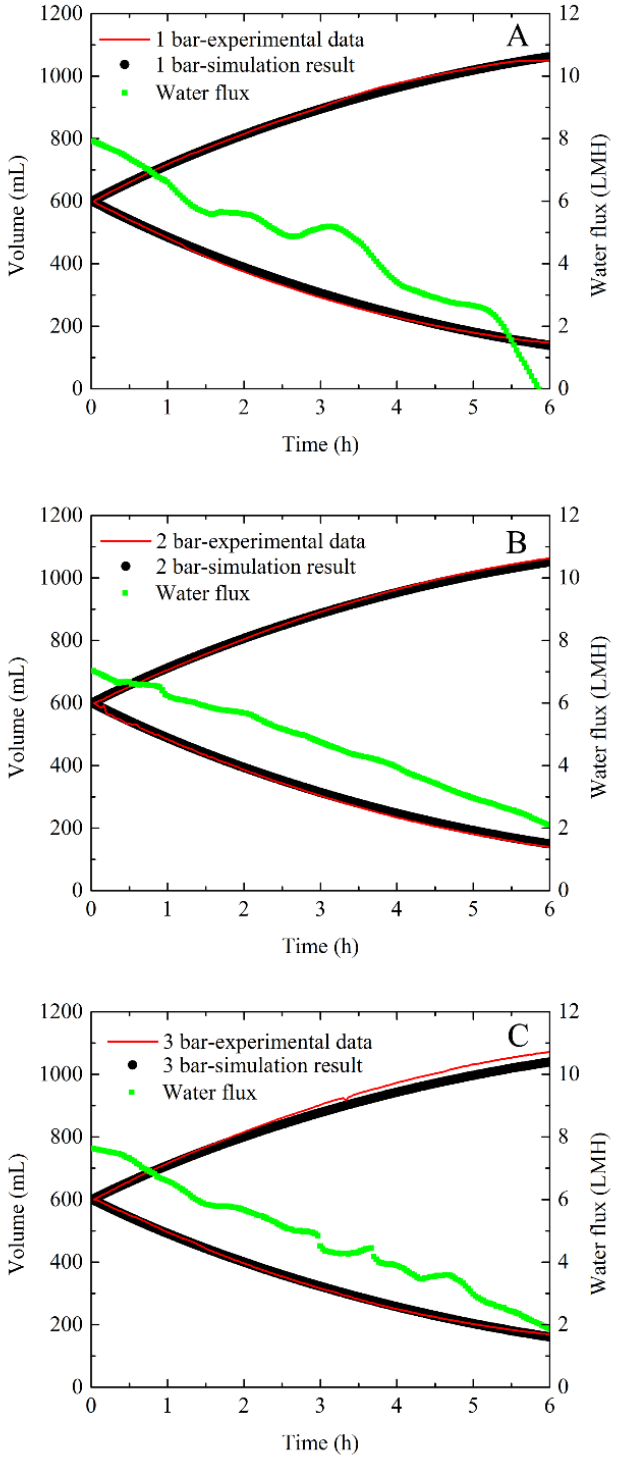

Figure E1 Experimental data and simulation results of draw (increase over time), feed volume (decrease over time) and water flux at (A) 1 bar, (B) 2 bar and (C) 3 bar.

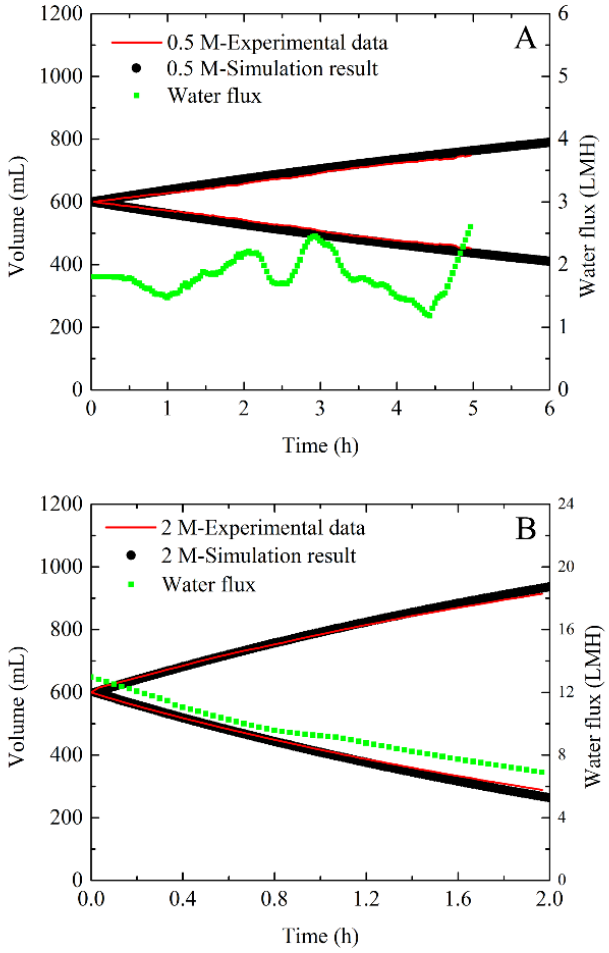

Figure E2 Experimental data and simulation results of draw (increase over time), feed volume (decrease over time) and water flux with (A) 0.5 and (B) 2.0 M NaCl.

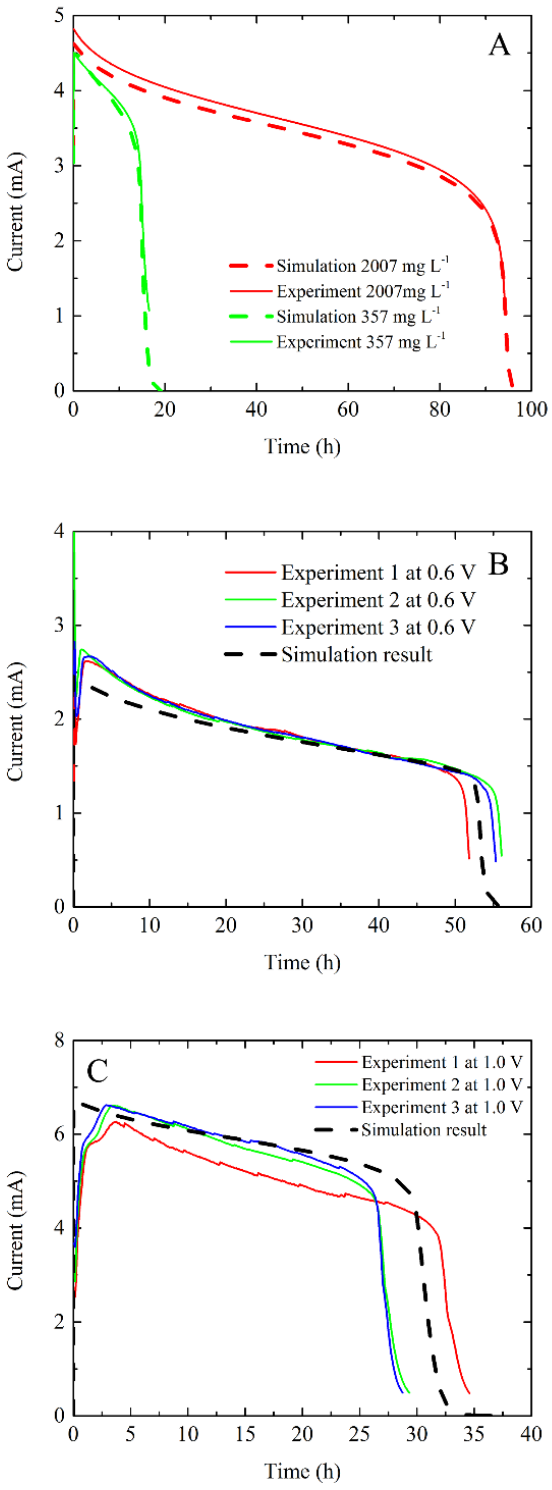

Figure E3 (A) Experimental data and simulation result of current generation in the MEC with 357 and 2007 mg L^{-1} substrate in the MEC anolyte, and at the external voltage of (B) 0.6 and (C) 1.0 V.

Appendix F Supplemental Information for Chapter 9

Table F1 Primer sequence and annealing temperature.

Gene	Primer	Sequence	Annealing T (ºC)	Amplicon size (bp)	Reference
16S rRNA	1369F 1492R	CGGTGAATACGTTCYCGG GGWTACCTTGTTACGACTT	60	142	[461]
*uid*A	UAL1939b UAL2105b	ATGGAATTTCGCCGATTTTGC ATTGTTTGCCTCCCTGCTGC	60	187	[462]
intI	HS463a HS464	CTGGATTTCGATCACGGCACG ACATGCGTGTAAATCATCGTCG	60	473	[463]
sulI	sulI-F sulI-R	CGCACCGGAAACATCGCTGCAC TGAAGTTCCGCCGCAAGGCTCG	69.6	163	[422]
tet(E)	tetE-F tetE-R	GTTATTACGGGAGTTTGTTGG AATACAACACCCACACTACGC	44	199	[464]

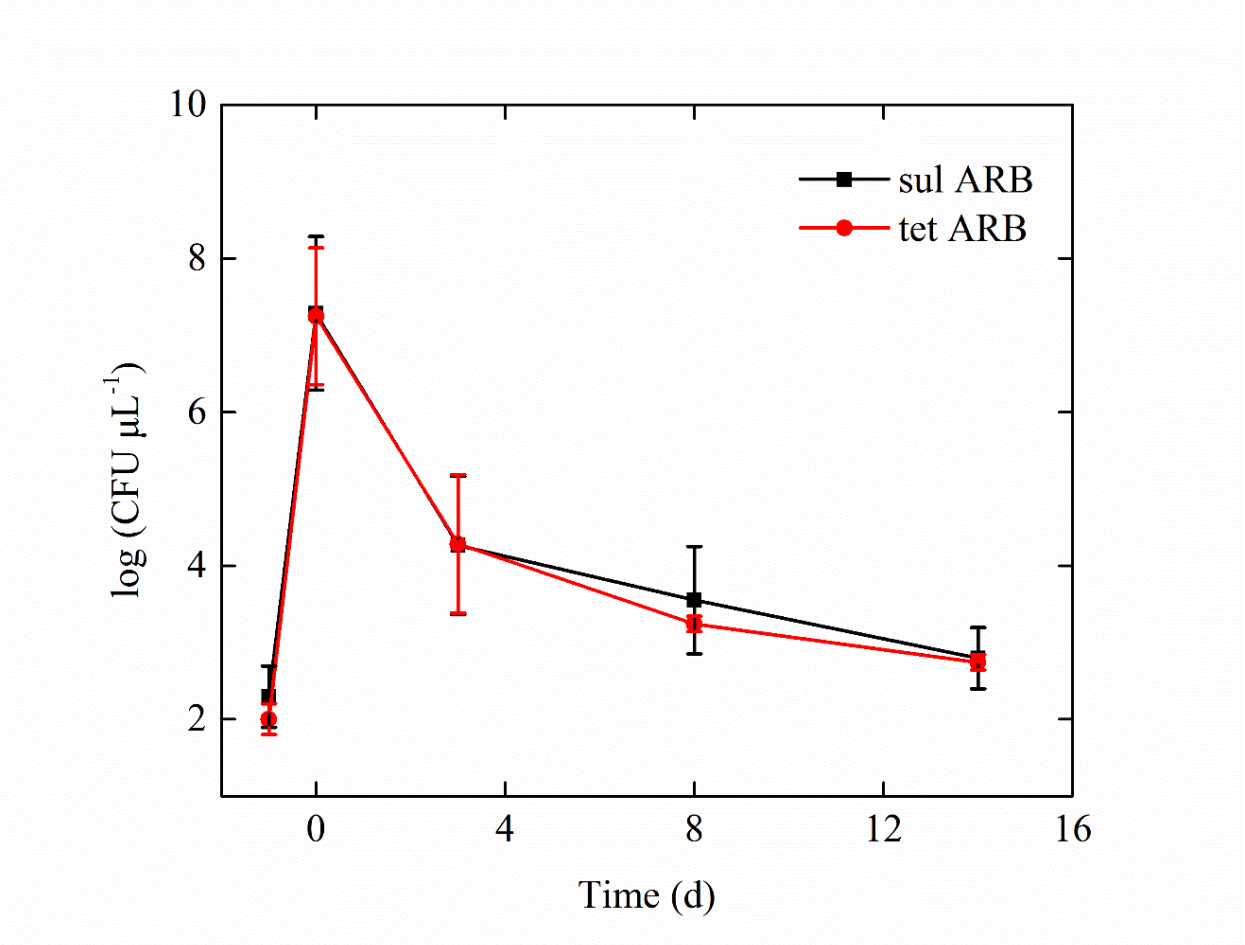

Figure F1 CFU of sulfonamide and tetracycline resistant bacteria in the BES effluent after 14 days of operation without dosing antibiotic resistant *E. coli*.

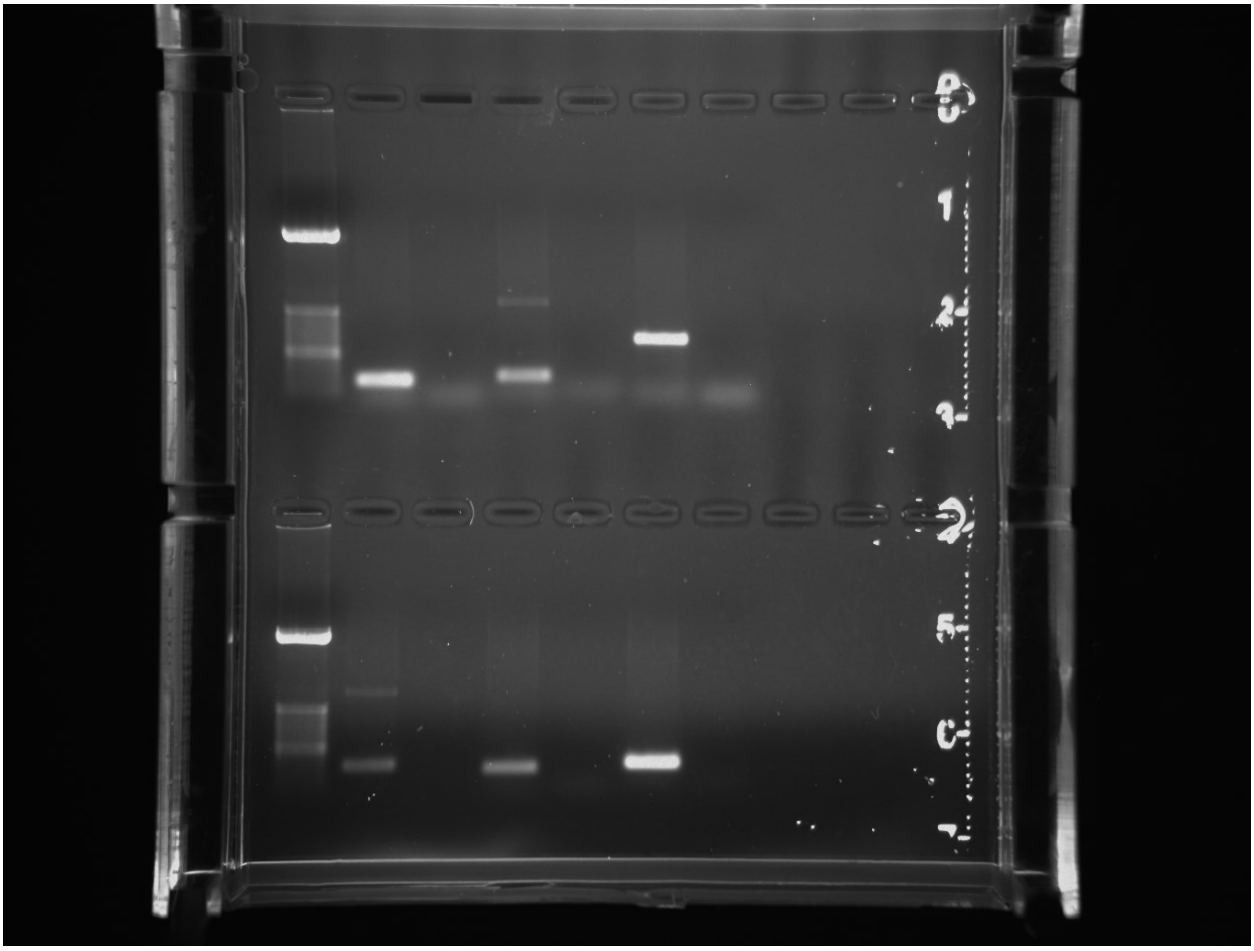

Figure F2 Gel electrophoresis of PCR products of ARGs measure contained in the DNA extract of pure c. First line (left to right): 1 kb ladder, 16S rRNA gene, blank, *uid*A, blank, *int*I1, blank. Second line (left to right): 1 kb ladder, *tet*E, blank, *sul*I, blank, *sul*II (not studied in this work), blank.